sustainability

Sustainable Development of Energy, Water and Environment Systems (SDEWES 2021)

Edited by

Oz Sahin and Edoardo Bertone

Printed Edition of the Special Issue Published in *Sustainability*

www.mdpi.com/journal/sustainability

MDPI

Sustainable Development of Energy, Water and Environment Systems (SDEWES 2021)

Sustainable Development of Energy, Water and Environment Systems (SDEWES 2021)

Editors

Oz Sahin
Edoardo Bertone

MDPI • Basel • Beijing • Wuhan • Barcelona • Belgrade • Manchester • Tokyo • Cluj • Tianjin

Editors

Oz Sahin
Griffith University
Australia

Edoardo Bertone
Griffith University
Australia

Editorial Office
MDPI
St. Alban-Anlage 66
4052 Basel, Switzerland

This is a reprint of articles from the Special Issue published online in the open access journal *Sustainability* (ISSN 2071-1050) (available at: https://www.mdpi.com/journal/sustainability/special_issues/SDEWES_2021_Sustainability).

For citation purposes, cite each article independently as indicated on the article page online and as indicated below:

LastName, A.A.; LastName, B.B.; LastName, C.C. Article Title. *Journal Name* **Year**, *Volume Number*, Page Range.

ISBN 978-3-0365-6063-2 (Hbk)
ISBN 978-3-0365-6064-9 (PDF)

Contents

About the Editors

Oz Sahin

Oz Sahin is a systems modeller with specialised expertise in a range of modelling approaches to various issues of natural resource management, risk assessment and climate change adaptation. His research interests include: sustainable built environment; climate change adaptation risk assessment; ecosystem based approaches; integrated water, energy and climate modelling; integrated decision support systems using coupled system dynamics and GIS modelling; Bayesian network modelling, multiple criteria decision analysis, and operational research methods and models. He is currently working as senior modeller at the University of Queensland (School of Public Health, Faculty of Medicine) and Griffith University (Griffith Climate Change Response Program and Cities Research Institute).

Edoardo Bertone

Edoardo Bertone is a senior lecturer at the School of Engineering & Built Environment at Griffith University. His research interests include data-driven modelling, Bayesian network and System dynamics modelling applied to the water resources management, the water–energy nexus, and environmental health and climate change adaptation fields.

sustainability

Editorial

Sustainable Development of Energy, Water and Environment Systems (SDEWES)

Oz Sahin [1,2,3,*] and Edoardo Bertone [1,2,4]

[1] School of Engineering and Built Environment, Griffith University, Southport, QLD 4222, Australia
[2] Cities Research Institute, Griffith University, Southport, QLD 4222, Australia
[3] School of Public Health, Faculty of Medicine, The University of Queensland, Herston, QLD 4006, Australia
[4] Australian Rivers Institute, Griffith University, Nathan, QLD 4111, Australia
* Correspondence: o.sahin@griffith.edu.au

Earth's natural systems provide essential resources such as water, food, energy, and materials that we all are dependent upon. These resources would be depleted if they are consumed at a faster rate than their replacement. Overpopulation, overconsumption, deforestation, mining of minerals, erosion, pollution, and contaminations are the main causes of the depletion of natural resources.

Additionally, the planet is more than just a source of fundamentals: we also rely on Earth's systems to assimilate our waste, cycle nutrients, and provide a climate and conditions favorable for our survival. Inefficient use of materials usually results in considerable waste generation. Once generated, waste should be handled by utilizing a range of methods including recycling, reuse, treatment, energy recovery and storage.

Importantly, our activities are connected to environmental effects such as air and water pollution, climate change, and declining biodiversity. In particular, human actions on water, food, energy, waste, and urbanization have significant impacts on the environment. Such impacts both raise concerns about the future and set the stage for understanding how our own behaviors and practices can reduce such effects. As highlighted by UNEP [1], if we continue consuming our resources in the same way as today, 180 billion tons of material would be needed to meet the global demand by 2050. Consequently, this ever-increasing demand for natural resources would potentially escalate local conflicts such as those observed in areas where mining competes with farming and urban development. Our individual and collective choices that affect the environment determine whether our future will be sustainable. Decisions such as where we live, how we live, how we power our cities and industries, how we dispose of our waste, and how we use our limited water resources will play important roles in building a sustainable future.

Sustainable development has been defined by the UN [2] as "*developments that meet the needs of the present without compromising the ability of future generations to meet their own needs*." That is, the management of natural resources in ways that do not diminish or degrade our planet's ability to provide them in the future. Although the definition is short, it is not simple. It requires that we select and think ahead to a specific goal (what we aim to sustain) and also consider the factors that will affect our ability to achieve that goal. To make decisions that will help us meet our goal, we will need to answer questions such as: What kind of uses and benefits are we trying to sustain? What sorts of factors affect the continuation of those uses and benefits?

Engaging deeply with sustainability also takes us beyond environmental science, into other fields of inquiry. Science alone cannot tell us what kind of future we ought to work toward, what ought to be sustained, or how environmental benefits and harms ought to be distributed in society. Questions like these, and the decisions and actions that stem from them, invoke values. Therefore, in this Special Issue, several articles present relevant tools and concepts from a range of different perspectives.

Citation: Sahin, O.; Bertone, E. Sustainable Development of Energy, Water and Environment Systems (SDEWES). *Sustainability* **2022**, *14*, 14184. https://doi.org/10.3390/su142114184

Received: 6 October 2022
Accepted: 27 October 2022
Published: 31 October 2022

In 2002, the first Sustainable Development of Energy, Water, and Environment Systems (SDEWES) Conference was held in Dubrovnik, Croatia. Since then, a total of 21 conferences around the world have been organized to address the above-mentioned issues. In 2021, the 16th SDEWES conference was held, from October 10 to 15 in Dubrovnik, Croatia. The conference brought together around 630 scientists, researchers, and experts in the field of sustainable development from 58 countries.

The tradition of SDEWES conferences is that, after each event, the authors of the most valuable papers are invited to publish their research results in Special Issues of high-ranking journals. Seven papers presented at the conference were selected for this Special Issue of *Sustainability* as reviewed below.

The first contribution to this Special Issue was provided by Serna-Loaiza et al. [3]. They acknowledge the importance of biorefineries for future sustainable societies, and they conducted experiments and analyses to identify optimal conditions for an important pre-treatment step, namely the liquid-hot-water. After running different experiments, they found the ideal temperature and duration minimizing the degradation products and lignin hydrolysis. By applying such an inclusive approach where lignin hydrolysis is analyzed within the liquid-hot-water pre-treatment processes, this study allows for more integrated decisions that value all the different lignocellulosic components of wheat straw. The same TU Wien team, this time led by Adamcyk, conducted further experimental work on lignin in the fourth Special Issue contribution, looking at the effect of temperature on the precipitation of colloidal lignin particles [4]. The different results depending on temperature and initial concentration pave the way for future research in the optimization of lignin precipitation processes. Lignin is an abundant biopolymer, with several prospective applications as a material, such as in sunscreens, emulsifiers and food packaging, thus making it more efficient to be produced and can increase its use.

In the second contribution, Papapolymerou and colleagues tackle existing issues with respect to microalgae and anaerobic digestate [5]. For a sustainable society, founded on principles of the circular economy, new further applications and uses of the nutrient-rich anaerobic digestate, produced by biogas plants, should be explored. While studies already exist, assessing the economic feasibility of using anaerobically digested sludge as fertilizer, their results are usually conditions- and location-dependent [6], in turn implying that more potential uses may provide effective, suitable alternatives when/where appropriate. As such, this study assesses the effect of adding the digestate to the growth medium of a specific microalgae species and checks how its growth rate is affected. Results were promising towards future higher uptake of anaerobic digestate as a raw material for microalgae growth media formulation, thus potentially leading to higher biomass production.

Another advancement in relation to waste minimization associated with novel products is presented in the third Special Issue contribution, by Daza-Serna and colleagues [7]. Acknowledging the increasing demand for erythritol as a sugar substitute, they assess through experiments the potential of electrodialysis as a more efficient method for ions removal and recovery, in order to develop a cleaner, optimized industrial process for erythritol production. Although with relatively low efficiency values, implying the need for more research into improved energy utilization, desalination of 96% was achieved, making electrodialysis an attractive process for this application, worth future investigation. With the three pillars of sustainability (environmental, economic, and social) typically interconnected, here the authors show the importance of public awareness to increase the uptake of new technologies and ideas.

A very different, but nonetheless intriguing, research work linking current biotechnologies and future sustainable societies was provided in the fifth contribution, by You et al. [8]. With cities and communities becoming increasingly reliant on digital tools and technologies, the related power consumption is nothing but negligible. In the study, a “bio-digital” interface powered by microbial fuel cells was developed and continuously operated over one year, producing enough power to be self-sufficient in relation to data logging, transmission, LED and more.

Arguably the greatest opportunities for energy efficiency benefits still pertain to the building sector, due to their large share of total energy consumption. As such, this was the focus of Novelli et al. in the sixth contribution to this Special Issue [9]. More specifically, they simulated a medium-scale commercial office building according to the Quality-Matched Energy Flows framework, with positive implications for lighting demands, cooling, and heating loads, peak demands, net energy use, operational costs, and design considerations. Significant energy and cost reduction were modelled, though remained considerable, thus highlighting an opportunity for further research. Overall, buildings will remain a central focus of sustainability research, due to not only their high energy footprint, but also their related construction and demolition waste, which has prompted research into potential waste trading schemes and a more sustainable project/construction management process [10]. In addition, less commonly used materials will need to be considered more often as an alternative to concrete and steel, which are linked to significant embodied energy, water and carbon. For instance, recent studies have analyzed the footprint of wooden houses in relation to indoor environment quality risks and life cycle assessment [11].

The Special Issue concludes with its seventh contribution, by He and all, which mainly deals with economic aspects of sustainability [12]. Specifically, a novel mathematical modelling approach was developed and applied to assess African countries' petroleum investment environment. A similar study, though utilizing a more traditional multi-criteria decision approach, recently assessed the merits of different electricity generation technologies for Niger [13]. Applying credible, reliable, and robust modelling approaches, especially those that can deal with and quantify uncertainty, together with effective data collection methods [14], will be increasingly crucial for future studies in all of the several interconnected fields of research related to the "Sustainable Development of Energy, Water and Environment Systems". It is argued that more systematically applying a system thinking approach, could help researchers and the society as a whole to understand the interactions among sustainable development goals, and thus their synergies and tradeoffs [15,16], in turn facilitating the achievement of the ambitious, but crucial, global targets.

This Special Issue of *Sustainability* overviews the selected papers submitted to the SDEWES Conferences in 2020 and 2021. These papers address the issues in the fields of sustainable development, energy, water, buildings, infrastructure, and waste management. Translating the contributions of these papers into impacts is highly important for developing policies and strategies for a sustainable future through gaining knowledge and further increasing public awareness. The editors of this Special Issue believe that the papers published here will be of interest to the readership of *Sustainability*. Future SDEWES conferences will maintain the tradition of disseminating new research methods and findings on sustainability. Readers are referred to the International Centre for Sustainable Development of Energy, Water, and Environment Systems (SDEWES) for information on the upcoming events [17].

Author Contributions: Conceptualization, E.B. and O.S.; methodology, E.B. and O.S.; investigation, E.B. and O.S.; resources, E.B. and O.S.; writing—original draft preparation, E.B. and O.S.; writing—review and editing, E.B. and O.S.; project administration, E.B. and O.S. All authors have read and agreed to the published version of the manuscript.

Funding: This research received no external funding.

Conflicts of Interest: The authors declare no conflict of interest.

References

1. UN Environment Programme. Available online: https://www.unep.org/news-and-stories/press-release/worldwide-extraction-materials-triples-four-decades-intensifying (accessed on 15 July 2022).
2. Sustainable Development Goals. Available online: https://www.un.org/sustainabledevelopment/development-agenda/ (accessed on 31 July 2022).
3. Serna-Loaiza, S.; Dias, M.; Daza-Serna, L.; de Carvalho, C.C.; Friedl, A. Integral analysis of liquid-hot-water pretreatment of wheat straw: Evaluation of the production of sugars, degradation products, and lignin. *Sustainability* **2022**, *14*, 362. [CrossRef]

4. Adamcyk, J.; Serna-Loaiza, S.; Beisl, S.; Miltner, M.; Friedl, A. Influence of temperature and lignin concentration on formation of colloidal lignin particles in solvent-shifting precipitation. *Sustainability* **2022**, *14*, 1219. [CrossRef]
5. Papapolymerou, G.; Kokkalis, A.; Kasiteropoulou, D.; Gougoulias, N.; Mpesios, A.; Papadopoulou, A.; Metsoviti, M.N.; Spiliotis, X. Effect of anaerobic digestate on the fatty acid profile and biodiesel properties of chlorella sorokiniana grown heterotrophically. *Sustainability* **2022**, *14*, 561. [CrossRef]
6. Tesfamariam, E.H.; Ogbazghi, Z.M.; Annandale, J.G.; Gebrehiwot, Y. Cost–benefit analysis of municipal sludge as a low-grade nutrient source: A case study from South Africa. *Sustainability* **2020**, *12*, 9950. [CrossRef]
7. Daza-Serna, L.; Knežević, K.; Kreuzinger, N.; Mach-Aigner, A.R.; Mach, R.L.; Krampe, J.; Friedl, A. Recovery of salts from synthetic erythritol culture broth via electrodialysis: An alternative strategy from the bin to the loop. *Sustainability* **2022**, *14*, 734. [CrossRef]
8. You, J.; Mendis, A.; Greenman, J.; Freeman, J.; Wolff, S.; Armstrong, R.; Hughes, R.; Ieropoulos, I.A. Development of a bio-digital interface powered by microbial fuel cells. *Sustainability* **2022**, *14*, 1735. [CrossRef]
9. Novelli, N.; Shultz, J.S.; Aly Etman, M.; Phillips, K.; Vollen, J.O.; Jensen, M.; Dyson, A. Towards energy-positive buildings through a quality-matched energy flow strategy. *Sustainability* **2022**, *14*, 4275. [CrossRef]
10. Borg, R.; Dalli Gonzi, R.; Borg, S.P. Building sustainably: A pilot study on the project manager's contribution in delivering sustainable construction projects—A maltese and international perspective. *Sustainability* **2020**, *12*, 10162. [CrossRef]
11. Vilčeková, S.; Harčárová, K.; Moňoková, A.; Burdová, E.K. Life cycle assessment and indoor environmental quality of wooden family houses. *Sustainability* **2020**, *12*, 10557. [CrossRef]
12. He, H.; Li, W.; Xing, R.; Zhao, Y. An evaluation of the petroleum investment environment in african oil-producing countries based on combination weighting and uncertainty measure theory. *Sustainability* **2022**, *14*, 5882. [CrossRef]
13. Bhandari, R.; Arce, B.E.; Sessa, V.; Adamou, R. Sustainability assessment of electricity generation in niger using a weighted multi-criteria decision approach. *Sustainability* **2021**, *13*, 385. [CrossRef]
14. Vujadinović, R.; Jovanović, J.Š.; Plevnik, A.; Mladenovič, L.; Rye, T. Key challenges in the status analysis for the sustainable urban mobility plan in Podgorica, Montenegro. *Sustainability* **2021**, *13*, 1037. [CrossRef]
15. Moallemi, E.A.; Hosseini, S.H.; Eker, S.; Gao, L.; Bertone, E.; Szetey, K.; Bryan, B.A. Eight archetypes of sustainable development goal (SDG) synergies and trade-offs. *Earth's Future* **2022**, *10*, e2022EF002873. [CrossRef]
16. Moallemi, E.A.; Bertone, E.; Eker, S.; Gao, L.; Szetey, K.; Taylor, N.; Bryan, B.A. A review of systems modelling for local sustainability. *Environ. Res. Lett.* **2021**, *16*, 113004. [CrossRef]
17. SDEWES Centre. Available online: https://www.sdewes.org (accessed on 31 July 2022).

sustainability

MDPI

Article

Integral Analysis of Liquid-Hot-Water Pretreatment of Wheat Straw: Evaluation of the Production of Sugars, Degradation Products, and Lignin

Sebastian Serna-Loaiza [1],*, Manuel Dias [2,3], Laura Daza-Serna [1], Carla C. C. R. de Carvalho [2,3] and Anton Friedl [1]

[1] Institute of Chemical, Environmental and Bioscience Engineering, Technische Universität Wien, 1060 Vienna, Austria; laura.serna@tuwien.ac.at (L.D.-S.); anton.friedl@tuwien.ac.at (A.F.)
[2] iBB—Institute for Bioengineering and Biosciences, Department of Bioengineering, Instituto Superior Técnico, Universidade de Lisboa, Av. Rovisco Pais, 1049-001 Lisboa, Portugal; manuel.francisco.nunes.dias@tecnico.ulisboa.pt (M.D.); ccarvalho@tecnico.ulisboa.pt (C.C.C.R.d.C.)
[3] Associate Laboratory i4HB—Institute for Health and Bioeconomy, Instituto Superior Técnico, Universidade de Lisboa, Av. Rovisco Pais, 1049-001 Lisboa, Portugal
* Correspondence: sebastian.serna@tuwien.ac.at; Tel.: +43-1-58801-166262

Abstract: Developing sustainable biorefineries is an urgent matter to support the transition to a sustainable society. Lignocellulosic biomass (LCB) is a crucial renewable feedstock for this purpose, and its complete valorization is essential for the sustainability of biorefineries. However, it is improbable that a single pretreatment will extract both sugars and lignin from LCB. Therefore, a combination of pretreatments must be applied. Liquid-hot-water (LHW) is highlighted as a pretreatment for hemicellulose hydrolysis, conventionally analyzed only in terms of sugars and degradation products. However, lignin is also hydrolyzed in the process. The objective of this work was to evaluate LHW at different conditions for sugars, degradation products, and lignin. We performed LHW at 160, 180, and 200 °C for 30, 60, and 90 min using wheat straw and characterized the extract for sugars, degradation products (furfural, hydroxymethylfurfural, and acetic acid), and lignin. Three conditions allowed reaching similar total sugar concentrations (~12 g/L): 160 °C for 90 min, 180 °C for 30 min, and 180 °C for 60 min. Among these, LHW performed at 160 °C for 90 min allowed the lowest concentration of degradation products (0.2, 0.01, and 1.4 g/L for furfural, hydroxymethylfurfural, and acetic acid, respectively) and lignin hydrolysis (2.2 g/L). These values indicate the potential use of the obtained sugars as a fermentation substrate while leaving the lignin in the solid phase for a following stage focused on its extraction and valorization.

Keywords: biorefineries; hemicellulose; lignin; liquid hot water; wheat straw

Citation: Serna-Loaiza, S.; Dias, M.; Daza-Serna, L.; de Carvalho, C.C.C.R.; Friedl, A. Integral Analysis of Liquid-Hot-Water Pretreatment of Wheat Straw: Evaluation of the Production of Sugars, Degradation Products, and Lignin. *Sustainability* **2022**, *14*, 362. https://doi.org/10.3390/su14010362

Academic Editors: Oz Sahin and Edoardo Bertone

Received: 2 December 2021
Accepted: 23 December 2021
Published: 30 December 2021

1. Introduction

Developing sustainable biorefineries is urgent to address the fossil-based environmental impacts and transition to a sustainable model [1]. Lignocellulosic biomass is a critical renewable feedstock to achieve this purpose. However, the resistance to degradation of biomass still represents a challenge to effectively fractionate its different components: cellulose, hemicellulose, and lignin [2,3]. Besides, the overall valorization of biomass is essential for biorefinery sustainability, including the valorization of hemicellulose and lignin [4]. This would provide two different platforms for value-added products, and cellulose could still be valorized either as a fiber or through enzymatic conversion [5].

In many cases, the ultimate goal of the pretreatment stage is to deconstruct the lignin−hemicellulose complex and increase cellulose availability. However, the three fractions have valorization potential, and pretreatments should be designed to use hemicellulose and lignin. One of the major challenges in this regard is the simultaneous valorization of sugars from the hemicellulose fraction and lignin valorization [6].

Multiple pretreatment clusters focused on the deconstruction of the lignocellulosic matrix have been proposed. Each of these technologies has advantages and disadvantages [7]. Liquid Hot Water (LHW) uses only water as a reagent, but on the other hand, it requires high amounts of energy for heating and cooling. Similarly, steam explosion uses only water, but it requires higher pressures than LHW, which implies higher energy consumption. Organosolv pretreatment uses an aqueous solution of an organic solvent, which allows solubilizing both hemicellulose and lignin. However, the process feasibility is strictly related to the recovery of the solvent in a distillation setup. Alkaline pretreatments are also used for a similar purpose, such as the Organosolv process. However, the concentrations of alkalis, such as sodium hydroxide and sodium carbonate, lead to higher corrosion, and alkali recovery is a challenging task. Among the pretreatments, LHW stands out for hemicellulose hydrolysis, using water as a reactant without further input of acids/bases. Besides, this pretreatment is auto-catalyzed by the acetic acid formed from the acetyl groups released from the hemicellulose backbone [8,9].

However, a single pretreatment to obtain simultaneously high sugar and lignin yields has not been found yet, and a combination of pretreatments is usually applied [5]. Previous studies have evaluated different combinations of pretreatments. Xia et al. (2020) evaluated LHW followed by sodium carbonate-oxygen pretreatment to improve the reed enzymatic saccharification [10]. Neves et al. (2016) and Rocha et al. (2012) studied steam explosion followed by alkaline pretreatment of sugarcane bagasse [11,12]. Tian et al. (2019) combined LHW with mechanical extrusion from rigid hardwood [13]. Wang et al. (2012) combined fungal treatment with LHW of white poplar [14]. Serna-Loaiza et al. (2021) combined LHW and Organosolv to produce sugars from the hemicellulose and hydrolyze the lignin from wheat straw. This work found that performing LHW before Organosolv increased the lignin extraction yield by 1.6-times (from 7 to 11 g/L in the OS-stage) [15]. Other authors have evaluated the same configuration, LHW followed by Organosolv, for different raw materials such as hazelnut shells [16] and corncobs [17].

This research trend shows the potential of pretreatment combinations as a strategy to valorize the different fractions of lignocellulosic biomass integrally. Nonetheless, a combination of pretreatments implicates analyzing every stage in terms of the different components to be extracted, as this will provide more detailed information to establish the mass balance of the process. Traditionally, LHW has been analyzed solely as a stage for hemicellulose hydrolysis, as this is its primary purpose. Hence, it is analyzed only in terms of sugar and respective degradation products. However, LHW also hydrolyses part of the lignin present in the feedstock. Therefore, it is necessary to analyze LHW from an integral perspective, including lignin hydrolysis. This information is essential to design subsequent pretreatment stages, mainly focused on the lignin fraction. Therefore, in the present work, LHW of wheat straw at multiple temperatures (160, 180, 200 °C) for different times (30, 60, 90 min) was performed and the extracts were analyzed for sugars, degradation products, and lignin concentration. The main goal of this study was to gain a better insight into which of the tested conditions allow obtaining a sugar hydrolysate with the highest sugar concentration and the lowest concentration of degradation products and extracted lignin. The lignin remaining in the solid phase could be extracted in a further process step.

2. Materials and Methods

2.1. Raw Material and Reagents

Wheat straw used in this work was harvested in 2019 (Margarethen am Moos, State of Lower Austria) and stored under dry conditions at room temperature. The straw was milled in a cutting mill, equipped with a 2 mm mesh. The raw material composition was 2.13%, 0.67%, 35.31%, 21.94%, 0.72%, 17.35%, 20.45%, and 1.09% (wt; dry basis) for arabinan, galactan, glucan, xylan, mannan, lignin, extractives, and ash, respectively [15]. The wheat straw used in this work corresponds to the same sample and batch as the one characterized in the cited study. In addition, it was selected as a test raw material due to its high content of hemicellulose and lignin, which is the main targeted lignocellulosic components for the experimental section. In addition, this raw material has been significantly studied for both processes, LHW and Organosolv [15,18–22], which shows the relevance of understanding more deeply the influence of LHW, including the lignin determination. The moisture content was 7.16 wt %. Ultra-pure water (18 MΩ/cm) was used for the LHW. Standards for carbohydrates (arabinose, galactose, glucose, xylose, and mannose), acetic acid (99.7%), 2-furaldehyde (furfural, 99%), hydroxymethylfurfural (HMF, 99%), and sulfuric acid (98%) were purchased from Merck (Darmstadt, Germany).

2.2. Process Condition and Description

LHW is generally performed in the temperature range between 160–240 °C during 30–120 min [23]. The present study chose low to intermediate values within these ranges: temperatures tested were 160, 180, and 200 °C, and selected times were 30, 60, and 90 min. Each combination of conditions was performed in triplicate. The time corresponds to the holding time, meaning that once the reactor reaches the desired temperature, the temperature is maintained constant for the fixed time.

LHW was carried out in a stainless steel pressurized autoclave (Zirbus, HAD 9/16, Bad Grund, Germany) with a capacity of 1 L and maximum temperature and pressure of 250 °C and 60 bar, respectively. The autoclave was equipped with a controller registering every second the inlet temperature of the reactor, which was used to calculate the severity factor. The reactor stirring speed was set to 200 rpm. The reactor was heated to the operating temperature and rapidly cooled down to room temperature after the defined holding time. At the end of the process, the sample was collected, and the solid and liquid fractions were separated using a hydraulic press (Hapa, HPH 2.5) at 200 bar. The liquid fraction was centrifuged (Sorvall, RC 6+) at 24,104× *g* for 20 min, and the supernatant was stored at 5 °C until further analysis. The density of the extract was determined using a density meter (DE45 DeltaRange, Mettler Toledo, Columbus, OH, USA).

The initial wet mass of wheat straw was approximately 32.31 g (corresponding to 30 g dry weight). The solid/liquid ratio was 1 g of dry solid per 11 g of solvent (solid loading of 8.3 wt %), while the added water was 327.69 g (after subtracting the water in the wet straw). The severity factor (R_0) was calculated using Equation (1) considering the heating (from 100 °C to the set temperature), temperature holding according to the set time, and cooling (from the set temperature to 100 °C), as shown in Equation (2). t is the time (min), $T(t)$ is the temperature (°C), and Total R_0 is the sum of the contribution of each stage to the severity factor. The constant "14.75" corresponds to an empirical parameter calculated assuming an overall reaction following first-order kinetics and Arrhenius relation of temperature [24]. This integral was solved by the trapezoidal rule shown in Equations (3) and (4) using the data collected by the reactor controller with at Δt of 1 s.

$$R_{0,i} = \int_0^t \exp\left(\frac{T(t) - 100}{14.75}\right) dt \tag{1}$$

$$\text{Total } R_0 = \log_{10} R_{0,Heating} \tag{2}$$

$$\int_a^b f(t)dt \approx (b - a) * \frac{f(a) + f(b)}{2} \tag{3}$$

$$\int_0^{t_{op}} f(t)dt \approx \sum_{i=0}^{t_{op}} \left(\Delta t * \frac{\exp\left(\frac{T_t - 100}{14.75}\right) + \exp\left(\frac{T_{t+\Delta t} - 100}{14.75}\right)}{2} \right) \tag{4}$$

2.3. Product Characterization

The liquid fraction was characterized for sugars (monomeric and total), degradation products (furfural, HMF, and acetic acid), and lignin (acid-soluble and acid-insoluble). Sugars and degradation products were characterized according to the NREL/TP-510-42623 [25].

Monomeric sugars were analyzed using high-performance ion-exchange chromatography (HPIEC-PAD) (DionexTM ICS-5000, Thermo Scientific, Waltham, MA, USA) with deionized water as eluent. The extract was hydrolyzed with diluted sulfuric acid at 120 °C and analyzed the sugars as monomers; this corresponded to the total sugars. Oligomeric sugars were calculated as the difference between total and monomeric sugars. A sugar recovery standard was used to account for losses. Furfural, HMF, and acetic acid were determined using HPLC (LC-20A HPLC system, Shimadzu, Kyoto, Japan), with UV and RI detection, with a Shodex SH1011 analytic column at 40 °C with 0.005 M H_2SO_4 as mobile phase. The extract was dried and analyzed for lignin determination according to the NREL/TP-510-42618. Acid insoluble lignin (AIL) was determined gravimetrically, and acid-soluble lignin (ASL) by UV/VIS absorption at 205 nm using a Shimadzu UV-1800 spectrophotometer [26].

3. Results

First, we present the calculated severity factors for the different temperature and time combinations. Then, we present the results for sugars, degradation products, and lignin in this respective order. Finally, we analyze the three indicators to identify the conditions that provide the highest sugar concentration, with the lowest concentration of degradation products and lignin.

3.1. Calculated Severity Factor

Table 1 shows the calculated severity factors for the different combinations of temperature and time. Due to the definition of Equation (1), an increase in the holding temperature influences more the severity factor than an increase in time. For example, increasing the holding time from 60 to 90 min, at 160 °C, increased the severity factor by 0.16, whereas increasing the temperature from 160 to 180 °C (at 60 min holding time) increased the severity factor by 0.60. Besides, as the holding time at a given temperature increased, the heating and cooling contribution decreased. Additionally, the cooling contribution could be neglected since, for all performed experiments, the cooling time was 9.0 ± 0.7 min and contributed 2.4 ± 0.7% to the total severity factor. Between the replicates, the actual time and respective standard deviations show only one condition with an error percentage of 7.9% (200 °C and 60 min), while the rest had errors below 3.9%.

Table 1. Calculated severity factors for the performed LHW extractions.

Temp (°C)	Aimed Holding Time (min)	Real Holding Time (min)	Severity Factor (R_0, min)	Contribution of Stages to the Severity Factor (%)		
				Heating	Holding	Cooling
160	30	30.7 ± 0.2	3.38 ± 0.02	16.4	79.4	4.2
	60	61.0 ± 0.3	3.61 ± 0.00	6.5	91.0	2.4
	90	90.2 ± 0.2	3.77 ± 0.01	5.7	92.3	2.0
180	30	31.6 ± 0.6	4.05 ± 0.02	20.6	76.1	3.2
	60	60.7 ± 0.3	4.22 ± 0.01	7.6	90.2	2.2
	90	91.1 ± 0.6	4.38 ± 0.01	5.3	93.1	1.7
200	30	30.6 ± 0.4	4.60 ± 0.04	20.8	76.1	3.1
	60	60.5 ± 0.3	4.81 ± 0.02	11.9	86.3	1.8
	90	87.1 ± 4.2	4.97 ± 0.02	12.6	86.2	1.2

3.2. Sugar Content

Table 2 shows the sugar concentrations, both monomeric and total, for the performed LHW extractions. As can be observed, the sugars with higher concentrations in increasing order were arabinose, glucose, and xylose. Galactose and mannose showed lower concentrations in all extraction conditions. This trend is in accordance with the composition previously shown in Section 2 for the used wheat straw [15]: the glucoarabinoxylan polymer is significantly more abundant than the galactomannan. We summed the respective C5 (arabinose and xylose) and C6 (galactose, glucose, and mannose) sugars to better represent the overall production of sugars at the different conditions.

Table 2. Sugar concentrations (monomeric and total) for the performed LHW extractions.

T (°C)	Time (min)	Severity Factor	Concentration (mg/L)									
			Arabinose		**Galactose**		**Glucose**		**Xylose**		**Mannose**	
			M	**T**	**M**	**T**	**M**	**T**	**M**	**T**	**M**	**T**
160	30	3.38	422 ± 23	987 ± 53	18 ± 1	385 ± 15	63 ± 7	1014 ± 17	58 ± 6	2146 ± 193	10 ± 1	165 ± 11
	60	3.61	582 ± 8	1465 ± 172	36 ± 1	616 ± 63	59 ± 0	1333 ± 144	105 ± 3	5526 ± 564	12 ± 0	335 ± 38
	90	3.77	666 ± 2	1499 ± 163	56 ± 2	660 ± 73	57 ± 3	1431 ± 161	186 ± 13	8063 ± 604	12 ± 1	366 ± 33
180	30	4.05	487 ± 18	923 ± 50	98 ± 2	580 ± 14	59 ± 2	1264 ± 33	670 ± 85	8852 ± 139	21 ± 2	304 ± 11
	60	4.22	439 ± 39	471 ± 13	158 ± 2	416 ± 12	105 ± 0	1621 ± 58	2181 ± 91	9678 ± 222	62 ± 4	334 ± 31
	90	4.38	205 ± 6	247 ± 29	156 ± 6	426 ± 50	168 ± 8	1655 ± 172	2771 ± 58	7868 ± 696	93 ± 22	362 ± 43
200	30	4.60	66 ± 4	73 ± 7	145 ± 1	149 ± 26	336 ± 13	1098 ± 115	1700 ± 59	1630 ± 49	105 ± 3	146 ± 19
	60	4.81	5 ± 2	0 ± 0	34 ± 4	47 ± 4	233 ± 12	640 ± 28	116 ± 16	172 ± 13	37 ± 3	68 ± 9
	90	4.97	1 ± 0	0 ± 0	7 ± 2	15 ± 5	135 ± 7	393 ± 26	40 ± 6	77 ± 3	18 ± 5	29 ± 1

M: Monomeric. T: Total.

Figure 1 shows the summed concentrations of C5 and C6 sugars for the different LHW pretreatment conditions. Most of the performed extractions have error percentages below 13%, except for monomeric mannose at 180 °C for 90 min (23%) and 200 °C for 90 min (26%), monomeric arabinose at 200 °C for 60 min (33%) and 200 °C for 90 min (26%), and monomeric/total galactose (both 33%) at 200 °C for 90 min. However, the average value at these conditions is low and close to the detection limit.

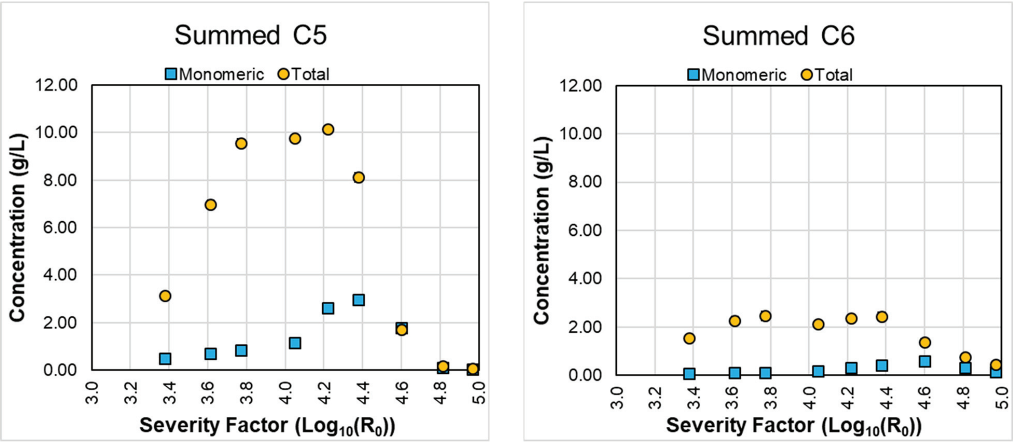

(**a**) (**b**)

Figure 1. *Cont.*

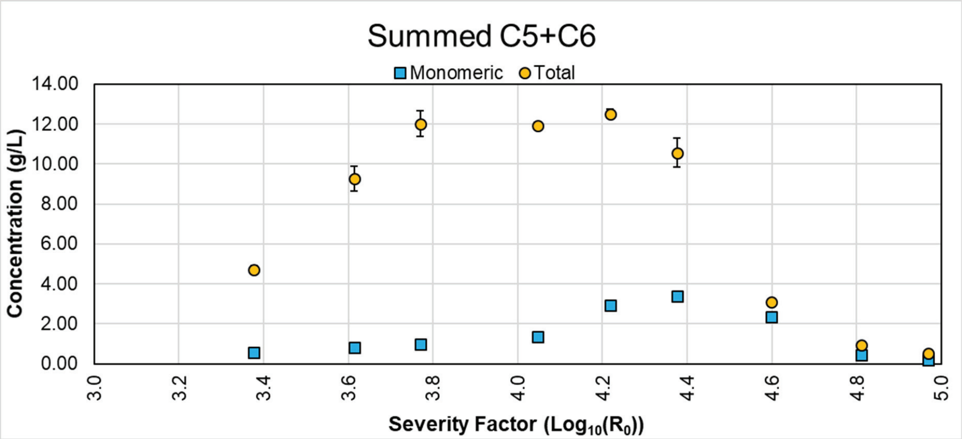

(**c**)

Figure 1. Summed concentrations of C5 and C6 sugars for the different LHW pretreatment conditions. Summed C5 (**a**), C6 (**b**), and C5 + C6 sugars (**c**).

LHW is a process mainly focused on the hydrolysis of hemicellulose. Thus, the expected concentrations of C5 sugars should be higher than that of C6 sugars. This was confirmed by the results presented in Figure 1a,b. Besides, in all conditions (except the extractions at 200 °C), the hydrolyzed sugars mainly consisted of oligomers (as observed by the difference between the blue bar corresponding to the monomeric sugars and the green bar for total sugars in Figure 1). Three conditions reached very similar concentrations of total sugars (~12.2 g/L): 160 °C for 90 min, 180 °C for 30 min, and 180 °C for 60 min. This same trend was observed for the total C5 sugar concentration (~10.0 g/L). After the last condition (180 °C for 60 min), the total sugar and C5 sugar concentrations decreased, converting the sugars into degradation products. This will be further discussed in the following section covering the degradation products. The total C6 sugar concentration reached similar concentrations in the range of severity factors between 3.61 (160 °C for 60 min) and 4.38 (180 °C for 90 min).

We found similar trends when comparing these results with other works published in the literature. Huang et al. (2017) evaluated isothermal LHW conditions for wheat straw, between 140–220 °C for 40 min. Within this temperature range, the values at 160, 180, and 200 °C for 40 min can be compared with those obtained in this published work: severity factors are similar (3.37, 3.96, and 4.55, respectively). They reported monomeric xylose concentrations of 1.3, 0.6, and 0.2 g/100 g of wheat straw and oligomeric xylose concentrations of 0.3, 4.9, and 2.0 g/100 g of wheat straw, respectively [27]. These values are within the same ranges found in our work. Carvalheiro et al. (2009) also evaluated isothermal LHW conditions, and comparable severity factors were achieved at 200 °C and 26 min: monomeric xylose and glucose concentrations of, respectively, 1.6 and 0.8 g/L were reported, which are within the ranges obtained in our work [19].

In terms of the usability of the obtained sugars, the obtained concentrations of monomeric sugars in the present work were considerably low, meaning that the hydrolysate should not be directed to microorganisms only able to metabolize monomeric xylose and glucose. This requires further steps of hydrolysis of the oligomeric sugars into monomers. Instead, the hydrolysate could be used for fermentation with microorganisms metabolizing monomeric and oligomeric sugars. Some studies have been carried out to produce, e.g., polyhydroxybutyrate and tetraether lipids [18,28]. In this context, three of the studied conditions reached similar levels of total sugars to be potentially used, namely, 160 °C for 90 min, 180 °C for 30 min, and 180 °C for 60 min. However, due to the different severity factors, each set of conditions has a different profile of degradation products, restricting their usage, as further explained in the following section.

3.3. Degradation Products

Figure 2 shows the concentrations of degradation products reached under each studied condition. The analysis of these components is relevant as they may condition future usages of the hydrolysates as a substrate for fermentation. We observed a steady increase in the concentration of acetic acid until a severity factor of 4.60 (200 °C for 30 min). Acetic acid is produced from the release of the acetyl groups connected to the hemicellulose matrix. This suggests that hemicellulose is hydrolyzed until the above severity factor is reached. However, even with the maximum acetic acid concentration reached in this work, ~3.2 g/L, the concentrations are below reported thresholds at which acetic acid inhibits microorganism growth (e.g., 7.5–15.0 g/L for yeast growth [29,30]).

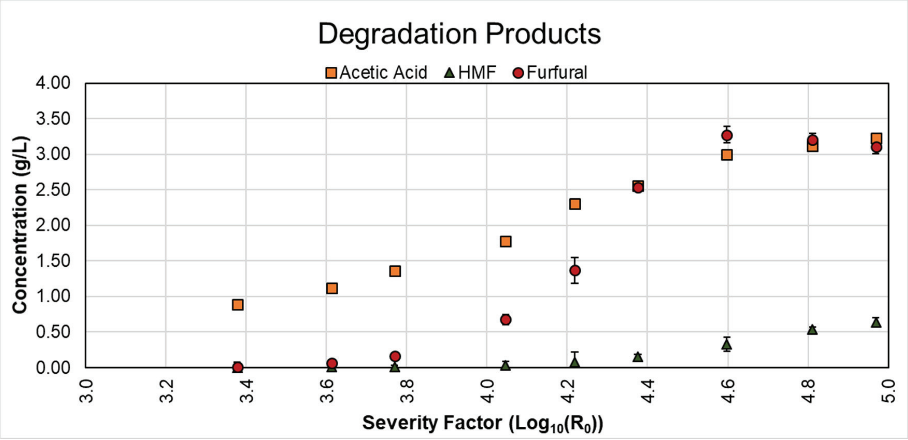

Figure 2. Concentration of degradation products for the different LHW pretreatment conditions.

Regarding HMF, significant concentrations only started to be reached at a severity factor of 4.22 (180 °C for 60 min), and it continued increasing steadily until reaching 0.5–0.6 g/L for the two final conditions studied in this work. This severity factor coincided with the decrease of C6 sugars, as observed in Figure 1b. According to HMF results from the dehydration of C6 sugars, meaning those above a severity factor of 4.22, the produced C6 sugars were degraded into HMF. Previous studies reported that the presence of HMF increases the duration of the lag phase for yeast [31], and significant growth inhibition (45%) has been observed at concentrations of 0.5 g/L [32,33]. This value was achieved in the present study using 200 °C for 60 min (severity factor: 4.81) or higher.

Regarding furfural, significant concentrations started to be reached at a severity factor of 3.77 (160 °C for 90 min), and it continued increasing steadily until reaching ~3.2 g/L at a severity factor of 4.60 (200 °C for 30 min). Its concentration remained nearly constant for the remaining conditions. Regarding furfural from C5 sugars dehydration, Figure 1a shows that, after a severity factor of 4.22 (180 °C for 60 min), the C5 concentration decreased, meaning that no C5 sugars were being hydrolyzed but were being degraded into furfural. In terms of inhibition thresholds, different authors reported growth inhibition and biomass yield decreases for yeast and bacteria with furfural concentrations between 0.5 and 1.5 g/L and higher [31,33,34]. This is a critical indicator to choose the conditions with furfural levels behind this concentration. Accordingly, the maximum severity factor that can be reached is 4.22 (180 °C for 60 min) in a conservative scenario taking the upper limit of the furfural inhibition threshold, or below 4.05 (180 °C for 30 min) for a stricter scenario taking the lower limit. These results are comparable with the values reported for wheat straw by Huang et al. (2017): furfural concentrations of 0.4, 0.1, and 0 g/L and acetic acid concentration of 2.1, 1.9, and 1 g/L at 160, 180, and 200 °C for 40 min were observed. At 180 °C for 60 min, concentrations of 0.2 and 1 g/L, for furfural and acetic acid, respectively, were attained [27].

3.4. Lignin

Generally, publications analyzing LHW present the results regarding sugar production and degradation products as a core section and cover other topics, mainly the resulting solid's enzymatic digestibility. However, creating an integral perspective that provides information on the lignin hydrolyzed by LHW is still missing, and this is essential to further design pretreatment stages focused on the lignin fraction. This section will now cover the obtained lignin hydrolysis yields under the different studied conditions, as shown in Figure 3.

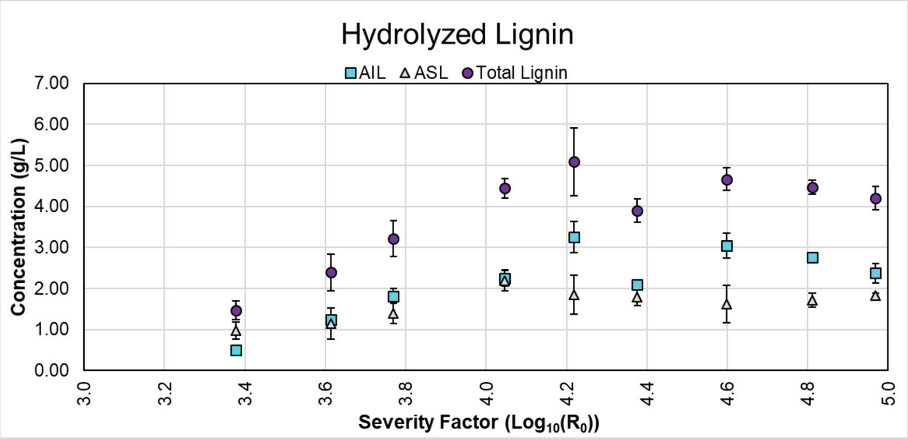

Figure 3. Concentration of hydrolyzed lignin for the different LHW pretreatment conditions tested. AIL: Acid Insoluble Lignin; ASL: Acid Soluble Lignin. Total lignin corresponds to the sum of AIL and ASL.

The goal regarding lignin should be to maintain it as much as possible in the solid fraction. We can observe that the total lignin increases steadily until reaching a maximum value between severity factors of 4.05 and 4.22 (180 °C for 30 min and 180 °C for 60 min, respectively) and then decreases. AIL followed this same trend, reaching a maximum value of 3.2 g/L at the same severity factor at which total lignin reached the maximum. A maximum lignin concentration with an increasing severity factor for LHW is explained because after a specific set of temperature and time (namely, a value of severity factor), the solubilized lignin re-condensates and would not be soluble anymore. This means the lignin would remain as part of the solid fraction. Therefore, once the LHW extraction is finished, the resulting mixture is pressed, and the extract is further centrifuged (as described in the methodology), the lignin would go to the solid fraction and the respective precipitate from centrifugation. Therefore, when the extract is characterized, even though the solid was submitted to a higher severity factor, this does not implicate that more lignin would remain solubilized in the extract. Compared to the initial value of lignin in the raw material, LHW conditions at 160 °C reached lignin solubilization yields between 10% and 15%, at 180 °C between 26% and 35%, and 200 °C between 16% and 29%. Based on this, the extractions carried out at 160 °C fulfilled the purpose of solubilizing less lignin. It is important to stress again that LHW is a process not meant to solubilize and valorize lignin but hemicellulose.

Therefore, the next step should be to couple the results from the three analyzed conditions, which will be done in the following section.

3.5. Integrated Analysis of Sugars, Degradation Products, and Lignin

This section focuses on integrating the results obtained in the previous sections. For this purpose, we will use the most relevant values from each section. To evaluate the extraction of sugars, we will take as base the total summed C5 + C6 sugars, as it was shown that the potential use of the LHW hydrolysate as fermentation substrate should be for microorganisms metabolizing both monomeric/oligomeric C5 and C6 sugars. We performed the analysis for the three conditions that reached higher total summed C5 + C6 sugars (160 °C for 90 min, 180 °C for 30 min, and 180 °C for 60 min). We observed that furfural was the component that reached critical concentrations at a lower severity factor when analyzing the degradation products. Therefore, we will use the concentration of furfural as the decision criteria. Regarding lignin extraction, we will use the total lignin extracted, given that this value reflects the entire amount removed from the solid matrix at given conditions. Figure 4 shows the combined results of total sugars, furfural, and total lignin for the three sets of conditions that allowed the higher total concentration of sugars.

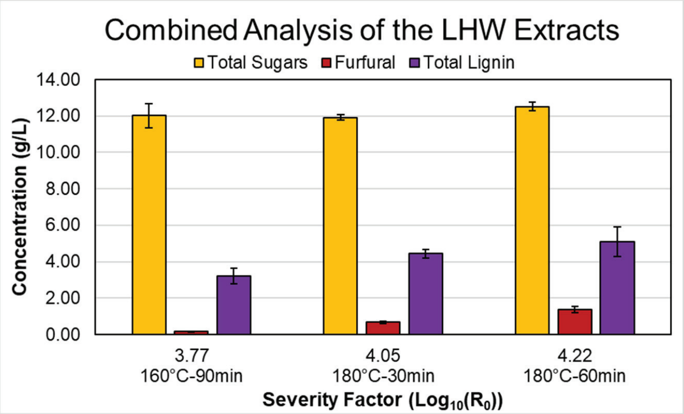

Figure 4. Combined analysis of sugars, degradation products, and lignin for the LHW pretreatment conditions. Total sugars correspond to the total summed C5 and C6 sugars. Total lignin corresponds to the sum of AIL and ASL.

Based on the primary goal of this study, to reach a high sugar concentration and low concentration of degradations products and extracted lignin, it is clear that performing the pretreatment at 160 °C for 90 min (severity factor of 3.77) rendered the best overall results. Sugar production reached 98% of the maximum achieved value (at 180 °C for 60 min), and on the other hand, furfural and lignin corresponded only to 11.8% and 43.9%, respectively. Therefore, the produced hydrolysate is below the inhibition threshold, and most of the lignin remains in the solid phase for further valorization. Based on the amount determined in the liquid extract for the extraction at 160 °C for 90 min and the wheat straw composition, we calculated the solid composition, assuming that all of the glucose corresponded to cellulose and the other characterized sugars corresponded to hemicellulose as shown in Figure 5. As observed, the remaining solid still contains around 80% of the lignin and 61% of the hemicellulosic sugars contained in the initial feedstock. Cellulose increased from 45.2 to 53.4 wt %, while hemicellulose and lignin decreased from 32.6 to 24.6 wt % and 22.2 to 22.0 wt %, respectively. This LHW solid could be used, for example, to replace lignin-rich pulps used in papermaking (e.g., mechanical pulps). On the other hand, wheat straw has been extensively studied for lignin production, and previous studies have shown that performing LHW before a delignification stage improves the extraction yield [5,15]. Therefore, LHW solids from wheat straw can be used further for lignin extraction, and this study case will be developed further in the next section.

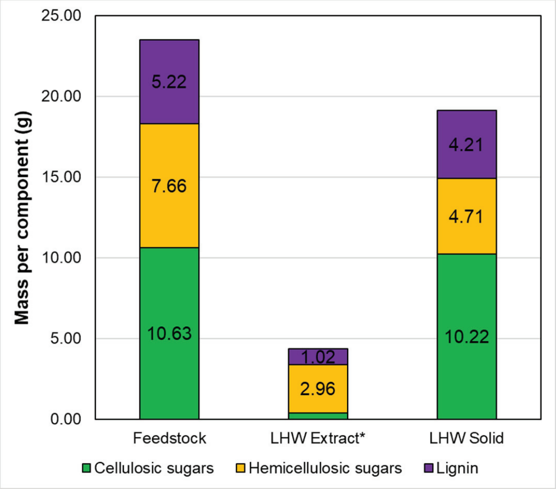

Figure 5. Absolute mass balance for cellulose, hemicellulose, and lignin in the feedstock, LHW extract, and the solid leaving the LHW stage for the LHW carried out at 160 °C for 90 min. * Cellulosic sugars for the LHW Extract are 0.41 g.

3.6. Future Outlook: Study Case—Theoretical Valorization of the Solids for Lignin Hydrolysis

Considering the previous results and following the strategy proposed by Serna-Loaiza et al. (2021), we decided to evaluate theoretically the sequential hydrolysis of hemicellulose and lignin using LHW followed by Organosolv (OS) [15]. These authors reached hydrolyzed lignin concentrations of ~7 g/L in the standalone Organosolv, and this value increased to ~11 g/L when LHW was performed before the OS. We evaluated the scenario of subsequent valorization of the solids remaining after the LHW using the latter concentration (11 g/L). The conditions chosen for the LHW stage were 160 °C for 90 min. Figure 6 shows the mass balances for the LHW followed by OS (LHW→OS).

Based on the composition and moisture of the solid leaving the LHW stage, we calculated the solvent required for the OS stage (Figure 6a). We used the same proportions proposed by Serna-Loaiza et al. (2021) (S/L ratio of 1 g dry matter per 1 mL of solvent, 60 wt % ethanol as solvent), and the reached concentrations of sugars, degradation products, and lignin [15]. We calculated the composition of the lignin extract and the respective solid with this information. We proceeded to calculate the mass balance using the density of the extracts (1.01 g/mL and 0.9 g/mL for sugar and lignin extracts, respectively). We provide all the information related to each extraction's mass balance in the Supplementary Materials. These results correspond to a valorization outlook of the solids after LHW pretreatment, as the specific values obtained from the OS extraction of the LHW solid depend on variables and conditions that can result only from carrying out the specific experiments.

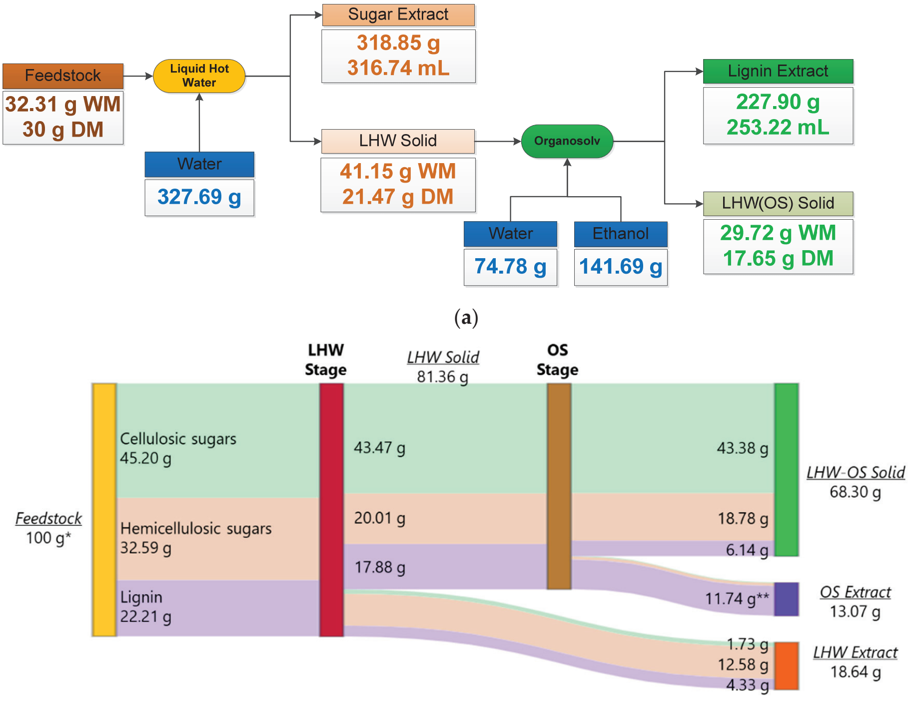

(**a**)

(**b**)

Figure 6. Mass balances and distributions of the streams for the theoretical LHW-OS combination. (**a**) General mass balance of the LHW and OS stages. (**b**) Distribution of cellulose, hemicellulose, and lignin along the stages of the theoretical LHW-OS combination. * Feedstock composition only corresponds to the amount of cellulose, hemicellulose, and lignin. ** The amounts of cellulose and hemicellulose in the OS extract are below 1.2 g and cannot be visualized adequately in the figures.

Figure 6b shows the distribution of cellulose, hemicellulose, and lignin along the LHW and OS stages. We can observe an excellent distribution of the lignocellulosic components along the different streams; an LHW extract, an OS extract, and a final solid mainly composed of hemicellulosic sugars, and cellulose, respectively. Cellulose conversion into sugars corresponded only to 5%, meaning that the final solid preserves around 95% of the initial cellulose. Regarding the LHW extract, 38.6% of hemicellulosic sugars went to this stream, while 57% of these sugars remained in the LHW-OS solid. Finally, regarding lignin, 52.9% of this component is extracted in the OS extract and 33.6% remain in the LHW-OS solid. This scenario provides an outlook on the solid fraction's possible use and further valorization after the LHW stage. Cellulose represents ~50% of the solid mass, and as previously analyzed, 72% of the lignin has been removed. This shows a potential application in materials (pulp and paper).

This combinatorial pretreatment (LHW followed by OS) allows obtaining three intermediate products streams (a sugar-rich and a lignin-rich extract and a cellulose-enriched solid), increasing the possible economic outputs of the process. On the other hand, these two technologies as standalone processes entail significant energy consumption associated with the heating and recovery of the solvent of the OS stage, which implicates a challenge to the feasibility of the process. However, the actual combinatorial pretreatment may implicate an improvement for the OS-standalone process. By performing LHW first, around 28% of the initial mass is solubilized (as observed in Figure 6a,b), which implicates lower solvent requirements and fewer liquid extracts to be processed in the downstream, which could compensate for the inclusion of a further step. However, this hypothesis requires further investigation to evaluate this strategy's technical and environmental benefits.

4. Conclusions

This study tested different temperatures and times for the LHW pretreatment of wheat straw and determined the extent of lignin solubilization, in addition to the determination of sugars and degradation products. We showed that the LHW at 160 °C for 90 min (severity factor of 3.77) allowed the best extraction of components, reaching a total concentration of sugars of ca. 12 g/L, and 0.2, 0.01, and 1.4 g/L for furfural, HMF, and acetic acid, respectively. A lignin concentration of 2.2 g/L was also attained. By including the analysis of lignin hydrolysis into the standard sugar and degradation products in LHW, it was possible to make a more integrated decision to valorize the different lignocellulosic components of wheat straw. The theoretical study case presented for lignin extraction in a subsequent OS stage indicates the potential of lignin extraction and valorization of the final solid for real, sound applications.

Supplementary Materials: The following are available online at https://www.mdpi.com/article/10.3390/su14010362/s1, Supplementary Material S1—Summary of the characterization of the LHW extracts, S2—Mass balance of the LHW stage, S3—Mass balance for the LHW-OS combination, S4—Streams balance for the LHW-OS combination.

Author Contributions: Conceptualization, S.S.-L., L.D.-S. and A.F.; investigation, S.S.-L. and M.D.; writing—original draft preparation, S.S.-L.; writing—review and editing, M.D., L.D.-S., C.C.C.R.d.C. and A.F.; supervision, C.C.C.R.d.C. and A.F. All authors have read and agreed to the published version of the manuscript.

Funding: This research received no external funding.

Acknowledgments: The authors acknowledge TU Wien for funding the Doctoral College "Bioactive", under which this research was performed, and TU Wien Bibliothek for the financial support through its Open Access Funding Programme. The authors are grateful to the ERASMUS + Program of Higher Education for Traineeships of the European Commission for financing the research stay of Manuel Francisco Nunes Dias in TU Wien.

Conflicts of Interest: The authors declare no conflict of interest.

References

1. Palmeros Parada, M.; Osseweijer, P.; Posada Duque, J.A. Sustainable biorefineries, an analysis of practices for incorporating sustainability in biorefinery design. *Ind. Crops Prod.* **2017**, *106*, 105–123. [CrossRef]
2. Hassan, S.S.; Williams, G.A.; Jaiswal, A.K. Moving towards the second generation of lignocellulosic biorefineries in the EU: Drivers, challenges, and opportunities. *Renew. Sustain. Energy Rev.* **2019**, *101*, 590–599. [CrossRef]
3. Cardona-Alzate, C.A.; Serna-Loaiza, S.; Ortiz-Sanchez, M.; Cardona Alzate, C.A.; Serna-Loaiza, S.; Ortiz-Sanchez, M. Sustainable Biorefineries: What was learned from the design, analysis and implementation. *J. Sustain. Dev. Energy Water Environ. Syst.* **2020**, *8*, 88–117. [CrossRef]
4. Serna-Loaiza, S.; Miltner, A.; Miltner, M.; Friedl, A.A. Review on the Feedstocks for the Sustainable Production of Bioactive Compounds in Biorefineries. *Sustainability* **2019**, *11*, 6765. [CrossRef]
5. Liu, Z.H.; Hao, N.; Shinde, S.; Olson, M.L.; Bhagia, S.; Dunlap, J.R.; Kao, K.C.; Kang, X.; Ragauskas, A.J.; Yuan, J.S. Codesign of Combinatorial Organosolv Pretreatment (COP) and Lignin Nanoparticles (LNPs) in Biorefineries. *ACS Sustain. Chem. Eng.* **2019**, *7*, 2634–2647. [CrossRef]
6. Ragauskas, A.J.; Beckham, G.T.; Biddy, M.J.; Chandra, R.; Chen, F.; Davis, M.F.; Davison, B.H.; Dixon, R.A.; Gilna, P.; Keller, M.; et al. Lignin valorization: Improving lignin processing in the biorefinery. *Science* **2014**, *344*, 6185. [CrossRef]
7. Karimi, K.; Taherzadeh, M.J. A critical review of analytical methods in pretreatment of lignocelluloses: Composition, imaging, and crystallinity. *Bioresour. Technol.* **2016**, *200*, 1008–1018. [CrossRef]
8. Agrawal, R.; Satlewal, A.; Kapoor, M.; Mondal, S.; Basu, B. Investigating the enzyme-lignin binding with surfactants for improved saccharification of pilot scale pretreated wheat straw. *Bioresour. Technol.* **2017**, *224*, 411–418. [CrossRef]
9. Satlewal, A.; Agrawal, R.; Das, P.; Bhagia, S.; Pu, Y.; Puri, S.K.; Ramakumar, S.S.V.; Ragauskas, A.J. Assessing the Facile Pretreatments of Bagasse for Efficient Enzymatic Conversion and Their Impacts on Structural and Chemical Properties. *ACS Sustain. Chem. Eng.* **2019**, *7*, 1095–1104. [CrossRef]

10. Xia, F.; Gong, J.; Lu, J.; Cheng, Y.; Zhai, S.; An, Q.; Wang, H. Combined liquid hot water with sodium carbonate-oxygen pretreatment to improve enzymatic saccharification of reed. *Bioresour. Technol.* **2020**, *297*, 122498. [CrossRef]
11. Rocha, G.J.M.; Gonçalves, A.R.; Oliveira, B.R.; Olivares, E.G.; Rossell, C.E.V. Steam explosion pretreatment reproduction and alkaline delignification reactions performed on a pilot scale with sugarcane bagasse for bioethanol production. *Ind. Crops Prod.* **2012**, *35*, 274–279. [CrossRef]
12. Neves, P.V.; Pitarelo, A.P.; Ramos, L.P. Production of cellulosic ethanol from sugarcane bagasse by steam explosion: Effect of extractives content, acid catalysis and different fermentation technologies. *Bioresour. Technol.* **2016**, *208*, 184–194. [CrossRef] [PubMed]
13. Tian, D.; Shen, F.; Yang, G.; Deng, S.; Long, L.; He, J.; Zhang, J.; Huang, C.; Luo, L. Liquid hot water extraction followed by mechanical extrusion as a chemical-free pretreatment approach for cellulosic ethanol production from rigid hardwood. *Fuel* **2019**, *252*, 589–597. [CrossRef]
14. Wang, W.; Yuan, T.; Wang, K.; Cui, B.; Dai, Y. Combination of biological pretreatment with liquid hot water pretreatment to enhance enzymatic hydrolysis of Populus tomentosa. *Bioresour. Technol.* **2012**, *107*, 282–286. [CrossRef] [PubMed]
15. Serna-Loaiza, S.S.; Zikeli, F.; Adamcyk, J.; Friedl, A. Towards a wheat straw biorefinery: Combination of Organosolv and Liquid Hot Water for the improved hydrolysis of lignin and hemicellulose. *Bioresour. Technol. Reports* **2020**, *14*, 100667. [CrossRef]
16. López, L.; Rivas, S.; Moure, A.; Vila, C.; Parajó, J.C. Development of Pretreatment Strategies for the Fractionation of Hazelnut Shells in the Scope of Biorefinery. *Agronomy* **2020**, *10*, 1568. [CrossRef]
17. Michelin, M.; Liebentritt, S.; Vicente, A.A.; Teixeira, J.A. Lignin from an integrated process consisting of liquid hot water and ethanol organosolv: Physicochemical and antioxidant properties. *Int. J. Biol. Macromol.* **2018**, *120*, 159–169. [CrossRef]
18. Michelin, M.; Teixeira, J.A. Liquid hot water pretreatment of multi feedstocks and enzymatic hydrolysis of solids obtained thereof. *Bioresour. Technol.* **2016**, *216*, 862–869. [CrossRef]
19. Carvalheiro, F.; Silva-Fernandes, T.; Duarte, L.C.; Gírio, F.M. Wheat Straw Autohydrolysis: Process Optimization and Products Characterization. *Appl. Biochem. Biotechnol.* **2009**, *153*, 84–93. [CrossRef]
20. Pérez, J.A.; Ballesteros, I.; Ballesteros, M.; Sáez, F.; Negro, M.J.; Manzanares, P. Optimizing Liquid Hot Water pretreatment conditions to enhance sugar recovery from wheat straw for fuel-ethanol production. *Fuel* **2008**, *87*, 3640–3647. [CrossRef]
21. Wildschut, J.; Smit, A.T.; Reith, J.H.; Huijgen, W.J.J. Ethanol-based organosolv fractionation of wheat straw for the production of lignin and enzymatically digestible cellulose. *Bioresour. Technol.* **2013**, *135*, 58–66. [CrossRef]
22. Weinwurm, F.; Turk, T.; Denner, J.; Whitmore, K.; Friedl, A. Combined liquid hot water and ethanol organosolv treatment of wheat straw for extraction and reaction modeling. *J. Clean. Prod.* **2017**, *165*, 1473–1484. [CrossRef]
23. Alvira, P.; Tomás-Pejó, E.; Ballesteros, M.; Negro, M.J. Pretreatment technologies for an efficient bioethanol production process based on enzymatic hydrolysis: A review. *Bioresour. Technol.* **2010**, *101*, 4851–4861. [CrossRef] [PubMed]
24. Kim, Y.; Kreke, T.; Mosier, N.S.; Ladisch, M.R. Severity factor coefficients for subcritical liquid hot water pretreatment of hardwood chips. *Biotechnol. Bioeng.* **2014**, *111*, 254–263. [CrossRef] [PubMed]
25. Sluiter, A.; Ruiz, R.; Scarlata, C.; Sluiter, J.; Templeton, D.; Hames, B.; Ruiz, R. Technical Report NREL/TP-510-42623: Determination of Sugars, Byproducts, and Degradation Products in Liquid Fraction Process Samples. *Gold. Natl. Renew. Energy Lab.* **2006**, *11*, 65–71.
26. Sluiter, A.; Hames, B.; Ruiz, R.; Scarlata, C.; Sluiter, J.; Templeton, D. Technical Report NREL/TP-510-42618: Determination of Structural Carbohydrates and Lignin in Biomass. *Lab. Anal. Proced.* **2008**, *1617*, 1–16.
27. Huang, C.; Lai, C.; Wu, X.; Huang, Y.; He, J.; Huang, C.; Li, X.; Yong, Q. An integrated process to produce bio-ethanol and xylooligosaccharides rich in xylobiose and xylotriose from high ash content waste wheat straw. *Bioresour. Technol.* **2017**, *241*, 228–235. [CrossRef] [PubMed]
28. Beisl, S.; Quehenberger, J.; Kamravamanesh, D.; Spadiut, O.; Friedl, A. Exploitation of Wheat Straw Biorefinery Side Streams as Sustainable Substrates for Microorganisms: A Feasibility Study. *Processes* **2019**, *7*, 956. [CrossRef]
29. Palmqvist, E.; Grage, H.; Meinander, N.Q.; Hahn-Hägerdal, B. Main and interaction effects of acetic acid, furfural, and p-hydroxybenzoic acid on growth and ethanol productivity of yeasts. *Biotechnol. Bioeng.* **1999**, *63*, 46–55. [CrossRef]
30. Casey, E.; Sedlak, M.; Ho, N.W.Y.; Mosier, N.S. Effect of acetic acid and pH on the cofermentation of glucose and xylose to ethanol by a genetically engineered strain of Saccharomyces cerevisiae. *FEMS Yeast Res.* **2010**, *10*, 385–393. [CrossRef] [PubMed]
31. Sanchez, B.; Bautista, J. Effects of furfural and 5-hydroxymethylfurfural on the fermentation of Saccharomyces cerevisiae and biomass production from Candida guilliermondii. *Enzyme Microb. Technol.* **1988**, *10*, 315–318. [CrossRef]
32. Mussatto, S.I.; Roberto, I.C. Alternatives for detoxification of diluted-acid lignocellulosic hydrolyzates for use in fermentative processes: A review. *Bioresour. Technol.* **2004**, *93*, 1–10. [CrossRef] [PubMed]
33. Delgenes, J.P.; Moletta, R.; Navarro, J.M. Effects of lignocellulose degradation products on ethanol fermentations of glucose and xylose by Saccharomyces cerevisiae, Zymomonas mobilis, Pichia stipitis, and Candida shehatae. *Enzym. Microb. Technol.* **1996**, *19*, 220–225. [CrossRef]
34. Nigam, J.N. Ethanol production from wheat straw hemicellulose hydrolysate by Pichia stipitis. *J. Biotechnol.* **2001**, *87*, 17–27. [CrossRef]

sustainability

Article

Effect of Anaerobic Digestate on the Fatty Acid Profile and Biodiesel Properties of *Chlorella sorokiniana* Grown Heterotrophically

George Papapolymerou [1,*], Athanasios Kokkalis [2], Dorothea Kasiteropoulou [1], Nikolaos Gougoulias [3], Anastasios Mpesios [1], Aikaterini Papadopoulou [1], Maria N. Metsoviti [1] and Xenofon Spiliotis [1]

[1] Department of Environmental Studies, University of Thessaly, 41500 Larissa, Greece; dkasiter@uth.gr (D.K.); bes_tas@yahoo.gr (A.M.); aikapapa@uth.gr (A.P.); mametsov@uth.gr (M.N.M.); spil@uth.gr (X.S.)
[2] GRINCO S.A., Industrial Area of Larisa, 41303 Larissa, Greece; kokkalis@grinco.gr
[3] Department of Agrotechnology, University of Thessaly, 41500 Larissa, Greece; ngougoulias@uth.gr
* Correspondence: papapoly@uth.gr; Tel.: +30-2410-684428

Abstract: The growth kinetics and the lipid and protein content of the microalgal species *Chlorella sorokiniana* (CS) grown heterotrophically in growth media containing glycerol and increasing amounts of anaerobic digestate (AD) equal to 0%, 15%, 30%, and 50% was studied. The effect of the AD on the fatty acid (FA) distribution of the bio-oil extracted from the CS, as well as on the fatty acid methyl ester (FAME) properties such as the saponification number (SN), the iodine value (IV), the cetane number (CN), and the higher heating value (HHV) was also estimated. The percentage of AD in the growth medium affects the rate of carbon uptake. The maximum carbon uptake rate occurs at about 30% AD. Protein and lipid content ranged from 32.3–38.4% and 18.1–23.1%, respectively. Fatty acid distribution ranged from C10 to C26. In all AD percentages the predominant fatty acids were the medium chain FA C16 to C18 constituting up to about 89% of the total FA at 0% AD and 15% AD and up to about 54% of the total FA at 30% AD and 50% AD. With respect to unsaturation, monounsaturated FA (MUFA) were predominant, up to 56%, while significant percentages, up to about 38%, of saturated FA (SFA) were also produced. The SN, IV, CN, and HHV ranged from 198.5–208.3 mg KOH/g FA, 74.5–93.1 g I/100 g FAME, 52.7–56.1, and 39.7–40.0 MJ/kg, respectively. The results showed that with increasing AD percentage, the CN values tend to increase, while decrease in IV leads to biofuel with better ignition quality.

Keywords: *Chlorella sorokiniana*; heterotrophic; anaerobic digestate; glycerol; FAME

Citation: Papapolymerou, G.; Kokkalis, A.; Kasiteropoulou, D.; Gougoulias, N.; Mpesios, A.; Papadopoulou, A.; Metsoviti, M.N.; Spiliotis, X. Effect of Anaerobic Digestate on the Fatty Acid Profile and Biodiesel Properties of *Chlorella sorokiniana* Grown Heterotrophically. *Sustainability* **2022**, *14*, 561. https://doi.org/10.3390/su14010561

Academic Editors: Oz Sahin and Edoardo Bertone

Received: 14 December 2021
Accepted: 4 January 2022
Published: 5 January 2022

1. Introduction

Microalgae are unicellular photosynthetic organisms that use light and carbon dioxide, with higher photosynthetic efficiency than plants, for the production of biomass. Some microalgae species can also grow and multiply heterotrophically in the absence of light if an organic carbon source becomes available [1]. The main advantage of heterotrophic growth is higher biomass growth rates and biomass production as, unlike autotrophic growth, heterotrophic growth is not limited by light transmission through the growth medium. Another advantage of heterotrophic growth is the potential of achieving higher lipid content and, as a result, higher lipid productivities. This is needed if microalgal cultivation is to be useful for biodiesel production. Disadvantages of heterotrophic growth are the susceptibility to contamination, which requires that all parts of the bioreactors, as well as all growth media, must be carefully sterilized in order to minimize the risk of contamination, and the cost of organic carbon which must be provided to the growth medium.

The microalgae growth rate, as well as the protein and lipid content, are influenced by many parameters, such as the cultivated species, the temperature, the concentration of carbon, the ratio of carbon to nitrogen, the medium pH, the concentration of potassium, phosphorus and micronutrients, dissolved oxygen availability, and the mixing rate [2]. For biodiesel production, except for a high lipid productivity a favorable fatty acid profile of the lipids is needed as well. Currently, biodiesel is mainly produced from used oils and various seed oils such as sunflower and cotton seed oils. Vegetable oils contain fatty acid mostly from C14:0 to about C22:0. Used oils contain a small amount of animal fats which have a lower fatty acid chain length.

Depending on the cultivated species and the cultivation mode and parameters, the microalgal biomass can be directed towards specific uses, as various components such as proteins, lipids, antioxidants, and other compounds can be maximized [3]. Therefore, the microalgal biomass composition can be altered by altering the growth conditions and furthermore microalgal cultivation can be carried out on an industrial scale using basic biochemical engineering principles. In addition to the production of biodiesel, the biomass can be used in a variety of applications. The biomass of microalgae is rich in antioxidants and some organic substances of pharmaceutical value, so some applications are in the cosmetic and pharmaceutical industry [4]. The high protein and lipid content can be of value in aquaculture for the replacement of fishmeal in fish feeds and in the poultry industry [5].

In heterotrophic cultivation mode, microalgae use organic carbon and oxygen under dark conditions for growth and biomass production [6]. A number of review papers focus on the heterotrophic growth of several microalgal species, and the trend is that heterotrophic growth enhances both the biomass and lipid productivity [7,8]. Different sources of carbon can be used for microalgae growth, such as glucose, sucrose, fructose, mannose, glycerol, lactose, or galactose [9]. Additionally, various industrial effluents and by-products, such as anaerobic digestate, can be used as a carbon and nitrogen source. Studies on the heterotrophic cultivation of different microalgal species using glucose as carbon source have been published [10,11], while work on the cultivation of microalgae using glycerol is limited. It should be mentioned that studies on cultivation using industrial effluents and by-products, such as anaerobic digestate are lacking.

In the heterotrophic cultivation of *Chlorella sorokiniana*, the growth rate was higher using glucose and sodium acetate as the carbon source compared to fructose [12]. In *Chlorella vulgaris*, optimal cell growth and lipid productivity were attained using glucose at 1% (w/v). Growth of *C. vulgaris* on glycerol had similar dose effects as those from glucose [13]. Ogbonna et al. [14] report that the heterotrophic cultivation of *Euglena gracilis* was enhanced when cultivated with glucose in comparison with cultivation with ethanol. In *Chlorella protothecoides*, corn powder hydrolysate was used instead of glucose as an organic carbon source in heterotrophic culture medium in fermenters, in order to increase the biomass and reduce the cost of cultivation [15]. O'Grady and Morgan [16] studied the heterotrophic growth of *Chlorella protothecoides* with different carbon sources, specifically glycerol, glucose, and a glucose/glycerol mixture. They found that the specific growth rate and lipid yields when using glycerol and a glucose/glycerol mixture were higher in comparison when using only glucose. Similarly, Kong et al. [17] found that the growth rate of *C. vulgaris*, as well as the biomass production of the species, was enhanced when cultivated with a mixture of glycerol and glucose.

Anaerobic digestate (AD) produced by biogas plants is mainly used for field fertilization in various crops such as corn. When there are no adequate fields available, or the land is not sufficiently flat, nitrification of underground and surface water and high soil salinity may result as excess anaerobic digestate is applied. Therefore, developing new applications for the efficient use of anaerobic digestate is needed in order to utilize the macro- and micronutrient content of the AD in the framework of circular economy. A good solution is the use of anaerobic digestate for microalgae cultivation, as it is a good source of nitrogen, phosphorus, and potassium, as well as a source of over 30 different micronutrients. Potassium and phosphorus availability are projected to decrease in the future.

The microalgae species *Chlorella sorokiniana* was cultivated with glycerol as the main source of carbon and 0%, 15%, 30%, and 50% AD added to the growth media. In all four cultivation treatments using glycerol and AD, both initial carbon and nitrogen concentrations, as well as pH and temperature, were held constant in order to determine the effect of AD on the growth rate, the lipid and protein content of the biomass, and the FA distribution. The four FAME properties, namely SN, IV, CN, and HHV, were calculated from the FA distribution and empirical equations. Nitrogen was in the form of ammonium as this is the form found in AD. Potassium and phosphorus were held constant as well. In addition, *Chlorella sorokiniana* was cultivated without glycerol, (AD/water (*v*/*v*): 75:25, 50:50, and 25:75) in order to determine the rate of carbon uptake of the partly digested organic material present in the AD.

Most studies have been carried out with piggery and municipal wastewater, with or without glycerol, with autotrophic or mixotrophic cultivations, and using other than *Chlorella sorokiniana* species. There are no studies which examine the effect of anaerobic digestate on the fatty acid distribution of the lipids obtained from a heterotrophic cultivation, with or without glycerol. The purpose of the present study was to investigate the effect of different percentages of anaerobic digestate enriched with crude glycerol in the growth medium of *Chlorella sorokiniana* under heterotrophic growth conditions on the fatty acid distribution of the lipids obtained and the basic biodiesel properties.

2. Materials and Methods

2.1. Bioreactors

The cultivation of *C. sorokiniana* was carried out in glass cylindrical bioreactors of 42 L capacity each that were filled to 80% of their volume. Air was continuously provided to each bioreactor though a perforated network of piping placed at the bottom of the bioreactor tank. The temperature of the cultures was kept at 30 ± 1 °C with the use of temperature thermostats (Aquael 250 W heaters, Suwalki, Poland) and the pH was held constant at 7 ± 0.3. The pH was adjusted manually as needed two or three times daily with the use of HCl or NaOH solutions. The bioreactors, the glass tubing, and the culture medium were sterilized before use.

2.2. Inoculum Preparation

The microalgae species *C. sorokiniana* (SAG strain 211-31) was obtained from Culture Collection of Algae from the University of Göttingen in Germany (EPSAG). The cultivation medium used for the inoculum growth was the Basal Medium (=ES "Erddekokt + Salze") and each liter of it contained: 0.2 g KNO_3/L, 0.02 g K_2HPO_4/L, 0.02 g $MgSO_4 \cdot 7H_2O$/L, 30 mL of soil extract/L, and 5 mL/L of a solution containing the following micronutrients: (1 mg $ZnSO_4 \cdot 7H_2O$, 2 mg $MnSO_4 \cdot 4H_2O$, 10 mg H_3BO_3, 1 mg $Co(NO_3)_2 .6H_2O$, 1 mg $MoO_4 \cdot 2H_2O$, 0.005 mg $CuSO_4 \cdot 5H_2O$, 700 mg $FeSO_4 \cdot 7H_2O$, and 800 mg EDTA)/L [18].

The culture medium was inoculated with a standard quantity (250 mL of *C. sorokiniana* inoculum) which was prepared as follows: 1 L flasks, containing the necessary culture medium, were inoculated with *C. sorokiniana* culture directly obtained from EPSAG and cultivated in a sterile environment until they reached an optical density of about 0.5. The cultivation of the inoculum was always performed under the same conditions, namely at a temperature of 25 °C, under natural illumination, and by using an orbital shaker at 60 rpm in order to prevent sticking of algae to the surfaces of the flask.

2.3. Measurements

In all experiments, the organic carbon concentration was measured daily so that its uptake by the microalgae could be monitored. Initial nitrogen concentration (Co), in the form of ammonium, was also held constant. The organic carbon reduction kinetics (as rate of Carbon uptake) was determined from the slope of the experimental data of C(t) vs. t, by plotting the C(t) vs. t data and obtaining the average slope $\Delta C(t)/\Delta t$.

The saponification number (*SN*) and the iodine value (*IV*) were calculated theoretically from the FA distribution using the equations suggested by Kalayasiri et al. [19] and by Azam et al. [20]. Similarly, the cetane number (*CN*) was evaluated from the theoretical equation suggested by Krisnangkura [21] and the higher heating value (*HHV*) from the equation suggested by Demirbas [22].

$$SN = \sum\left[\frac{(560 \times (\%W_i)}{MW_i}\right] \tag{1}$$

$$IV = \sum\left[\frac{(254 \times N_{db} \times (\%W_i)}{MW_i}\right] \tag{2}$$

$$CN = 46.3 + \left(\frac{5458}{SN}\right) - (0.225IV) \tag{3}$$

$$HHV = 49.43 - (0.041SN) - (0.015IV) \tag{4}$$

where $\%W_i$ is the % weight of each FA, N_{db} is the number of double bonds, and MW_i is the molecular weight of the respective FAME.

2.4. Method of Analyses

The composition of the samples was determined according to AOAC [23] methods.

Total nitrogen content in samples was measured with liquid digestion. Digestion is accomplished by boiling of the samples in concentrated sulphuric acid with catalyst potassium sulphate, copper sulphate, and selenium. After cooling, the digestion product was distilled with NaOH in a solution 2% H_3BO_3 in presence of indicator methyl red and was titrated with 0.1 N HCl [24]. Total protein content of plant tissues was calculated from the total nitrogen using a conversion factor of 6.25 [25].

For the determination of organic carbon, the method of Walkley–Black was used. The samples were first centrifuged and then filtered. According to this method, organic carbon was oxidized by a mixture of $K_2Cr_2O_7$ and H_2SO_4 in a ratio of 1:2. The remaining $K_2Cr_2O_7$ was titrated with 0.5 N $FeSO_4$ $7H_2O$.

The total lipid content was determined with extraction using co-solvents of n-hexane/isopropanol in the microalgal biomass in accordance with the method of Bian et al. [26]. The solvent ratio of n-hexane to isopropanol was 3/2 (*v*/*v*) and the ratio of co-solvents to microalgal dry biomass was 10/1 (*v*/*w*). Extraction was carried out in horizontal-circular movement "tehtnica Zelezniki EV-402" machine. Stirring speed was 300 rpm, and the extraction time was 48 h. The total lipid extract was determined gravimetrically after filtration and evaporation of the solvents.

The bio-oil was subjected to transesterification and the fatty acid distribution was determined by gas chromatography. Specifically, the bio-oil was filtered and 100 mg of the bio-oil was reacted with a mixture of heptane and KOH/MeOH (2 N). The anhydrous MeOH was filtered. Following the separation of the two phases, 1 μL of the FAME (Fatty Acid Methyl Ester) phase was injected into an Agilent Gas Chromatographer Model 6890 N. Analysis of the FAME distribution was performed according to the EN 14103 method.

2.5. Materials

Crude glycerol was used as the carbon source. It was obtained from a local biodiesel manufacturing plant. Its methanol was removed, and its composition was 86% glycerin, 0.5% methanol, 7.5% water, 3.5% MONG (Non-Glycerin Organic Matter), and 2.5% ash. Anaerobic digestate was provided by a local biogas producing plant. It was first filtered through three successive sieves and then centrifuged at 4000 rpm for 10 min. It was then sterilized by boiling for about 10 min. Following its cooling, the macronutrient content of the AD was determined. Nitrogen in the AD is present in the form of ammonium ions while carbon comes from partly digested organic material. The ammonium concentration in the biofertilizer was measured at 1129 mg/L, which corresponds to 878.1 mg/L of elemental nitrogen. Therefore, at the maximum percentage of 50% biofertilizer, the concentration of elemental nitrogen is 439 mg/L. In the first 3 bioreactors the remaining nitrogen was added as NH_4Cl. Organic carbon concentration in the AD was 1.95 g/L.

2.6. Initial Parameters of the Variable AD Experiment

Table 1 summarizes the initial concentrations of carbon and nitrogen, the Co/No ratio, and the AD used for the experiments where AD varied from 0% to 50% (*v*/*v*) in the growth media.

Table 1. The initial parameters of the four cultivation treatments.

Cultivation Treatment	1	2	3	4
AD (%)	0	15	30	50
Co (g/L)	7.58	7.53	7.43	7.29
N (mg/L)	439	439	439	439
C_0/N_0	17.3	17.2	16.9	16.6

2.7. Statistical Analysis

Data were analyzed using the IBM SPSS Statistics 24 statistical package [27]. The experiment had four replications. Analysis of variance was used to assess treatment effects. Mean separation was made using Tukey's test when significant differences ($p = 0.05$) between treatments were found. All presented numeric values are means of four measurements ± standard deviation (SD).

3. Results and Discussion

3.1. Growth and Carbon Uptake Rate Using Only Anaerobic Digestate

Figure 1 shows the carbon concentration as a function of cultivation time for *Chlorella sorokiniana* cultivated only in diluted pure anaerobic digestate without any glycerol and other macro- or micronutrient added. The AD concentration was approximately 75%, 50%, and 25%, and water was used in order to dilute the AD. Therefore, both carbon and nitrogen are solely supplied by the AD. The only purpose of this experiment was to determine the utilization or uptake, by the microalgal species *Chlorella sorokiniana,* of the organic carbon found as undigested or partly digested organic compounds in the AD. Carbon in AD is a mixture of unspecified fragments of various organic molecules present in the raw materials such as proteins, lipids, carbohydrates, hemi-cellulose, and cellulose.

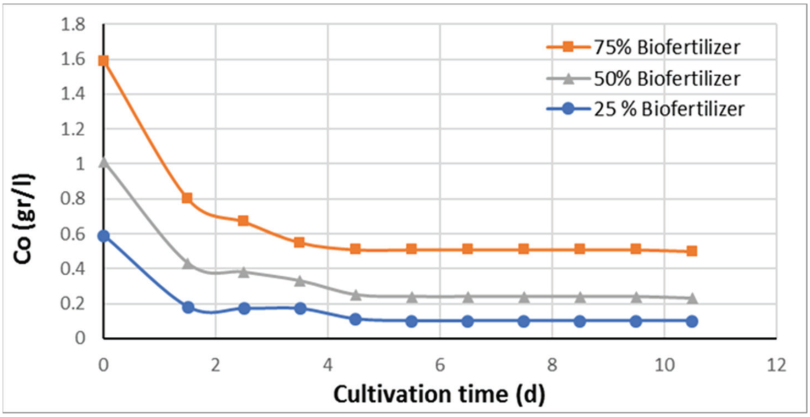

Figure 1. The concentration of organic carbon as a function of cultivation time for three different diluted AD concentrations in the growth medium as shown. No glycerol was added. Organic carbon is solely from the undigested organic material of the AD. The Co/No ratio is 2.2 in all three curves. Temperature and pH were fixed at 30 °C (±1 °C) and 7 (±0.3), respectively. Curves are drawn between data points for clarity.

The organic carbon and ammonium ion concentrations of the AD (100%) were determined and were equal to 1129 mg/L and 1.95 g/L, respectively. Therefore, the initial concentration of elemental nitrogen is equal to 878 mg/L and the initial Co/No is equal to 2.2. From the data of Figure 1, it appears that the organic carbon in the AD is easily absorbed and utilized by *Chlorella sorokiniana*, as there is a high percentage of carbon uptake in just 2 to 4 days, and 70% to almost 85% of the undigested organic carbon in the AD is utilized.

3.2. Kinetics of the Growth Rate Using Anaerobic Digestate and Glycerol

Figure 2 shows the rate of carbon decrease for four different AD concentrations in the growth medium equal to 0% (standard), 15%, 30%, and 50%, using glycerol as the main carbon source. The measured Co/No ratio was basically the same for all bioreactors and ranged from 18.2 to 19.0. Carbon was mostly from glycerol and the amount of glycerol added in each bioreactor was adjusted so as to take into account the undigested carbon found in the AD. Nitrogen in the form of ammonium came from the AD and ammonium chloride. Its initial concentration was constant in all bioreactors by adjusting the ammonium chloride added to the first three bioreactors. Its initial nitrogen concentration was 439 mg/L. Therefore, the purpose of this experiment was to (a) examine the effect of the AD on the growth rate, (b) examine the lipid and protein content of the biomass, and (c) determine the FA distribution of the bio-oil extracted from the biomass and estimate basic properties of the corresponding fatty acid methyl esters (FAME).

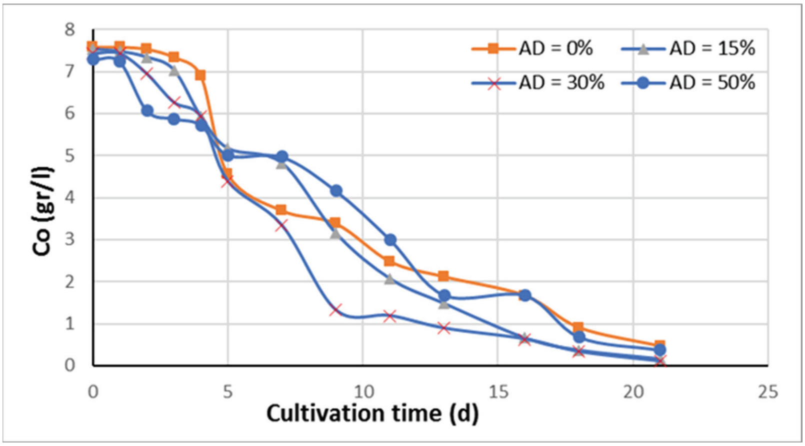

Figure 2. The concentration of organic carbon as a function of cultivation time for four different AD concentrations in the growth medium as shown. Initial organic carbon and nitrogen concentrations were the same in all four experiments. Co/No = 16.6–17.3 and No = 439 mg/L. Temperature and pH were fixed at 30 °C (±1 °C) and 7 (± 0.3), respectively. Curves are drawn between data points for clarity.

Carbon concentration fell to a value less than 0.5 g/L in about 18–20 days. The lag phase was from 1 to 2 days. During the intermediate growth of *Chlorella sorokiniana*, between about the 3rd and 12th day, the growth is fast, as is the carbon rate of decrease. This is the exponential gorwth phase which is very fast. In cultivations, there are realized four growth phases: (a) the lag phase in which the microorganisms adjust to the growth media environment, (b) the exponential growth phase, characterized by fast growth, (c) the stationary phase during which growth is slowed, and (d) the death phase occurring much later in time.

From the data of Figure 2, the average carbon uptake rate in the exponential growth phase was calculated and shown in Figure 3. It is seen that the carbon uptake rate goes through a maximum at 30% AD. It is higher by about 33% compared to 0% AD. Carbon concentration drops to less than 1 g/L in 13 days for the 30% AD, while the respective time for the 0% AD and 50% is about 18 days.

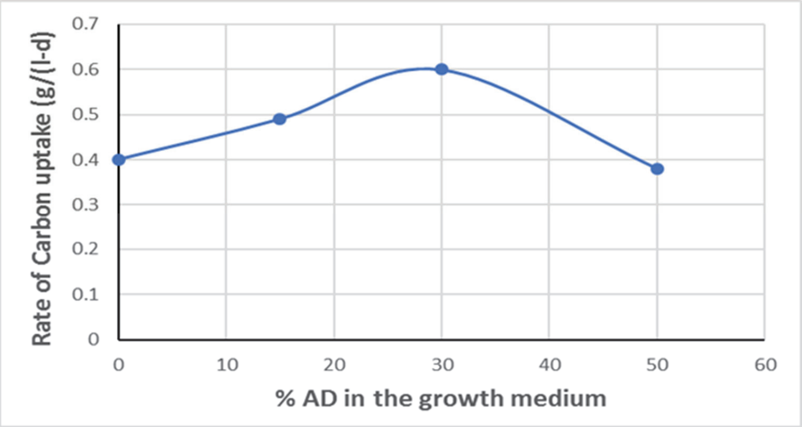

Figure 3. Comparison of the carbon uptake rate as a function of % AD added to the growth medium. Co/No = 16.6–17.3 and No = 439 mg/L.

Anaerobic digestate is a very complex medium. It is used, as it contains all the macro- and micronutrients needed for the cultivation of microalgae. Specifically, it contains a great number of elements, basically all elements, as well as various organic compounds. To add to this complexity, other unknown compounds may be formed from the anaerobic digestion. Micronutrients present in the AD, especially cobalt, molybdenum, and iron, may be affecting carbon uptake kinetics; this is presently being investigated. Cobalt and especially molybdenum may also be affecting nitrogen uptake by the microalgal cells which utilize these micronutrients for cell growth and therefore may be directly involved in the carbon utilization process.

Several studies have been conducted investigating the use of anaerobic digestion as a nutrient source for the cultivation of a variety of microalgal sp. Chuka-ogwudea et al. [28] reviewed research on microalgal cultivation using anaerobic digestate produced from food waste. Various food wastes and agricultural energy plants were used. Various *Chlorella* sp., such as *pyrenoidosa*, *vulgaris*, *minutissima*, and *sorokiniana*, as well as various *Scenedesmus* sp., *Nannochloropsis* sp., and *Tetraselmis* sp. were used. Singh et al. [29] studied the mixotrophic cultivation of *Chlorella sorokiniana* using different growth media from anaerobic effluent from a poultry litter anaerobic digester. The lipid content varied between 8.2% and 12.4%, while the protein content varied between 37.9% and 39.2%. The biomass productivity was 63 mg L^{-1} d^{-1}. Rajagopal et al. [30] studied the autotrophic cultivation of *Chlorella vulgaris* strain CPCC 90 using anaerobic digestate (AD) from chicken manure. They diluted the AD and prepared AD media containing AD from 10% up to 90% in increments of 20%. They found that, due to the high ammonia content of the AD, growth was inhibited in growth media containing AD. Sekine et al. [31] studied the cultivation of *Chlorella sorokiniana* strain NIES-2173 using undiluted anaerobic digestate and compared with the cultivation using a synthetic growth medium. The growth of *Chlorella sorokiniana* strain NIES-2173 using undiluted anaerobic digestate was almost the same as that with using the synthetic growth medium. Dilution of the anaerobic digestate resulted in a decrease in the specific growth rate coefficient.

3.3. Lipid and Protein Content of the Biomass

The lipid and protein content of the biomass in the experiments where the concentration of the AD varied between 0% and 50% is shown in Table 2. The protein content in the biomass of *Chlorella sorokiniana* increased by the addition of 30% and 50% percentages of AD in the growth medium compared with the control (crude glycerol + 0% AD), while, by the addition of 15% of AD in the growth medium, the protein content in the biomass of *Chlorella sorokiniana* did not show statistically significant differences compared with the control (Table 2). In contrast, the lipid content in the biomass of *Chlorella sorokiniana* decreased by the addition of 30% and 50% of AD in the growth medium compared with the control (crude glycerol + 0% AD), while the addition of 15% of AD in the growth medium did not show statistically significant differences in the lipid content in the biomass of *Chlorella sorokiniana* compared with the control (Table 2).

Table 2. Protein and lipid content of the biomass of *Chlorella sorokiniana* grown with 0%, 15%, 30%, and 50% AD.

Property	0% AD	15% AD	30% AD	50% AD
Protein %	32.3 ± 1.74^{b}	32.9 ± 1.74^{b}	37.6 ± 1.89^{a}	38.4 ± 1.91^{a}
Lipid %	23.1 ± 1.24^{a}	22.4 ± 1.19^{a}	19.3 ± 1.01^{b}	18.1 ± 0.93^{b}

Data represent average means and SE deviation, (n) = 4; in each chemical property of the table, different letters indicate significant differences according to the Tukey's test ($p = 0.05$).

It is noted that up to 15% AD protein and lipid contents are basically unaltered. However, increasing the AD% to 30% and 50% decreases the lipid content by about 3% and 4%, respectively. However, smaller or equal to 15% percentages of AD can be used without a substantial reduction in lipid content of the biomass. Additionally, other modes of using the AD, such as semi-batch addition, may be used in order to improve the lipid content of the biomass, or the Co/No ratio can be increased, and this will lead to an increase in the lipid content of the biomass. The lipid content is relatively low as, although a relatively high Co was used, the high No value (439 mg/L), which was used due to the AD, favors protein synthesis instead.

3.4. Fatty Acid Distribution and Estimation of Biodiesel (FAME) Properties

Following collection of the biomass, the bio-oil was extracted. The Fatty Acid distribution is shown in Table 3.

It is noted that, as the percentage of AD in the growth medium is increased, FA with longer chain length are produced. With respect to the chain length, it is observed that the predominant FA are C16:0, C16:1, C18:1, and C18:2. Of these, C18:1, i.e., oleic acid, is predominant. Oleic acid and C18:2, i.e., linoleic acid, decrease substantially at high AD percentages. In most vegetable and seed oils C18:2 is higher than C18:1, while in *Chlorella sorokiniana* at 0% and 15% AD, the C18:1/C18:2 ratio is about 2 at 30% AD and increases to about 4 at 50% AD. Additionally, palmitic acid, C16:0, is present in significant amounts up to 15% AD but decreases substantially at higher AD percentages. It can also be seen that chain lengths up to C26 are obtained, and in general increasing the amount of AD in the growth medium results in FA with higher chain length. FA with chain lengths higher than C20 are absent at 0% AD, but increase in chain length progressively as the percentage of AD is increased.

If the fatty acids are separated in three categories as: short chain FA from C10 to C14, medium chain FA from C16 to C18, and long chain FA higher than C18, then Figure 4 shows a histogram of the distribution of short, medium, and long chain FA versus the percentage of AD used. It was observed that the use of AD has a profound effect on the chain length of the FA in the biomass of *Chlorella sorokiniana*. In particular, the percentage of short chain length FA of the total FA increased by the addition of 15%, 30%, and 50% of AD in the growth medium compared with the control (crude glycerol + 0% AD). In contrast, the percentage of medium chain FA of the total FA decreased when AD was added to the growth medium at 30% and 50% compared with the control, while by the addition of 15% AD in the growth medium, the percentage of medium chain FA did not show statistically significant differences compared with the control. Additionally, the percentage of long chain FA of the total FA increased by the addition of 30% and 50% of AD in the growth medium compared with the control, while by the addition of 15% AD in the growth medium, the percentage of long chain FA did not show statistically significant differences compared with the control (Figure 4). The medium chain length FA, so predominant up to 15% AD, decrease significantly from 85–89% of the total FA to 52–53% at 30% and 50% AD. Instead, at 30% and 50% AD, the percentage of short chain and long chain FA increases substantially from 7.6% to 30.16%, respectively. Long chain FA also increase from about 4% to about 17% at 30% AD and to about 20% at 50% AD. This re-arrangement of the distribution of the chain length of the FA affects the properties of the biodiesel as discussed in the following paragraph.

Table 3. The Fatty Acid (FA) distribution for the biomass obtained using 0%, 15%, 30%, and 50% AD in the growth medium.

		0% AD	**15% AD**	**30% AD**	**50% AD**
A/A	**FA**	**% OF TOTAL FA**			
1	C10:0	0.61 ± 0.03	0.25 ± 0.01	3.60 ± 0.19	3.49 ± 0.19
2	C10:1	0.97 ± 0.05	0.83 ± 0.04	3.85 ± 2.00	1.91 ± 0.11
3	C12:0	1.42 ± 0.08	1.89 ± 0.10	1.71 ± 0.09	3.51 ± 0.19
4	C12:1	1.26 ± 0.07	0.83 ± 0.04	6.18 ± 0.32	4.81 ± 0.26
5	C14:0	1.66 ± 0.09	4.65 ± 0.25	10.75 ± 0.56	4.69 ± 0.24
6	C14:1	1.68 ± 0.09	3.44 ± 0.19	4.07 ± 0.21	8.02 ± 0.43
7	C16:0	14.54 ± 0.76	15.73 ± 0.81	7.51 ± 0.39	7.96 ± 0.41
8	C16:1	13.58 ± 0.71	5.53 ± 0.28	14.40 ± 0.77	15.57 ±0.81
9	C16:2	3.55 ± 0.18	1.95 ± 0.11	2.42 ±0.13	2.25 ±0.12
10	C18:0	3.99 ± 0.88	3.53 ± 0.18	1.62 ± 0.09	1.60 ± 0.09
11	C18:1	31.96 ± 1.68	35.48 ± 1.91	16.31 ± 0.85	18.31 ± 1.01
12	C18:2	15.99 ± 0.85	19.90 ± 1.04	4.98 ± 0.27	4.58 ± 0.24
13	C18:3	5.01 ± 0.27	1.71 ± 0.09	5.74 ± 0.29	3.65 ± 0.19
14	C20:0	2.73 ± 0.14	0.34 ± 0.02	3.14 ± 0.17	4.71 ± 0.25
15	C20:1	1.05 ± 0.06	0.44 ± 0.02	1.55 ± 0.08	2.15 ± 0.11
16	C22:0	-	0.21 ± 0.01	1.83 ± 0.11	1.39 ± 0.07
17	C22:1	-	0.89 ± 0.05	2.27 ± 0.13	3.94 ± 0.21
18	C24:0	-	-	1.60 ± 0.09	1.22 ± 0.06
19	C24:1	-	-	-	1.47 ± 0.08
20	C26:0	-	1.42 ± 0.07	6.47 ± 0.34	4.77 ± 0.25
21	C26:1	-	0.98 ± 0.05	-	-

Data represent average means and SE deviation, (*n*) = 4.

Figure 5 shows the distribution of SFA (Saturated FA), MUFA (Mono-Unsaturated FA), and PUFA (Poly-Unsaturated FA) versus the percentage of AD added to the growth medium. From Figure 5, it is evident that the percentage of AD also has an effect on the relative distribution of SFA, MUFA, and PUFA. In particular, the percentage of SFA of the total FA increased by the addition of 30% and 50% of AD in the growth medium compared with the control (crude glycerol + 0% AD), while by the addition of 15% AD in the growth medium, the percentage of SFA did not show statistically significant differences compared with the control. The percentage of MUFA of the total FA by the addition of 15%, 30%, and 50% of AD in the growth medium did not show statistically significant differences compared with the control. Furthermore, the percentage of PUFA of the total FA decreased by the addition of 30% and 50% of AD in the growth medium compared with the control, while by the addition of 15% AD in the growth medium, the percentage of PUFA did not show statistically significant differences compared with the control.

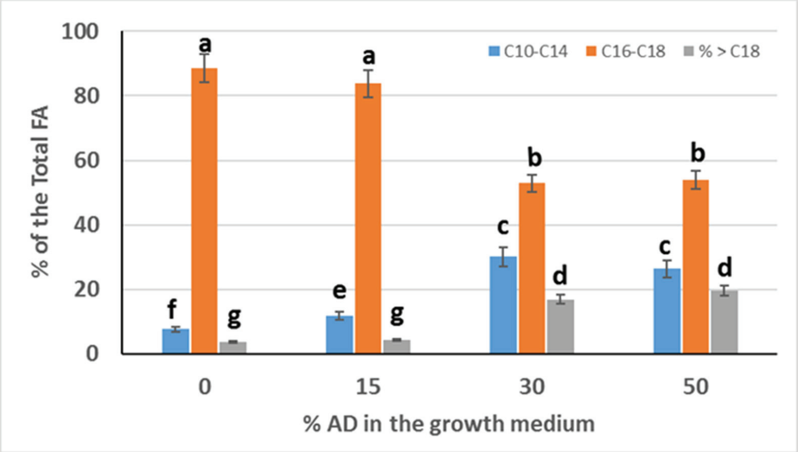

Figure 4. The distribution of FA in the biomass of *Chlorella sorokiniana* according to the chain length versus the percentage of AD added to the growth medium. Bar values with the same letter on the top are not significantly different according to Tukey's test ($p = 0.05$).

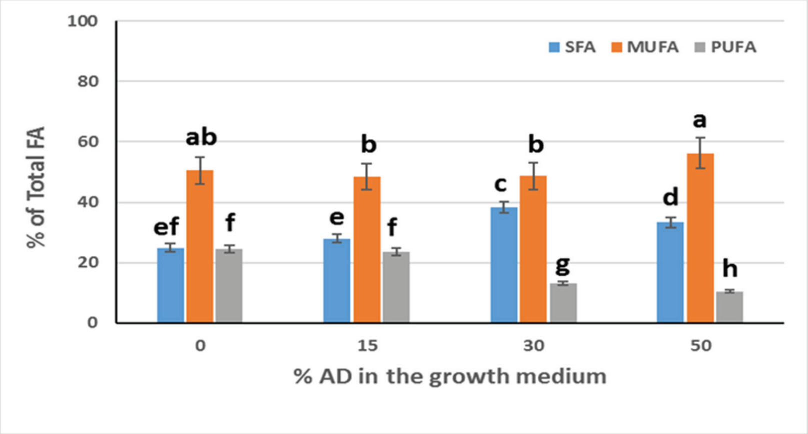

Figure 5. Effect of AD on the distribution of SFA, MUFA, and PUFA. Bar values with the same letter on the top are not significantly different according to Tukey's test ($p = 0.05$).

This should affect the biodiesel properties. Increasing the degree of saturation leads to a decrease in ignition delay [32]. The ignition delay is related to the cetane number (CN). As the ignition delay increases, the CN number decreases; the CN number is an indication of the quality of the biodiesel produced [20]. The ignition delay is an important parameter which characterizes the initiation of combustion process and consequently its development in diesel engines. Diesel engines, compared to gasoline engines, typically produce lower carbon monoxide and partially burned hydrocarbons. However, nitric oxides and particulate matter are significant pollutants from diesel engines. Changes in ignition delay affect the exhaust emissions indirectly. A decrease in the ignition delay leads to a longer time for complete combustion to take place in the cylinder and this results in lower emissions. Reversely, increased ignition delay leads to insufficient combustion time and therefore to higher exhaust emission. Therefore, ignition delay affects the combustion performance of a diesel engine. Higher CN leads to better engine performance. Additionally, the degree of saturation affects the iodine number. As the degree of saturation increases the IV number decreases. However, low iodine values lead to biodiesel, which is more combustible but not suitable for colder climates as it has rather poor flow properties at low temperatures [32].

3.5. Fatty Acid Methyl Ester (FAME) Properties

The saponification number (SN) is the weight (mg) of potassium hydroxide that is needed to convert one gram of fatty acid into soap. It relates to the average molecular weight, or the average chain length of all fatty acids present in the bio-oil. Therefore, longer chain FA give lower SN and vice versa. As the chain length becomes longer, the ratio of the mass of carboxylate (1) to the rest of the molecule of the FA decreases, hence less KOH is needed per g of FA.

The iodine value (IV) is the amount of iodine in grams absorbed by 100 mL of FA or FAME and is a measure of the degree of unsaturation of the FAs present in the oil or the respective FAME. Unsaturated fatty acid methyl esters are needed, as they improve the cold properties of the biodiesel, that is they prevent its solidification at low temperatures. As the degree of unsaturation increases, the IV of the biodiesel increases as well. However, a degree of unsaturation in the biodiesel leads to unwanted reactions with atmospheric oxygen leading to the formation of polymerization products in the internal combustion engine [20]. Therefore, a higher IV equal to 120 g I/100 g FAME has been set.

The cetane number (CN) relates to the quality of the fuel. As the cetane number increases the ignition delay, which the time between the injection of the fuel into the cylinder and the onset of ignition, decreases. Therefore, a higher CN leads to a shorter ignition delay. A minimum CN equal to 51 has been set by EN standards. The CN value depends on the number of unsaturated fatty acids, the number of double bonds, and the molecular weight of the FAME. Therefore, it correlates with the IV and the SN. The CN should not be very high as, as it increases, the IV and subsequently the degree of unsaturation decrease, and this may lead to poor cold flow properties of the biodiesel. Therefore, a maximum value for CN has been set to 65 by the ASTEM standard.

Table 4 shows the SN, IV, CN, and HHV values of the FAME, obtained from Table 3 of the bio-oil extracted from the biomass of *Chlorella sorokiniana* cultivated with 0%, 15%, 30%, and 50% AD, using Equations (1)–(4). Values of FAME properties in Table 4 can be explained in terms of the FA distribution with respect to the chain length (Figure 4) and the degree of saturation (Figure 5). Increasing the degree of saturation leads to a decrease in the iodine number (IV). Additionally, increasing the average chain length decreases both the iodine number (IV) and the saponification number (SN) and increases the cetane number (CN). However, according to Equation (3), a decrease in the SN has more profound effect on the CN than a decrease in IV. The combined results showed that the SN, HHV, and CN values of the FAME by the addition of 15%, 30%, and 50% of AD in the growth medium did not show statistically significant differences compared with the control (crude glycerol + 0% AD), while increasing the percentage of AD in the growth medium the CN values show an increase trend from 52.68 to 56.12. The IV values of the FAME decreased by the addition of 30% and 50% of AD in the growth medium compared with the control while, by the addition of 15% AD in the growth medium, the IV values of the FAME did not show statistically significant differences compared with the control (Table 4).

Table 4. Calculated FAME properties of the biodiesel obtained from the cultivation of *Chlorella sorokiniana* with 0%, 15%, 30%, and 50% AD.

Property *	0% AD	15% AD	30% AD	50% AD
Saponification Number (SN)	199.79 ± 10.46 ^{a}	198.47 ± 10.39 ^{a}	208.29 ± 10.62 ^{a}	205.38 ± 10.58 ^{a}
Iodine Value (IV)	93.07 ± 4.72 ^{a}	85.49 ± 4.36 ^{a}	75.6 ± 3.91 ^{b}	74.47 ± 3.76 ^{b}
Cetane number (CN)	52.68 ± 2.74 ^{a}	54.57 ± 2.75 ^{a}	55.49 ± 2.87 ^{a}	56.12 ± 2.85 ^{a}
Higher Heating value (HHV)	39.84 ± 2.08 ^{a}	40.01 ± 2.13 ^{a}	39.76 ± 2.06 ^{a}	39.89 ± 2.12 ^{a}

* Units: SN: mg KOH/g FA, IV: g I/100 g FAME and HHV: MJ/kg; Data represent average means and SE deviation, (*n*) = 4; in each chemical property of the table different letters indicate significant differences according to the Tukey's test (p = 0.05).

4. Conclusions

Chlorella sorokiniana was cultivated heterotrophically using glycerol and varying amounts of AD such as 0%, 15%, 30%, and 50%, respectively. Glycerin, a biodiesel by-product, seems to be a potential substrate for the heterotrophic cultivation of *Chlorella sorokiniana*, while the AD can be an additional source of carbon for heterotrophic or mixotrophic growth.

These results indicate that different addition rates of AD in the growth medium affect the rate of carbon uptake up by the *Chlorella sorokiniana* cells, as well as its protein and lipid content. The maximum carbon uptake rate occurs at about 30% AD. Increasing the percentage of AD from 0% to 50% in the growth medium, the lipid content gradually decreases by up to 5%. This decrease can be ameliorated or reversed by other modes of cultivation, based of biochemical engineering principles, such as fed-batch mode rather than batch cultivation.

Additionally, the different addition rates of AD in the growth medium affect the FA distribution in the oil extracted and the FAME properties. FA distribution ranged from C10 to C26. Increasing the percentage of AD from 0% to 50% increased the percentage of the FA with $C < 16$ from 7.6 to 26.4% of total FA and the percentage of the FA with $C > 18$ from 3.8 to 19.7% of total FA. On the contrary, the percentage of the FA with C16–C18 decreased from 88.6% to 53.9% of total FA. In addition, increasing the percentage of AD from 0% to 50% increased the percentage of SFA by 33% and decreased the percentage of PUFA by 57%. In all AD percentages, the percentage of MUFA did not vary significantly and ranged from 48% to 56% of the total FA. The changes in the FA distribution as the percentage of AD increases from 0% to 50% in the growth medium, lead to increase cetane numbers by 6.5% and decrease iodine values by 20%. AD is a useful raw material for the formulation of growth media for the cultivation of *Chlorella sorokiniana*.

These results could stimulate the scientific community in order to use anaerobic digestate, enriched with carbon sources other than glycerol, into the formulation of growth media for the cultivation of microalgae and investigate growth kinetics and the biodiesel properties. Further research is needed in order to determine the effect of other modes of cultivation using glycerol and AD in microalgal cultivation for producing lipids for biodiesel production. As different strains of microalgae can utilize glycerol in varying degrees, glycerol and AD can be tried on different strains, especially genetically modified strains.

Author Contributions: All authors took part in the experiments and in the preparation of the growth media and the digestate. However, each author contributed more heavily to the following: G.P. was a major contributor in writing the manuscript and a general supervisor of all experimental set- up. A.M., M.N.M., A.P. and A.K. contributed mostly to the experimental set up of bioreactors, the control of the parameters of the experiments, and the processing of the digestate. D.K. and X.S. analyzed and interpreted the data of the experiments, and N.G. performed all the chemical analyses of the experiments. All authors have read and agreed to the published version of the manuscript.

Funding: This research was co-financed by the European Regional Development Fund of the European Union and Greek national funds through the Operational Program Competitiveness, Entrepreneurship and Innovation, under the call RESEARCH—CREATE—INNOVATE (project code: T1EDK-01580).

Institutional Review Board Statement: Not applicable.

Informed Consent Statement: Not applicable.

Data Availability Statement: Not applicable.

Acknowledgments: The authors are grateful to the Company SEITIS BROS BIOGAS S.A., Argyropouli Tyrnavou, for supplying the anaerobic digestate.

Conflicts of Interest: The authors declare no conflict of interest.

References

1. Mata, T.M.; Martins, A.A.; Caetano, N.S. Microalgae for biodiesel production and other applications: A review. *Renew. Sust. Energy Rev.* **2010**, *14*, 217–232. [CrossRef]
2. Gouveia, L.; Oliveira, A.C. Microalgae as a raw material for biofuels production. *J. Ind. Microbiol. Biotechnol.* **2009**, *36*, 269–274. [CrossRef] [PubMed]
3. Dean, A.; Sigee, D.; Estrada, B.; Pittman, J. Using FTIR spectroscopy for rapid determination of lipid accumulation in response to nitrogen limitation in freshwater Microalgae. *Biores. Technol.* **2010**, *101*, 4499–4507. [CrossRef] [PubMed]
4. Spolaore, P.; Joannis-Cassan, C.; Duran, E.; Isambert, A. Commercial applications of microalgae. *J. Biosci. Bioeng.* **2006**, *101*, 87–96. [CrossRef]
5. Patil, V.; Reitan, K.I.; Knutsen, G.; Mortensen, L.M.; Källqvist, T.; Olsen, E.; Vogt, G.; Gislerød, H.R. Microalgae as source of polyunsaturated fatty acids for aquaculture. *Plant Biol.* **2005**, *6*, 57–65.
6. Chojnacka, K.; Marquez-Rocha, F.J. Kinetic and stoichiometric relationships of the energy and carbon metabolism in the culture of Microalgae. *Biotechnology* **2004**, *3*, 21–34. [CrossRef]
7. Bumbak, F.; Cook, S.; Zachleder, V.; Hauser, S.; Kovar, K. Best practices in heterotrophic high-cell-density microalgal processes: Achievements, potential and possible limitations. *Appl. Microbol. Biotechnol.* **2011**, *91*, 31–46. [CrossRef]
8. Perez-Garcia, O.; Bashan, Y. Microalgal heterotrophic and mixotrophic culturing for bio-refining: From metabolic routes to techno-economics. In *Algal Biorefineries*; Prokop, A., Bajpai, R., Zappi, M., Eds.; Springer: Cham, Switzerland, 2015.
9. Perez-Garcia, O.; Escalante, F.M.; De-Bashan, L.E.; Bashan, Y. Heterotrophic cultures of microalgae: Metabolism and potential products. *Water Res.* **2011**, *45*, 11–36. [CrossRef]
10. Li, X.; Xu, H.; Wu, Q. Large-scale biodiesel production from microalga *Chlorella protothecoides* through heterotrophic cultivation in bioreactors. *Biotechnol. Bioeng.* **2007**, *98*, 764–771. [CrossRef]
11. Xiong, W.; Li, X.; Xiang, J.; Wu, Q. High-density fermentation of microalga *Chlorella protothecoides* in bioreactor for microbio-diesel production. *Appl. Microbol. Biotechnol.* **2008**, *78*, 29–36. [CrossRef] [PubMed]
12. Qiao, H.; Wang, G. Effect of carbon source on growth and lipid accumulation in *Chlorella sorokiniana* GXNN01. *Chin. J. Oceanol. Limnol.* **2009**, *27*, 762–768. [CrossRef]
13. Liang, Y.; Sarkany, N.; Cui, Y. Biomass and lipid productivities of *Chlorella vulgaris* under autotrophic, heterotrophic and mixotrophic growth conditions. *Biotechnol. Lett.* **2009**, *31*, 1043–1049. [CrossRef]
14. Ogbonna, J.C.; Tomiyamal, S.; Tanaka, H. Heterotrophic cultivation of *Euglena gracilis* Z for efficient production of α-tocopherol. *J. Appl. Phys.* **1998**, *10*, 67–74.
15. Xu, H.; Miao, X.; Wu, Q. High quality biodiesel production from a microalga *Chlorella protothecoides* by heterotrophic growth in fermenters. *J. Biotechnol.* **2006**, *126*, 499–507. [CrossRef] [PubMed]
16. O'Grady, J.; Morgan, J.A. Heterotrophic growth and lipid production of *Chlorella protothecoides* on glycerol. *Bioprocess Biosyst. Eng.* **2011**, *34*, 121–125. [CrossRef]
17. Kong, W.B.; Yang, H.; Cao, Y.T.; Song, H.; Hua, S.F.; Xia, C.G. Effect of Glycerol and Glucose on the Enhancement of Biomass, Lipid and Soluble Carbohydrate Production by *Chlorella vulgaris* in Mixotrophic Culture. *Food Technol. Biotechnol.* **2013**, *51*, 62–69.
18. SAG. Sammlung von Algenkulturen der Universität Göttingen. Culture Collection of Algae, Abteilung Experimentelle Phykologie und Sammlung von Algenkulturen (EPSAG), Universität Göttingen, Deutschland. 2007. Available online: http://epsag.uni-goettingen.de (accessed on 1 October 2021).
19. Kalayasiri, P.; Jayashoke, N.; Krisnangkura, K. Survey of seed oils for use as diesel fuels. *J. Am. Oil Chem. Soc.* **1996**, *73*, 471–474. [CrossRef]
20. Azam, M.M.; Waris, A.; Nahar, N.M. Prospects and potential of fatty acid methyl esters of some non-traditional seed oils for use as biodiesel in India. *Biomass Bioenergy* **2005**, *29*, 293–302.
21. Krisnangkura, K. A simple method for estimation of cetane index of vegetable oil methyl esters. *J. Am. Oil Chem. Soc.* **1986**, *63*, 552–553. [CrossRef]
22. Demirbaş, A. Fuel properties and calculation of higher heating values of vegetable oils. *Fuel* **1998**, *77*, 1117–1120. [CrossRef]
23. Association of Official Analytical Chemists (AOAC). *Official Methods of Analysis of the Association of Official Analytical Chemists International*, 16th ed.; AOAC: Arlington, VA, USA, 1995.
24. Jones, L.J.B., Jr. *Plant Nutrition Manual*; CRC Press: New York, NY, USA, 1998.
25. Biancarosa, I.; Espe, M.; Bruckner, C.G.; Heesch, S.; Liland, N.; Waagbø, R.; Torstensen, B.; Lock, E.J. Amino acid composition, protein content, and nitrogen-to-protein conversion factors of 21 seaweed species from Norwegian waters. *J. Appl. Phys.* **2017**, *29*, 1001–1009. [CrossRef]
26. Bian, X.; Jin, W.; Gu, Q.; Zhou, X.; Xi, Y.; Tu, R.; Han, S.; Xie, G.; Gao, S.; Wang, Q. Subcritical n-hexane/isopropanol extraction of lipid from wet microalgal pastes of Scenedesmus obliquus. *World J. Microbol. Biotechnol.* **2018**, *34*, 39. [CrossRef]
27. Stehlik-Barry, K.; Babinec, A.J. *Data Analysis with IBM SPSS Statistics*; Packt Publishing Ltd.: Birmingham, Mumbai, 2017.
28. Chuka-ogwudea, D.; Ogbonnab, J.; Moheimania, N.R. A review on microalgal culture to treat anaerobic digestate food waste effluent. *Algal Res.* **2020**, *47*, 101841. [CrossRef]
29. Singh, M.; Reynolds, D.L.; Das, K.C. Microalgal system for treatment of effluent from poultry litter anaerobic digestion. *Bioresour. Technol.* **2011**, *102*, 10841–10848. [CrossRef] [PubMed]

30. Rajagopal, R.; Mousavi, S.E.; Goyette, B.; Adhikary, S. Coupling of Microalgae Cultivation with Anaerobic Digestion of Poultry Wastes: Toward Sustainable Value Added Bioproducts. *Bioengineering* **2021**, *8*, 57. [CrossRef] [PubMed]
31. Sekine, M.; Yoshida, A.; Akizuki, S.; Kishi, M.; Toda, T. Microalgae cultivation using undiluted anaerobic digestate by introducing aerobic ditrification–desulfurization treatment. *Water Sci. Technol.* **2020**, *82*, 1070–1080. [CrossRef] [PubMed]
32. Schönborn, A.; Ladommatos, N.; Williams, J.; Allan, R.; Rogerson, J. The influence of molecular structure of fatty acid monoalkyl esters on diesel combustion. *Combust. Flame* **2009**, *156*, 1396–1412. [CrossRef]

sustainability

Article

Recovery of Salts from Synthetic Erythritol Culture Broth via Electrodialysis: An Alternative Strategy from the Bin to the Loop

Laura Daza-Serna [1,*], Katarina Knežević [2], Norbert Kreuzinger [2], Astrid Rosa Mach-Aigner [1,3], Robert Ludwig Mach [3], Jörg Krampe [2] and Anton Friedl [4]

[1] Christian Doppler Laboratory for Optimized Expression of Carbohydrate-Active Enzymes, Research Division Biochemical Technology, Institute of Chemical, Environmental and Bioscience Engineering, Technische Universität Wien, 1060 Vienna, Austria; astrid.mach-aigner@tuwien.ac.at
[2] Institute for Water Quality and Resource Management, Technische Universität Wien, 1040 Vienna, Austria; katarina.knezevic@tuwien.ac.at (K.K.); norbkreu@iwag.tuwien.ac.at (N.K.); jkrampe@iwag.tuwien.ac.at (J.K.)
[3] Research Division Biochemical Technology, Institute of Chemical, Environmental and Bioscience Engineering, Technische Universität Wien, 1060 Vienna, Austria; robert.mach@tuwien.ac.at
[4] Research Division Bioresource and Plant Science, Institute of Chemical, Environmental and Bioscience Engineering, Technische Universität Wien, 1060 Vienna, Austria; anton.friedl@tuwien.ac.at
* Correspondence: laura.serna@tuwien.ac.at

Abstract: Sustainability and circularity are currently two relevant drivers in the development and optimisation of industrial processes. This study assessed the use of electrodialysis (ED) to purify synthetic erythritol culture broth and for the recovery of the salts in solution, for minimising the generation of waste by representing an efficient alternative to remove ions, ensuring their recovery process contributing to reaching cleaner standards in erythritol production. Removal and recovery of ions was evaluated for synthetic erythritol culture broth at three different levels of complexity using a stepwise voltage in the experimental settings. ED was demonstrated to be a potential technology removing between 91.7–99.0% of ions from the synthetic culture broth, with 49–54% current efficiency. Besides this, further recovery of ions into the concentrated fraction was accomplished. The anions and cations were recovered in a second fraction reaching concentration factors between 1.5 to 2.5 times while observing low level of erythritol losses (<2%), with an energy consumption of 4.10 kWh/m^3.

Keywords: electrodialysis; erythritol downstream; desalination; waste reduction; current efficiency

Citation: Daza-Serna, L.; Knežević, K.; Kreuzinger, N.; Mach-Aigner, A.R.; Mach, R.L.; Krampe, J.; Friedl, A. Recovery of Salts from Synthetic Erythritol Culture Broth via Electrodialysis: An Alternative Strategy from the Bin to the Loop. *Sustainability* **2022**, *14*, 734. https://doi.org/10.3390/su14020734

Academic Editors: Oz Sahin and Edoardo Bertone

Received: 15 December 2021
Accepted: 2 January 2022
Published: 10 January 2022

1. Introduction

Erythritol is a four-carbon polyol used for foods, pharmaceutical and cosmetic products manufacture, among others [1–5]. Its high relative sweetness [1,2], and low caloric content [3,4] makes erythritol a competitive sugar substitute with promissory increases of demand in the market [6]. Erythritol is produced as an extracellular product in submerged cultures by various osmotolerant microorganisms from yeast, fungi-like yeast and fungi, including *Moniliella tormentosa pollinis*, *Yarrowia lipolytica*, *Moliniella Pollinis*, *Candida magnoliae*, *Candida sorbosivorans*, and *Pseudozyma tsukubaensis* [7–11]. The growth and metabolism of microorganisms are affected by osmotic stress modulated by salts, polyethyleneglycol, and carbon source addition [12–15]. At high osmotic pressure conditions, the growth rate decreases, while osmotolerant erythritol-producing microorganisms favour erythritol production and accumulation as a protective response to hyperosmotic conditions [16–18]. The effect of the hyperosmotic conditions by adding salts has been studied in the production of erythritol using NaCl and KCl as osmotic agents in concentration levels up to 50 g/L increasing the concentration of erythritol up to 50% compared to the control without the addition of salt [17–21].

To accomplish essential cellular tasks (maintenance, growth, and synthesis of products), microorganisms require a source of carbon, macronutrients (N, S, and P), micronutrients (K, Ca, Mg, Na, and Fe), and trace elements (Mn, Zn, Co, Mo, Ni, and Cu) [22–27]. Main components in culture media for erythritol production include salts as KH_2PO_4, $MgSO_4$, NaCl, $CuSO_4$, $FeSO_4$, $MnSO_4$, $CuSO_4$, $(NH_4)_2SO_4$; and other compounds from different sources as surfactants, peptone, and polysorbate 80 [8,28,29]. These compounds are added in concentrations between 0.2 g/L to 26 g/L in the culture stage [7,8,10,28,30–33].

The remaining salts from the culture media have to be separated from the culture broth to obtain pure erythritol, and therefore the non-used salts in the culture broth leave the process as a residual stream that has to be removed in the downstream section [34]. In the last decades, the recovery of nutrients has gained interest, becoming a multidisciplinary challenge for industry, water resources management, soil conservation, among other fields [34–37]. The transition from conventional processes to industrial circular processes represents an opportunity to tackle resource management and climate change concerns. In order to attend the depicted necessities, the European Union has developed projects as *Zero Brine* [36], *INCOVER* [37], *NITROMAN* [38], among other initiatives looking for technological alternatives that are able to reduce the impact caused by the waste and to evaluate the recovery of valuable compounds as phosphorus, sulphate, ammonia, and others. However, there is not enough scientific evidence regarding the consumption and recovery and reutilisation of salts from submerged cultures, especially considering the mandatory demand for salts in these biotechnological processes.

The removal of salts from erythritol culture broth is used as an example of a more general approach for recycling residuals from biotechnological culture and so far has been addressed by adsorption on ion exchange resins in the downstream section [34,39–41]. The principle behind this separation is the removal of salts by exchanging their position with other exchangeable ions (Na^+, H^+, among others) within cationic and anionic exchange resins. However, despite the high performance and efficiency of this conventional approach, downstream regeneration of ion-exchange resins requires chemical substances. It generates large amounts of alkaline and acid residual waste streams mainly composed of the salts removed from the culture broth. This fact represents a drawback to reach sustainable and cleaner production goals.

Alternatives for removing salts include membrane-based technologies, like forward osmosis, membrane distillation and electrodialysis [42]. Electrodialysis (ED) is an environmentally friendly and low energy demanding membrane-based technology suitable for the recovery of ionisable molecules from spent culture broths [42–46]. An electrical potential applied to the ED cell serves as the driving force for separating ionic species from the uncharged matter in an aqueous solution. Studies in ED application include recovery and reutilisation of alkaline fractions [47], separation and purification of L-phenylalanine [48], lactic acid [49], glycerol [50], glutamine [51], and 1,3-propanediol [52].

During the ED batch process, the feed located in the diluted and concentrated reservoir is recirculated in a closed loop through a stack of membranes in the ED batch mode, driven by a directly applied direct current. Cations and anions migrate from the feed solution to a concentrated fraction by going through cation- and anion-selective membranes, respectively. Two fractions are obtained at the end of the ED treatment: a purified product fraction with a low content of ions and a concentrated fraction rich in ions [50,53]. The main factors affecting the performance of ED treatment include the applied current density, the selectivity of the membranes (monovalent or multivalent), the flow of diluted and concentrated fractions, temperature, and pH [50,51,54].

Limiting current density (LCD) is a critical parameter that rules the overall performance of electrodialysis. The LCD value represents a threshold of a maximum current applied to the ED cell, at and above which adverse effects take place in the ED separation process. If the ED is operated in the limiting (at the threshold) or over-limiting (above the threshold) regime, dissociation of water molecules occurs in a thin layer at the membrane/diluted-solution interface. The H^+ and OH^- ions from water dissociation participate in the transfer of current (through the ED membrane stack), reducing the overall ED process efficiency and increasing the energy consumption. Besides water splitting, fluid leakage, current leakage, and co-ion transfer occur if the threshold current density is exceeded [50].

This paper aims to evaluate the performance of the ED to separate and recover valuable ions from culture-broth process streams. Firstly, remove salts from erythritol culture broth, and then concentrate the same salts in a potentially reusable concentrated fraction. This assessment could become the first stage to evaluate the reutilisation of ions as an approach to treat waste stream from bin to loop.

The experiments were designed in three stages, gradually increasing the complexity of the fed solution. In this sense, the research question was to understand how can the complexity of culture broth solutions affect the performance of ED treatments. For this purpose, three different solutions were tested, and a stepwise voltage approach was used for the experiments. Each stage was judged upon the removal efficiency of ions in the diluted fraction, the concentration factor in the concentrated fraction, and the overall losses of products, by-products, and glucose used as a carbon source. Considering the industrial projection of this ED application, the current efficiency and energy consumption were also determined.

2. Materials and Methods

2.1. Reagents

All the reagents used in this study were purchased from Merck KGaA (Darmstadt, Germany). Anion multi-element standards (Certipur® Anion-Multielement-Standard I (PO_4^{3-}) and II (Cl^-, SO_4^{2-})) and cation multi-element standard (Certipur® Cationic-Multielement-Standard VI) (NH_4^+, K^+, Na^+, Ca^{2+}, Mg^{2+}) were used as standards for Ion-Chromatography. HPLC grade erythritol, glucose, and glycerol were used as the calibration curve standards. Milli-Q-Water was prepared according to DIN ISO 3696 (1991) [55].

2.2. Feed Solutions

The experimental part was developed in three stages, increasing the complexity of the solutions by adding compounds from three different groups present in the erythritol culture media:

2.2.1. Salts from Culture Media

This fraction includes all the ionisable compounds added as macronutrients, micronutrients, and traces elements, namely ammonium sulphate ($(NH_4)_2SO_4$), magnesium sulphate heptahydrate ($MgSO_47H_2O$), potassium dihydrogen phosphate (KH_2PO_4), ferrous sulphate heptahydrate ($FeSO_47H_2O$), manganese sulphate monohydrate ($MnSO_4H_2O$), zinc sulphate heptahydrate ($ZnSO_47H_2O$), calcium chloride dihydrate ($CaCl_2H_2O$), and sodium chloride (NaCl) as the osmotic agent used. These compounds are separated in the concentrated fraction.

2.2.2. Erythritol and By-Products

This fraction included erythritol as the main product, glycerol, and residual glucose as by-products. These compounds are neutral and not dissociable at the operational conditions (erythritol, glycerol, and glucose pKa values 13.9, 14.4, and 12.28, respectively) [56–58]. These compounds should remain in the diluted fraction.

2.2.3. Other Compounds from Culture Media

This fraction includes surfactant (tween 80) and peptone used as surfactant and emulsifier for membrane cell protection. These compounds should remain in the diluted fraction.

Table 1 presents the concentration levels and compounds added to the experiments. The solution fed to the system increased its complexity in each stage (S, SP, and SCB solutions), while the initial concentrated solution (equivalent to the S solution) remained unchanged during the experiments as the receiving media for the salts. The compounds and concentrations in the feed solutions were defined based on a preliminary characterisation of ions and conductivity of a real erythritol culture broth after the fermentation stage (data not shown). According to these results, the concentrations used in this work corresponded to 50% culture media before fermentation. Considering the lack of studies regarding the consumption of osmotic agents, in this study sodium chloride was added only to adjust the conductivity of feed solutions.

Table 1. Description of the evaluated solutions.

Compound	Molecular Formula	[g/L]	Sample		
			S	SP	SCB
Ammonium sulphate	$(NH_4)_2\ SO_4$	1.4	x	x	x
Magnesium sulphate heptahydrate	$MgSO_4\ 7H_2O$	0.5	x	x	x
Potassium dihydrogen phosphate	KH_2PO_4	4.2	x	x	x
Ferrous sulphate heptahydrate	$FeSO_4\ 7H_2O$	0.0025	x	x	x
Manganese sulphate monohydrate	$MnSO_4\ H_2O$	0.00085	x	x	x
Zinc sulphate heptahydrate	$ZnSO_4\ 7H_2O$	0.0007	x	x	x
Calcium chloride dihydrate	$CaCl_2\ 2H_2O$	0.001	x	x	x
Sodium chloride *	NaCl	0.8	x	x	x
Tween 80	$C_{64}H_{124}O_{26}$	0.25			x
Peptone	n.a.	0.05			x
Erythritol	$C_4H_{10}O_4$	5		x	x
Glycerol	$C_3H_8O_3$	5		x	x
Glucose	$C_6H_{12}O_6$	2		x	x

Note: n.a.: not available. * NaCl was added to adjust conductivity to the measured value in the real culture broth. S: only salts solution, SP: salts + product, SCB: synthetic culture broth.

The compounds added to the three feed solutions are marked with a cross in Table 1. The first stage considers only the salt content in spent culture media (S solution), where both the diluted and the concentrated solution have the same initial composition. The initial concentrated solution is kept the same (S solution) in further stages, whereas the diluted solution complexity gradually increased. The main products and by-products were added to the diluted stream in the second stage (SP solution). Finally, the third stage studied the treatment of the complete erythritol synthetic culture broth (SCB), including tween 80 and peptone, introduced to the diluted stream.

2.3. Experimental Settings

An electrodialysis laboratory unit ED 64004 (PCCell GmbH, Heusweiler, Germany) was used in this work. The ED 64004 consisted of a current generator supplying constant voltage (0–30 V), a control unit, an online measuring system for pH, temperature, conductivity, and voltage (JUMO GmbH & Co. KG, Fulda, Germany), and three independent storage containers for diluted, concentrated and electrode rinsing solution connected in circuits with three magnetically coupled centrifugal pumps NDP 25/4 (ITS-Betzel, Hatterscheim, Germany).

The ED membrane stack was composed of two electrode compartments with 10 identical cells. Each cell unit has an anion exchange membrane (AEM. Ref: PC SA 10x) and a cation exchange membrane (CEM. Ref: PC SK 9x). The effective membrane area was 64 cm^2 per membrane, with 1 mm of spacing between membranes. The anode and cathode materials were Pt/Ir-coated titanium and theV4A steel, respectively. They were placed in the polypropylene electrode housing material.

All the voltages assessed in this approach corresponded to 80% of the limiting current density (LCD) determined using the Cowan and Brown method [59]. A stepwise voltage was the approach used for the application of the direct current in this work. Through this approach, four different voltages (10, 9, 7 and 6 V) were kept constant during a period and changed as soon as the conductivity of the diluted fraction turned from 5.47 mS/cm (initial value) to 3, 2 and 1.4 mS/cm. The four voltage-conductivity pairs were selected from preliminary assays finding the LCD for different conductivity levels (data not shown).

S, SP, and SCB experiments were performed in triplicates. In situ parameters as pH, conductivity, and temperature were recorded at the beginning and during the treatment. 1.5 L of diluted and concentrated solution were pumped and recirculated to the system at a constant flowrate rate of 15 L/h, whereas the electrode-rinsing solution (0.25 M Na_2SO_4) was recirculated at 150 L/h.

A total of 12 samples per experiment were taken at different interval times, considering the reduction in the concentration of ions. The first nine samples were taken every 5 min, the 10th and 11th were taken every 10 min, and the last sample was taken after the conductivity of the diluted fraction reached a chosen value of 0.28 mS/cm. This value was selected, having as reference tap water conductivities. Due to the short-term characteristics of the experiments, scaling and fouling phenomena were not considered in the analysis.

2.4. Analysis of Anions and Cations with Ion Chromatography (IC)

Inorganic ions (Na^+, $NH_4{}^+$, K^+, Mg^{2+}, Cl^-, $SO_4{}^{2-}$, $PO_4{}^{3-}$) in diluted and concentrated fractions were determined by ion chromatography (IC) on a Dionex ICS 5000+ system (Thermo Scientific, Waltham, MA, USA) equipped with conductivity detectors and an autosampler Dionex AS-DV (Thermo Scientific, Waltham, MA, USA) for simultaneous injection onto both anion and cation columns.

Anions were separated using a Dionex ATV-HC trap pre-column (9 × 75 mm) using gradient elution. Cations were separated on a Dionex CS12A analytical column (4 × 250 mm) with a CG12A guard column (4 × 50 mm) using an isocratic elution. The mobile phases used were 5mM NaOH, 25mM NaOH, and 20 mM methanesulphonic acid. All the flows, gradient specifications, and current suppression programs are described by Linderman et al. (2020) [60].

2.5. Analysis of Erythritol, Glycerol, and Glucose with HPLC

Erythritol, glycerol, and glucose were determined on a High-Performance Liquid Chromatography (HPLC) equipped with a degasser unit DGU-20A3R (Shimadzu, Kyoto, Japan), an autosampler unit SIL-20ACHT (Shimadzu, Kyoto, Japan), a column oven CTO-20A (Shimadzu, Kyoto, Japan), and a refractive index detector RID-20A (Shimadzu, Kyoto, Japan). The mentioned compounds were separated on a Shodex SH1011 column (80 × 300 mm) with a guard column Shodex Sugar SH-G (6.0 × 50 mm). The HPLC was coupled with a refractive index detector RID-20A (Shimadzu, Kyoto, Japan). The separation was performed at an isocratic gradient. The mobile phase used was 5 mM H_2SO_4 at 0.6 mL/min for 20 min. The oven and RID temperature were 50 °C.

2.6. Removal of Ions and Current Efficiency (CE)

The percentage of removal (R_j) of ions was calculated by using Equation (1), where $C_j(t_i)$ means an initial or a given time, and $C_j(t_{i+1})$ means the final time of the period to be evaluated.

$$R_j(\%) = \frac{C_j(t_i) - C_j(t_{i+1})}{C_j(t_i)} \times 100\% \tag{1}$$

Current efficiency (CE) was calculated based on Faraday's Law following the approach suggested by Wu et al. (2011) [47] (Equation (2)). Where $n_j{}^i$ and $n_j{}^f$ are the initial and final number of moles of salts in diluted fraction, F is the Faraday constant (96,485.33 sA/mol), I is the current value (A), t is the time (s), N is the number of cell pairs in the stack, and z is the ionic charge (pH-dependent for polyvalent ions).

$$CE(\%) = \frac{F \times \sum_j z_j(n_j^i - n_j^f)}{N \times I \times t} \tag{2}$$

Considering that the energy applied is used to promote the simultaneous migration of cations and anions towards the electrodes, CE was estimated only based on the behaviour of anions in the solution.

2.7. Energy Consumption

The energy required for the desalination (E_d) of the feed solution was calculated following Equation (3), where U is the applied voltage (V), I is the applied current (A), t is the desalination duration (h), and V is the treated volume of the feed solution (m^3).

$$E_d\left(\frac{kWh}{m^3}\right) = \frac{U \times I \times t}{V} \tag{3}$$

Energy consumed by the pumps (E_p) in the diluted, concentrated, and electrode-rinsing solutions was calculated following Equation (4), where Q is the flow of the diluted, concentrated, or electrode-rinsing solution (m^3/s), Δp is the differential pressure (Pa) between the inlet and outlet of the ED stack, η is the pump efficiency (assumed as 75% for all three pumps), and V is the treated volume of the diluted solution (m^3).

$$E_p\left(\frac{kWh}{m^3}\right) = \frac{Q \times \Delta p}{\eta \times V} \tag{4}$$

3. Results

3.1. Chemical Composition of S, SP, and SCB Solutions

Table 2 presents the characterisation of initial monovalent and bivalent ions in the S, SP, and SCB solutions. The preparation process causes minor deviations in the chemical composition of the solutions. Due to the pH levels and the polyvalent nature, sulphur and phosphorus ions can adopt different dissociation values. Considering the initial pH value (Table 3), the main form of these ions was the monovalent dihydrogen phosphate ($H_2PO_4^-$) and sulphate (SO_4^{2-}) with −1 valence.

Table 2. Ion concentration in feed S, SP and SCB solutions.

Ion	S * [mg/L]	SP [mg/L]	SCB [mg/L]
Cl^-	426.9	399.6 ± 17.6	431.5 ± 8.2
SO_4^{2-}	1162.2	1088.6 ± 29.8	1165.7 ± 11.0
$H_2PO_4^-$	1281.7	1216.8 ± 47.7	1236.5 ± 7.8
Na^+	272.1	279.4 ± 31.2	289.6 ± 1.5
NH_4^+	230.4	221.8 ± 15.0	248.9 ± 34.5
K^+	515.4	516.9 ± 75.6	588.1 ± 13.6
Mg^{2+}	67.2	71.6 ± 15.3	69.1 ± 2.6

Note: * Only one sample was characterised.

Table 3. Physicochemical parameters of the diluted and concentrated fraction at the initial and final stages of the ED separation process.

		Diluted Fraction					
Parameter	Units	S		SP		SCB	
		Initial	Final	Initial	Final	Initial	Final
pH		4.59–4.60	3.92–4.07	4.59–4.63	4.29–4.30	4.53–4.55	4.23–4.42
Temperature	°C	21.7 ± 2.9	20.2 ± 0.5	21.2 ± 1.1	20.8 ± 0.5	20.8 ± 3.8	20.2 ± 0.2
Conductivity	mS/cm	5.57 ±0.03	0.28 ± 0.00	5.41 ± 0.05	0.28 ± 0.00	5.43 ± 0.03	0.28 ± 0.00

Table 3. *Cont.*

Parameter	Units	Concentrated Fraction					
		S		SP		SCB	
		Initial	Final	Initial	Final	Initial	Final
pH		4.59–4.60	4.40–4.59	4.56–4.64	4.39–4.52	4.58–4.59	4.48–4.72
Temperature	°C	21.7 ± 2.9	20.3 ± 1.1	22.2 ± 1.1	20.8 ± 0.5	24.2 ± 1.4	19.8 ± 0.5
Conductivity	mS/cm	5.57 ± 0.03	11.79 ± 0.51	5.57 ± 0.02	10.02 ± 0.02	5.54 ± 0.01	11.2 ± 0.06

According to the measured concentrations in Table 2, an average erythritol culture media would need more anions (72% wt.) than cations (28% wt.); and more total monovalent (69% wt.) than bivalent ions (31% wt.). Differences in the amounts of ions added per species are expressed in the concentration gradients. These differences are considered in other sections for the analysis of removal and current efficiency.

3.2. Physicochemical Parameters

Table 3 presents the physicochemical parameters measured at the beginning and the end of each experiment. A slight drop between 0.13–0.67 units in pH value was observed in the diluted fraction and between 0.01 and 0.19 in S and SP feed solutions in the concentrated fraction. However, this level of pH variations did not affect the overall removal of cations and anions from the diluted fraction (Table 4). Temperature control plays an important role in avoiding effects caused by temperature depending processes as diffusion and changes in the affinity and selectivity through the cation-exchange and anion-exchange membranes [61]. Finally, the reduction and increase of the conductivity values in the diluted and concentrated fraction, respectively, represent in situ proof of the effectiveness of the ED treatment for the removal of ions from erythritol synthetic culture broth.

Table 4. Average removal efficiency per ion.

Sample	Solution		
	S [%]	SP [%]	SCB [%]
Cl^-	99.3 ± 0.1	99.0 ± 0.3	99.0 ± 0.3
SO_4^{2-}	98.6 ± 0.3	95.4 ± 0.6	97.3 ± 0.0
$H_2PO_4^-$	86.6 ± 0.8	91.0 ± 0.6	93.9 ± 0.7
Na^+	86.3 ± 1.5	88.4 ± 3.2	91.9 ± 1.0
NH_4^+	92.6 ± 1.5	91.8 ± 0.8	94.5 ± 1.6
K^+	94.6 ± 0.1	94.5 ± 0.6	94.9 ± 0.6
Mg^{2+}	92.9 ± 0.6	93.7± 0.5	91.7 ± 0.7
Total av.	93%	93%	96%

3.3. Desalination of Product in the Diluted Fraction

A final conductivity value of 0.28 mS/cm was reached after 78 min for S and SP solutions and min 84 for SCB solution, representing an increase of 8% in the treatment time compared to S and SP solution. This 8% increase is related to the differences in the composition of the solutions involved. SCB solution included two substances of different nature: the non-ionic surfactant, Tween 80, and the protein hydrolysate, peptone, widely used in biotechnological cultures.

Table 4 shows the removal efficiency of ions in the diluted fraction, the total removal efficiency values were 93%, 93%, and 96% for S, SP, and SCB solutions. In all cases, the removal of individual anions and cations was higher than 86%. Among anions, chloride exhibited the highest and dihydrogen phosphate the lowest removal efficiency. For the cations, the highest removal efficiency was reached for potassium and the lowest for sodium.

The ion removal efficiency over time is presented in Figure 1. Similar removal efficiency was observed within the three solutions, meaning that complex solutions (SCB) presented the same general behaviour as the simplest solution (S). The addition of non-charged compounds to the SP solution did not affect the treatment time and removal of ions kept at the same level as S solutions. Slightly large error bars were observed for some ions in solutions, this is due to the difference in concentration levels and the accuracy of the analytical tools. Besides that, the concentration values exposed in the error bars can be explained by differences during sampling, or the response of the electrodes to the application of current. Notwithstanding, the samples followed a clear trend for ion removal. This consideration is also valid for the concentration of products going to the concentrate fraction (Figure 2).

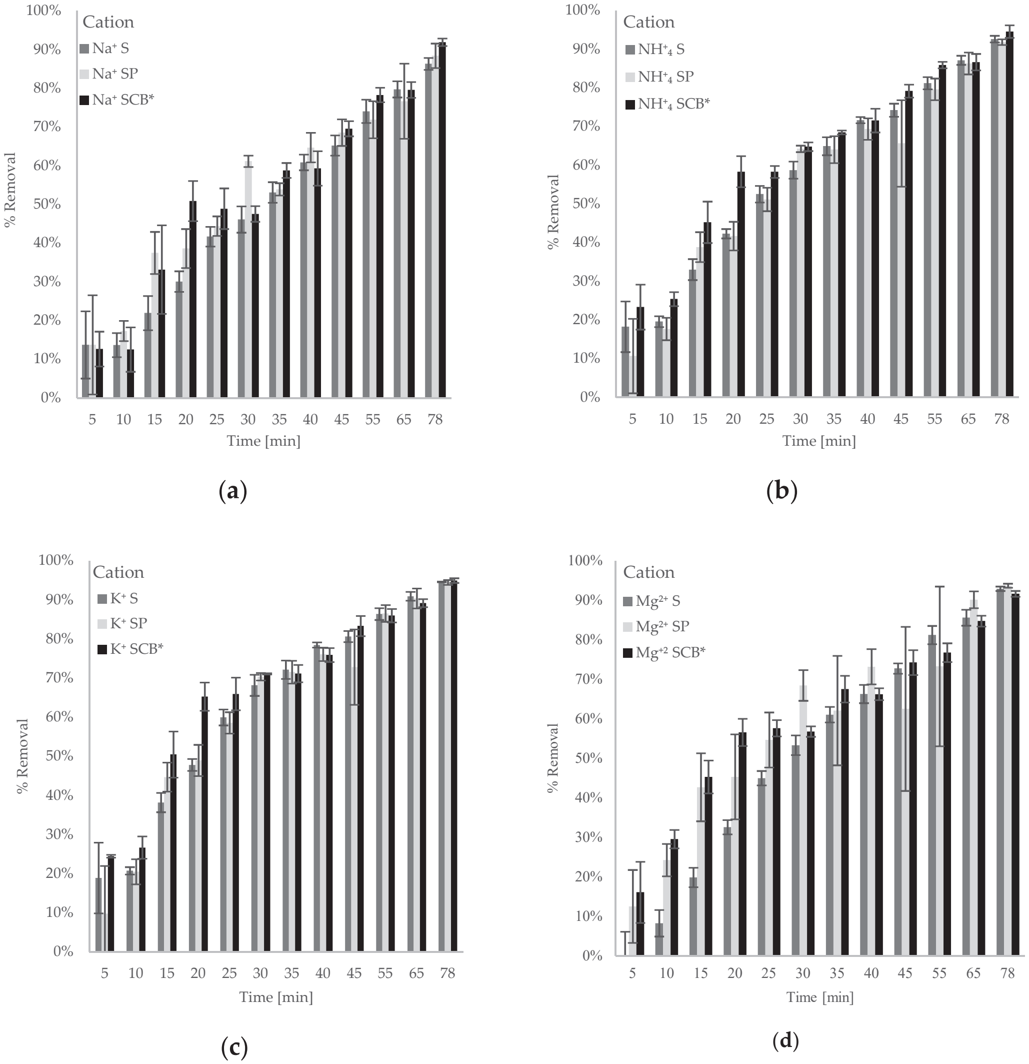

Figure 1. *Cont*.

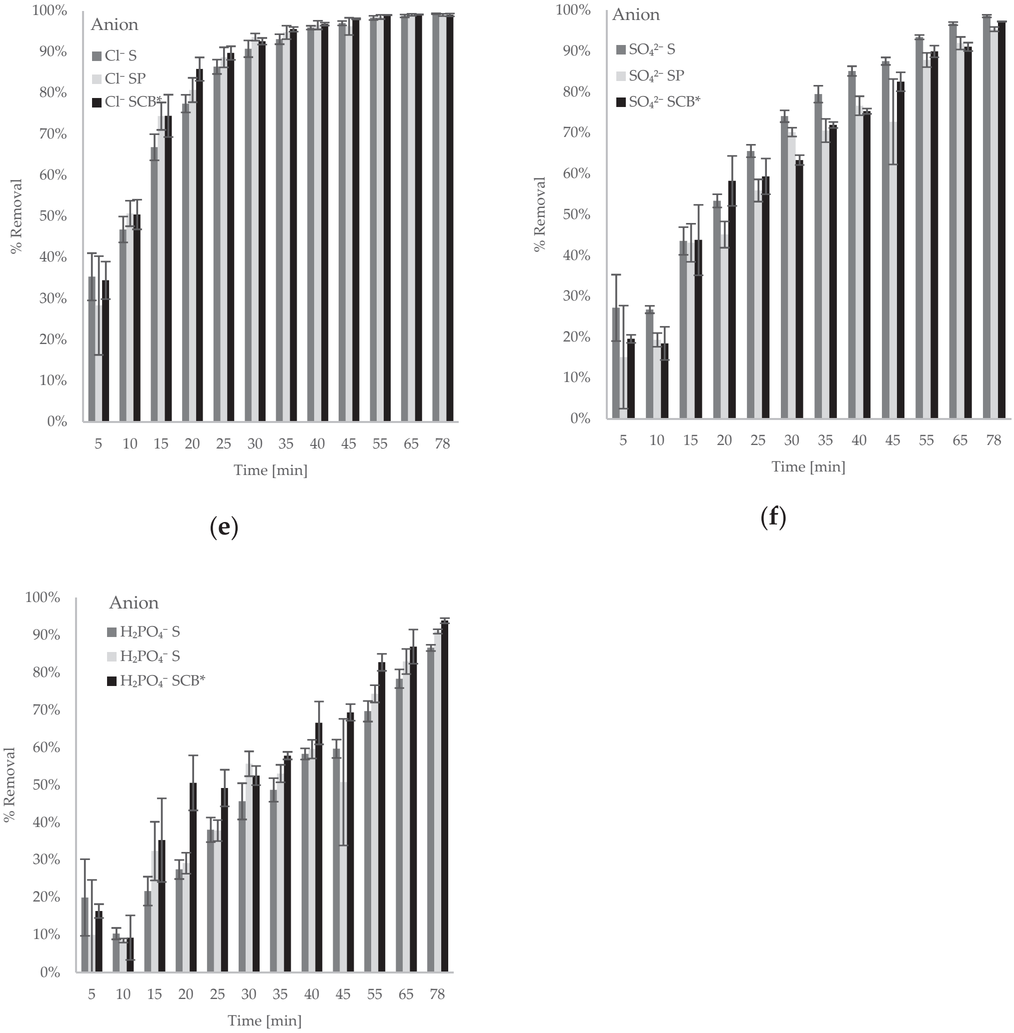

(**e**) (**f**)

(**g**)

Figure 1. Removal of ions in diluted fraction. (**a**) sodium; (**b**) ammonia; (**c**) potassium; (**d**) magnesium; (**e**) chloride; (**f**) sulphate; (**g**) dihydrogen phosphate for salts solution (S), salts + product solution (SP), and synthetic culture broth solution (SCB). * Final time for SCB samples was 84 min.

Rakicka et al. (2016) [62] developed a study for the desalination of an erythritol culture broth using ion exclusion resins (Lewatit S3428 and S2568H). Three different fractions were obtained: a saline waste, recycle, and product fraction with a 95% degree of desalination (based on NaCl removal).

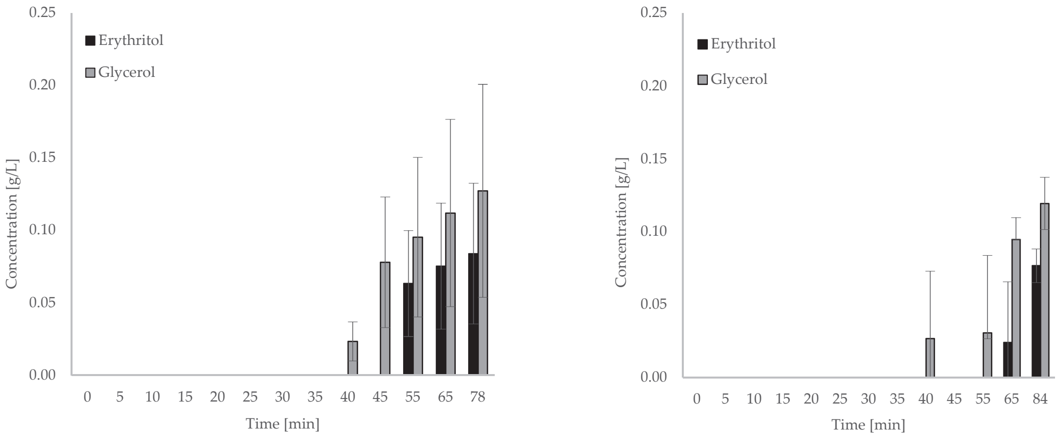

(**a**) (**b**)

Figure 2. Concentration of products in the concentrated fraction (**a**) salts + product solution (SP); (**b**) synthetic culture broth solution (SCB).

The results obtained in this study exhibited a remarkable performance of ions removal (96%), comparable to the reported by Rakicka et al. (2016) [62]. However, an advantage of ED is the absence of a waste stream, compared to large volumes of saline waste, operation recycles and regeneration-wastewater generated for ion-exchange treatments.

3.4. Performance of Ion-Removal Rate in S, SP, and SCB Samples

The ion-removal rate is defined as the average percentage of ions removed divided per time (%removed/min); this rate is strongly influenced by the concentration of ions in the diluted fraction and the voltage applied. Hence, reductions in the ion-removal rate within the time depend on the driving force given by the electrical potential, the mobility of the ions, the molecule charges, and concentration gradient (Table 2). The breakpoint time (BKP) indicates that sudden reductions in the removal rate occur, caused by the downturn in the driving force.

By identifying the BKP it was possible to characterise two periods of ions removal: a fast removal period and a slow removal period. Therefore, the determination of BKP time allows one to understand the processes and determine possible alternatives to improve CE, avoid back diffusion, product losses, and reduce energy consumption. Table 5 presents the breakpoint time (BKP), the reduction in the ion-removal rate after the BKP, the amounts of ions removed (%) until BKP and the average values of the rate of ions removal before and after BKP (% removed/min).

The effect over the mobilities of ions is depicted in the reduction of the ion-removal rate presented at different BKP time as shown in Table 5. In the first place, the ion mobility is decelerated due to the decreasing ionic strength of the diluted fraction among all three solutions (S, SP, and SCB), especially after the BKP time. In the second place, differences in ion mobilities between stages with increasing solution complexity can be observed, as discussed in the following paragraphs.

In S solutions, two BKP times were observed. The trend reflected by the average value of ions-removal rate before and after BKP time allows determining that chlorine was the ion with the highest mobility and overall removal. Notwithstanding the different levels of concentration described in Table 2, phosphate and sodium have a lower average value of ions-removal rate before and after BKP time, demonstrating lower mobilities than the other ions despite the initial concentration. Chloride was the first ion presenting a reduction in the removal rate of 90.3% after 25 min of treatment (BKP time). By that time, approximately

86.4% of the total chloride ions were already removed from the diluted fraction. The second BKP time was observed at 40 min for the other ions in solution with reduction levels in the removal rate between 52.3–81.8% when approximately 58.3–85.1% of the total ions were already removed (SO_4^{2-} > K^+ > NH_4^+ > Mg^{2+} > Na^+ > $H_2PO_4^-$).

Table 5. Breakpoint time for ions removal in S, SP, and SCB samples.

Ion	S			SP			SCB		
	BKP Time *	**Reduction in Removal Rate ****	**Removed at BKP Time *****	**BKP Time ***	**Reduction in Removal Rate ****	**Removed at BKP Time *****	**BKP Time ***	**Reduction in Removal Rate ****	**Removed at BKP Time *****
	[min]	**%**	**%**	**[min]**	**%**	**%**	**[min]**	**%**	**%**
K^+	40	77.8	78.5	55	78.1	86.5	45	84.0	83.3
NH_4^+	40	69.0	71.7	55	62.4	79.6	45	78.0	79.2
Na^+	40	53.5	60.8	40	61.6	64.7	45	64.4	69.5
Mg^{2+}	40	61.8	66.3	65	80.3	90.2	45	71.5	74.3
Cl^-	25	90.3	86.4	25	92.8	88.7	25	92.6	85.8
SO_4^{2-}	40	81.8	85.1	55	79.0	87.9	45	78.5	82.5
$H_2PO_4^-$	40	52.3	58.3	55	40.9	74.4	55	74.3	82.8

Average ions-removal rate before and after BKP [%removal/min]

	K^+		NH_4^+		Na^+		Mg^{2+}		Cl^-		SO_4^{2-}		$H_2PO_4^-$	
	t < BKP	t > BKP	t < BKP	t > BKP	t < BKP	t > BKP	t < BKP	t > BKP	t < BKP	t > BKP	t < BKP	t > BKP	t < BKP	t > BKP
S	2.0	0.4	1.8	0.5	1.5	0.7	1.6	0.6	3.5	0.3	2.1	0.4	1.5	0.7
SP	1.6	0.3	1.5	0.4	1.6	0.6	1.4	0.3	3.5	0.3	1.6	0.3	1.3	0.7
SCB	1.9	0.3	1.5	0.4	1.5	0.5	1.7	0.5	4.3	0.3	1.8	0.4	1.5	0.4

Note: * BKP time: breakpoint time. ** reduction in the average ion-removal rate after the BKP. *** % of ions removed until reaching the BKP. t < BKP: time before BKP. t > BKP: time after BKP.

SP solutions presented slower removal rates compared to S solutions. In addition, four BKP times at 25, 40, 55, and 65 min were observed indicating a late onset of reduction in the removal rate, while slightly higher overall removal values than S samples were reached.

Despite requiring a longer time to reach the final conductivity value, the SCB solution presented similar levels of the total reduction in the removal rate (74.3–92.6%) compared to SP. In this case, three different BKP times 25, 45, and 55 min were obtained at the moment when approximately 69.5–95.8% of ions were removed. The average value of ions-removal before the BKP point showed an increase compared to SP data. SCB results allow us to make conclusions about three possible phenomena presented. The first regards the effects of non-charged compounds on possible polarisation concentration phenomena presented due to concentration gradients generated between the bulk liquid and the interfacial layer, which increases within the concentration of non-charged compounds. The second regards increases in the membrane resistance due to electrostatic and hydrophobic interactions presented between peptone and the membrane surfaces, specifically on cationic membranes [63,64]. The third phenomena relate to possible effects of polysorbate 80 as a non-charged surfactant on the increase of the average ions-removal rate and the mobility of the ions due to minimisations of the polarisation concentration phenomena, resulting in consequence in slightly higher overall removal values (Figure 1) while demanding longer treatment times. These results are in line with the study developed by Gohil et al. (2005) [65], who described the reduction in the polarisation concentration phenomena caused by the addition of surfactants. The authors proved the formation of a layer of surfactants due to their amphiphilic nature (hydrophobic head and hydrophilic tail). The ions can accumulate temporarily over this layer, reducing the concentration gradients in the membrane-solution interfacial layer, and therefore reducing possible polarisation concentration effects [65].

3.5. Current Efficiency (CE)

Current efficiency (CE) is a measure of the current utilisation to transmit ions instead for other uses, such as water splitting. An efficient process can separate the ions while ensuring a continuous movement and transfer of ions between the cathode and anode.

Table 6 presents a comparison of the results obtained in this work and other solutions with similar and even higher complexity levels like lignocellulosic effluent, molasses, and brine solutions from downstream processes and waste treatment. This table includes the energy application approach, CE, and removal values. Studies that have reported high CE values (90–220%) indicating the dependence of the energy approach used and the initial levels of ions in diluted fraction by the order of 2–414 g/L [66–69]. By understanding this dependence, appropriated current densities or current application approaches can be selected, avoiding back diffusion of ions and water splitting, and therefore reach high CE [70]. These conditions can be obtained by applying the appropriate arrangement of the operating parameters such as voltage and feed flow rate with the initial concentration of ions. In this work, CE values between 49% and 54% were obtained for S, SP, and SCB solutions (Table 6), meaning that around 54% of the energy applied is used to transport the ions, rather lower than most of the studies presented in Table 6. Even though it was not rigorously followed, there were no significant changes in the volume observed. However, water splitting and electro-osmosis transport could be responsible for the remaining 46% of the energy provided.

Table 6. Current efficiency values.

Treated Sample	Initial Concentration [g/L]	Energy Application Approach	Removal/ Concentration	Current Efficiency	Ref.
Saline solution	10	Constant voltage 6 V	3.92%	47.54%	[68]
Formic acid solution	276–414	Constant current density	140% *	100–220%	[70]
Saline solution	29.8	Non-uniform current 5.75 A (total)	92.7%	94%	[71]
Brine from pickled prunes	100	Constant current density <10 mA/cm^2	87.6%	90–95%	[66]
Lignocellulosic effluent [1,2]	14.05	Constant current density 39.1 mA/m^2	~96%	~95%	[67]
Sugarcane juice [2]	2.03	Constant current density 17.2 mA/m^2	>90%	~75%	[67]
Molasses [2]	81.2	Constant current density 101.6 mA/m^2	~60%	~104%	[67]
S	3.90	Stepwise voltage 10, 9, 7 and 6 V	93%	54 ± 3%	This work
SP	3.80	Stepwise voltage 10, 9, 7 and 6 V	93%	49 ± 4%	This work
SCB	4.00	Stepwise voltage 10, 9, 7 and 6 V	96%	53 ± 2%	This work

Note: * Concentration factor. [1] hydrolysate from acid hydrolysis. [2] Only cations were considered.

3.6. Recovery of Salts in the Concentrated Fraction

At the end of the treatment, the concentration of ions in the concentrated fraction was 1.5 to 2.5 times higher than the initial concentrations (Table 7). These concentration levels are in agreement with the increases in conductivity presented in Table 3. The results showed different behaviours analogously with the composition of the feed solutions. It can be observed that cation selectivity decreases as the complexity of the solution increases. This fact is analogous to the trend of ions removal presented in the last section and connected to the possible effects of peptone over CEM. With the concentration levels obtained, the number of ions in the concentrated solution is similar to the initial ions used for the culture stage, this represents an attractive alternative to reuse the ions either into erythritol culture media or other processes to reduce waste, close loops, and go deep into circular economy standards.

Table 7. Concentration factor in the concentrated fraction.

Stage	Compound						
	Na^+	**$NH_4{}^+$**	**K^+**	**Mg^{2+}**	**Cl^-**	**$SO_4{}^{2-}$**	**$H_2PO_4{}^-$**
S	2.4 ± 0.1	2.1 ± 0.1	2.3 ± 0.1	2.7 ± 0.0	1.9 ± 0.2	1.9 ± 0.1	1.5 ± 0.1
SP	2.5 ± 0.3	1.8 ± 0.2	2.0 ± 0.3	1.4 ± 0.1	2.6 ± 0.6	2.3 ± 0.3	2.3 ± 0.4
SCB	2.1 ± 0.2	1.8 ± 0.3	2.0 ± 0.5	1.5 ± 0.0	2.4 ± 0.7	2.4 ± 0.6	2.1 ± 0.3

3.7. Losses of Products in the Concentrated Fraction

The concentration of erythritol, glycerol, and glucose in the concentrated fraction (Figure 2) was measured to determine the losses of product passing the membrane. Concentrations of 0.13 g/L and 0.12 g/L of glycerol and 0.08 g/L of erythritol were determined in the concentrated fractions of SP and SCB solutions after 40 min of treatment. The presence of products in the concentrated fraction was determined after the BKP time when the rate of removal of ions decreased significantly for all the ions. These concentrations represented losses of about 2.31% and 1.96% of glycerol and 1.7% and 1.39% of erythritol in SP and SCB solutions.

Product losses in ED can be related to different factors: the charge of molecules in solution susceptible to pH value and pH changes (e.g., amphoterism), affinity by membrane material, and diffusional effects [48,69,72]. Considering the non-amphoteric nature of the substances and the pH stability of the process (Table 2), a movement of products due to protonation and electric charge is unfeasible. Consequently, losses of product going through the membranes can be mainly associated with diffusional phenomena like diffusion-driven for the difference in concentrations or electro-osmosis caused by water cotransport [69,72]. Besides losses of valuable material, this diffusional phenomenon can cause biofouling, reducing the life of the membranes and the performance of separation.

To illustrate the level of losses in ED, Shen et al. (2005) [44] reported overall losses of about 16% of glutamine (initial concentration glutamine 32 g/L) while removing 95% of ammonium sulphate using ED, which are notably higher than the levels obtained in this work. This fact confirms the suitability of the use of ED in the purification of erythritol [64]. A possible alternative for reducing diffusional effects can be assessed through the decrease of treatment times by adopting a different strategy for the application of voltage.

3.8. Energy Consumption

Total energy consumption includes the energy required for the desalination and the energy consumed to pump the water fractions and electrode-rinsing solution through the ED stack. The total average energy consumption for the triplicates of S, SP, and SCB solutions is 3.96 kWh/m^3, 3.87 kWh/m^3, and 4.10 kWh/m^3 of the treated solution, respectively. The energy consumed for the treatment of the SCB solution is increased compared to the S and SP solutions due to the increased desalination time required for the same diluted fraction quality. The energy consumed for desalination makes roughly 40%, for pumping the diluted and concentrated fractions 10%, while the pumping of the electrode-rinsing solution used around 50% of the total energy in all tested solutions (S, SP, and SCB).

The energy consumption for culture broth desalination presented in this work is in a similar range to the values reported by Doornbusch et al. (2020) [73]. They attained 4.88–1.72kWh/m^3 for desalting NaCl solution (approx. conductivity 49.3 mS/cm) to drinking water quality, however without accounting for the energy consumed for the pumping of the electrode-rinsing solution.

4. Discussion

The selectivity for removing ions presented in this study did not follow any pattern based on molar mass, charge, or initial concentration. For the cations, a higher selectivity towards potassium and magnesium than sodium was observed, which is in correspondence to results reported by Luo et al. (2020) [73]. Whereas the anions removal showed significantly higher selectivity for chloride compared to dihydrogen phosphate. Several authors have discussed ion selectivity remarking on some important issues such as the interaction between the ions and the AEM/CEM. These interactions include the groups attached to the membrane skeleton, membrane moisture, mobility in the membranes, rheological conditions [73–77].

The main effect caused by the addition of Tween 80 and peptone to SCB solution was the increase in the treatment time, without reductions in the ions-removal efficiency. (Figure 1). The increase in the treatment time is related to interactions between peptone and the ion exchange membranes. In long-term ED processes, this fact might represent membrane fouling, increasing the energy consumption, and affecting the overall performance of the separation. Ruiz et al. (2007) [62], Mikhaylin and Bazinet (2016) [78], and Nichka et al. (2020) [63], reported fouling on ion-exchange membranes due to the electrostatic and hydrophobic interactions between protein fractions and membranes. These interactions cause material deposition over the membrane surface, producing alterations that increase the membrane electrical resistance, reducing the rate of ion migration through the membranes and the overall performance of the separation. Some alternatives are used to mitigate fouling effects, namely the cleaning-in-place (CIP) routines and the implementation of pulsed electric field routines during treatment [64].

The ED application was capable of removing up to 96% of ions in the complex SCB sample. Chloride showed a separation behaviour significantly better in terms of mobility and removal efficiency in all the feed solutions evaluated, followed by sulphate, potassium, and ammonium. In general terms, the experimental results demonstrated a higher affinity and selectivity for anions than cations, explained by the faster movement of anions than cations at the same conditions. Similar results were reported by Kooistra (1967), who described the polarisation curves for the characterisation of ion-exchange membranes [79].

Considering that ED was demonstrated to be a suitable alternative for removing ions from erythritol culture broth, additional research work is required to improve CE and to increase the knowledge about membrane performance. These efforts could be directed towards the assessment of samples with a higher concentration of ions (concentrated culture broths, increasing the driving force), determining the maintenance requirements for the membrane and increase in the effectivity of the current applied (reduction of the resistance). To address current effectiveness, it is recommendable to explore different current application approaches, including constant current density [66] or new approaches as pulsed electric field routines [64].

5. Conclusions

Electrodialysis proved to be a suitable alternative to remove and recover salts from synthetic culture broth (SCB) solution, obtaining a remarkable desalination of 96%, comparable with values reported in the literature. The ion-removal rates followed the same trends in the three solutions (S, SP, and SCB), suggesting that ion selectivity and mobility are influenced by interactions between the species in solution and the groups attached to the membrane.

The salts removed from the synthetic culture broth and other solutions were concentrated 1.5 to 2.5 times in a second fraction. Producing a solution with similar characteristics to the initial culture media. Besides, less than 2% of products were found in the concentrate fraction after 40 min of treatment, with average energy consumption up to 4.10 kWh/m^3.

Current efficiency values of 49–54% were observed during the experiments. These values are still below the average reported in the literature. To improve the CE performance and address product losses, it is necessary to implement strategies to reduce the resistance and improve energy utilisation. The strategies include the concentration of the fed solution, reduction in the total treatment time, and the assessment of different current applications (e.g., constant current treatment or pulsed electric treatment).

ED for culture broth desalination represents an attractive option to be implemented in biotechnological downstreaming as an alternative to remove ions, returning them either into culture media or other processes, reducing waste generation, and closing loops moving towards circular economy processes.

Author Contributions: Conceptualisation, L.D.-S., K.K., N.K., A.F. and A.R.M.-A.; methodology, A.R.M.-A. and K.K.; formal analysis, L.D.-S. and K.K.; investigation, L.D.-S. and K.K.; resources, J.K., N.K. and R.L.M.; writing—original draft preparation, L.D.-S. and K.K.; writing—review and editing, N.K., A.R.M.-A., R.L.M., J.K. and A.F.; supervision, J.K., A.R.M.-A. and A.F.; funding acquisition, A.R.M.-A., R.L.M. and J.K. All authors have read and agreed to the published version of the manuscript.

Funding: The financial support provided by the Christian Doppler Research Association, the Austrian Federal Ministry for Digital and Economic Affairs, the National Foundation for Research, Technology and Development, and Conzil Estate GmbH is gratefully acknowledged.

Institutional Review Board Statement: Not applicable.

Informed Consent Statement: Not applicable.

Acknowledgments: The authors want to acknowledge the TU Wien and the Institutional Open Access Program (IOAP) for financial support (Open Access Funding by TU Wien). To the Doctoral College "Bioactive", under which this research was performed. The authors want to acknowledge the Bioactive Journal Club members from TU Wien for the insights and review of the manuscript.

Conflicts of Interest: The authors declare no conflict of interest. The funders had no role in the design of the study; in the collection, analyses, or interpretation of data; in the writing of the manuscript, or in the decision to publish the results.

References

1. Martău, G.A.; Coman, V.; Vodnar, D.C. Recent advances in the biotechnological production of erythritol and mannitol. *Crit. Rev. Biotechnol.* **2020**, *40*, 608–622. [CrossRef]
2. Boesten, D.M.P.H.J.; den Hartog, G.J.M.; de Cock, P.; Bosscher, D.; Bonnema, A.; Bast, A. Health effects of erythritol. *Nutrafoods* **2015**, *14*, 3–9. [CrossRef]
3. Kasumi, T. Fermentative production of polyols and utilization for food and other products in Japan. *Japan Agric. Res. Q.* **1995**, *29*, 49–55.
4. BeMiller, J.N. Carbohydrate and Noncarbohydrate Sweeteners. In *Carbohydrate Chemistry for Food Scientists*; Ball, M., Ed.; Elsevier: Amsterdam, The Netherlands, 2018; pp. 371–399. ISBN 9780128120699.
5. Hao, H.X.; Hou, B.H.; Wang, J.K.; Zhang, M.J. Solubility of erythritol in different solvents. *J. Chem. Eng. Data* **2005**, *50*, 1454–1456. [CrossRef]
6. Ahuja, K.; Rawat, A. *Erythritol Market Size by Form (Powder, Granular), by Application (Beverage, Bakery, Confectionery & Dairy Products, Personal Care, Pharmaceutical), Regional Outlook, Application Potential, Price Trends, Competitive Market Share & Forecast, 2020–2026*; Global Market Insights: Selbyville, DE, USA, 2020.
7. Guo, J.; Li, J.; Chen, Y.; Guo, X.; Xiao, D. Improving Erythritol Production of Aureobasidium pullulans from Xylose by Mutagenesis and Medium Optimization. *Appl. Biochem. Biotechnol.* **2016**, *180*, 717–727. [CrossRef]
8. Kang, P.; Li, L.; Yan, L.; Ju, X.; Hu, C.; Yao, X. Enhancement of erythritol production in Trichosporonoides oedocephalis by regulating cellular morphology with betaine. *Chem. Pap.* **2019**, *73*, 2065–2072. [CrossRef]
9. Ghezelbash, G.R.; Nahvi, I.; Malekpour, A. Erythritol production with minimum By-product using Candida magnoliae mutant. *Appl. Biochem. Microbiol.* **2014**, *50*, 292–296. [CrossRef]
10. Kobayashi, Y.; Iwata, H.; Mizushima, D.; Ogihara, J.; Kasumi, T. Erythritol production by Moniliella megachiliensis using nonrefined glycerol waste as carbon source. *Lett. Appl. Microbiol.* **2015**, *60*, 475–480. [CrossRef] [PubMed]
11. Regnat, K.; Mach, R.L.; Mach-Aigner, A.R. Erythritol as sweetener—wherefrom and whereto? *Appl. Microbiol. Biotechnol.* **2018**, *102*, 587–595. [CrossRef]
12. Zhu, D.; Luo, F.; Zou, R.; Liu, J.; Yan, Y. Integrated physiological and chloroplast proteome analysis of wheat seedling leaves under salt and osmotic stresses. *J. Proteom.* **2021**, *234*, 104097. [CrossRef]
13. Yang, C.; Ji, X.; Pan, W.; Liu, Y.; Zhou, L.; Chen, Q.; Tang, X. Paliperidone ascending controlled-release pellets with osmotic core and driven by delayed osmotic pressure. *J. Drug Deliv. Sci. Technol.* **2018**, *48*, 193–199. [CrossRef]
14. Tian, X.; Wang, Y.; Chu, J.; Mohsin, A.; Zhuang, Y. Exploring cellular fatty acid composition and intracellular metabolites of osmotic-tolerant mutant Lactobacillus paracasei NCBIO-M2 for highly efficient lactic acid production with high initial glucose concentration. *J. Biotechnol.* **2018**, *286*, 27–35. [CrossRef] [PubMed]

15. Kim, S.I.; Choi, H.K.; Kim, J.H.; Lee, H.S.; Hong, S.S. Effect of osmotic pressure on paclitaxel production in suspension cell cultures of Taxus chinensis. *Enzyme Microb. Technol.* **2001**, *28*, 202–209. [CrossRef]
16. Gutierrez, C.; Abee, T.; Booth, I.R. Physiology of the osmotic stress response in microorganisms. *Int. J. Food Microbiol.* **1995**, *28*, 233–244. [CrossRef]
17. Kim, S.; Lee, K.; Kim, J.; Oh, D. Erythritol production by controlling osmotic pressure in Trigonopsis variabilis. *Biotechnol. Lett.* **1997**, *19*, 727–729. [CrossRef]
18. Li, L.; Gu, L.; Ju, X.; Hu, C.; Fu, J.; Cheng, H.; Kang, P. Osmotic pressure regulation using KCl for enhanced erythritol production using trichosporonoides oedocephalis ATCC 16958. *Food Sci. Technol. Res.* **2017**, *23*, 793–800. [CrossRef]
19. Liu, X.; Yu, X.; Xia, J.; Lv, J.; Xu, J.; Dai, B.; Xu, X.; Xu, J. Erythritol production by Yarrowia lipolytica from okara pretreated with the in-house enzyme pools of fungi. *Bioresour. Technol.* **2017**, *244*, 1089–1095. [CrossRef] [PubMed]
20. Frigaard, N. Sugar and Sugar Alcohol Production. In *Genetically Engineered Foods*; Grumezescu, A., Butu, A., Eds.; Elsevier: Helsingor, Denmark, 2018; pp. 31–47. ISBN 9780128115190.
21. Hernández-Pérez, A.F.; Machado, F.; De Souza Queiroz, S.; Vaz De Arruda, P.; Chandel, A.K.; Das Graças, M.D.A. Biotechnological production of sweeteners. In *Biotechnological Production of Bioactive Compounds*; Elsevier: Amsterdam, The Netherlands, 2019; pp. 261–292. ISBN 9780444643230.
22. Chan, E.C.S. Microbial nutrition and basic metabolism. In *Handbook of Water and Wastewater Microbiology*; Mara, D., Horan, N., Eds.; Elsevier: London, UK, 2003; pp. 3–33. ISBN 9780080478197.
23. Devanthi, P.V.P.; Gkatzionis, K. Soy sauce fermentation: Microorganisms, aroma formation, and process modification. *Food Res. Int.* **2019**, *120*, 364–374. [CrossRef]
24. Reihani, S.F.S.; Khosravi-Darani, K. Influencing factors on single-cell protein production by submerged fermentation: A review. *Electron. J. Biotechnol.* **2019**, *37*, 34–40. [CrossRef]
25. Ren, H.Y.; Kong, F.; Ma, J.; Zhao, L.; Xie, G.J.; Xing, D.; Guo, W.Q.; Liu, B.F.; Ren, N.Q. Continuous energy recovery and nutrients removal from molasses wastewater by synergistic system of dark fermentation and algal culture under various fermentation types. *Bioresour. Technol.* **2018**, *252*, 110–117. [CrossRef] [PubMed]
26. He, L.; Lv, H.; Xing, Y.; Wang, C.; You, X.; Chen, X.; Zhang, Q. The nutrients in Moringa oleifera leaf contribute to the improvement of stylo and alfalfa silage: Fermentation, nutrition and bacterial community. *Bioresour. Technol.* **2020**, *301*, 122733. [CrossRef]
27. Zhang, Y.; Meng, L.; Ai, M.; Qiao, Y.; Liu, G.; Fan, X.; Lv, X.; Feng, Z. Nutrient requirements of Lactobacillus casei Shirota and their application in fermented milk. *LWT* **2020**, *118*, 108735. [CrossRef]
28. Koh, E.S.; Lee, T.H.; Lee, D.Y.; Kim, H.J.; Ryu, Y.W.; Seo, J.H. Scale-up of erythritol production by an osmophilic mutant of Candida magnoliae. *Biotechnol. Lett.* **2003**, *25*, 2103–2105. [CrossRef] [PubMed]
29. Jeya, M.; Lee, K.M.; Tiwari, M.K.; Kim, J.S.; Gunasekaran, P.; Kim, S.Y.; Kim, I.W.; Lee, J.K. Isolation of a novel high erythritol-producing Pseudozyma tsukubaensis and scale-up of erythritol fermentation to industrial level. *Appl. Microbiol. Biotechnol.* **2009**, *83*, 225–231. [CrossRef] [PubMed]
30. Saran, S.; Mukherjee, S.; Dalal, J.; Saxena, R.K. High production of erythritol from Candida sorbosivorans SSE-24 and its inhibitory effect on biofilm formation of Streptococcus mutans. *Bioresour. Technol.* **2015**, *198*, 31–38. [CrossRef] [PubMed]
31. Mirończuk, A.M.; Rakicka, M.; Biegalska, A.; Rymowicz, W.; Dobrowolski, A. A two-stage fermentation process of erythritol production by yeast Y. lipolytica from molasses and glycerol. *Bioresour. Technol.* **2015**, *198*, 445–455. [CrossRef] [PubMed]
32. Rakicka, M.; Rywińska, A.; Lazar, Z.; Rymowicz, W. Two-stage continuous culture—Technology boosting erythritol production. *J. Clean. Prod.* **2017**, *168*, 420–427. [CrossRef]
33. Mirończuk, A.M.; Furgała, J.; Rakicka, M.; Rymowicz, W. Enhanced production of erythritol by Yarrowia lipolytica on glycerol in repeated batch cultures. *J. Ind. Microbiol. Biotechnol.* **2014**, *41*, 57–64. [CrossRef] [PubMed]
34. Daza-Serna, L.; Serna-Loaiza, S.; Masi, A.; Mach, R.L.; Mach-Aigner, A.R.; Friedl, A. From the culture broth to the erythritol crystals: An opportunity for circular economy. *Appl. Microbiol. Biotechnol.* **2021**, *105*, 4467–4486. [CrossRef] [PubMed]
35. Ward, A.J.; Arola, K.; Thompson Brewster, E.; Mehta, C.M.; Batstone, D.J. Nutrient recovery from wastewater through pilot scale electrodialysis. *Water Res.* **2018**, *135*, 57–65. [CrossRef]
36. European Commission. *Recovering Resources from Industrial Wastewater to Minimise Environmental Impact*; Zero Brine Project; Cordis EU Research Results; European Commission: Brussel, Belgium, 2020.
37. European Commission. *Wastewater Treatment Progresses towards a Circular Economy*; Incover Project; European Commission: Brussel, Belgium, 2019.
38. European Commission. *Unlocking New Value from Urban bioWASTE*; Value Waste Project; European Commission: Brussel, Belgium, 2018.
39. VCM. Nitroman Project. Interreg EU Project. 2019. Available online: https://www.vcm-mestverwerking.be/nl/kenniscentrum/20262/nitroman (accessed on 16 May 2021).
40. Ding, Y.; Sartaj, M. Optimization of ammonia removal by ion-exchange resin using response surface methodology. *Int. J. Environ. Sci. Technol.* **2016**, *13*, 985–994. [CrossRef]
41. Richardson, J.; Harker, J.; Backhurst, J. Ion Exchange. In *Coulson and Richarson's Chemical Engineering by Coulson & Richardson*; Butterworth Heinemann: Oxford, UK, 2002; pp. 1053–1075.
42. Xie, M.; Shon, H.K.; Gray, S.R.; Elimelech, M. Membrane-based processes for wastewater nutrient recovery: Technology, challenges, and future direction. *Water Res.* **2016**, *89*, 210–221. [CrossRef] [PubMed]

43. Prochaska, K.; Staszak, K.; Woźniak-Budych, M.J.; Regel-Rosocka, M.; Adamczak, M.; Wiśniewski, M.; Staniewski, J. Nanofiltration, bipolar electrodialysis and reactive extraction hybrid system for separation of fumaric acid from fermentation broth. *Bioresour. Technol.* **2014**, *167*, 219–225. [CrossRef] [PubMed]
44. Shen, J.; Duan, J.; Liu, Y.; Yu, L.; Xing, X. Demineralization of glutamine fermentation broth by electrodialysis. *Desalination* **2005**, *172*, 129–135. [CrossRef]
45. Phanthumchinda, N.; Thitiprasert, S.; Tanasupawat, S.; Assabumrungrat, S.; Thongchul, N. Process and cost modeling of lactic acid recovery from fermentation broths by membrane-based process. *Process Biochem.* **2018**, *68*, 205–213. [CrossRef]
46. Cheryan, M.; Parekh, S.R. Separation of glycerol and organic acids in model ethanol stillage by electrodialysis and precipitation. *Process Biochem.* **1995**, *30*, 17–23. [CrossRef]
47. Wu, R.C.; Xu, Y.Z.; Song, Y.Q.; Luo, J.A.; Liu, D. A novel strategy for salts recovery from 1,3-propanediol fermentation broth by bipolar membrane electrodialysis. *Sep. Purif. Technol.* **2011**, *83*, 9–14. [CrossRef]
48. Sun, Z.; Gao, X.; Zhang, Y.; Gao, C. Separation and purification of L-phenylalanine from the fermentation broth by electrodialysis. *Desalin. Water Treat.* **2016**, *57*, 22304–22310. [CrossRef]
49. Hboová, V.; Melzoch, K.; Rychtera, M.; Sekavová, B. Electrodialysis as a useful technique for lactic acid separation from a model solution and a fermentation broth. *Desalination* **2004**, *162*, 361–372. [CrossRef]
50. Vadthya, P.; Kumari, A.; Sumana, C.; Sridhar, S. Electrodialysis aided desalination of crude glycerol in the production of biodiesel from oil feed stock. *Desalination* **2015**, *362*, 133–140. [CrossRef]
51. Shen, J.Y.; Duan, J.R.; Yu, L.X.; Xing, X.H.; Xu, P. Desalination of glutamine fermentation broth by electrodialysis. *Process Biochem.* **2006**, *41*, 716–720. [CrossRef]
52. Wu, R.C.; Ren, H.J.; Xu, Y.Z.; Liu, D. The final recover of salt from 1,3-propanadiol fermentation broth. *Sep. Purif. Technol.* **2010**, *73*, 122–125. [CrossRef]
53. Kresnowati, M.T.A.P.; Regina, D.; Bella, C.; Wardani, A.K.; Wenten, I.G. Combined ultrafiltration and electrodeionization techniques for microbial xylitol purification. *Food Bioprod. Process.* **2019**, *114*, 245–252. [CrossRef]
54. Scarazzato, T.; Panossian, Z.; Tenório, J.A.S.; Pérez-Herranz, V.; Espinosa, D.C.R. A review of cleaner production in electroplating industries using electrodialysis. *J. Clean. Prod.* **2017**, *168*, 1590–1602. [CrossRef]
55. *ISO 3696:1987*; ISO Water for Analytical Laboratory Use; Specification and Test Methods; International Organization for Standardization: Geneva, Switzerland, 1991.
56. National Center for Biotechnology Information. *PubChem Compound Summary for CID 222285, Erythritol*; National Center for Biotechnology Information: Bethesda, MD, USA, 2021.
57. National Center for Biotechnology Information. *PubChem Compound Summary for CID 753, Glycerol*; National Center for Biotechnology Information: Bethesda, MD, USA, 2021.
58. Wang, T.; Meng, Y.; Qin, Y.; Feng, W.; Wang, C. Removal of furfural and HMF from monosaccharides by nanofiltration and reverse osmosis membranes. *J. Energy Inst.* **2018**, *91*, 473–480. [CrossRef]
59. Cowan, D.A.; Brown, J.H. Effect of Turbulence on Limiting Current in Electrodialysis Cells. *Ind. Eng. Chem.* **1959**, *51*, 1445–1448. [CrossRef]
60. Lindemann, M.; Widhalm, B.; Kuncinger, T.; Srebotnik, E. An integrated process for combined microbial VOC reduction and effluent valorization in the wood processing industry. *Bioresour. Technol. Rep.* **2020**, *11*, 100471. [CrossRef]
61. Chaabouni, A.; Guesmi, F.; Louati, I.; Hannachi, C.; Hamrouni, B. Temperature effect on ion exchange equilibrium between CMX membrane and electrolyte solutions. *Water Reuse Desalin.* **2015**, *4*, 535–541. [CrossRef]
62. Rakicka, M.; Rukowicz, B.; Rywińska, A.; Lazar, Z.; Rymowicz, W. Technology of efficient continuous erythritol production from glycerol. *J. Clean. Prod.* **2016**, *139*, 905–913. [CrossRef]
63. Nichka, V.S.; Geoffroy, T.R.; Nikonenko, V.; Bazinet, L. Impacts of flow rate and pulsed electric field current mode on protein fouling formation during bipolar membrane electroacidification of skim milk. *Membranes* **2020**, *10*, 200. [CrossRef]
64. Ruiz, B.; Sistat, P.; Huguet, P.; Pourcelly, G.; Araya-Farias, M.; Bazinet, L. Application of relaxation periods during electrodialysis of a casein solution: Impact on anion-exchange membrane fouling. *J. Memb. Sci.* **2007**, *287*, 41–50. [CrossRef]
65. Gohil, G.S.; Nagarale, R.K.; Shahi, V.K.; Rangarajan, R. Micellar-enhanced electrodialysis: Influence of surfactants on the transport properties of ion-exchange membranes. *Sep. Purif. Technol.* **2005**, *47*, 1–9. [CrossRef]
66. Der Pan, W.; Chiang, B.; Chiang, P. Desalination of the Spent Brine from Pickled Prunes Processing by Electrodialysis. *J. Food Sci.* **1988**, *53*, 134–137. [CrossRef]
67. Luiz, A.; McClure, D.D.; Lim, K.; Leslie, G.; Coster, H.G.L.; Barton, G.W.; Kavanagh, J.M. Potential upgrading of bio-refinery streams by electrodialysis. *Desalination* **2017**, *415*, 20–28. [CrossRef]
68. Sadrzadeh, M.; Mohammadi, T. Treatment of sea water using electrodialysis: Current efficiency evaluation. *Desalination* **2009**, *249*, 279–285. [CrossRef]
69. Sun, B.; Zhang, M.; Huang, S.; Wang, J.; Zhang, X. Limiting concentration during batch electrodialysis process for concentrating high salinity solutions: A theoretical and experimental study. *Desalination* **2021**, *498*, 114793. [CrossRef]
70. Luo, G.S.; Pan, S.; Liu, J.G. Use of the electrodialysis process to concentrate a formic acid solution. *Desalination* **2002**, *150*, 227–234. [CrossRef]
71. Doornbusch, G.; Swart, H.; Tedesco, M.; Post, J.; Borneman, Z.; Nijmeijer, K. Current utilization in electrodialysis: Electrode segmentation as alternative for multistaging. *Desalination* **2020**, *480*, 114243. [CrossRef]

72. Han, L.; Galier, S.; Roux-de Balmann, H. Ion hydration number and electro-osmosis during electrodialysis of mixed salt solution. *Desalination* **2015**, *373*, 38–46. [CrossRef]
73. Luo, T.; Roghmans, F.; Wessling, M. Ion mobility and partition determine the counter-ion selectivity of ion exchange membranes. *J. Memb. Sci.* **2020**, *597*, 117645. [CrossRef]
74. Luo, T.; Abdu, S.; Wessling, M. Selectivity of ion exchange membranes: A review. *J. Memb. Sci.* **2018**, *555*, 429–454. [CrossRef]
75. Sata, T.; Sata, T.; Yang, W. Studies on cation-exchange membranes having permselectivity between cations in electrodialysis. *J. Memb. Sci.* **2002**, *206*, 31–60. [CrossRef]
76. Sata, T. Studies on anion exchange membranes having permselectivity for specific anions in electrodialysis—Effect of hydrophilicity of anion exchange membranes on permselectivity of anions. *J. Memb. Sci.* **2000**, *167*, 1–31. [CrossRef]
77. Stenina, I.; Golubenko, D.; Nikonenko, V.; Yaroslavtsev, A. Selectivity of transport processes in ion-exchange membranes: Relationship with the structure and methods for its improvement. *Int. J. Mol. Sci.* **2020**, *21*, 5517. [CrossRef]
78. Mikhaylin, S.; Bazinet, L. Fouling on ion-exchange membranes: Classification, characterization and strategies of prevention and control. *Adv. Colloid Interface Sci.* **2016**, *229*, 34–56. [CrossRef]
79. Kooistra, W. Characterization of ion exchange membranes by polarization curves. *Desalination* **1967**, *2*, 139–147. [CrossRef]

sustainability

MDPI

Article

Influence of Temperature and Lignin Concentration on Formation of Colloidal Lignin Particles in Solvent-Shifting Precipitation

Johannes Adamcyk *, Sebastian Serna-Loaiza, Stefan Beisl, Martin Miltner and Anton Friedl

Institute of Chemical, Environmental and Bioscience Engineering, TU Wien, 1060 Vienna, Austria;
sebastian.serna@tuwien.ac.at (S.S.-L.); stefan.beisl@tuwien.ac.at (S.B.);
martin.miltner@tuwien.ac.at (M.M.); anton.friedl@tuwien.ac.at (A.F.)
* Correspondence: johannes.adamcyk@tuwien.ac.at

Abstract: Colloidal lignin particles offer a promising route towards material applications of lignin. While many parameters influencing the formation of these particles in solvent-shifting precipitation have been studied, only a small amount of research on the influence of temperature has been conducted so far, despite it being a major influence parameter in the precipitation of colloidal lignin particles. Temperature influences various other relevant properties, such as viscosity, density, and lignin solubility. This makes investigation of both temperature and lignin concentration in combination interesting. The present work investigates the precipitation at different temperatures and initial lignin concentrations, revealing that an increased mixing temperature results in smaller particle sizes, while the yield is slightly lowered. This effect was strongest at the highest lignin concentration, lowering the hydrodynamic diameter of the particles from 205 to 168 nm. Decreasing the lignin concentration resulted in significantly smaller particles (from 205 to 121 nm at 20 °C mixing temperature) but almost no change in particle yield (between 81.2 and 84.6% at 20 °C mixing temperature). This opens up possibilities for the process control and optimization of lignin precipitation.

Keywords: lignin; colloidal particles; biorefinery; organosolv; precipitation; self-assembly; solvent shifting

Citation: Adamcyk, J.; Serna-Loaiza, S.; Beisl, S.; Miltner, M.; Friedl, A. Influence of Temperature and Lignin Concentration on Formation of Colloidal Lignin Particles in Solvent-Shifting Precipitation. *Sustainability* **2022**, *14*, 1219. https://doi.org/10.3390/su14031219

Academic Editors: Oz Sahin and Edoardo Bertone

Received: 6 December 2021
Accepted: 18 January 2022
Published: 21 January 2022

1. Introduction

Lignin is an abundantly available biopolymer, which is currently mostly used for energy production and thus underutilized as a material. Several authors have stressed the importance of lignin valorization into high added-value products for the sustainability of biorefineries [1–3]. Therefore, evaluating the material uses of lignin becomes more relevant, especially considering the multiple properties and functionalities that lignin has (biodegradability, biocompatibility, UV-resistance, and low toxicity) [4]. In recent years, investigations of colloidal lignin particles (CLPs) for material applications have shown some promising results [4–8]. Due to the high specific surface area, lignin nanomaterials have shown improved qualities compared to bulk materials [9], which makes them interesting for applications such as sunscreens [8], food packaging [5], and emulsifiers [7], among others [4].

Organosolv pretreatment is a well-known method for the extraction of lignin suitable for high-value applications, using organic solvents such as aqueous ethanol, organic acids, or acetone [10,11]. There are several methods to produce CLPs from the extracted lignin (ideally directly from the liquor), such as pH shifting, solvent shifting, or polymerization [12]. Among these methods, solvent shifting (lignin precipitation by mixing lignin solution with an antisolvent) has been intensively investigated and has shown promising results [12] but has the downside of high solvent consumption and often low precipitation yields [13]. This leads to a low overall process efficiency, since solvents need to be recovered downstream, and substantial amounts of lignin stay in solution after precipitation. Thus, methods to improve the efficiency of CLP production need to be investigated.

In previous works [13], the influence of the antisolvent, ratio, and flowrate in the mixer were investigated, which indicated that the flow regime in the mixer has a strong impact on particle formation. The flow regime in a tube can be characterized by the Reynolds number, which is influenced by fluid viscosity and density, both temperature dependent properties. Additionally, the degree of local supersaturation is known to influence particle formation [14], which is influenced by the temperature-dependent solubility of the precipitated compound. In summary, the temperature influences several properties that are critical for the formation of colloidal lignin particles. This makes predicting the influence of temperature on particle formation difficult and requires experimental research, which has not been investigated much, despite being a major process parameter [15].

Varying the precipitation temperature also opens up interesting possibilities from a process perspective. On a laboratory scale, lignin precipitations are usually conducted at ambient temperature [13,16–18]. This is not necessarily representative of precipitation in a biorefinery process, since temperatures in the range of 150–210 °C are commonly applied in organosolv pretreatment [19,20]. Hence, cooling the liquor to ambient temperature after pretreatment implicates an energy demand that should be fulfilled only if necessary, which is currently a matter of uncertainty. If higher liquor temperatures still result in colloidal particles, this could be a step towards the optimization of a biorefinery process producing CLPs. Additionally, since lignin solubility increases with the temperature [21], the process efficiency could be further improved if the lignin concentration can be increased at higher temperatures. This would reduce the amount of solvent needed per the number of CLPs produced.

To summarize, the influence of the temperature in the solvent-shifting precipitation of lignin has not been sufficiently investigated so far, despite being a major process parameter with high relevance in scaled-up processes. Since the temperature influences lignin solubility, which in turn impacts process efficiency, it makes sense to investigate temperature and lignin concentration simultaneously. In this work, we therefore varied the temperature of the lignin solution and the mixer, as well as the initial lignin concentration in the precipitation of a commercial organosolv-lignin solution using a T-mixer. The resulting suspensions were characterized by particle diameter and yield to gain knowledge on the impacts on product quality and process efficiency. Selected samples were analyzed regarding their molecular weight distribution.

2. Materials and Methods

2.1. Materials

The lignin used in this work was a commercial organosolv-lignin from an annual plant supplied by ChemicalPoint (Oberhaching, Germany), which had a lignin content of 93.7 wt%, ash content of 1.6 wt%, and carbohydrate content of 0.2 wt%. For the solutions, 99.9 wt% undenatured ethanol (Chem-Lab, Zedelgem, Belgium), and ultrapure water (produced with a Sartorius arium pro system at 18 $M\Omega/cm^2$) were used.

2.2. Preparation of Lignin Solutions

Commercial organosolv-lignin and 60 wt% aqueous ethanol where mixed in a ratio of 15 g dry lignin per 1 L of aqueous ethanol and stirred at 20 °C for 24 h. After that, the liquids and solids were separated by filtration using cellulose nitrate filters (Whatman, Maidstone, Great Britain) with a pore size of 0.1 µm. The particle-free filtrate was used as lignin stock solution in the precipitation experiments. The concentration of this stock solution was 12 g/kg, which was determined by drying a sample of the stock solution in a drying oven at 105 °C until it reached a constant weight.

2.3. Precipitation

For the precipitation experiments, the lignin concentration of the solution was set to three different concentrations by volumetric addition of 60 wt% aqueous ethanol. The concentration levels used were that of the lignin stock solution (12 g/kg), a dilution to 75% (9 g/kg), and a dilution to 50% (6 g/kg) of that concentration. The lignin was precipitated in a T-mixer with ultrapure water as the antisolvent, as described by Beisl et al. [22] and depicted in Figure 1. The volumetric flow in the mixer was set to 112.5 mL/min and the volumetric ratio of extract to antisolvent was kept at 1:5 for all experiments. The temperature of the lignin solution, the antisolvent, and the mixer was controlled with water baths. Antisolvent and lignin solution were overheated to compensate for heat losses during syringe filling and pumping. The temperature was checked at the mixer inlet before the precipitation, in the bath, and in the tempered beaker where the suspension was collected. The temperature was varied over three different values, 20, 40, and 60 °C. Three precipitations were carried out for each experimental condition; the presented results are averages and standard deviations of the three repetitions. Two sets of precipitation experiments were conducted. In the first set, the temperature of lignin solution, antisolvent, and mixer was always set to the same value to facilitate a better understanding of the temperature's influence. In the second set, only the lignin solution's temperature was varied, while the other temperatures were always set to 20 °C, to simulate conditions closer to an industrial process.

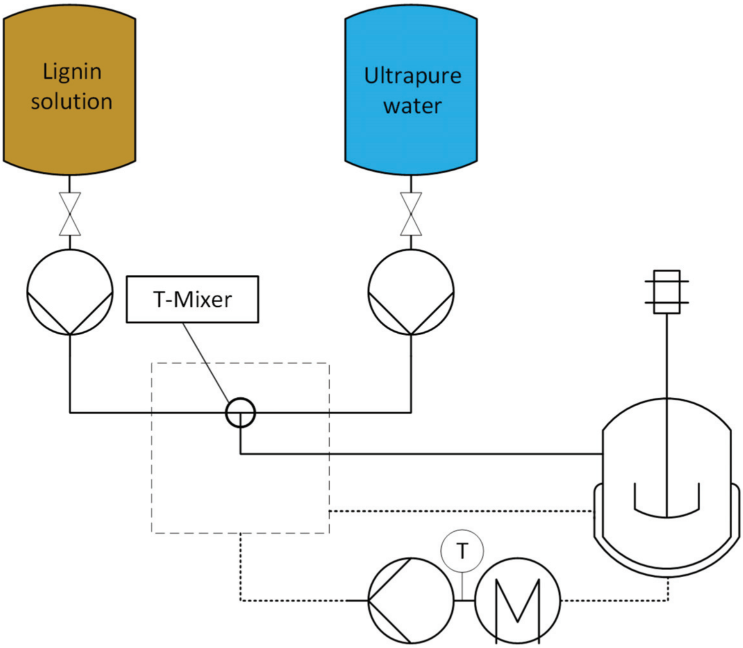

Figure 1. Schematic of the precipitation setup.

2.4. Analytics

2.4.1. Particle Size

The hydrodynamic diameter of the lignin particles was determined with an Anton Paar Litesizer 500 (Graz, Austria). The suspensions were diluted 1:150 with ultrapure water before the measurements. The refractive index of the particles was set to 1.53 and the absorbance to 0.1. For each precipitation, the average of three measurements was calculated.

2.4.2. Yield

The particle yield of the precipitations was determined by filtering (filtrate) the suspensions through a hydrophilic polyethersulfone membrane with a 30 kDa cutoff (supplied by Nadir®) and comparing the dry matter content of the filtrate to that of the suspensions, as shown in Equation (1). The dry matter content was determined by drying the samples in a drying oven at 105 °C until they reached a constant weight.

$$\text{Particle Yield} = (\text{DMS} - \text{DMF})/\text{DMS} \times 100\%, \quad (1)$$

where DMS is the dry matter of the suspension and DMF is the dry matter of the particle-free filtrate. Preliminary tests showed that this filtration method leads to similar but more consistent results compared to the ultracentrifugation used in previous works [13], with lower operational and material expenditure.

2.4.3. Molecular Weight Distribution

The molecular weight distribution was determined through high-performance size exclusion chromatography (HP–SEC), with 10 mM NaOH as eluent with three TSK-Gel columns in series at 40 °C (PW5000, PW4000, PW3000; TOSOH Bioscience, Darmstadt, Germany) using an Agilent 1200 HPLC system (flow rate: 1 mL/min, DAD detection at 280 nm). The pH of liquid samples was adjusted to that of the eluent with NaOH for analysis. Polystyrene sulfonate reference standards (PSS GmbH, Mainz, Germany) with molar mass peak Maxima at 78,400 Da, 33,500 Da, 15,800 Da, 6430 Da, 1670 Da, 891 Da, and 208 Da were used for calibration.

3. Results and Discussion

3.1. First Experimental Plan: Variation of Mixing Temperature

Both the lignin concentration and the temperature were varied to three different levels (6 to 12 g/kg and 20 to 60 °C, respectively). For the first set of experiments, the temperature for the lignin solution and the antisolvent was set to the same temperature for each precipitation. As can be seen in Figure 2, increasing the mixing temperature in the lignin precipitation led to smaller particle sizes, while an increased lignin concentration increased the particle size. This means that the increase in particle size at higher lignin concentrations can be at least partially compensated for by increasing the mixing temperature. In the temperature and concentration ranges used in this work, the influence of the initial lignin concentration was stronger than that of the mixing temperature. Increasing the lignin concentration is advantageous for process efficiency, since less solvent and antisolvent are needed per the number of CLPs produced. However, this also leads to larger particles, which can be partially compensated for by increasing the mixing temperature, as the results indicate. Significantly higher lignin concentrations than those used in this study have been reported in the literature (Goldmann et al. [23] achieved a kraft lignin concentration of 235.89 g/L in 60 wt% aqueous ethanol). However, the temperature cannot be increased much higher than the maximum temperature applied in this work without potentially significantly altering the lignin molecular structure. Thus, the results indicate that the possibility to compensate for higher concentrations by higher mixing temperatures is limited. Additionally, the influence of the temperature is stronger for higher lignin concentrations, while the particle diameter stays similar for all temperatures at the lowest concentration. This indicates that the particle size converges towards a lower limit with increasing precipitation temperatures.

The increase in particle size with the increasing concentration of lignin is a well-documented phenomenon [24,25] and can be explained by a larger number of solubilized molecules available for particle growth after primary nucleation [26]; however, contrasting results have also been reported [27]. So far, little research has been conducted on the influence of temperature on lignin precipitation [15]. According to Elnashaie et al. [14], an elevated temperature tends to lead to larger particles due to it hindering primary nucleation.

However, in the case examined in this work, other effects seem to have had a stronger influence, since the particle size decreased with the mixing temperature.

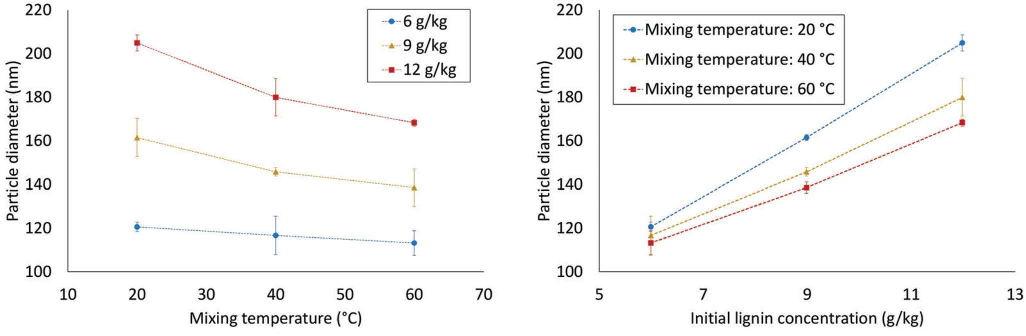

(**a**) (**b**)

Figure 2. Influence of mixing temperature (**a**) and initial lignin concentration (**b**) on particle diameter.

In this work, the particle size was only determined by dynamic light scattering (DLS), which cannot differentiate between single particles and aggregates. However, pictures obtained by scatter electron microscopy (SEM) published in previous works [13,22] showed that the particle diameters as determined by DLS are in the same order of magnitude as those determined by SEM.

A previous work [13] showed that increasing the volumetric flow in the T-mixer up to a certain point leads to decreasing particle sizes. This was explained by improved mixing at higher flowrates, which can be expressed as higher Reynolds (Re) numbers in the mixer. Therefore, a possible explanation for the decreasing particle sizes with increasing mixing temperature could be the increase in the Reynolds number in the mixer from 396 to 1017 due to the decrease in the viscosity with the temperature (from 1.6 to 0.6*10^3 Pas). The correlation of particle size with Re in the mixer and the viscosity of the mixture are shown in Figure 3. The density and dynamic viscosity of the suspension were approximated using literature data from Belda et al. [28]. Due to the proportional increase in the Re with the temperature in the mixer, the correlation of particle size and Re is similar to that of particle size and temperature (Figure 3a). On the other hand, Figure 3b shows that the particle size linearly increased with the viscosity. These correlations suggest that the particle size is primarily determined by the mixing quality, which improves with an increased mixing temperature due to the decrease in viscosity. These results are in agreement with results from other works correlating smaller particle sizes with improved mixing quality [29,30].

Another relevant factor for the particle formation is the lignin supersaturation in the mixture, the driving force for precipitation. The solubility of lignin increases with increasing temperature [21], which should lower the driving force for precipitation and thus lead to higher particle diameters due to the lower precipitation speed [14]. While the lower supersaturation might still be a factor, the results indicate that the improved mixing quality outweighs its influence and leads to smaller particle diameters.

Since the experiments were carried out with ethanol–water mixtures, it is not certain whether the results can be transferred to other solvents commonly used for solvent-shifting precipitation, such as acetone [25] or tetrahydrofuran (THF) [31]. However, the increase in particle size with increasing concentration is well-established for precipitation [24,25]. As stated earlier, information from the literature on the influence of temperature on lignin precipitation is limited. Based on the explanation that the particle size decreases due to improved mixing with decreasing viscosity, it should be possible to also transfer the results to other solvents, since the same principles should apply. This could be investigated in future works to confirm or refute the explanation given in the present work.

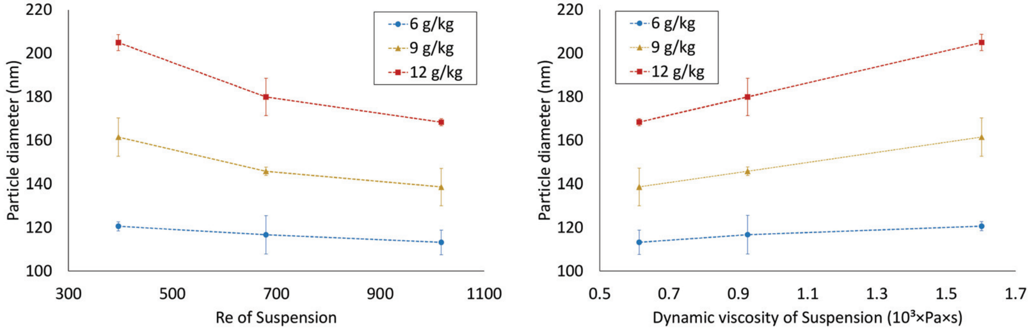

(**a**) (**b**)

Figure 3. Influence of Re (**a**) and dynamic viscosity (**b**) in the mixer on the hydrodynamic diameter of CLPs.

The particle yield of the precipitations ranged from 76.7 to 85.8% (Figure 4), which can be considered high compared to the results of previous works [13]. When comparing the results from different conditions, there was a slight trend to lower yields at higher temperatures, and higher yields at higher initial lignin concentrations. The latter result matches findings by Xiong et al. [24], who precipitated enzymatic hydrolysis lignin from THF at initial lignin concentrations ranging from 0.5 to 2 mg/mL; however, the changes in the yield were small in the present work, especially considering the deviations of the experiments at the same conditions. Since the yield was determined gravimetrically, the influence of random errors was higher at lower dry matter concentrations, which explains the tendentially higher deviations for yield and filtrate dry matter at lower lignin concentrations (e.g., Figure 4).

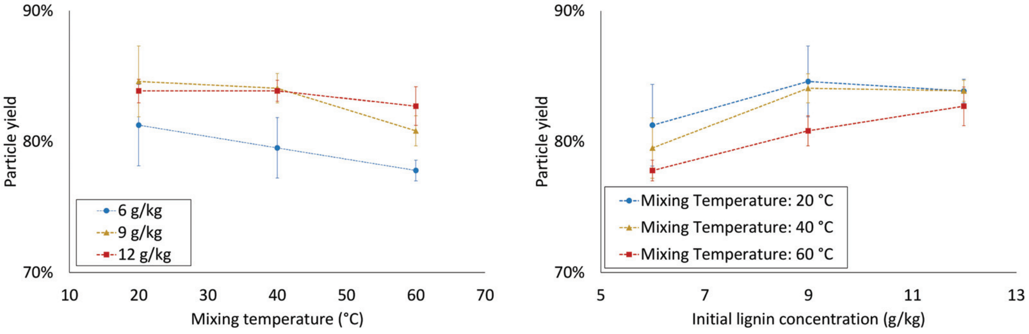

(**a**) (**b**)

Figure 4. Influence of mixing temperature (**a**) and lignin concentration (**b**) on particle yield.

The decreased yield at higher temperatures could be explained by the increasing solubility of lignin, leading more lignin to stay in solution. The yield was determined at ambient temperature, which would suggest that nonprecipitated lignin stays in solution even after cooling down.

Since the precipitation is assumed to be solubility-driven, it is noteworthy that there was only a slight decrease in the yields with decreasing initial lignin concentrations (Figure 4b). If the solubility limit of lignin at a certain ethanol content is assumed to be constant, the concentration of solubilized lignin after the precipitation should be constant. This would result in a direct correlation between initial lignin concentration and particle yield. For the particle yield determination, the lignin particles were removed using membrane filtration (30 kDa cutoff), and the dry matter contents of the particle-free filtrates were calculated. These dry matter contents are plotted in Figure 5, showing that the dry matter content of the filtrates from the two lower lignin concentrations was significantly lower than that of the highest concentration. This indicates that the concentration of solubilized lignin after precipitation depends on the initial lignin concentration, meaning that the amount of solubilized lignin is higher when more lignin is present.

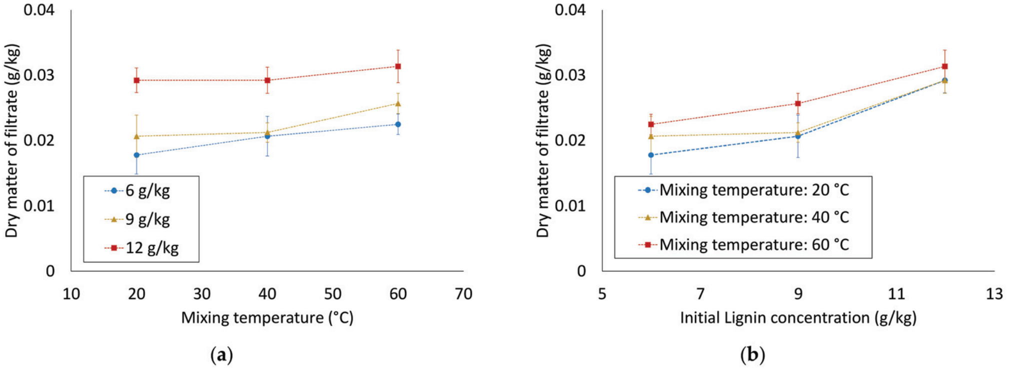

Figure 5. Dry matter content of filtrate for different mixing temperatures (**a**) and lignin concentrations (**b**).

This could be explained by the polydispersity of lignin and the different solubility limits of lignins with different molecular structures and weights, which was also found by Buranov et al. [32]. Previous studies have also shown the fractionation of lignin by molecular weight in solvent-shifting precipitation, meaning that predominately high-molecular-weight lignin precipitates while low-molecular-weight lignin predominately stays in solution [33,34]. Figure 6 shows the molecular weight distributions of lignin in filtrates from experiments at different initial lignin concentrations. The non-normalized distributions (Figure 6a) show a significant increase in lignin concentration over the whole molecular weight spectrum from the lowest initial lignin concentration. Interestingly, the distribution of the filtrates from two higher initial concentrations are very similar, despite a difference in dry matter content; the main difference is an increase in the peak at 400 Da, which was found in earlier works to be influenced by *p*-hydroxycinnamic acids such as ferulic acid and *p*-coumaric acid, both monomeric and connected to lignin fragments [35]. This suggests that the difference in residual solubilized lignin between these samples is mostly influenced by this lignin fraction.

The area-normalized distributions (Figure 6b) show that the filtrate from the lowest initial concentration has the highest ratio of lignin at 400 Da, while the ratio of the highest molecular weight fraction is very low. The distributions of the two higher initial concentrations are very similar, the main difference being a higher ratio of the 400 Da fraction for the highest initial lignin concentration.

The results suggest that the higher-molecular-weight fractions soluble at 10 wt% ethanol (ethanol content after precipitation) are completely dissolved at 6 g/kg initial lignin concentration, but hit a solubility limit at 9 g/kg. The lignin fraction at 400 Da exhibits better solubility. The increase of this fraction from 9 to 12 g/kg suggests that the concentration of this fraction is limited by the concentration in the solution at 9 g/kg, not by solubility. Generally, the results demonstrate the high complexity of lignin solubility. Therefore, the solubility of different lignin fractions will be further investigated in future works.

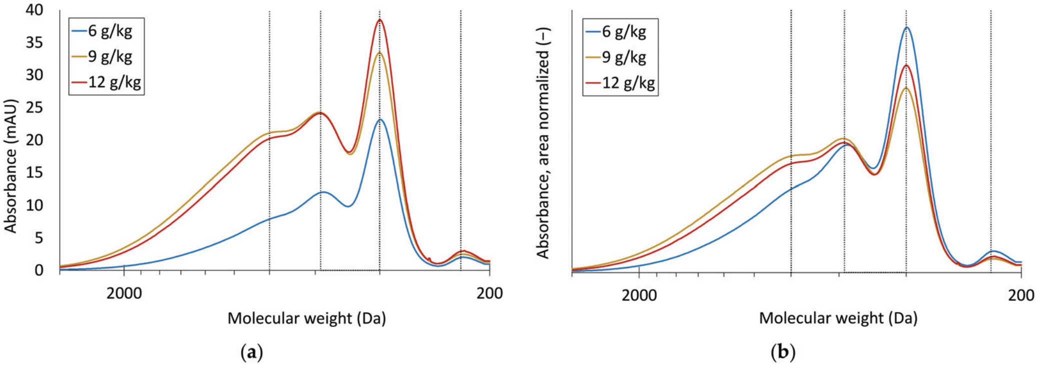

Figure 6. Molecular weight distribution of filtrates from precipitations at 20 °C at different initial lignin concentrations, as in sample (**a**) and area-normalized (**b**).

From a process perspective, the observation that the decrease in yield was less than proportional with the decrease in lignin concentration has interesting implications, since it would allow the tailoring of the particle size by adjusting the lignin concentration of the solution with only a minor impact on the yield. For example, when the lignin concentration of the solution is reduced to 50% at 20 °C mixing temperature, the particle size is reduced from 205 ± 4 to 121 ± 2 nm (reduction by 41%), while the yield does not change significantly. However, the merits of this depend on the requirements and value of the final product, since a higher solvent consumption lowers process efficiency.

In the context of a biorefinery process producing CLPs by precipitation directly from the organosolv extract [13], the results of the first set of experiments lead to the conclusion that cooling the extract to ambient temperature after lignin extraction is not necessary. Higher mixing temperatures still result in colloidal particles and even lower particle diameters compared to ambient mixing temperature, while the yield does not change significantly.

3.2. Second Experimental Plan—Variation of Lignin Solution Temperature

While it may be advantageous to use warm extract from a process perspective, it is disadvantageous to use warm antisolvent, since this would result in increased energy demand for the precipitation process. While warming antisolvent and lignin solution to the same temperatures for the precipitations was necessary to facilitate a better understanding of the influence of the temperature, in an industrial process, different temperatures for the solution and antisolvent are more likely. Thus, a second experimental plan was conducted, in which the temperatures of the antisolvent and the mixer were kept at 20 °C, while the temperature of the lignin solution was varied.

Figure 7 shows that there are only small differences in the particle diameter for different solution temperatures. The ratio of extract to antisolvent was kept at 1:5 for all experiments, so the mixing temperature was influenced more by the temperature of the antisolvent and the mixer than that of the lignin solution. This meant there were only small temperature changes in the temperature of the suspension after mixing in this experimental plan. It is noteworthy that the experiments with the solution warmed to 60 °C consistently resulted in the smallest average particle sizes. As in the first set of experiments, the influence of temperature was most visible at the highest lignin concentration. This supports the findings from the first experimental plan, since a higher solution temperature results in higher temperatures in the mixer. These results suggest that the temperature and properties of the mixture are relevant for the precipitation, rather than the temperature and properties of the lignin solution or antisolvent. This could mean that the size of the final particles is decided after the solution and antisolvent are mixed.

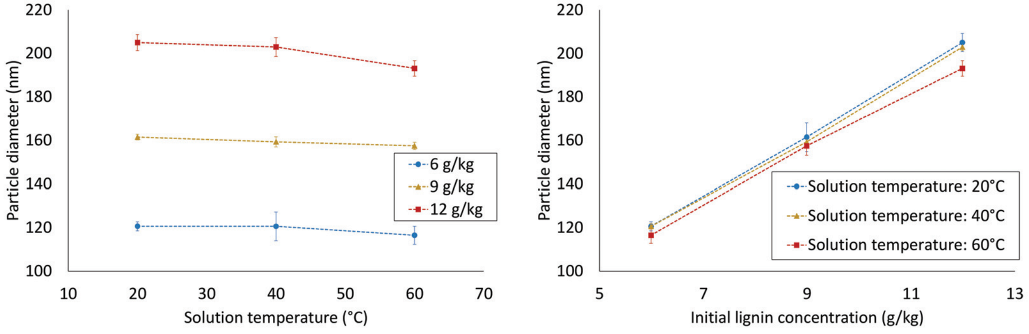

(**a**) (**b**)

Figure 7. Influence of solution temperature (**a**) and lignin concentration (**b**) on particle diameter with constant antisolvent temperature.

Similar to the particle sizes, the particle yield of the second experimental plan showed no strong dependency on the lignin solution temperature (Figure 8a). As in the first experimental plan, the correlation between the initial lignin concentration and the particle yield was less than proportional (Figure 8b). The results from the second experimental plan indicate that elevated temperatures of the lignin solution alone have a negligible influence on both the particle size and yield. In a biorefinery process, this would mean that it is not necessary to cool the liquor to ambient temperature after biomass pretreatment.

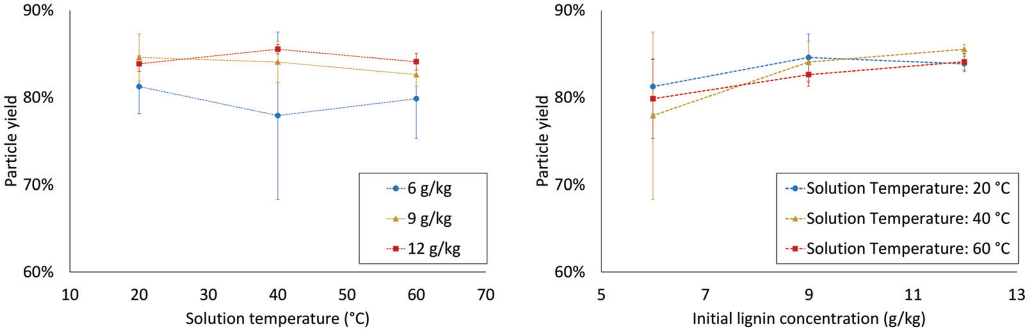

(**a**) (**b**)

Figure 8. Influence of lignin solution temperature (**a**) and initial lignin concentration (**b**) on particle yield.

4. Conclusions

In the present work, the influence of the temperature and lignin concentration on the precipitation of CLPs was investigated. The particle size increased with an increasing concentration of lignin in the solution and decreased with increasing mixing temperatures. The particle yield was slightly lowered by increasing the mixing temperature, while lower initial lignin concentrations resulted in lower yields. The correlation between the particle yield and lignin concentration was underproportional, which was explained by the polydispersity of lignin and the different solubilities of different lignin fractions. In a second set of experiments, lignin solutions warmed to different temperatures were precipitated with antisolvent at ambient temperature, which had only a minor influence on the particle size and no significant influence on the yield. The lignin concentration showed the same influence on the particle size as in the first set of experiments.

From a process perspective, the results suggest that the precipitation of lignin particles directly from warm extract is not disadvantageous with respect to particle size and yield, but may in fact be advantageous for the formation of CLPs with smaller diameters. This finding could help to increase the efficiency of a biorefinery producing CLPs by removing the necessity to cool the liquor to ambient temperature after lignin extraction.

The changes in the molecular weights of lignin still dissolved after precipitation demonstrate the complexity of lignin solubility even in a relatively simple experimental plan and stress the necessity of further investigating this topic. The solubility and interaction of different lignin fractions will be investigated in future works, as well as downstreaming and valorization methods for the nonprecipitated lignin.

Author Contributions: Conceptualization, J.A.; methodology, J.A.; formal analysis, J.A., S.B. and M.M.; investigation, J.A.; writing—original draft preparation, J.A.; writing—review and editing, S.B., S.S.-L., M.M. and A.F. All authors have read and agreed to the published version of the manuscript.

Funding: This research was partially funded by FFG Spin-off Fellowship project (FFG project no. 874260).

Data Availability Statement: Data supporting the results are included within the paper.

Acknowledgments: Open Access Funding by TU Wien. This paper builds on a paper on the same topic that was presented by the first author at the 2021 Sustainable Development of Energy, Water, and Environment Systems (SDEWES) Conference (10–15 October, Dubrovnik).

Conflicts of Interest: The authors declare no conflict of interest. The funders had no role in the design of the study; in the collection, analyses, or interpretation of data; in the writing of the manuscript; or in the decision to publish the results.

References

1. Ragauskas, A.J.; Beckham, G.T.; Biddy, M.J.; Chandra, R.; Chen, F.; Davis, M.F.; Davison, B.H.; Dixon, R.A.; Gilna, P.; Keller, M.; et al. Lignin valorization: Improving lignin processing in the biorefinery. *Science* **2014**, *344*, 1246843. [CrossRef]
2. Liu, Z.-H.; Hao, N.; Shinde, S.; Olson, M.L.; Bhagia, S.; Dunlap, J.R.; Kao, K.C.; Kang, X.; Ragauskas, A.J.; Yuan, J.S. Codesign of Combinatorial Organosolv Pretreatment (COP) and Lignin Nanoparticles (LNPs) in Biorefineries. *ACS Sustain. Chem. Eng.* **2019**, *7*, 2634–2647. [CrossRef]
3. Serna-Loaiza, S.; Zikeli, F.; Adamcyk, J.; Friedl, A. Towards a wheat straw biorefinery: Combination of Organosolv and Liquid Hot Water for the improved production of sugars from hemicellulose and lignin hydrolysis. *Bioresour. Technol. Rep.* **2021**, *14*, 100667. [CrossRef]
4. Beisl, S.; Friedl, A.; Miltner, A. Lignin from Micro- to Nanosize: Applications. *Int. J. Mol. Sci.* **2017**, *18*, 2367. [CrossRef]
5. Domenek, S.; Louaifi, A.; Guinault, A.; Baumberger, S. Potential of Lignins as Antioxidant Additive in Active Biodegradable Packaging Materials. *J. Polym. Environ.* **2013**, *21*, 692–701. [CrossRef]
6. Jiang, C.; He, H.; Jiang, H.; Ma, L.; Jia, D.M. Nano-lignin filled natural rubber composites: Preparation and characterization. *Express Polym. Lett.* **2013**, *7*, 480–493. [CrossRef]
7. Silmore, K.S.; Gupta, C.; Washburn, N.R. Tunable Pickering emulsions with polymer-grafted lignin nanoparticles (PGLNs). *J. Colloid Interface Sci.* **2016**, *466*, 91–100. [CrossRef] [PubMed]
8. Lee, S.C.; Tran, T.M.T.; Choi, J.W.; Won, K. Lignin for white natural sunscreens. *Int. J. Biol. Macromol.* **2019**, *122*, 549–554. [CrossRef]
9. Cai, X.; Riedl, B.; Zhang, S.Y.; Wan, H. The impact of the nature of nanofillers on the performance of wood polymer nanocomposites. *Compos. Part A Appl. Sci. Manuf.* **2008**, *39*, 727–737. [CrossRef]
10. Chen, H.; Zhao, J.; Hu, T.; Zhao, X.; Liu, D. A comparison of several organosolv pretreatments for improving the enzymatic hydrolysis of wheat straw: Substrate digestibility, fermentability and structural features. *Appl. Energy* **2015**, *150*, 224–232. [CrossRef]
11. Tan, X.; Zhang, Q.; Wang, W.; Zhuang, X.; Deng, Y.; Yuan, Z. Comparison study of organosolv pretreatment on hybrid pennisetum for enzymatic saccharification and lignin isolation. *Fuel* **2019**, *249*, 334–340. [CrossRef]
12. Beisl, S.; Miltner, A.; Friedl, A. Lignin from Micro- to Nanosize: Production Methods. *Int. J. Mol. Sci.* **2017**, *18*, 1244. [CrossRef]
13. Beisl, S.; Adamcyk, J.; Friedl, A. Direct Precipitation of Lignin Nanoparticles from Wheat Straw Organosolv Liquors Using a Static Mixer. *Molecules* **2020**, *25*, 1388. [CrossRef]
14. Elnashaie, S.S.; Danafar, F.; Hashemipour, H.R. *Nanotechnology for Chemical Engineers*; Springer: Singapore, 2015; ISBN 9789812874955.
15. Mishra, P.K.; Ekielski, A. The Self-Assembly of Lignin and Its Application in Nanoparticle Synthesis: A Short Review. *Nanomaterials* **2019**, *9*, 243. [CrossRef] [PubMed]

16. Agustin, M.B.; Penttilä, P.A.; Lahtinen, M.; Mikkonen, K.S. Rapid and Direct Preparation of Lignin Nanoparticles from Alkaline Pulping Liquor by Mild Ultrasonication. *ACS Sustainable Chem. Eng.* **2019**, *7*, 19925–19934. [CrossRef]
17. Yearla, S.R.; Padmasree, K. Preparation and characterisation of lignin nanoparticles: Evaluation of their potential as antioxidants and UV protectants. *J. Exp. Nanosci.* **2016**, *11*, 289–302. [CrossRef]
18. Bangalore Ashok, R.P.; Xiao, Y.; Lintinen, K.; Oinas, P.; Kostiainen, M.A.; Österberg, M. Self-assembly of colloidal lignin particles in a continuous flow tubular reactor. *Colloids Surf. A Physicochem. Eng. Asp.* **2020**, *587*, 124228. [CrossRef]
19. Behera, S.; Arora, R.; Nandhagopal, N.; Kumar, S. Importance of chemical pretreatment for bioconversion of lignocellulosic biomass. *Renew. Sustain. Energy Rev.* **2014**, *36*, 91–106. [CrossRef]
20. Zhao, X.; Cheng, K.; Liu, D. Organosolv pretreatment of lignocellulosic biomass for enzymatic hydrolysis. *Appl. Microbiol. Biotechnol.* **2009**, *82*, 815–827. [CrossRef] [PubMed]
21. Evstigneev, E.I. Factors affecting lignin solubility. *Russ. J. Appl. Chem.* **2011**, *84*, 1040–1045. [CrossRef]
22. Beisl, S.; Loidolt, P.; Miltner, A.; Harasek, M.; Friedl, A. Production of Micro- and Nanoscale Lignin from Wheat Straw Using Different Precipitation Setups. *Molecules* **2018**, *23*, 633. [CrossRef] [PubMed]
23. Goldmann, W.M.; Ahola, J.; Mikola, M.; Tanskanen, J. Solubility and fractionation of Indulin AT kraft lignin in ethanol-water media. *Sep. Purif. Technol.* **2019**, *209*, 826–832. [CrossRef]
24. Xiong, K.; Jin, C.; Liu, G.; Wu, G.; Chen, J.; Kong, Z. Preparation and characterization of lignin nanoparticles with controllable size by nanoprecipitation method. *Chem. Ind. For. Prod.* **2015**, *35*, 85–92. [CrossRef]
25. Richter, A.P.; Bharti, B.; Armstrong, H.B.; Brown, J.S.; Plemmons, D.; Paunov, V.N.; Stoyanov, S.D.; Velev, O.D. Synthesis and Characterization of Biodegradable Lignin Nanoparticles with Tunable Surface Properties. *Langmuir* **2016**, *32*, 6468–6477. [CrossRef] [PubMed]
26. Lewis, A.; Seckler, M.M.; Kramer, H.; van Rosmalen, G. *Industrial Crystallization: Fundamentals and Applications*, 1st ed.; Cambridge University Press: Cambridge, UK, 2015; ISBN 9781107280427.
27. Frangville, C.; Rutkevičius, M.; Richter, A.P.; Velev, O.D.; Stoyanov, S.D.; Paunov, V.N. Fabrication of environmentally biodegradable lignin nanoparticles. *ChemPhysChem* **2012**, *13*, 4235–4243. [CrossRef] [PubMed]
28. Belda, R.; Herraez, J.V.; Diez, O. Rheological study and thermodynamic analysis of the binary system (water/ethanol): Influence of concentration. *Phys. Chem. Liq.* **2004**, *42*, 467–479. [CrossRef]
29. Schwarzer, H.-C.; Peukert, W. Experimental Investigation into the Influence of Mixing on Nanoparticle Precipitation. *Chem. Eng. Technol.* **2002**, *25*, 657. [CrossRef]
30. Gradl, J.; Schwarzer, H.-C.; Schwertfirm, F.; Manhart, M.; Peukert, W. Precipitation of nanoparticles in a T-mixer: Coupling the particle population dynamics with hydrodynamics through direct numerical simulation. *Chem. Eng. Processing Process Intensif.* **2006**, *45*, 908–916. [CrossRef]
31. Lievonen, M.; Valle-Delgado, J.J.; Mattinen, M.-L.; Hult, E.-L.; Lintinen, K.; Kostiainen, M.A.; Paananen, A.; Szilvay, G.R.; Setälä, H.; Österberg, M. A simple process for lignin nanoparticle preparation. *Green Chem.* **2016**, *18*, 1416–1422. [CrossRef]
32. Buranov, A.U.; Ross, K.A.; Mazza, G. Isolation and characterization of lignins extracted from flax shives using pressurized aqueous ethanol. *Bioresour. Technol.* **2010**, *101*, 7446–7455. [CrossRef]
33. Sipponen, M.H.; Lange, H.; Ago, M.; Crestini, C. Understanding Lignin Aggregation Processes. A Case Study: Budesonide Entrapment and Stimuli Controlled Release from Lignin Nanoparticles. *ACS Sustain. Chem. Eng.* **2018**, *6*, 9342–9351. [CrossRef] [PubMed]
34. Adamcyk, J.; Beisl, S.; Amini, S.; Jung, T.; Zikeli, F.; Labidi, J.; Friedl, A. Production and Properties of Lignin Nanoparticles from Ethanol Organosolv Liquors-Influence of Origin and Pretreatment Conditions. *Polymers* **2021**, *13*, 384. [CrossRef] [PubMed]
35. Zikeli, F.; Ters, T.; Fackler, K.; Srebotnik, E.; Li, J. Fractionation of wheat straw Dioxane lignin reveals molar mass dependent structural differences. *Ind. Crops Prod.* **2016**, *91*, 186–193. [CrossRef]

sustainability

MDPI

Article

Development of a Bio-Digital Interface Powered by Microbial Fuel Cells

Jiseon You [1,*], Arjuna Mendis [1], John Greenman [1], Julie Freeman [2], Stephen Wolff [2], Rachel Armstrong [3], Rolf Hughes [3] and Ioannis A. Ieropoulos [1,4,*]

[1] Bristol BioEnergy Centre (BBiC), Bristol Robotics Laboratory, T Block, Frenchay Campus, University of the West of England, Bristol BS16 1QY, UK; arjuna.mendis@uwe.ac.uk (A.M.); john.greenman@uwe.ac.uk (J.G.)
[2] Translating Nature, 11 Palm Bay Avenue, Margate CT9 3DH, UK; julie@translatingnature.org (J.F.); stephen.wolff@gmail.com (S.W.)
[3] Department of Architecture, Campus Sint-Lucas, KU Leuven, Hoogstraat 51, B-9000 Ghent/Paleizenstraat 65, B-1030 Brussels, Belgium; rachel.armstrong@kuleuven.be (R.A.); rolf.hughes@kuleuven.be (R.H.)
[4] Water & Environmental Engineering Group, School of Engineering, Bolderwood Campus, University of Southampton, Burgess Street, Southampton SO16 7QF, UK
* Correspondence: jiseon.you@uwe.ac.uk (J.Y.); i.ieropoulos@soton.ac.uk (I.A.I.)

Abstract: This paper reports the first relatable bio-digital interface powered by microbial fuel cells (MFCs) that was developed to inform the public and introduce the concept of using live microbes as waste processors within our homes and cities. An innovative design for the MFC and peripherals system was built as a digital data generator and bioreactor, with a custom-built energy-harvesting controller that was connected to the system to enable efficient system operation using adaptive dynamic cell reconfiguration and transmit data for the bio-digital interface. This system has accomplished multiple (parallel) tasks such as electricity generation, wastewater treatment and autonomous operation. Moreover, the controller demonstrated that microbial behaviour and consequent system operation can benefit from smart algorithms. In addition to these technical achievements, the bio-digital interface is a site for the production of digital art that aims to gain acceptance from a wider-interest community and potential audiences by showcasing the capabilities of living microorganisms in the context of green technologies.

Keywords: sustainable built environment; microbial fuel cell; bio-digital interface; adaptive dynamic cell reconfiguration

Citation: You, J.; Mendis, A.; Greenman, J.; Freeman, J.; Wolff, S.; Armstrong, R.; Hughes, R.; Ieropoulos, I.A. Development of a Bio-Digital Interface Powered by Microbial Fuel Cells. *Sustainability* **2022**, *14*, 1735. https://doi.org/10.3390/su14031735

Academic Editors: Oz Sahin and Edoardo Bertone

Received: 13 December 2021
Accepted: 8 January 2022
Published: 2 February 2022

1. Introduction

Although the first discovery of microbial electricity generation was made over 100 years ago [1], attention towards microbial fuel cell (MFC) technology has only begun to grow fairly recently (1990s), and it is still unfamiliar to the public. Whether or not future developers have encountered a technology, either directly or indirectly, this is crucial in its development. In contrast to existing large-scale sewage treatment facilities, MFCs enable medium/small-scale, decentralised, remote, on-site sewage treatment, as well as energy generation [2,3]. While there are still several technical challenges to overcome to achieve full commercialisation, such as the relatively low power density and high initial investment costs [4], additional challenges that cannot be overlooked include the perception, public acceptability and usability of the technology, which do not have technological solutions and, therefore, require different approaches.

Microbial fuel cell technology is being developed for real-world implementation as a commercially viable product, with demonstrations in various settings such as public science events, music festivals [5] and field trials [6], as an essential tool for technology evaluation. One of the previous study investigated user perception of the technology where everyday use enabled end users to understand its benefits [7]. Such studies have revealed that MFC technology could be highly acceptable and help tackle sanitation issues by providing not only electricity but also accompanying benefits such as feeling safe and improving toilet cleanliness. Despite very positive feedback received so far, the broader uptake of MFC technology into our daily lives requires further work. For example, although there is a growing social consensus on the need for wastewater reuse, the biggest challenge lies in changing the stakeholders' perception of the water cycle more than technological developments [8,9]. Therefore, in order to develop and disseminate a particular technology, efforts must be made in many respects, such as understanding the need, technical context of the solution and cultural acceptance/resistance to this.

The goal of this project is to develop a bio-digital interface that encompasses technological advancements in an art installation, to better articulate how the technology works and encourage public engagement through curiosity that assists its progress towards the market. By developing an attractive interface that enables people and microbes to interact, enhances the user experience and increases the probability of technology uptake. This approach may further result in the same system being utilised as an educational tool or become part of the emerging market of ecohomes [10]. Following the successful completion of the Living Architecture project [11], which demonstrated a selectively programmable bioreactor wall for future living spaces, development of the first relatable bio-digital interface powered by MFCs was set to inspire the public and to introduce the concept of using live microbes as processors of waste within our homes and cities. This 'sociable' interface is a first-generation bio-digital hardware and user experience that translates microbial activity into meaningful encounters with human audiences, establishing a trans-species communications platform. Beginning with an electronic interface powered by MFCs, it extracts data from sensors, which is translated into a lively, communicable display that is showcased in a range of social contexts—from art galleries to exhibition spaces and festivals. From a scientific perspective, the following objectives were pursued: (i) develop an innovative MFC design capable of generating sufficient levels of power; (ii) develop an energy-efficient, multi-functional electronic controller; (iii) better understand microbial behaviour in functioning MFCs when subjected to external stimuli from the electronic controller.

2. Materials and Methods

2.1. System Design, Operation and Performance Measurement

For this work, a total of 15 MFC units were built and placed in five cascade groups of three MFCs. The bioreactor chassis was 3D printed in ABS (acrylonitrile butadiene styrene) with dimensions of 193 × 100 × 80 mm (W × H × D). Each MFC bioreactor consists of two anode chambers and two cathode chambers alternately located. This is to increase the contact area between the anode and cathode chambers within the volume of a given individual MFC unit; the two anodes and two cathodes of each MFC were connected in parallel. Each chamber holds approximately 100 mL and 120 mL volumes of anolyte and catholyte, respectively. The anode electrodes were made from plain carbon veil (20 g/m^2 carbon loading, PRF Composite Materials, Poole, Dorset, UK) modified with activated carbon ink [12]. Each anode electrode had a macro surface area of 1,350 cm^2 (30 × 45 cm). A U-shaped cathode made of thermally compressed activated carbon on stainless steel mesh [13] was placed inside each cathode chamber in contact with ceramic membranes. The size of the cathode (macro surface area) was 68 cm^2 (17 × 4 cm). Custom-made ceramic membrane sheets (65 × 85 mm each, thickness of 3 mm) [14] were placed between the anode and cathode chambers. The MFCs were designed to be gravity fed (the effluent of the MFC above becomes the influent of the MFC below) in order to reduce the energy input requirements. The flow of both anolyte and catholyte of the MFC system is described in Figure 1.

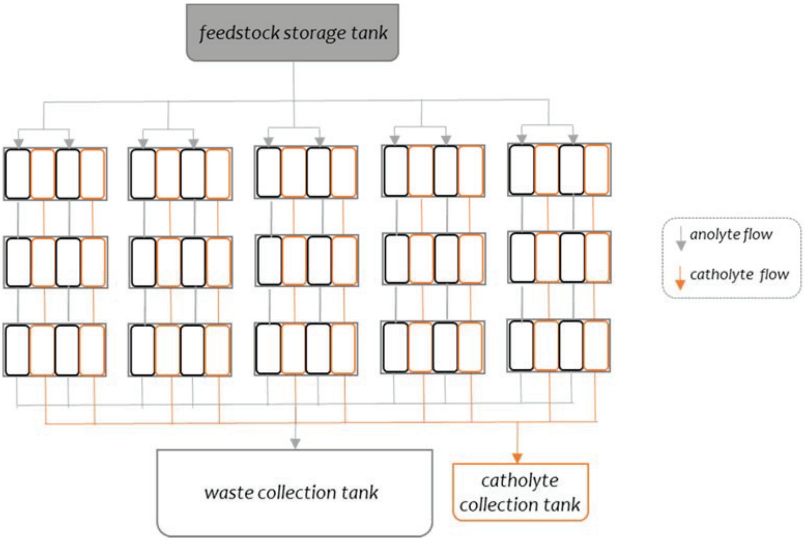

Figure 1. Flow diagram of the system. The black- and orange-coloured squares represent the anode and cathode chambers, respectively.

MFC anodes were inoculated with activated sludge collected from a local sewage treatment plant (Wessex Water, Saltford, UK), after being cultivated for 24 h in artificial urine medium (AUM). AUM was also used as feedstock and supplied to the system at various flow rates ranging between 1.5 L/d and 16.0 L/d. The composition of feedstock was modified from a previous study [15], containing the following: 2.5 g/L peptone, 0.5 g/L yeast extract, 5 g/L urea, 5.2 g/L sodium chloride, 1.4 g/L sodium sulphate, 0.95 g/L potassium dihydrogen phosphate, 1.2 g/L di-potassium hydrogen phosphate. A day after inoculation, a fixed external resistance of 200 Ω was connected to each MFC. The value of external resistance was gradually decreased to 100 Ω before being connected to a bespoke electronic controller on day 14.

The voltage output levels of 15 MFCs in volts (V) were initially monitored against time using a data logger (34972A DAQ unit, Agilent Technologies, Santa Clara, CA, USA) every 5 min. Once the aforementioned electronic controller was connected to the system, MFC power performance, including voltage, current, power and information of electrical configurations, was monitored by the controller in different time intervals. Power density (P_D) of an MFC unit or of the entire MFC system was normalised by the anolyte volume of 200 mL (per unit) or 3 L (for the whole system). In order to verify an individual MFC performance, periodic polarisation experiments were performed. For this, MFCs were left open circuit for at least 3 h before the run to reach stable open circuit voltages (OCVs). Then, various external resistances ranging from 1.2 kΩ to 4 Ω were loaded every 5 min and the potential between the anode and cathode was recorded every 30 s. For measuring chemical oxygen demand (COD), water samples were filtered using 0.45 µm syringe filters and then immediately analysed using a COD test kit (COD test tubes, Camlab, Cambridge, UK).

2.2. Electrical Infrastructure

A bespoke system, consisting of the electronic control system (ECS), power connections, external sensors, external actuators such as pumps and LEDs and a data-communication link, was developed to interface the MFC system located in the laboratory with the users' virtual experience. This infrastructure was autonomously harvesting electrical energy generated from the MFC array to measure, filter and collect the parameters of interest used for the live animation on the web user interface and transmit these collected data over a secure link to the user interface application; this app allows the user to visualise the data in a truly unique fashion (Figure 2).

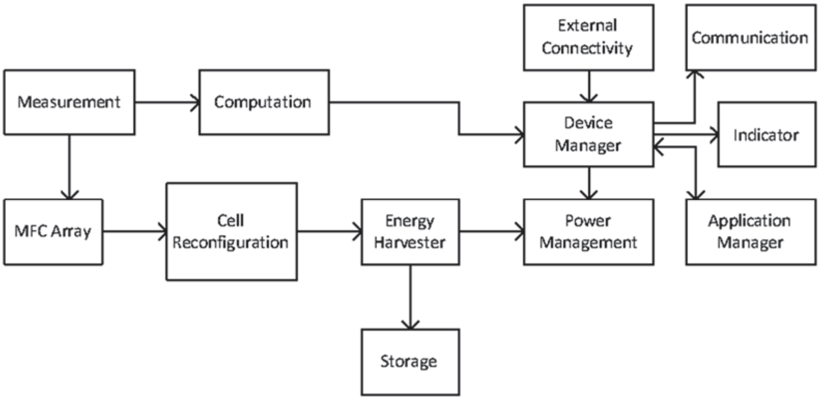

Figure 2. System high level functional block diagram.

The electrical infrastructure system is broken down into a number of functional subsystems, including energy harvesting, cell management (dynamic reconfiguration), self-regulation, measurement, data logging and transmission. The autonomous self-regulating system was designed, based on the EcoBot principle [16,17], to mimic a living organism in which actions are governed by energy availability (Figure 3).

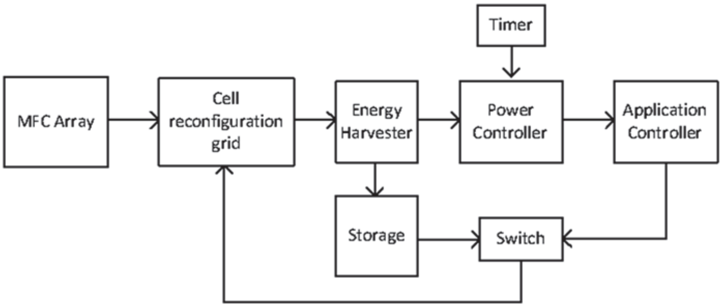

Figure 3. Cell reconfiguration module design.

The ECS electronics consist of two microcontroller units (MCUs), which are software driven and thus require electronic firmware. The firmware consists of device drivers, diagnostics and applications. The first MCU consists of a power management module, which operates and manages the energy harvester, and other power-related functions. It operates in low-power (sleep) mode and is awakened periodically by a timer. It operates the main power switches that supply the ECS and monitors bulk capacitor voltage and bus power. The second MCU is responsible for all the applications and communications. This MCU is user programmable, and applications can be uploaded via a universal serial bus (USB) link. The applications consist of cell reconfiguration, measurement, data logging, external sensors and other external devices such as pumps and LEDs.

2.3. Bio-Digital Interface

The interaction infrastructure design aims to capture meaningful data from the MFC system and visualise it appropriately to inform the user experience. The interactive live-streamed animations and live system information are either measured or processed parameter data such as individual cell voltage, cell current, cell power, stack current, stack power, ambient temperature, humidity, rate of change of power, ECS internal voltage, bulk capacitor store voltage, cell configuration information and LED actuation. Data transmission infrastructure enabled the MFC system to be used for the user experience, which involved transferring data from the ECS to the user experience server. This was accomplished via the periodic publication of data by the ECS to a single board computer attached to the ECS, which in turn executes a program to save sensor data to a local MySQL (My Structured Query Language) based database, and via encrypted SSH (Secure Shell) to a remote MySQL database on the external server. The SSH connection is secured with a public/private RSA (Rivest–Shamir–Adleman) key pair, with the private key living on the single board computer and the public key on the server. Once the connection is made, an application saves the data on the server.

Figure 4 shows the established responsive feedback loop between microbial action mediated through the MFC array that generates live data for the user experience, which the participant responds to by interacting with the microbes through animations shaped by live data and, in doing so, generates new data. Participants can choose from several actions, such as feeding the microbes, changing both the ambient and fluid temperature (warming or cooling) and changing the supply rate of feedstock to the microbes. The data from these interactions will feed forward into the live data animations, so that a broader community of participants can see the online events unfolding.

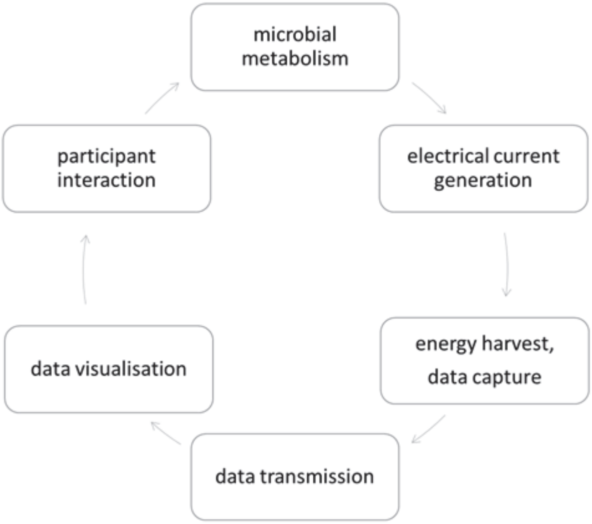

Figure 4. Responsive feedback loop between MFC microbial metabolism and planned interactive user experience.

3. Results and Discussion

3.1. Individual MFC Performance

Figure 5 shows the average power-generating performance of the 15 MFCs. The polarisation sweep was performed on day 20, when the cells were assumed to have reached a quasi-steady state. The average open circuit (OCV) value was 663 ± 55 mV and the maximum power output was 5.3 ± 0.9 mW (power density: 26.5 W/m^3) on average, reaching up to 6.5 mW (32.5 W/m^3).

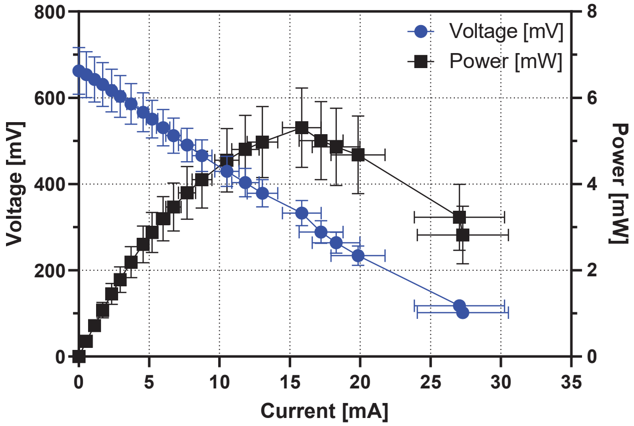

Figure 5. Polarisation and power curves of 15 individual matured MFCs measured on day 20. Each data point represents the average value of all MFCs (n = 15).

During the same period, when the MFCs were running individually without being electrically connected through the ECS, the organic content of the feedstock measured in COD decreased by 18.9 ± 2.3, 27.4 ± 7.5 and 19.6 ± 3.9% in the top, middle and bottom rows of the MFCs, respectively. Although the amount of organic consumption differs depending on the location within a cascade, there was no significant difference in the maximum power output. This means that this flow rate (4.0 L/d) and organic concentration (COD of 3.45 mg/L) were sufficient to feed the last cell of each cascade following a sequential cascade treatment.

Several strategies have been established to increase the wastewater treatment efficiency, such as increasing the hydraulic retention time (HRT) by reducing the flow rate or enlarging the cell footprint [18], increasing the operating temperature [19] or increasing the external load [20]. Among these, increased HRT and operating temperature can lead to higher operating costs unless properly optimised. External load changes can be relatively simple to apply at no significant additional cost. Several research groups have reported that appropriately changing the value of the external resistance over a certain period of time, can increase the power output [21,22], as it is related to the microbial metabolic rate. Dynamic reconfiguration, using smart algorithms, is therefore worth pursuing as an efficient MFC operation strategy and is discussed in more detail in the next section.

The MFC reactor design used in this study employed a partial open-to-air cathode, in which 1/2 of the cathode and 1/3 of the membrane (on the cathode side) are submerged in the catholyte. The cathode chamber was initially empty, and catholyte began to accumulate as the MFC started operating. A complete air cathode is a popular choice in the field due to its design simplicity, smaller footprint and lower material cost, but precipitation of salts on the cathode electrode has been reported [23,24], which can be problematic. However, in this design, the ceramic membrane can remain wet, and no significant reduction in power output was observed during the one-year operation period.

3.2. MFC Stack Performance as a Digital Data Generator

The ECS (electronic control system) is an energy management unit consisting of an energy harvester, power management unit and a mechanism to reconfigure cell connection topologies (cell reconfiguration). During operation, the ECS attempts to harvest the maximum energy while sustaining the MFCs for long-term operation. This is useful as the loading of the harvester on the MFC stack dynamically changes depending on the state of the MFCs, based on feedback [25].

The electrical connection of the 15 MFC units was dynamically changed by the ECS to the following four topologies: all in parallel (15P), all in series (15S), five cells in parallel with the three groups in series (5P3S) and three cells in parallel within the five groups in series (3P5S). Initially, the MFC stack operated at a fixed setting of 15P during inoculation and maturation. An 'adaptive gain' (AG) method, based on dynamic gain allocation and the rate of change of power with voltage clamping in the range of 350~450 mV, was used during subsequent operation. The energy harvester acted as a pseudo-time-varying non-linear voltage-controlled current sink with a voltage range of 0.15~5 V and a max sink current of 70 mA.

The performance of the energy harvester and MFC stack was evaluated by observation of the mean instantaneous power, mean instantaneous voltage and by the number of actuations per day (Figure 6). The ECS checked energy levels approximately every two minutes and performed data logging and/or actuation depending on the energy acquisition. During the first 200 days of operation, the system harvested a mean instantaneous power of 28.36 ± 5.5 mW, with a minimum of 13.02 mW and a maximum of 36.34 mW; this was at a mean voltage of 339.63 ± 70.75 mV with a minimum voltage of 110.13 mV and a maximum voltage of 477.24 mV at each check. An LED configuration acted as the demonstrable actuation of the 15-MFC system (in addition to all the energy management and data communication) with a 20-s actuation/display; the mean number of 20-s actuations per day was 905, with a minimum of 6 and a maximum of 1578. Overall, the MFC system showed a consistently stable performance, except during days 90–105 when the feed rate was reduced to a minimum (0.7 L/d) due to the Christmas break. Figure 7 shows the MFC system installed in the laboratory actuating the LED lights (top left).

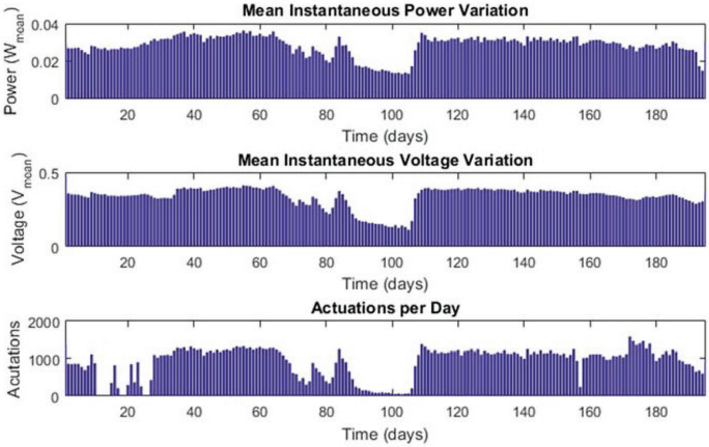

Figure 6. Harvester performance: mean instantaneous power variation, mean instantaneous voltage variation and actuations per day.

By utilising a cell reconfiguration mechanism, the system maintains the microbial activity within the MFCs as well as the power output at optimum levels [26,27]. External electrical loading can change the internal impedance and the impedance is varied by changing the connection topology. Here, we create four dynamic impedances which also have an effect on the loading of MFCs, drawing optimum levels of current depending on state of performance. By employing dynamic cell reconfiguration, the MFCs are maintained such that they increase in power output over time until a steady state is reached.

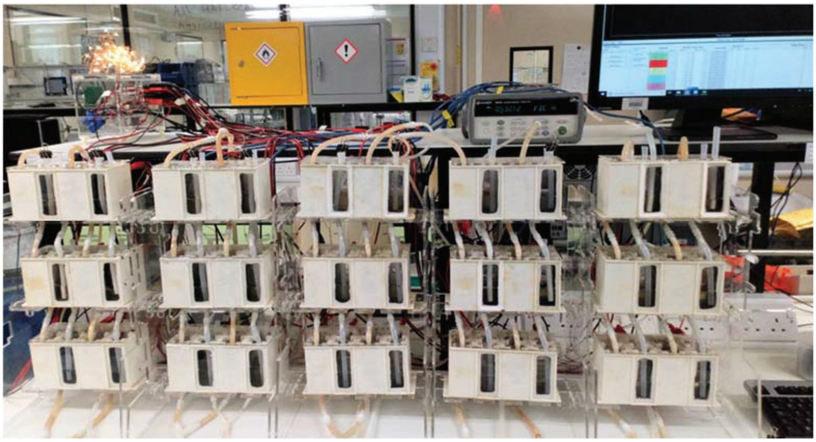

Figure 7. The MFC system in action, with the LED lights (located in upper left corner) switched on.

During normal operation, the ECS system was programmed to reconfigure every five minutes, with each cycle being subject to the availability of adequate energy. The control algorithm would adaptively reconfigure the MFCs based on the rate of change of power. Thus, as the rate of change of power increased, the topologies shifted towards a low Thévenin impedance and vice versa [28]. Analysing 200 days of data, a median power generation of 16.21 ± 0.77 mW was maintained with the configurations of series, parallel, 3P5S, and 5P3S at a daily active percentage of 0.17, 0.25, 0.33 and 0.25%, respectively (Figure 8). During low-power-output periods, a mean power level of 29.75 ± 0.35 mW was maintained at a daily activity percentage vector of (0.16, 0.26, 0.35, 0.22)%; likewise, at high power output, a mean power level of 34.77 ± 0.77 mW was maintained at a daily activity percentage vector of (0.1, 0.23, 0.35, 0.32)%. Based on Thévenin resistances of series and parallel networks of MFCs, for a given low impedance load, as the Thévenin resistance increases in a series network, unless the matched load decreases, the MFCs will be under stress to deliver equivalent power. The results corroborate this model, whereby the series topology indicates higher loading in comparison to the parallel one. As power increases, the time spent on parallel and series topologies is less. More time is spent on mid topologies, which enable a balance of loading. It was observed that the system selected the configuration 3S5P. Topologically, this configuration provided an apt balance between parallel and series configurations during peak power-harvesting periods. When power was lowest, the system maintained itself by choosing parallel configurations, which prevented suboptimal performance (also known as 'weakening'), which can result in weaker cells reversing their polarity, so any form of a series topology is harmful. These are findings that can nicely feed into novel AI strategies in further optimising MFC systems, and this will form part of our future work.

Performing as a digital data generator, the overall activity of the MFC-powered bio-digital interface was digitally represented. All critical parameters (including, but not limited to, MFC voltages, power, current, system states, temperature) for monitoring the system were transmitted from the ECS to a remote server, where users can monitor and interact with the system.

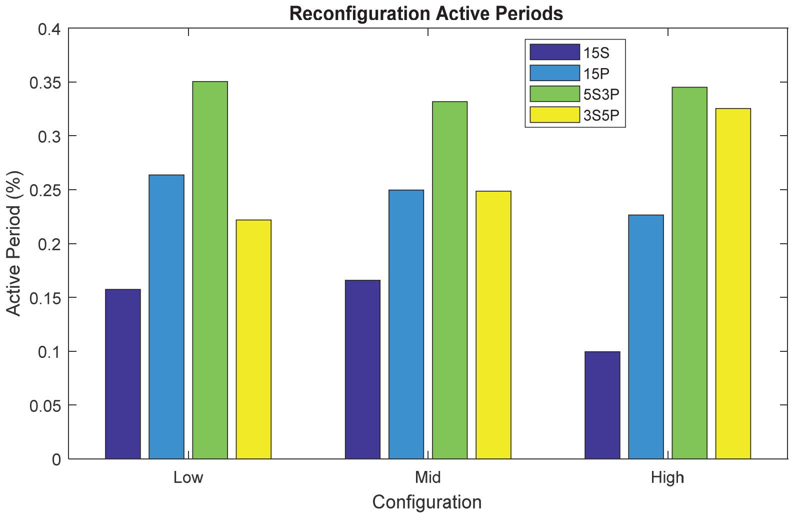

Figure 8. Configuration percentages for low-, mid- and high-power levels.

3.3. Bio-Digital Interface

A bio-digital interface where users can virtually interact with live microbes in the real MFC system was developed, as shown in Figure 9. Visitors would remotely access a full-screen website, which presents an abstract world of animated microbes ('mobes') moving, feeding and colonising in response to the data streaming from the MFC array installed in the laboratory. Viewers can interactively engage with the mobes simulations and see real-time data, which provides the ability to understand the microbial behaviour affected by the interactions. Technical information about the live system is also available for viewing. A live video feed from the lab, which captures the real-time action of the MFC system that is generating the data informing the animations, is also accessible.

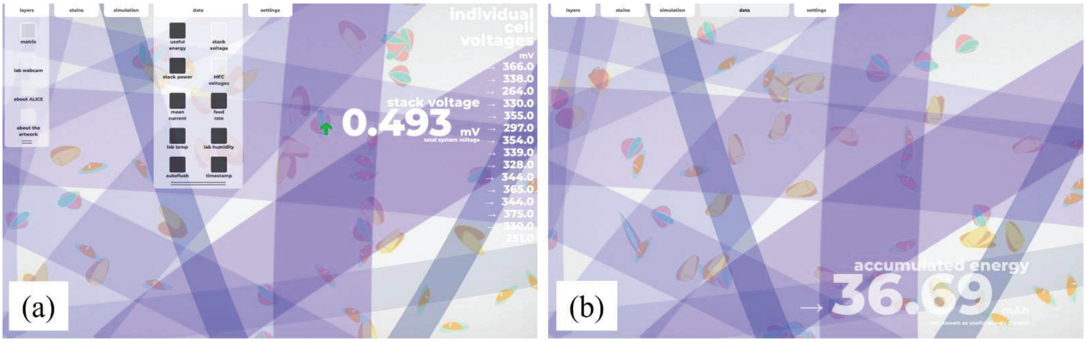

Figure 9. Exemplar interactive elements of the mobes user interaction interface (**a**) and exemplar user data visualisation application animating mobes (**b**). Images produced by Translating Nature.

The animated work considers the conceptual commonalities between data and microbes, including the different types of power they each harness (for example, MFCs generate electrical power; data are a power behind many critical decisions), and the social preconceptions which surround both data and microbes (for example: abundance, necessity, cleanliness). The algorithm used as a basis for the behaviours of the mobes in this work was from [29]. A bacterial foraging optimisation algorithm (BFOA) with social communication is used as a framework for the animated microbes by providing each mobe with a set of rules that generate a random walk within a two-dimensional area. The BFOA is 'seeded' with parameters, such as the number of microbial communities, the population of each and a fitness value. The close-to-real-time fluctuating data from the MFCs then directly affects the mobility of each mobe (direction, speed, step distance) and their attraction or repulsion to the matrix or food. The form of each mobe is designed as a minimal scalable vector graphic (SVG) with flexible anchor points which animate a Bézier curve. As the anchor points change in response to data, the mobes appear to flap and rotate. The animated world which emerges shows the fluctuating nature of the MFC outputs and is an artwork which raises questions about how we translate microbial data as a visual microbial system. It aims to be an experience to convey life, rather than a typical data visualisation, using data as an art material [30] to 'power' the animation.

This participatory technology–art experience is currently available on the website (https://mobes.alice-interface.eu, accessed on 12 December 2021) and is based on the first bio-digital interface powered by MFCs. Providing an interesting and stimulating space for thorough creative encounters with microbes, it generates innovative learning opportunities and striking artistic experiences. This was also exhibited at the Digital Design Weekend (24–26 September 2021, V&A Museum, London, UK) and received a great deal of public interest (Figure 10).

Figure 10. Bio-digital interface technology-art experience at the V&A Museum as part of the Digital Design Weekend, London Design Festival, 2021.

4. Conclusions

The first human–microbial interactive bio-digital interface powered by MFCs was developed and continuously operated over a one-year period. The system operated as a self-sustainable digital data generator, which produced an average power of 28.36 ± 5.5 mW (9.45 W/m^3). This level of power was sufficient to power data logging and data transmission, LEDs, system sensing and system control through adaptive dynamic cell reconfiguration. The dynamic reconfiguration allowed better maintenance of the microbial communities inside the MFCs, which resulted in establishing steady states and a consistent performance.

In addition to these technical achievements, the bio-digital interface as a site for digital art is presently scheduled for online public exhibitions. Enabling the visualisation of the otherwise invisible actions of microbes, the data art is expected to inspire users and the general public, thus helping them to understand how a complex biotechnology can be beneficial for society in the long term.

Author Contributions: Conceptualization, R.A., R.H., J.F., I.A.I. and J.G.; methodology, A.M., S.W. and J.Y.; software, A.M. and S.W.; formal analysis, A.M. and J.Y.; investigation, A.M. and J.Y.; writing—original draft preparation, A.M. and J.Y.; writing—review and editing, R.A., J.F. and I.A.I.; visualization, A.M., J.F. and J.Y.; funding acquisition, R.A., R.H., J.F., I.A.I. and J.G. All authors have read and agreed to the published version of the manuscript.

Funding: This project has been funded by the European Union's Horizon 2020 Innovation Action Programme, grant no. 851246. IAI is a Bill & Melinda Gates Foundation grantee, grant no. INV-006499.

Institutional Review Board Statement: Not applicable.

Conflicts of Interest: The authors declare no conflict of interest.

References

1. Potter, M.C. Electrical effects accompanying the decomposition of organic compounds. *Proc. R. Soc. B Biol. Sci.* **1911**, *84*, 260–276. [CrossRef]
2. You, J.; Greenman, J.; Ieropoulos, I.A. Microbial fuel cells in the house: A study on real household wastewater samples for treatment and power. *Sustain. Energy Technol. Assess.* **2021**, *48*, 101618. [CrossRef]
3. Khandaker, S.; Das, S.; Hossain, M.T.; Islam, A.; Miah, M.R.; Awual, M.R. Sustainable approach for wastewater treatment using microbial fuel cells and green energy generation—A comprehensive review. *J. Mol. Liq.* **2021**, *344*, 117795. [CrossRef]
4. Munoz-Cupa, C.; Hu, Y.; Xu, C.; Bassi, A. An overview of microbial fuel cell usage in wastewater treatment, resource recovery and energy production. *Sci. Total Environ.* **2021**, *754*, 142429. [CrossRef]
5. Walter, X.A.; Merino-Jiménez, I.; Greenman, J.; Ieropoulos, I. PEE POWER® urinal II—Urinal scale-up with microbial fuel cell scale-down for improved lighting. *J. Power Sources* **2018**, *392*, 150–158. [CrossRef]
6. Ieropoulos, I.A.; Stinchcombe, A.; Gajda, I.; Forbes, S.; Merino-Jimenez, I.; Pasternak, G.; Sanchez-Herranz, D.; Greenman, J. Pee power urinal—Microbial fuel cell technology field trials in the context of sanitation. *Environ. Sci. Water Res. Technol.* **2016**, *2*, 336–343. [CrossRef]
7. You, J.; Staddon, C.; Cook, A.; Walker, J.; Boulton, J.; Powell, W.; Ieropoulos, I. Multidimensional Benefits of Improved Sanitation: Evaluating 'PEE POWER®' in Kisoro, Uganda. *Int. J. Environ. Res. Public Health* **2020**, *17*, 2175. [CrossRef] [PubMed]
8. Bixio, D.; Thoeye, C.; De Koning, J.; Joksimovic, D.; Savic, D.; Wintgens, T.; Melin, T. Wastewater reuse in Europe. *Desalination* **2006**, *187*, 89–101. [CrossRef]
9. Lee, H.; Tan, T.P. Singapore's experience with reclaimed water: NEWater. *Int. J. Water Resour. Dev.* **2016**, *32*, 611–621. [CrossRef]
10. ALICE Consortium ALICE Interface—Active Living Infrastructure: Controlled Environment. Available online: https://alice-interface.eu/ (accessed on 16 September 2020).
11. LIAR Consortium Living Architecture—Transform Our Habitats from Inert Spaces into Programmable Sites. Available online: https://livingarchitecture-h2020.eu/ (accessed on 10 September 2019).
12. Gajda, I.; You, J.; Santoro, C.; Greenman, J.; Ieropoulos, I.A. A new method for urine electrofiltration and long term power enhancement using surface modified anodes with activated carbon in ceramic microbial fuel cells. *Electrochim. Acta* **2020**, *353*, 136388. [CrossRef]
13. Walter, X.A.; Greenman, J.; Ieropoulos, I.A. Microbial fuel cells directly powering a microcomputer. *J. Power Sources* **2020**, *446*, 227328. [CrossRef] [PubMed]
14. You, J.; Wallis, L.; Radisavljevic, N.; Pasternak, G.; Sglavo, V.M.; Hanczyc, M.M.; Greenman, J.; Ieropoulos, I. A Comprehensive Study of Custom-Made Ceramic Separators for Microbial Fuel Cells: Towards "Living" Bricks. *Energies* **2019**, *12*, 4071. [CrossRef]
15. Brooks, T.; Keevil, C.W. A simple artificial urine for the growth of urinary pathogens. *Lett. Appl. Microbiol.* **1997**, *24*, 203–206. [CrossRef] [PubMed]
16. Melhuish, C.; Ieropoulos, I.; Greenman, J.; Horsfield, I. Energetically autonomous robots: Food for thought. *Auton. Robots* **2006**, *21*, 187–198. [CrossRef]
17. Ieropoulos, I.; Greenman, J.; Melhuish, C.; Horsfield, I. EcoBot-III: A robot with guts. In Proceedings of the Alife XII Conference, Odense, Denmark, 19–23 August 2010; pp. 733–740.
18. You, J.; Greenman, J.; Ieropoulos, I. Novel analytical microbial fuel cell design for rapid in situ optimisation of dilution rate and substrate supply rate, by flow, volume control and anode placement. *Energies* **2018**, *11*, 2377. [CrossRef]
19. Jadhav, G.S.; Ghangrekar, M.M. Performance of microbial fuel cell subjected to variation in pH, temperature, external load and substrate concentration. *Bioresour. Technol.* **2009**, *100*, 717–723. [CrossRef]

20. Corbella, C.; Puigagut, J. Improving domestic wastewater treatment efficiency with constructed wetland microbial fuel cells: Influence of anode material and external resistance. *Sci. Total Environ.* **2018**, *631–632*, 1406–1414. [CrossRef]
21. Grondin, F.; Perrier, M.; Tartakovsky, B. Microbial fuel cell operation with intermittent connection of the electrical load. *J. Power Sources* **2012**, *208*, 18–23. [CrossRef]
22. Walter, X.A.; Greenman, J.; Ieropoulos, I.A. Intermittent load implementation in microbial fuel cells improves power performance. *Bioresour. Technol.* **2014**, *172*, 365–372. [CrossRef]
23. An, J.; Li, N.; Wan, L.; Zhou, L.; Du, Q.; Li, T.; Wang, X. Electric field induced salt precipitation into activated carbon air-cathode causes power decay in microbial fuel cells. *Water Res.* **2017**, *123*, 369–377. [CrossRef]
24. Al Lawati, M.J.; Jafary, T.; Baawain, M.S.; Al-Mamun, A. A mini review on biofouling on air cathode of single chamber microbial fuel cell; prevention and mitigation strategies. *Biocatal. Agric. Biotechnol.* **2019**, *22*, 101370. [CrossRef]
25. Faíña, A.; Nejatimoharrami, F.; Stoy, K.; Theodosiou, P.; Taylor, B.; Ieropoulos, I. *EvoBot: An Open-Source, Modular Liquid Handling Robot for Nurturing Microbial Fuel Cells*; MIT Press: Cambridge, MA, USA, 2016.
26. Papaharalabos, G.; Greenman, J.; Stinchcombe, A.; Horsfield, I.; Melhuish, C.; Ieropoulos, I. Dynamic electrical reconfiguration for improved capacitor charging in microbial fuel cell stacks. *J. Power Sources* **2014**, *272*, 34–38. [CrossRef]
27. Papaharalabos, G.; Stinchcombe, A.; Horsfield, I.; Melhuish, C.; Greenman, J.; Ieropoulos, I. Autonomous energy harvesting and prevention of cell reversal in MFC stacks. *J. Electrochem. Soc.* **2017**, *164*, H3047–H3051. [CrossRef]
28. Jaeger, R.C.; Blalock, T.N. *Microelectronic Circuit Design*; McGraw-Hill: New York, NY, USA, 1997; ISBN 0070324824.
29. Brabazon, A.; O'Neill, M.; McGarraghy, S. Chapter 11. Bacterial Foraging Algorithms. In *Natural Computing Algorithms*; Springer: Berlin/Heidelberg, Germany, 2015; pp. 187–199. ISBN 978-3-662-43630-1.
30. Freeman, J.; Wiggins, G.; Starks, G.; Sandler, M. A concise taxonomy for describing data as an art material. *Leonardo* **2018**, *51*, 75–79. [CrossRef]

sustainability

Article

Towards Energy-Positive Buildings through a Quality-Matched Energy Flow Strategy

Nick Novelli [1,*], Justin S. Shultz [2], Mohamed Aly Etman [1], Kenton Phillips [2], Jason O. Vollen [3], Michael Jensen [4] and Anna Dyson [1,*]

[1] Center for Ecosystems in Architecture, Yale University, 180 York St., New Haven, CT 06511, USA; mohamed.alyetman@yale.edu
[2] Center for Architecture, Science, and Ecology, Rensselaer Polytechnic Institute, 110 8th St., Troy, NY 12180, USA; justinsshultz@gmail.com (J.S.S.); kenton.a.phillips@gmail.com (K.P.)
[3] AECOM, 125 Broad St., New York, NY 10003, USA; jason.vollen@aecom.com
[4] Department of Mechanical, Aerospace, and Nuclear Engineering, Rensselaer Polytechnic Institute, 110 8th St., Troy, NY 12180, USA; jensenmk@gmail.com
* Correspondence: nick.novelli@gmail.com (N.N.); anna.dyson@yale.edu (A.D.)

Abstract: Current strategies for net-zero buildings favor envelopes with minimized aperture ratios and limiting of solar gains through reduced glazing transmittance and emissivity. This load-reduction approach precludes strategies that maximize on-site collection of solar energy, which could increase opportunities for net-zero electricity projects. To better leverage solar resources, a whole-building strategy is proposed, referred to as "Quality-Matched Energy Flows" (or Q-MEF): capturing, transforming, buffering, and transferring irradiance on a building's envelope—and energy derived from it—into distributed end-uses. A mid-scale commercial building was modeled in three climates with a novel Building-Integrated, Transparent, Concentrating Photovoltaic and Thermal fenestration technology (BITCoPT), thermal storage and circulation at three temperature ranges, adsorption chillers, and auxiliary heat pumps. BITCoPT generated electricity and collected thermal energy at high efficiencies while transmitting diffuse light and mitigating excess gains and illuminance. The balance of systems satisfied cooling and heating demands. Relative to baselines with similar glazing ratios, net electricity use decreased 71% in a continental climate and 100% or more in hot-arid and subtropical-moderate climates. Total EUI decreased 35%, 83%, and 52%, and peak purchased electrical demands decreased up to 6%, 32%, and 20%, respectively (with no provisions for on-site electrical storage). Decreases in utility services costs were also noted. These results suggest that with further development of electrification the Q-MEF strategy could contribute to energy-positive behavior for projects with similar typology and climate profiles.

Keywords: on-site net-zero electricity; energy-positive buildings; active integrated facades; thermal storage; distributed systems; exergy management

Citation: Novelli, N.; Shultz, J.S.; Aly Etman, M.; Phillips, K.; Vollen, J.O.; Jensen, M.; Dyson, A. Towards Energy-Positive Buildings through a Quality-Matched Energy Flow Strategy. *Sustainability* **2022**, *14*, 4275. https://doi.org/10.3390/su14074275

Academic Editors: Oz Sahin and Edoardo Bertone

Received: 26 December 2021
Accepted: 15 March 2022
Published: 4 April 2022

1. Introduction

Measures employed in the development of net-zero and net-generating building projects are determined through a design framework, whether implicit or explicit, and any such framework must address multiple criteria to develop traction and ultimately enjoy uptake. These criteria are occupant-related, physics-based, engineering and manufacturing, logistical, and economic in nature. One such framework, termed Quality-Matched Energy Flows (Q-MEF), is explored in this study, and focuses on maintaining and applying the inherent value of climatic energy resources as they pertain to the service demands of the built environment—namely, lighting, electricity supply, and heating and cooling. Specifically considering on-site solar resources, Q-MEF is explored through simulation with a specific generalized building type, in multiple climates. Measures proposed through the Q-MEF rubric comprise a novel Building-Integrated, Transparent, Concentrating Photovoltaic and

Thermal fenestration system (BITCoPT) coupled to an interconnected network of thermal storage and heat pumps (both thermally and electrically powered) which are distributed throughout the building. BITCoPT (investigated in earlier works through modeling, simulation, and experimentation [1–3]) uniquely enables the Q-MEF strategy by providing daylighting (illumination and glare control) in addition to generating electricity and collecting thermal energy from solar energy incidents on the building envelope. As Q-MEF and BITCoPT are architecturally grounded, they draw on multiple realms of expertise, and the context of these realms—and the state of their technology—is explored.

1.1. Addressing Limits of Load-Reduction Strategies with Active Envelope and Thermal Distribution

Traditionally, net-zero energy building (NZEB) strategies follow a three-tier approach to energy efficiency: load reduction is foremost, followed by the application of passive systems such as shading, and lastly the use of active systems such as energy harvesting [4]. Although load reduction is important, in contemporary architecture this approach begets façade designs that supply good daylighting and natural ventilation, but do not attempt energy harvesting [5,6]. The proliferation of on-site NZEB has been stalled by these legacy design frameworks, which remain grounded in efficient use of grid-supplied electricity and fuel, and employ envelope designs that offload solar energy gains through insulating, limiting apertures, shading, and glazing emissivity control. Moreover, prevalent building-integrated energy harvesting systems (such as roof-top and façade-integrated PV) exhibit sub-optimal exergetic efficiency and limited installable area, limiting the addressable fraction of a building's service demands, even though in many scenarios solar exergy available to a building is far greater than its own consumption.

Here, we propose an alternative approach, manipulating incident solar energy into daylighting (with minimal glare production) by intercepting that energy with an optically-concentrating photovoltaic fenestration system and hydronic mechanisms that capture and transfer "waste" heat. In this approach, solar gain is re-cast from a low-grade "load" to be remediated through energy intensive heating, ventilation, and air-conditioning (HVAC) systems into a high-grade (thermodynamically useful) energy source for cooling (and other) systems. This approach (Q-MEF) suggests re-distributing a building's systems out across its envelope to more-efficiently interface with the distributed solar resource. This distribution represents a revision of the traditional system topology that has evolved around grid-sourced energy supplies, of centralized plants and trunk-and-branch systems (Figure 1).

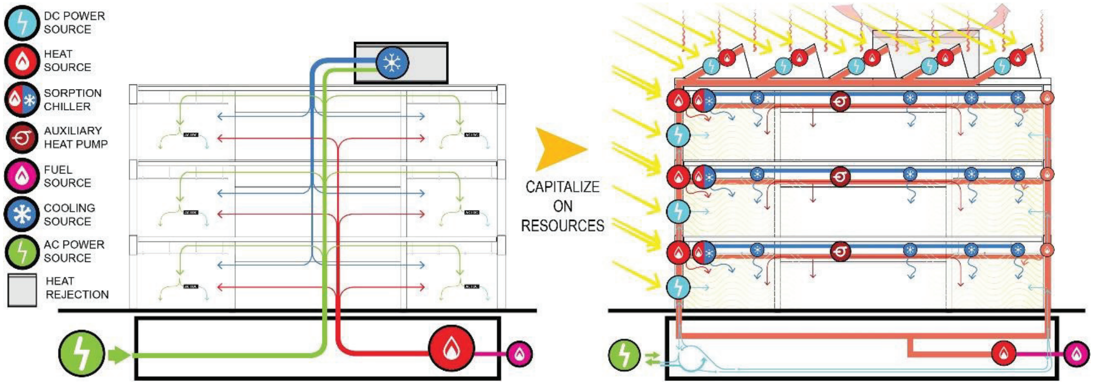

Figure 1. Transitioning from centralized (grid-source optimized) systems to distributed, integrated systems (climate-sourced optimized), matching resource (sunlight) to service demands (daylighting, power, cooling, heating).

If active control is thus shifted outward, the building envelope is empowered to redistribute the abundant light, heat, and power resources available, transferring solar energy towards the building's particular demands and, when necessary, transforming incident solar energy into consumable forms. In Q-MEF, this shift is implemented through integrating distributed coolth storage, (thermally driven) adsorption chillers, and a transparent, optically concentrating photovoltaic and thermal collecting fenestration system (BITCoPT). BITCoPT transmits diffuse irradiance for daylighting and views, and strips out direct normal irradiance, either transforming insolation into electricity or collecting it as thermal energy. Rather than exacerbating cooling demands, insolation can therefore be used directly, as electricity, or as thermal energy that supplies small, localized chillers. Local, distributed use of heat is important for avoiding losses from piping that energy to a central plant. The exergetic value of collected thermal energy is sensitive to such temperature losses, and the surface area-mass ratio of the system (potential for losses through insulation) is inherently high compared to centralized distribution networks with larger pipes. Generated heating and cooling capacities are stored as warm and cold water and circulated through the building via thermally massive hydronic circuits, redistributing these resources towards demands for cooling as well as heating and other process energy, maintaining small but useful temperature differences rather than immediately dispersing generated potential into the built environment. In concept, this integrated system of the multifunctional envelope collector and activated thermal mass distribution can uniquely maintain the quality of the solar resource (through daylighting), and its exergetic content, by collecting a high fraction of direct irradiance either as electricity or as thermal energy at elevated temperatures.

1.2. Precedents: Active Facades

The Q-MEF strategy builds on precedent and contemporary building-scale integrated strategies and is dependent on multifunctional envelope technologies. As such, a review of precedent active integrated envelopes and facades (AIFs) is relevant. Building-integrated technologies have been reviewed in such focus areas as photovoltaics [7], thermal collection and life cycle analysis [8], concentrating technologies [9,10], and architectural integration [11]. To the authors' knowledge, an investigation coupling a high-concentration/daylighting system such as BITCoPT to a full-building scale application and distribution strategy—designed specifically to leverage envelope-wide collection—has not yet been undertaken.

1.3. Benefits of Distributed Systems

Beyond deficits in energy harvesting capacity, the drawback of load-reduction NZEB strategies is in the utilization of harvested energy: Although high quality flows of electricity, light, and thermal energy can be developed with envelope-integrated systems, the building's mechanical infrastructure must be designed to apply these flows effectively. Specifically, generated electricity and thermal resources must be managed. DC microgrids can be employed to efficiently transfer envelope-generated electrical power to equipment and lighting, which often requires DC power natively, using available DC-DC conversion [12]. Harvested thermal resources can be distributed with hydronic systems if the network topology is designed to maintain the useful temperatures (and therefore exergy) that can be developed by a concentrating-type envelope collection system.

Traditionally, building mechanical systems are centrally organized as a logical result of the availability of grid electricity and fuels. Current NZEB strategies therefore involve centralized systems as well (save for active shading/daylighting and natural ventilation). Even on-site harvesting of electricity and heat is typically routed through the same wiring and plumbing that are optimized for the centralized resource-generating systems. To take advantage of envelope-generated energy resources, the mechanical processes that use these resources can be scaled down, parallelized, and located at the envelope, distributed in the same fashion as energy resources are harvested. This is especially relevant for thermal energy collected at high temperatures (beyond roughly 25 °C above the comfort range), which endures larger transport losses than electricity. Recent research into distributed ventilation and humidity control [13] and DC microgrids [14] indicates the inherent efficiency and demand–response benefits of co-locating processes with both their sources of power and the demands they service within a building. Analysis of coupling these end uses to a polygenerating envelope such as BITCoPT has not yet been done.

Many technological elements of load-reduction NZEB strategies can be successfully reconfigured to the distributed Q-MEF strategy. Radiant and mixed-mode heating and cooling, for example, is efficient at managing sensible thermal loads when coupled with effective ventilation and latent-controlled mechanisms such as dedicated outdoor air systems (DOAS) [15,16]. In standard practice, the heat and coolth these systems distribute are generated by centralized chillers and boilers. However, they integrate just as well with distributed thermal control and are employed in the Q-MEF framework.

1.4. Thermal Energy Storage for Resource-Matching and Dispatchability

In contrast to grid-sourced energy, which is available on-demand, climatic energy resources must be collected when they are available. To make these resources useful, they must be made dispatchable. Therefore, storing energy in a recoverable way is useful. The benefits of energy storage additionally extend to load factor reduction, grid efficiency and stability, primary fuel costs and pollution reduction, equipment longevity, and resiliency [17]. A range of technologies and materials are actively investigated to these ends [18].

On-site fluidic thermal energy storage (TES) at temperatures suitable for heating (over 30 °C) and cooling (under 18 °C) is attractive because of the potential for good round-trip efficiency: Losses can be minimized through proper insulation, and fluid pumps can be used to dispatch thermal power with little power consumption [19]. Although broadly applicable [20], on-site thermal storage can be limited because of space requirements as well as the relative unfamiliarity of Architecture, Engineering, Construction, and Operation (AECO) sector industries. The current commercial solution to this spatial limitation is to deploy ice storage [21]. Research into alternative phase-changing materials and systems that melt at higher temperatures than water [22–24] could improve system efficiencies (by reducing required temperature lifts and maintaining optimal temperatures for process efficiencies) and design desirability (by reducing system footprint). For the sake of conceptual clarity, in the present study, water is chosen as the heat transfer fluid and storage media. The media is well-characterized, but the system geometric configuration—with thermal mass distributed throughout the building's floorplate, along the fluid loop—is uniquely configured to distributed generation and, as such, adds a novel dimension to this investigation.

TES at three temperature ranges is important in the Q-MEF strategy, corresponding to the supply, re-cooling, and output circuits of thermally driven chillers. Because commercial buildings have significant cooling loads and electricity is typically used to create cooling, on-site coolth TES can reduce site energy use, as well as peak demands on the grid, by phase-shifting cooling [25].

In addition to the cool temperature range, TES at two higher ranges is important. In support of the envelope-integrated thermal collection, a buffering mechanism is required to match high-temperature collection to the operation of a thermally driven chiller. High-temperature storage has been deployed for utility-scale thermal power cycles such as solar electric plants [26], but the lower temperatures useful for driving adsorption chillers (above 60 °C) are easier to maintain in the building context.

A mid-range TES (at temperatures above the range of thermal comfort but below 50 °C) is also required and considered. This storage can act as both a sink for heat rejected from the chillers' operation and a source for heating processes, either as pre-heating for service hot water (SHW) demands or as space heating. Additionally, it has been shown that by storing rejected heat until night-time, when the temperature of the atmospheric sink is lower, the rejection process (and overall energy use) can be more efficient [27].

1.5. Entropic Efficiency of Thermal Cascade

By defining multiple temperature (or quality) ranges for thermal storage, a cascade develops through which harvested thermal resources can be matched to a building's service demands (Figure 2). Besides the demands discussed here, other uses such as humidity control through desiccant regeneration have been investigated. This cascading framework has been recognized in other research, such as the Building as Power Plant concept [28], and in studies and optimizations of latent thermal storage in the building context [23,29]. However, to the authors' knowledge, including daylighting as a primary product and analysis through the mechanism of a multifunctional envelope has not been undertaken.

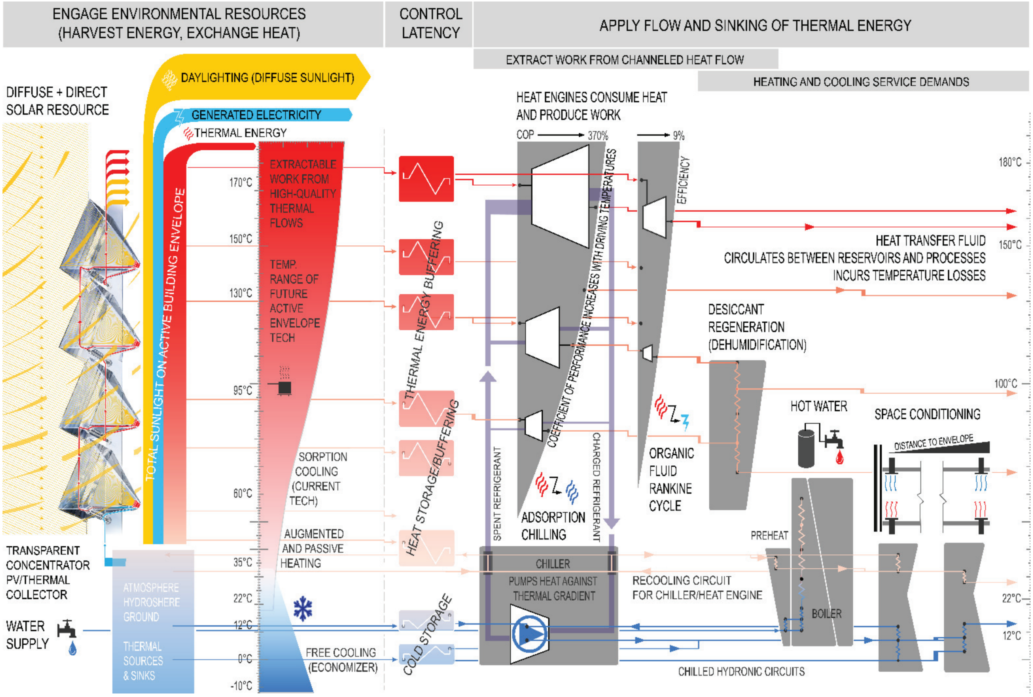

Figure 2. Cascade of thermal potentials for servicing built environment demands. Optimal exergy application performed by cascading heat through and into processes that require different grades (temperatures) of energy. In the current Q-MEF investigation, thermal storage in three discrete ranges (driving, rejection/heating, chilled) governs energy flow between processes.

1.6. Valuing Different Forms of Energy

To evaluate Q-MEF as a strategy, a rubric is devised for the value of the different energy flows—lighting, electricity, heat, and coolth—that can be gleaned from solar energy by BITCoPT. The relative values of these different flows must be grounded in reasonable goals for a given context [30].

Because well-distributed lighting with good color rendering is difficult to reproduce in the built environment, effective daylighting is a priority in a high-performance building. Diffuse sunlight is multi-directional, exhibits good color rendering, and has good luminous efficacy (relative to common tube fluorescents, although LED lamps are targeted to surpass [31,32]). Diffuse sunlight is easier to apply as daylighting than direct sunlight, which is typically strong and narrowly directional, causing overheating and glare through high contrasts and distracting reflections.

Of the resources into which direct irradiance can be transformed, electricity is more valuable than thermal energy, as it is easy to transduce into other forms of work, and its exergy content is not directly subject to the Carnot efficiency. DC electricity is objectively more efficient to use than AC power in many commercial building contexts, as most modern electrical equipment is DC-native, and DC-DC conversion efficiency has reached parity with AC-DC rectification. Although DC distribution is not yet common, standards are mature and gaining acceptance for integration of multiple sources, storage mechanisms, and use devices into sub-building scale microgrids [12].

Thermal energy stored as a heat transfer fluid (HTF) at high temperatures (here defined as over 60 °C, in the context of building systems) can be applied to drive processes such as adsorption chilling, so it can both do work and be applied as heat, in sequence. The higher the temperature developed in the working fluid (relative to an available thermal sink such as the atmosphere or earth), the greater the exergy content, if losses incurred in storage and transportation are managed.

In this study, cooling power is more valuable than heating power for two reasons: More cooling is typically required in medium-sized office buildings, and the coefficient of performance (COP) of a reversible heat pump acting as a chiller is lower than that of the same pump in heating mode.

1.7. Exergy-Efficient Solar Collection Aligned with Façade Criteria

Successful on-site energy strategies will internalize a large fraction of the solar exergy available to a building by integrating with the multiple objectives of a successful envelope—objectives such as thermal regulation, daylighting, privacy, and design identity. The method proposed here for gleaning maximum utility from solar energy is represented by the thermal/energy cascade (Figure 2), and, to functionalize it within the Q-MEF framework, a model is incorporated of BITCoPT, which has previously undergone development [33], simulation [34], and prototype characterization [2,3] (Figure 3).

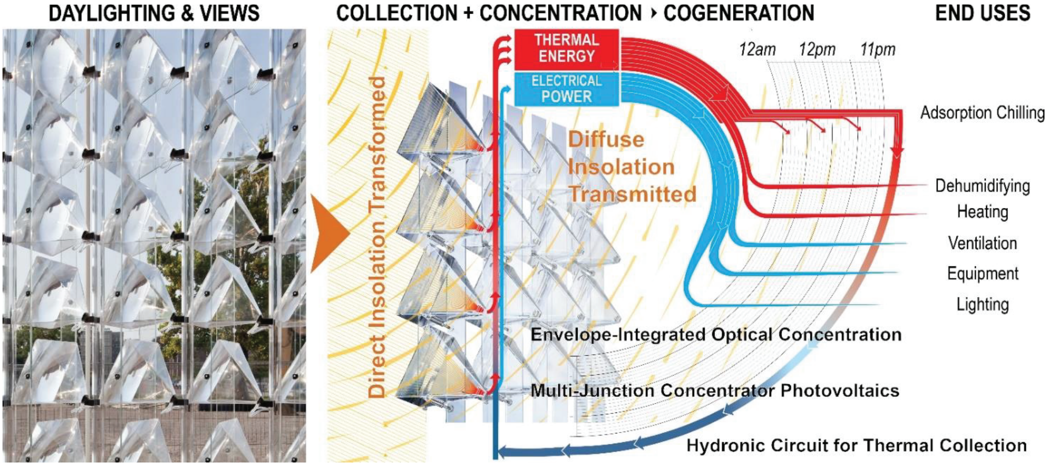

Figure 3. Multifunctional envelope-integrated solar collector: BITCoPT. Model of BITCoPT incorporated into Q-MEF modeling to represent spatially simultaneous daylighting and cogeneration from glazed envelope areas.

1.8. Comparison to Alternative Building Energy Schema

Existing schema cross over in purpose and methods with Q-MEF. Although whole-building polygeneration is typically considered component by component, as evidenced by review work on net-zero strategies [35], the impact of intersectional modeling is recognized [36]. Notably, high-performing built works achieve performance through combined strategies such as occupant-driven energy savings and multi-functional envelope structures. The Bullitt Center's canopy exemplifies this, reducing gains on the vertical envelope while increasing functional area for traditional photovoltaics [37]. Buildings such as Power Plants, mentioned earlier, emphasize the efficiency gains and building demand-matched resources from on-site cogeneration [28]. Exergy analysis provides a rubric for identifying appropriate quality matches between resources and demands [38] and for valuing both warming and cooling storage mechanisms according to temperature differences against an ambient state [39]. The Low Exergy (or LowEx) design emphasizes the application of thermal resources to the small-potential thermal demands of the built environment (heating, cooling, humidity control), the efficiency of heat pumps at maintaining small, useful temperature differences, and sequencing heat pumps to obtain larger temperature lifts [40,41]. LowEx has been extended to district scales [42]. Thermally Active Building Systems (TABS) emphasize the utility of hydronic thermal redistribution, activating thermal mass within the occupied regions of a building, and the efficiency benefits of transferring heat across the large surface areas that comprise indoor built spaces [43,44]. A Passive House is specific regarding the reduction of thermal loads, which can limit solar harvesting opportunities, although work is ongoing to integrate the strategy with on-site generation [45]. These frameworks can be employed to design systems that maximize wise use of available energy resources, but they do not explicitly tackle the provision of desirable lighting conditions in the built environment.

More holistically, Integrated Design emphasizes the consideration of an architectural design as a dynamic totality that shifts between states in a knowable fashion. Attention is paid to the thermal properties (particularly diffusivity) of a building design at the material, construction, and space scales [46,47]. Bioenergetic modeling emphasizes the pathways of potential, flow, and transformation for a broad category of resources, distributed sensing and response, and dynamic systems at the boundary between built and natural environments [48]. Furthermore, thermo-economic analysis is ongoing to ascertain the value of exergetic efficiency and on-site coupled generation and energy storage [49–53], and novel interpretive tools are developed towards these ends [54]. An intention of developing the Q-MEF framework is to leverage the insights of these other strategies to provide for a wide reach of building service demands, including quality lighting.

1.9. Research Objective: Modeling Q-MEF Building Energy Behavior

Overlapping with these complementary schemas, Q-MEF incorporates similar concepts. Q-MEF's combination of daylighting-primary operation, distributed high temperature buffering and active chilling, and distributed active thermal mass is potentially novel. Hence, this present work investigates Q-MEF's capacity to more fully leverage building-incident solar energy—and contribute to net-zero and energy-positive design—through integrating BITCoPT with thermal management at multiple temperature ranges and controlled redistribution.

As a platform for this investigation, a representative medium-scale office building with Q-MEF-aligned systems was modeled and tested in diverse climates, by first generating a pair of baseline (BL) building energy models with both moderate and high window-wall ratios (representing a desirable condition in commercial architecture), and then revising the high-ratio configuration to represent a full Q-MEF implementation with experimentally validated transparent active solar façade energy collectors, distributed thermally driven chillers, sequential thermal redistribution, and thermal storage at three temperature ranges. A fourth building energy model was also generated and tested, wherein the geometry of the building was modified to harvest additional solar energy. The Energy Use Intensity (EUI), peak demands, thermal load profiles, and economic benefits (based on energy consumption) that resulted from this matrix of full-building-scale simulations were compared, and salient behaviors were highlighted.

2. Methods

To evaluate the effects of Q-MEF on a building's energy flows and consumption, a model was constructed by combining (through post-processing) precursor building energy models of a medium-scale commercial office building (generated in the EnergyPlus environment) with an analytical model of an active façade system (BITCoPT). In addition to these two primary precursors, the Q-MEF model includes separate functions representing: hydronic thermal storage and redistribution, thermally driven chillers, electrically driven auxiliary heat pumps, a deep-mullion curtain wall cavity, fan-powered air volume exchanges in that cavity, and reactive (not predictive) controls. The models and functions were integrated through post-processing in a time-step fashion. The block diagram of the Q-MEF model is presented in Figure 4, and is referred to subsequently.

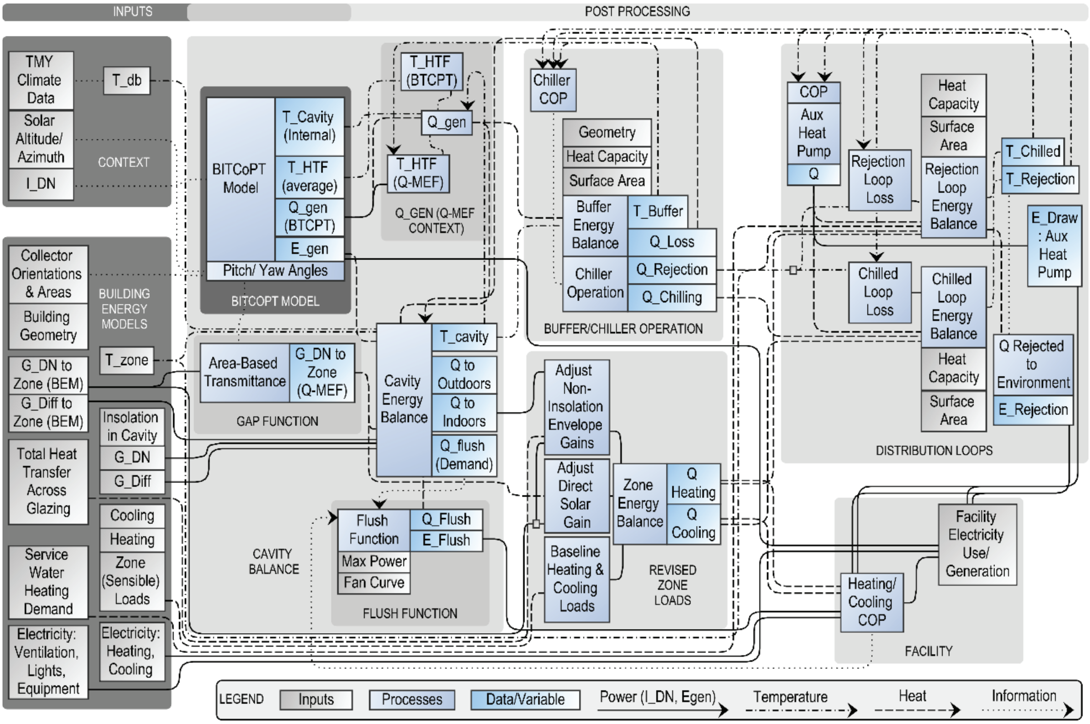

Figure 4. Q-MEF model block diagram, showing interfaces between precursor models and additional functions.

The model was configured in four ways, with two baseline options (low and high glazing ratios) and two options including Q-MEF components, which were both highly glazed, but with either normal (vertical) or outward-tilted fenestration. Three climates were analyzed, for twelve total model configurations (Figure 5).

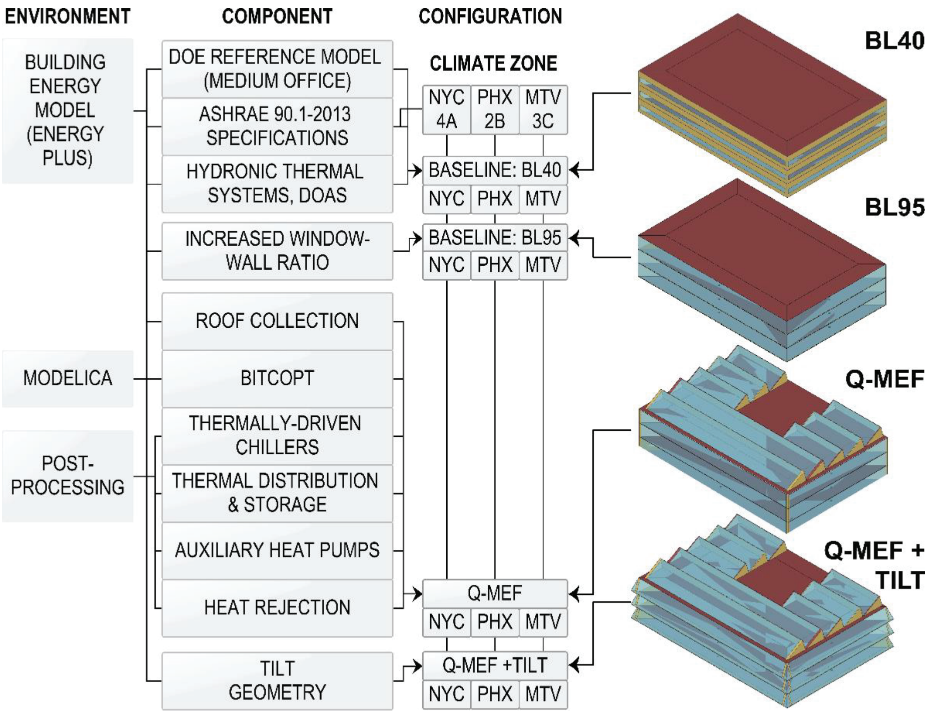

Figure 5. Building configurations and components from modeling environments.

2.1. Systems for Thermal Energy Collection, Redistribution and Use

In the Q-MEF rubric, solar energy on a building's glazed envelope areas is either transmitted as daylight, or concentrated and converted to electricity, or collected as thermal energy, where it is then passed through subsystems, applied to do work (such as chilling), and released as space or water heating, or directly out to climatic sinks. The modeled HVAC strategy (shared between all four configurations) is based on a four-pipe distribution that services all the building's conditioned zones and envelope collection areas (Figure 6). A chilled distribution loop is maintained at sub-ambient temperatures. A rejection-stage (heating) loop was maintained (through system control algorithms) at super-ambient or near-ambient temperatures, depending on the average demands for heating or cooling which varied seasonally.

Two parallel heat pump systems operate between the loops. In the Q-MEF configurations, small-capacity (<10 kW) adsorption chillers are distributed in the region of the building's envelope and driven by collected solar thermal energy, which is stored adjacently in small buffer tanks. Additionally, in all four configurations, electric water–water heat pumps act in parallel between the two loops.

In both the baseline and Q-MEF configurations, heating and cooling in a zone was modeled as transferring energy through baseboard units or chilled beams, from the rejection-range loop or to the chilled loop, respectively.

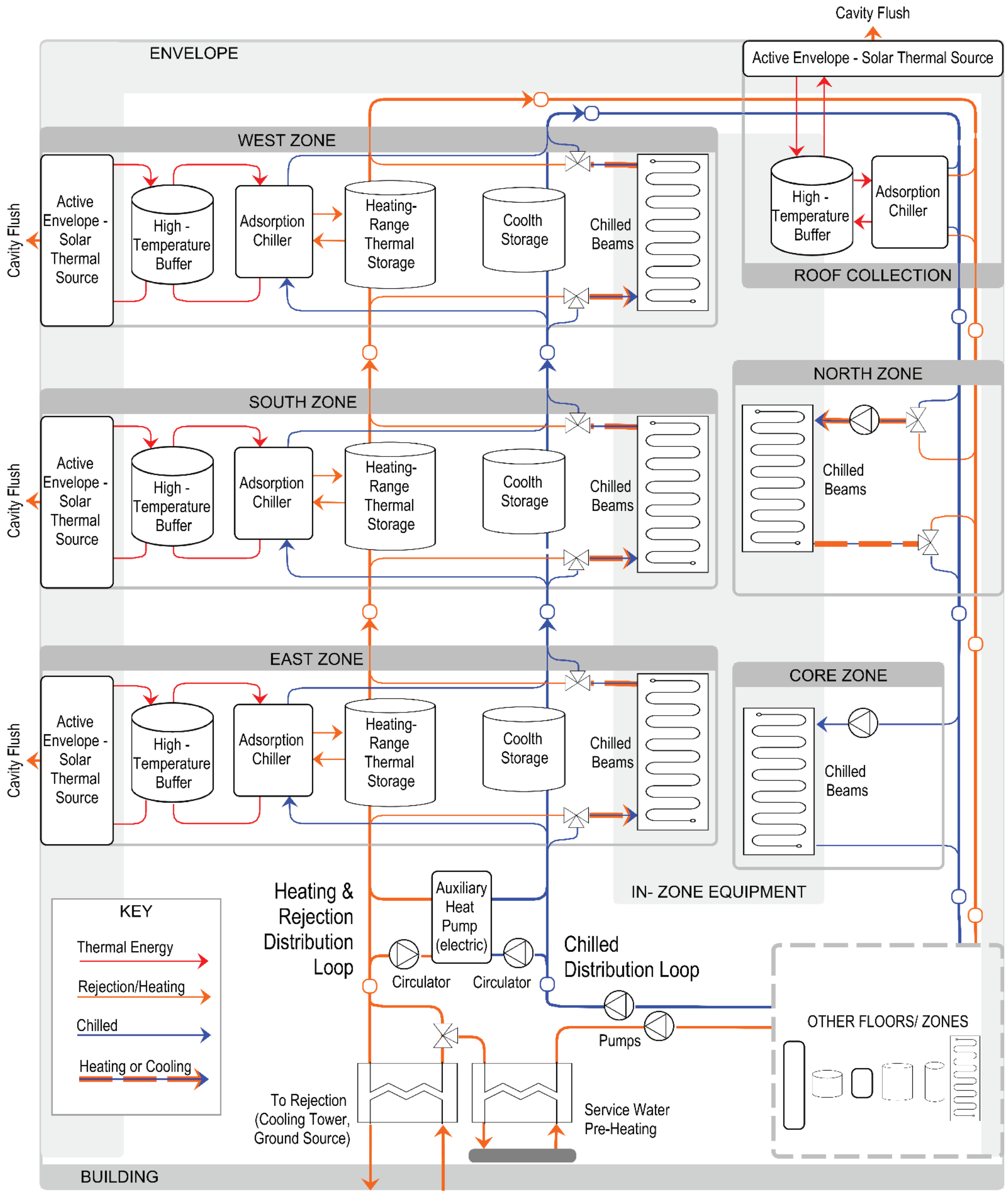

Figure 6. Plumbing schematic showing chilled and rejection-range distribution. Storage or distribution applied at three temperature ranges. Distributed adsorption chillers and auxiliary chiller operate in parallel between heating/rejection loop and chilled loop to maintain operating temperatures.

In the Q-MEF model configurations, thermal energy collected by BITCoPT was both used to drive adsorption chilling, and as heat. The glazed areas of the precursor BEMs were defined as BITCoPT collectors [34]. In post-processing, each collector fed a thermal buffer tank, which in turn was plumbed to a chiller ("Buffer/Chiller Operation" block in Figure 4). When a buffer's temperature (T_{buffer}) rose high enough to drive the connected chiller at a reasonable COP (over 0.5, requiring $T_{buffer} \geq 60$ °C, depending on rejection loop temperature), the chiller engaged, pumping heat from the chilled loop to the rejection loop. If the chilled loop became too warm, or the rejection loop cooled off too much, auxiliary heat pumps engaged, pumping heat in parallel to the thermally driven chillers.

Pre-heating for service hot water demands and the DOAS air intake were modeled to occur through water–water heat exchangers, subtracting energy from the rejection-range loop balance according to the difference between the supply temperature reported in the BEM and the loop temperature, less a 2.0 °C approach (Figure 6). The quantity of pre-heating was subtracted from boiler usage of the precursor BEM on a time step basis.

By modeling envelope-integrated solar thermal collection with distributed thermal systems and circulating thermal mass, it was possible to represent the application of thermal energy both as a driving force (for adsorption chillers, at high temperatures) and as useful heat (for zone demands and pre-heating), taking advantage of both the exergy and energy value of the collected energy.

2.2. Inputs to Q-MEF Model

Inputs to the overall Q-MEF analysis are described in this section, including precursor models (building energy model baselines, the BITCoPT model, and daylighting method) and boundary conditions (climates).

2.2.1. Climates Considered

The Q-MEF model was analyzed in three climates, exploring a range of system response patterns (Table 1, where $T_{db,outd}$ is outdoor dry bulb temperature). New York City (NYC, LaGuardia Airport TMY3 data) is a fluctuating climate: continental and seasonally humid, with varying weather and strong seasonal swings. Although the city is characteristically dense, and sites are typically shaded by adjacent structures, because this study parametrized climate context, not site, no external shading was defined in NYC or elsewhere. Phoenix (PHX) is an arid subtropical desert with a strong solar resource, high mean temperatures, and large diurnal swings. Mountain View (MTV) is in a semi-arid Mediterranean climate with mild temperatures and a significant solar resource.

Table 1. Climates used for analysis.

Location	**Climate Description (ASHRAE Zone)**	**Degree Days**			$T_{db,outd(99\%)}$ $T_{db,outd(1\%)}$
			Base 10 °C	**Base 18.3 °C**	
New York City (NYC)	Humid Subtropical/ Continental (4A)	HDD:	2118	672	31.8 °C
		CDD:	962	2557	−8.2 °C
Phoenix (PHX)	Subtropical Desert (2B)	HDD:	5067	2532	42.3 °C
		CDD:	17	523	5.2 °C
Mountain View (MTV)	Warm—summer Mediterranean (3C)	HDD:	2177	267	28.7 °C
		CDD:	64	1196	3.7 °C

2.2.2. Building Energy Models as Baselines

Four building energy models were developed (using the Open Studio [55] interface for EnergyPlus [56]), and used in two ways: directly, as two baseline configurations; and as precursors for two Q-MEF configurations. Each energy model, whether it was used directly as a baseline or as a precursor to the Q-MEF model, was configured for three distinct climates (Table 1) according to ASHRAE 90.1 (2013) building standards, resulting in a set of twelve analyzed configurations. Configurations are summarized in Table 2.

Table 2. Model configuration parameters.

Model Configuration	**40% Glazed BL40**	**95% Glazed BL95**	**Q-MEF**	**Q-MEF + Tilt**
Climates Modeled	New York City, NY/Phoenix, AZ/Mountain View, CA			
Geometry	DOE Prototype: medium office	DOE Prototype: medium office	DOE Prototype: medium office + inclined clerestories	DOE Prototype: medium office + inclined clerestories tilted facades
Length (east–west)	49.9 m			
Width (north–south)	33.3 m			
Floors	3			
Floor to floor height	3.96 m			
Perimeter zones depth	4.57 m			
Total floor area	4980 m^2			
Envelope Specifications				
Wall U value (W/m^2-K)	0.204/0.251/0.223	0.204/0.251/0.223	0.429	0.429
Roof U value (W/m^2-K)	0.223	0.223	0.223	0.223
Façade glazing ratio	40%	95%	95%	95%
BITCOPT integrated	NO	NO	YES	YES
Glazing System	to ASHRAE 90.1-2013	to ASHRAE 90.1-2013	deep-mullion with internal IGU	deep-mullion with internal IGU
T_{vis}	0.13/0.13/0.13	0.13/0.13/0.13	0.812	0.812
SHGC	0.40/0.25/0.25	0.40/0.25/0.25	0.764	0.764
U-factor (W/m^2-K)	4.6/5.2/4.8	4.6/5.2/4.8	2.72	2.72
Mechanical Systems	to ASHRAE 90.1-2013 with hydronic thermal distribution	to ASHRAE 90.1-2013 with hydronic thermal distribution	Q-MEF specified distributed systems	Q-MEF specified distributed systems
Plant(s)	Heating boiler, SHW boiler, electric chiller	Heating boiler, SHW boiler, electric chiller	Envelope solar collection, adsorption chillers, auxiliary heat pumps + boiler	Envelope solar collection, adsorption chillers, auxiliary heat pumps + boiler
System topology	central plants, zone unit loops in parallel	central plants, zone unit loops in parallel	Primary heating and cooling distribution/storage loops; secondary loops for plants, zones	Primary heating and cooling distribution/storage loops; secondary loops for plants, zones
Zone transfer units	Chilled beams, hydronic baseboard heating			
Heat rejection	air-side rejection from chiller	air-side rejection from chiller	air-side rejection from primary heating loop	air-side rejection from primary heating loop
Ventilation	Dedicated Outdoor Air System (DOAS)			
Lighting, Equipment	up to 8 W/m^2, up to 10 W/m^2, scheduled			
Daylighting controls	Stepped dimming with centered zone sensor			

The first baseline configuration (BL40) was a building energy model with no post-processing, based on the United States Department of Energy's (DOE) Medium Office Commercial Reference, with ASHRAE 90.1 (2013) specifications [57]. Default operation and occupancy schedules were used, including 5-day work weeks throughout the year, with reduced occupancy and thermostat setbacks outside working hours. The window-wall ratio was 40%. BL40′s HVAC systems were assigned per ASHRAE 189.1: hydronic thermal distribution, with zoned chilled beams, baseboard heating, and DOAS. These updates slightly reduced energy use, relative to the DOE reference.

Representing architectural trends towards highly glazed facades, the second baseline configuration (BL95) had a 95% window–wall ratio. The glazing specifications and systems behaviors were held constant, though systems were re-sized (through the auto-sizing algorithms in EnergyPlus). BL95 was the precursor to the Q-MEF configuration.

For the precursor BEM to the Q-MEF + Tilt configuration, the morphology of the Q-MEF BEM was revised to increase the solar gain on the building. At each floor, facades were swung upward at 20° (see Figure 5). The chosen angle maximized acquirable irradiance by maximizing solar flux through the exterior glazing on a per-area basis, while limiting the shading of a floor by the floor above.

2.2.3. BITCoPT Envelope Cavity Model

A model of the BITCoPT façade collector [34] was integrated into the Q-MEF model, contributing electrical generation, thermal collection, and direct solar gain reduction based on inputs of climate data and envelope orientation. A constant efficiency ($\eta_{conv,Egen} = 0.96$) was applied to the model's electrical output to represent the transformation of the collector's variable-voltage DC output to a useful form (constant-voltage DC for tying into to zone-level microgrids, or AC for tying into building distribution).

The thermal collection output was likewise modified to represent the heat transfer fluid inlet and envelope cavity temperatures in the Q-MEF model, which were distinct from those values in the BITCoPT simulation. Because the cavity temperatures (T_{cav}) in the Q-MEF model were held lower ($T_{outd,db} < T_{cav} < 38$ °C, less than 45 °C in the precursor model, to be realistic for mechanical control components), the Q-MEF-modeled array lost more heat, and thermal collection efficiency was lower than in the precursor model.

2.2.4. Daylighting Modeling Method

All baseline and precursor BEMs employed daylighting controls. Daylighting algorithms in EnergyPlus modified interior lighting schedules according to illuminance measured by virtual sensors. In a prior study [58], a threshold was noted in the room depth for which sufficient work-plane illuminance could be achieved when BITCoPT was introduced, but the perimeter zone depth here (4.57 m) was shallower than that threshold.

Precursor BEMs employed in this study did not include skylights, in keeping with the referenced DOE models. Daylighting from skylights would reduce the baseline lighting electrical loads in the core of the third floor (which comprises 20% of the building's floor area) but would likely contribute to net cooling loads due to solar gains. Although it is surmised that the zones' daylighting and thermal circumstances would improve with glazed roof expanses and installed BITCoPT, in this study the roof collection was treated as stand-alone equipment which did not interact (through lighting, or thermally) with the adjacent zones (in contrast to the vertical glazing expanses, for which light and thermal interactions were modeled).

2.3. Q-MEF Model Components and Functions

To represent the impacts of the Q-MEF strategy, components were incorporated with the collection of inputs through additional modeled functions.

2.3.1. Thermal Energy Storage Elements Model

Two types of thermal energy storage elements (TES) were modeled: high-range buffer tanks, and distribution loops. One buffer was defined for each solar collector. One cooling loop and one rejection-range loop were defined to service the building. Both TES types were defined to be well-mixed, rectangular water tanks with a fixed height and width. (Although higher-capacity thermal storage media such as PCMs might increase the overall performance of the Q-MEF system, water was modeled in this study for the sake of conceptual clarity.) As indicated in Figure 4 (“Buffer/Chiller . . . ” and “Distribution Loops” modules) the TES exchanged heat with the building’s systems (controlled) and with the interior environment (uncontrolled, due to losses through their insulated surface areas). Losses were modeled as the heat transferred across the TES boundary (tank walls) assuming insulation of 100 mm of polyisocyanurate foam, and negligible film coefficients on both interior and exterior surfaces, for an effective thermal resistance of $R_{TES,wall}$ = 0.4 W/m^2-K. The heat lost from the buffers transferred to the curtain wall cavity in which BITCoPT was installed. The heat lost from the distribution loops transferred to the occupied zones. Pumping power required to equalize the temperature between the storage elements in each loop was defined as equivalent to the power used by the equivalent circulation pumps in the contributing building energy model. Buffer TESs were each sized (through iterative testing) to maximize the yearly output of their paired chillers. The distribution loop capacities were sized to minimize whole-building electrical use (Table 3).

Table 3. Thermal capacities of modeled thermal energy storage (example: NYC climate).

TES Elements	**High-Temperature Buffers**				**Distribution Loops**	
	East or West (3X)	**South (3X)**	**Clerestory (First Row)**	**Clerestory (Balance)**	**Chilled**	**Rejection-Stage**
Thermal capacity (kWh/K)	0.9	1.4	4.9	2.1	450	583
Allowable Temperatures	Below 95 °C				10 to 18 °C	$T_{outd,db}$ to 35 °C

It can be noted that in an earlier (unreported) configuration of the Q-MEF model, a high-temperature-range distribution loop was considered as well, to simplify the work extraction from that source. However, the energy losses through the system insulation to indoor ambient temperatures were too high to justify, so a distributed configuration and 4-pipe distribution (reported here) were adopted, with paired buffers and adsorption chillers.

2.3.2. Deep-Mullion Cavity Energy Balance

The building envelopes for the baseline and precursor models were modeled natively in EnergyPlus. For the Q-MEF configurations, the deep-mullion curtain wall cavity (into which BITCoPT integrated) was represented by an energy balance in post-processing. Energy transfers across the glazing determined in the precursor BEMs were replaced by equivalent transfers as determined by this energy balance. The function did not account for variations of temperature or fluid movement within (or external to) the cavity control volume, or non-homogeneous masses. Overall conductivity values between the cavity and adjacent environments were constant, whereas these relationships were variable in the precursor BEM. More accurate heat transfers would be expected from a cavity model that included convection, surface emissivity, material diffusivity, and thermal bridging effects, but one-dimensional, steady state assumptions were deemed sufficient to contrast behavior between baseline and Q-MEF model configurations.

The energy balance comprised: the transmittance of direct and diffuse solar energy into and out from the cavity; the thermal and electrical energy generated by BITCoPT; the heat transferred (via conduction and convection) across glazing surfaces with the two adjoining environments; the heat extracted from the cavity by a flushing function; and the heat lost from high-range buffers (Figure 4: "Cavity balance" block). The balance was

$$\begin{aligned}\left(\sum m_{cav}c_{p,cav}\frac{dT}{dt}\right) \\ &= G_{DN,cav} + G_{DN,ind} + G_{Diff,cav} + G_{Diff,ind} - Q_{gen} - E_{gen} \\ &+Q_{cond,outd} + Q_{cond,ind} + Q_{cav,flush} + Q_{buffer,loss}\end{aligned} \tag{1}$$

where $m_{cav}c_p$ refers to the cavity's thermal mass (in kJ/K); G to transmitted solar power (in W); Q to thermal flow (in W); E_{gen} to electrical generation (in W); *DN* to direct irradiance; *Diff* to diffuse irradiance; *ind* and *outd* to the indoor and outdoor environments; *cond* to non-irradiation thermal transfer; *cav* to the cavity; and *flush* to the cavity flushing function (see Section 2.3.4).

2.3.3. BITCoPT Area-Based Gap Transmittance

The direct irradiance transmitted through the cavity to a building zone was modeled by multiplying the transmitted irradiance reported by the BEM by T_{gap}, a function that represents the collector's area-based transmittance of direct irradiance (the "Gap function" block in Figure 4). When the solar vector is near to normal with the surface of an envelope region that incorporates a collector, insolation passes through the gaps between BITCoPT modules. As the solar vector moves away from envelope-normal and the collector modules track around pitch and yaw axes, the gaps decrease, falling to zero width at an excursion angle determined by the collector's geometry. T_{gap} was defined as

$$T_{gap} = (1 - c_{vert})\left(\frac{\phi_{full} - \phi}{\phi_{full}}\right)(1 - c_{hz})\left(\frac{\lambda_{full} - \lambda}{\lambda_{full}}\right) \tag{2}$$

where c_{vert} and c_{hz} are vertical and horizontal components of the fractions of envelope area filled by BITCoPT lens modules; ϕ and λ are the rotations of the BITCoPT modules around their pitch and yaw axes (in radians); and ϕ_{full} and λ_{full} (radians) are the respective threshold angles where the gaps between lenses decreased to nil when observed parallel to the solar vector. The floor for T_{gap} was 0, when modules are rotated beyond the pitch and yaw thresholds, and no direct irradiance was transmitted. T_{gap} was applied to only direct insolation since, as modeled, BITCoPT does not intercept diffuse insolation.

2.3.4. Cavity Flushing Function

A cavity flushing function was implemented to simulate the removal of heat from the BITCoPT cavity, adjusting cavity temperature to complement the heating or cooling demands of the adjacent zone. The function simulated a fan moving air between the cavity and the environment (Figure 7). Flushing with outdoor air only was modeled, and the function remained decoupled from the building DOAS.

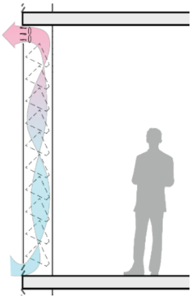

Figure 7. Modeled method of flushing excess heat from the cavity.

Flushing was implemented both in the precursor BEM (as a window:Airflow property in EnergyPlus, with a constant volumetric rate of 0.6 m^3/s-m and assumption of no fan power) and in post-processing. In post-processing, the maximum allowable cavity temperature was $T_{cav,lim,high}$ = 40 °C, but if zone cooling demand was significant, the target temperature was set to the outdoor (dry bulb) temperature). The post-processing flushing function was modeled as:

$$\begin{aligned} Q_{cav,flush(i)[n]} = K_{flush(i)} * C_{cav(i)} * \left(T_{cav[n-1]} - \left(T_{cav,target} + T_{cav,offset}\right)\right) \\ + K_{flush,IDN(i)}\left(I_{DN,cav(i)[n]}\right) \end{aligned} \tag{3}$$

where $Q_{cav,flush}$ was the resulting thermal flow (in W); K_{flush} was the (non-dimensional) proportional gain tuned for each zone; C_{cav} was the cavity thermal mass (in kJ/K); T_{cav} was the cavity temperature; $T_{cav,target}$ was set to either $T_{outd,db[n-1]}$ or T_{ind} depending on heating demand; and $T_{cav,offset}$ = 2 °C was used to establish a dead band, preventing the system from operating if heat removal would be inconsequential. $K_{flush,IDN}$ was a separate gain used to modify the flush rate according to zone's direct insolation at the current-time step. Fan power required to flush the cavity was determined assuming a constant pressure head (and therefore a constant power draw) multiplied by an hourly duty cycle. 100% of fan (electrical) power was designated to be taken up by the airflow (as increased temperature).

These flushing controls maintained the cavity temperature close to the chosen target, minimizing unwanted non-insolation thermal transfer from the envelope cavity to the building's interior, and contributing energy to under-heated zone conditions. Gains were tuned to optimize net generation at the building meter.

2.3.5. Thermally Driven Chillers Model

Adsorption chillers were modeled by fitting a solution surface to a manufacturer's COP data [59] relative to temperatures of buffers, chilled loop ($T_{chilled}$), and rejection loop (T_{rej}). Upper and lower limits on $COP_{chiller}$ were implemented to keep it between 0 and 0.56. The chillers were controlled to activate when the temperature of their paired buffer exceeded a threshold (T_{buffer} > 60 °C). Chillers drew energy according to the excess in the buffer over the threshold, with no capacity limit and no dependence of COP on the fractional capacity, representing multiple chillers ganged in parallel.

2.3.6. Auxiliary Heat Pumps and Heat Rejection Model

Water–water heat pumps were incorporated in the thermal control strategy to maintain the temperatures of the chilled and rejection-range distribution loops (see Figure 4, "Distribution Loops" block). If the chilled loop became too warm, energy was pumped from it to the rejection-range loop. Pumps are modeled steady state, at a COP varying with temperature lift, with functions sourced from the literature [41], capped at 16.0, with an 0.5 exergetic efficiency.

To prevent the rejection-range loop from getting too warm, heat removal from the loop to the outdoor environment was simulated by modeling a dry cooler, or fan-assisted water-to-air heat exchanger. The heat removal function, $Q_{rej,env}$ (in W) was:

$$Q_{rej,env[n]} = K_{rej} * C_{loop,rej.} * \left(T_{rej[n-1]} - T_{rej,target}\right) \tag{4}$$

where K_{rej} was the (non-dimensional) proportional gain; $C_{loop,rej}$ was the thermal mass of the rejection loop (in kJ/K); T_{rej} is the rejection distribution loop temperature; and $T_{rej,target}$ was the temperature set point. Like with the cavity flush fans, the fan power required to remove heat was determined with a constant power draw and an hourly duty cycle.

2.3.7. Loop Temperature Controls

The temperature of the chilled loop ($T_{chilled}$) was maintained by the activity of the adsorption chillers and auxiliary heat pump (when necessary), removing the energy gained from space cooling. If $T_{chilled}$ was ever driven too low ($T_{chilled} > 11.4$ °C), both the chillers and heat pumps were deactivated in the next time step. If the chilled loop temperature rose too high ($T_{chilled} > 17.0$ °C, representing over-loaded adsorption capacity) the auxiliary heat pump activated in the next time step.

The rejection-range loop temperature (T_{rej}) was controlled by the activity of the auxiliary boiler, the auxiliary heat pump, and the heat rejection system. A target temperature $T_{rej,target}$ was set, either to $T_{out,db}$ (if heating demands were expected to be low) or to $T_{rej} = 27$ °C. If T_{rej} dropped below $T_{rej,target}$, the auxiliary heat pump activated at the next time step. If the heat pump was unavailable (due to a low chilled loop temperature), the boiler activated. If T_{rej} was too high, the heat rejection system was called, proportional to the difference between T_{rej} and $T_{rej,target}$. An additional check of the current heat rejection COP ($COP_{rej} > 3.0$) prevented operation when the temperature difference was small, to favor night flushing of excess energy in the rejection loop. These controls together maintained loop temperatures within useful bounds, providing cooling and heating to the zones, and heat rejection capacity for the adsorption chillers.

2.3.8. Utility Cost Metrics

Costs for electrical use, capacity, and demand and gas use charges were initially computed within the BEM. Simulation outputs for the baseline configurations were used and scaled on an hourly basis for the Q-MEF configurations. Electricity costs were determined with monthly peak demand charges (USD 17.00/kW for the winter and USD 38.15/kW for the summer) and hourly energy charges (USD 0.125/kWh on-peak and USD 0.105/kWh off-peak), with surplus electricity generation net-metered at 100% of the current rate. The cost for natural gas was USD 1.30 per therm.

3. Results

Simulating a medium-scale commercial office building according to the Q-MEF framework demonstrated implications for lighting demands, cooling and heating loads, peak demands, net energy use, operational costs, and design considerations.

3.1. Daylighting Impact on Lighting Energy Use

Modeled lighting energy use in the high-glazing configurations improved between 13% and 17% over BL40 (Table 4). Daylighting controls were active in all configurations.

Table 4. Lighting loads under daylighting controls.

		Lighting Loads
		(kWh-E/m^2-yr)
NYC	BL40	23
	BL95	20
	Q-MEF	20
	Q-MEF + Tilt	20
PHX	BL40	23
	BL95	19
	Q-MEF	19
	Q-MEF + Tilt	20
MTV	BL40	23
	BL95	19
	Q-MEF	19
	Q-MEF + Tilt	20

Because daylighting controls were modeled in the precursor BEMs, the controls did not respond to the reduction of direct irradiance due to BITCoPT. Prior daylighting and glare analyses of BITCoPT [58] determined sufficient illuminance through the same depth as the perimeter zones modeled in this study (4.57 m), and as other equipment (such as blinds) was not modeled to control for over-lit moments, it was determined that the daylighting behavior would translate from the precursor BEMs to the Q-MEF configurations.

Daylighting potentially has a great effect on the energy use profile of a building, but because it is highly contingent on occupant behavior [60] representation in the simulation method employed here is difficult. It is possible that the daylighting energy benefits of BITCoPT are over-predicted, as cloudy moments would cause under-lighting. However, experimentation has suggested that lighting through the system increases with partial clouds, as there is more diffuse light to transmit [3]. It is also possible that benefits are under-predicted due to glare, as, during brighter moments in the baseline buildings, occupants who experience excessive brightness or glare might deploy blinds and electric lighting. More differentiation between the configurations might be noted if active technologies (blinds, BITCoPT) and occupant behavior were modeled dynamically with the sensors and dimmers.

3.2. Heating and Cooling Loads

The incorporation of Q-MEF systems resulted in various responses in heating and cooling loads across the climate types, demonstrating complex interdependencies between envelope loads and building demands (Table 5). Heating loads comprise the sum of modeled baseboard heating and DOAS preheating, while the cooling loads consist only of the modeled chilled beam responses.

Table 5. Yearly facility heating and cooling loads of twelve configurations (loads to be addressed by building thermal control systems).

		Heating Loads	**Cooling Loads**	**Heating/Cooling Ratio**
		(MWh-Q/yr)		
NYC	BL40	266	263	1:1
	BL95	364	346	1.1:1
	Q-MEF	388	274	1.4:1
	Q-MEF + Tilt	514	310	1.7:1
PHX	BL40	44	634	1:14.4
	BL95	78	959	1:12.3
	Q-MEF	167	729	1:4.4
	Q-MEF + Tilt	209	784	1:3.8
MTV	BL40	109	277	1:2.5
	BL95	174	357	1:2.1
	Q-MEF	316	261	1.2:1
	Q-MEF + Tilt	398	294	1.4:1

Due to the preponderance of cooling demands in the moderate MTV climate, the heating increases were low (though not negligible) relative to total demands. The NYC climate showed sensitivity to glazing area and type, as the BL95 and QMEF cases showed marked changes in the total loads. Installation of BITCoPT (the Q-MEF case vs. the BL95 case) resulted in reductions in cooling loads in all climates, although the Q-MEF + Tilt case did not decrease loads further.

The difference in loads occurred mainly in the south, east, and west perimeter zones, where decreased heat gain during direct solar conditions due to BITCoPT caused more frequent net-heating loads. In effect, the Q-MEF configurations resulted in more "skin-dominated" behavior of the building, where heating and cooling demands correlate to the difference between indoor and outdoor temperatures, as opposed to "core-dominated" behavior, where internal energy gains cause persistent cooling demands throughout the year (shown in the evolving Heating–Cooling ratio, in Table 5).

3.3. On-Site Thermal Collection and Application

In addition to driving chilling processes, thermal energy collected by BITCoPT was applied to building demands for zone heating and SHW preheating (Table 6). The final column in Table 6 is a sum of the zone heating loads, SHW preheating, collected thermal energy (negative sign), and DOAS heating (not described in a separate column).

Table 6. Summary of thermal collection and heating applications.

		Thermal Energy Collected	Zone Heating Loads	SHW Preheat	Heating Required (SHW, DOAS, Zone)
			(MWh-Q/yr)		
NYC	BL40	-	266	-	330
	BL95	-	364	-	449
	Q-MEF	149	388	9	430
	Q-MEF + Tilt	151	514	9	488
PHX	BL40	-	44	-	64
	BL95	-	78	-	95
	Q-MEF	308	167	8	241
	Q-MEF + Tilt	348	209	8	141
MTV	BL40	-	109	-	136
	BL95	-	174	-	219
	Q-MEF	234	316	9	431
	Q-MEF + Tilt	244	398	9	345

Via the rejection loop, collected thermal energy was applied to zone heating loads and SHW preheating (although with low demand in office-dominated buildings, the latter factor was small). Boiler (and fuel) usage was observed to increase in response to heating demands, despite net thermal collection in some cases exceeding net heating demands. This disparity indicates non-optimal behaviors in the thermal storage mechanisms, including mismatches between the times of collection and demand. This mismatch occurred largely over the annual cycle (Figure 8), indicating the usefulness of ground-source thermal storage, a function which was not implemented in the current Q-MEF model.

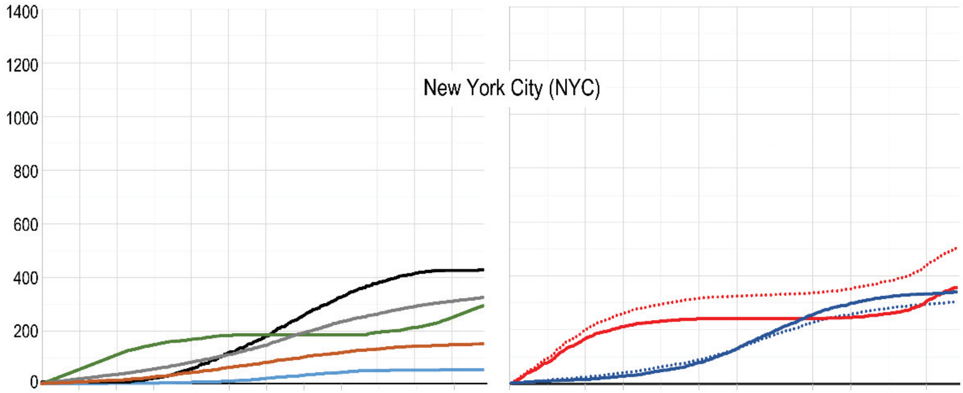

Figure 8. *Cont.*

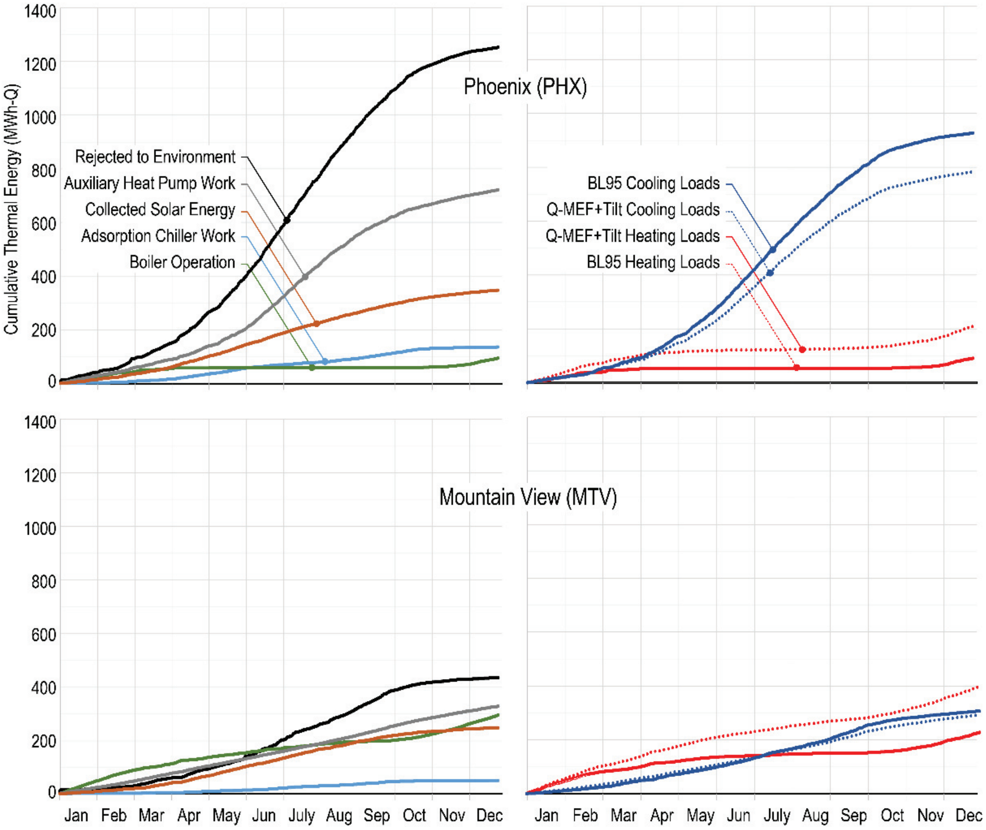

Figure 8. Thermal energy transfers, year-long cumulative summary.

3.4. Solar Cooling with Adsorption Chilling

Solar thermal energy, collected by BITCoPT, was applied to drive adsorption chillers (Table 7). This cooling was additive to any passive reductions in direct solar gains from the system, with the added benefit of dispatchability since the capacity was stored in the thermally massive, chilled distribution loop.

Cooling loads in the Q-MEF configurations were lower than in the BL95 configuration. The work done by adsorption chillers further reduced the cooling required from the auxiliary heat pump. The magnitude of collected thermal energy (Table 6) relative to loads suggests that more systems (such as night-flush controls and ground-source heat exchange) would be useful to perform more controlled storage and release of heat over both diurnal and annual cycles.

Cooling power produced from solar energy was not sufficient to provide 100% of modeled demands. Chilling processes capable of higher COPs might close that gap. This requires higher operating temperatures, and therefore higher solar concentration ratios, to boost exergy collection and offset losses from the thermal collection stage. A higher rejection temperature would also then be allowable, reducing the gap between that target and the target for zone heating (the two services being provided by the common loop). This tradeoff was not explored here, but it is noted that the required insulation of the hydronic system is complex, and at higher cell operating temperatures (roughly 100 °C and above) radiation from the cell becomes a significant thermal loss factor.

Table 7. Solar cooling systems summary, showing reduced cooling loads in Q-MEF configurations with adsorption chillers offsetting fraction of remainder.

		Net Cooling Loads	**Adsorption Chillers Work**
		(MWh-Q/yr)	**(MWh-Q/yr, % of net)**
NYC	BL40	263	-
	BL95	346	-
	Q-MEF	274	40 (15%)
	Q-MEF + Tilt	310	52 (17%)
PHX	BL40	634	-
	BL95	959	-
	Q-MEF	729	103 (14%)
	Q-MEF + Tilt	784	135 (17%)
MTV	BL40	277	-
	BL95	357	-
	Q-MEF	261	53 (20%)
	Q-MEF + Tilt	294	53 (18%)

3.5. Energy Use Profile Comparison

Broadly, Q-MEF simulations improved over the baselines for all observed metrics—net electrical demand, net energy demand, and peak electrical demand (defined as the maximum observed electrical demands between noon and 5 pm during the summer season). There were conditional exceptions: BL40 demonstrated the lowest peak demand of the NYC models, and the demand reductions of QMEF over BL40 were trivial. In both these cases, reductions in electrical EUI were still significant. Results are summarized in Table 8.

Table 8. Summary: net energy use intensities, by demand type (kWh-Q/m^2-yr, kWh-E/m^2-yr and kWh/m^2-yr), and peak electrical demand from grid (kW-E).

		Heating	**Heating & Cooling**	**Ventilation**	**Lights**	**Equipment**	**Power Generated**	**Net EUI, Electrical**	**Net EUI, Total Site**	**Peak Electrical Demand**
		kWh-Q/ m^2-yr	**kWh-E/m^2-yr**						**kWh/ m^2-yr**	**kW-E**
NYC	BL40	68	17	4	23	47	-	92	160	139
	BL95	92	29	3	20	47	-	99	191	156
	Q-MEF	86	26	3	20	47	−61	36	121	151
	Q-MEF + T	98	26	4	20	47	−71	27	124	147
PHX	BL40	13	47	9	23	47	-	127	139	189
	BL95	21	72	12	19	47	-	150	171	231
	Q-MEF	48	55	4	19	47	−106	20	68	157
	Q-MEF + T	28	54	5	20	47	−125	0	29	166
MTV	BL40	29	17	3	23	47	-	91	120	133
	BL95	46	26	4	19	47	-	96	142	164
	Q-MEF	86	31	4	19	47	−84	18	104	133
	Q-MEF + T	69	26	5	20	47	−99	−1	68	131

The Q-MEF + Tilt configuration demonstrated the highest generation and lowest total site EUI across climates. It is notable that electricity EUI reaches net zero in the Phoenix and Mountain View climates, although there remains significant consumption of gas for heating—higher than that of the baselines.

Maximum on-peak electrical draw (during summer-season afternoons) decreased from the BL95 to Q-MEF configurations by 3% (NYC), 32% (PHX), and 19% (MTV), while in the Phoenix climate, there was a decrease of 17% relative to BL40 as well. Peak demand reductions for the Q-MEF + Tilt configuration relative to BL95 were 6% (NYC), 28% (PHX), and 20% (MTV) (Table 9).

Table 9. Percent changes from baseline to Q-MEF configurations in electricity EUI, total EUI (electricity + gas), and peak electricity demand.

		Electricity EUI		**Total EUI**		**Peak Electricity Demand**	
		vs. BL40	**vs. BL95**	**vs. BL40**	**vs. BL95**	**vs. BL40**	**vs. BL95**
NYC	Q-MEF	−61%	−64%	−24%	−37%	9%	−3%
	Q-MEF + Tilt	−71%	−73%	−23%	−35%	6%	−6%
PHX	Q-MEF	−84%	−87%	−51%	−60%	−17%	−32%
	Q-MEF + Tilt	−100%	−100%	−79%	−83%	−12%	−28%
MTV	Q-MEF	−80%	−81%	−13%	−27%	0%	−19%
	Q-MEF + Tilt	−101%	−101%	−43%	−52%	−2%	−20%

Although it is significant that Q-MEF + Tilt demonstrated net zero electrical use, benefits were incremental (or negative) over the straight Q-MEF configuration, suggesting further analysis comparing the marginal utility of the energy benefits with the marginal costs of increasing the complexity of the building's design. It's notable that in the Phoenix condition, the Q-MEF + Tilt configuration showed higher peak demand than the straight Q-MEF configuration, differing from the other two climates. This is due to an attenuation of the cavity flush function from the combination of elevated outdoor temperatures and the increased available insolation.

3.6. Utility Cost Analysis

Annual energy costs were calculated for all configurations according to rates for electricity demand (kW), supply (kWh) and natural gas supply (therms or kWh) (Figure 9, Figure 10, Table 10). Q-MEF configurations reduced total use costs, while demand costs were generally lower than costs in BL95, and similar to costs in BL40.

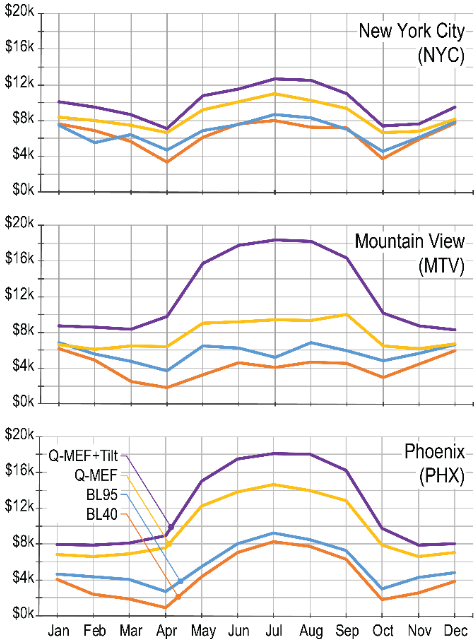

Figure 9. Monthly utility costs, summed (electrical energy, electrical demand, gas).

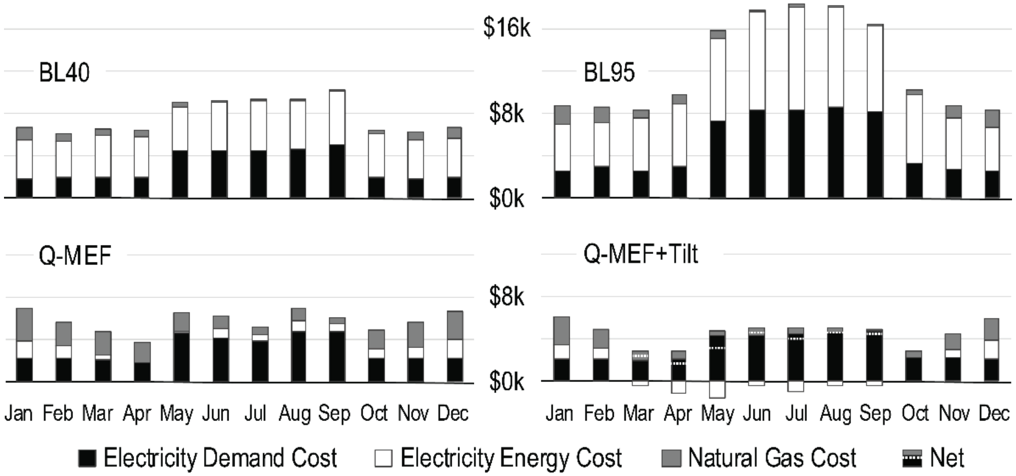

Figure 10. Monthly utility costs breakdown (Mountain View shown) showing net-meter benefits in the summer for Q-MEF + Tilt configuration.

Table 10. Utility annual cost summary.

		Demand Charges (USD)	Energy Charges (USD)	Natural Gas Charge (USD)	Total Utility Cost (USD)	Savings over BL40 (USD)	Savings over BL95 (USD)
NYC	BL40	37,000	50,000	15,000	102,000		
	BL95	43,000	55,000	20,000	119,000		
	Q-MEF	39,000	20,000	22,000	81,000	21,000 (21%)	38,000 (32%)
	Q-MEF + Tilt	40,000	15,000	22,000	77,000	25,000 (25%)	42,000 (35%)
PHX	BL40	49,000	66,000	2000	117,000		
	BL95	60,000	79,000	4000	143,000		
	Q-MEF	43,000	12,000	11,000	66,000	51,000 (44%)	77,000 (54%)
	Q-MEF + Tilt	44,000	2000	5000	51,000	66,000 (56%)	92,000 (64%)
MTV	BL40	37,000	49,000	6000	92,000		
	BL95	60,000	79,000	10,000	149,000		
	Q-MEF	37,000	11,000	22,000	69,000	23,000 (25%)	80,000 (42%)
	Q-MEF + Tilt	37,000	0	13,000	50,000	42,000 (46%)	99,000 (66%)

Observed in Table 8, Q-MEF configurations showed increased natural gas consumption, but due to lower electricity use, the total EUI was reduced in all Q-MEF cases, relative to BL40 and BL95. The analysis of costs demonstrates that (due to the low cost of natural gas compared to electricity) Q-MEF configurations showed annual reductions (Table 10).

Relative to the highly glazed baseline (BL95), peak electrical draw was reduced for each Q-MEF configuration, resulting in lower demand charges. Compared to BL40, the demand charge for Phoenix was reduced, but New York City and Mountain View had similar demand charges. On-site electrical storage was not included in this study, though if employed, it would be expected to further reduce peak demand in some months.

It is a natural goal of techno-economic analysis to reveal the cost/benefit impacts of the proposition. To determine the financial costs and benefits of Q-MEF, which is intended to address a broad range of architectural criteria, the savings in utility costs would be weighed along with the expected changes in lease rates due to changes in the thermal comfort and desirability of occupied spaces, and the installation and maintenance costs for Q-MEF systems. These costs would be considered relative to the costs of the baseline configuration's mechanical systems, or other common systems such as Variable Air Volume

HVAC, which incurs additional effects on a building project's value, such as reduced inhabitable room height due to the depth of duct work. The overall cost analysis of Q-MEF is highly contextual, due to the interaction of these factors and additional localized factors, such as capitalization rates expected on monies obtained to finance a project, which is an in-part function of a perceived risk. A detailed cost analysis is therefore usefully done at the scale of individual projects, or for broader applicability, by parameterizing these factors and undertaking the resulting matrix of sensitivity analyses. That breadth of analysis is outside the bounds of this study, which, for the sake of its own broader applicability, considered generalized circumstances. The present results, however, are a precursor to such a technoeconomic analysis, which merits further investigation.

4. Discussion

The modeled application of the specific systems described in this study according to the Q-MEF strategy resulted, in simulation, in significant reductions in energy use in the three modeled climates. On-site net-zero electricity was demonstrated in two of the climates—a significant result for buildings in the modeled size class. The results further suggest that additional modifications might show additional energy-use benefits: the baseline configurations were designed according to current minimum efficiency codes but did not incorporate the full gamut of currently available high-performance building strategies, such as DOAS enthalpy recovery (important in high-humidity climates such as New York) or ground-source heat exchange (particularly useful in climates with steady cycles such as Phoenix). Pursuing the current industrial interest in full electrification might also reveal further reductions, but as the modeling process dictates systems similarity between proposed and baseline models (which employ gas heating), these impacts were not represented. The application of these and other strategies would decrease the baselines' EUI, and therefore the EUI of the Q-MEF implementations as well.

Not all high-performance design strategies are synergistic with Q-MEF. External shading devices, for example, are a passive-design strategy to reduce fenestration gains. Q-MEF attempts to internalize these gains, which increases cooling loads, particularly over the BL40 baseline, but overall reduces both site energy use (all climates) and peak demands (in Phoenix, Table 8). Although counter-intuitive from the passive design perspective, these results suggest the benefits of engaging the solar resource.

A primary benefit to coolth storage systems is peak demand reduction, which commercial systems bank on for their value proposition [16]. The demand reductions demonstrated in this study, though significant, may not fully realize the benefits of this storage. The gap may be due to the simplified controls in the Q-MEF model, which were chosen in part for compatibility with the post-processing modeling method. Optimizing controls has been shown to benefit thermal storage applications [61] and might improve the utilization of the modeled storage.

A general shift from cooling loads to heating loads was observed with Q-MEF vs. baseline configurations (Table 5), which is in keeping with the Q-MEF concept of utilizing available solar resources, rather than mitigating and compensating for them. In the Mountain View climate, the cooling-dominated baselines were flipped to more heating operation. This flexibility around the balanced point suggests that introducing ground-source heat exchange, which benefits from that neutrality, might complement the Q-MEF strategy. Ground-sourcing would be worth investigating in the New York climate as well, which shifted from balanced to heating-dominated, as such heat pump-enabled strategies are intrinsically more effective at heating than cooling. Ground-source systems likely could not "keep up" with the required quantity of heat rejection in the more extreme Phoenix climate, suggesting other strategies might be useful, such as radiative night-sky sinking, which has recently advanced through material investigations [62].

In this study, the thermal collection efficiency of BITCoPT averaged lower than in precedent studies. This stems from conflicting demands on the envelope cavity: sensitivity analysis performed through multiple simulation runs showed that allowing elevated cavity temperatures reduced transport losses in BITCoPT, but increased perimeter zone cooling demands and overall net energy use. This trade-off reinforces how a building with Q-MEF is a coupled system of components that experience unique forcing functions. Optimizing overall objectives in such a system requires subordinating the peak performance of specific sub-systems.

5. Conclusions

To test the integration of technologies through an architectural, whole-system approach to design, the production of benefits from on-site solar resources was explored through simulations with a parametric group of building energy models. The models were assembled from precursors: a set of building energy models, a model of an active envelope technology, and representations of adsorption chillers, hydronic thermal distribution and storage elements, water-to-water heat pumps, and ancillary systems. The overall strategy was described as a quality-matched energy flow (Q-MEF) network. Simulations of a 5000 m^2, three-floor office building demonstrated reductions in electrical use over 70% from the baseline in a humid-continental climate (New York City), and on-site net zero electricity in arid subtropical (Phoenix) and semi-arid Mediterranean (Mountain View) climates. Peak purchased electrical demands decreased up to 6%, 32%, and 20% respectively. The magnitude of these results suggests the usefulness of deeply integrating the multifunctional envelope technology with the balance of a building's systems that process and distribute collected thermal energy. Demand for (purchased) electricity remained significant, indicating the potential for future investigation of on-site electrical storage, in addition to the modeled thermal storage. Cost outcomes were reported, with reductions (in summed energy and demand charges) of 35% in New York City, 64% in Phoenix, and 66% in Mountain View, relative to the highly glazed baseline model configurations. A shift was noted, from demand for cooling in the baseline configurations to demand for heating in the Q-MEF configurations. This shift indicates potential benefits from additional thermal storage technologies beyond those modeled in this study (such as ground-source heat exchange), and, overall, the possibility of energy-positive performance for this common class of buildings, in a range of climates.

Author Contributions: Conceptualization, N.N., J.O.V., M.J. and A.D.; Data curation, N.N., J.S.S., M.A.E. and K.P.; Formal analysis, N.N., J.S.S. and M.J.; Funding acquisition, N.N., J.O.V., M.J. and A.D.; Investigation, N.N., J.S.S., M.A.E. and K.P.; Methodology, N.N., K.P., J.O.V., M.J. and A.D.; Project administration, A.D.; Resources, N.N. and A.D.; Software, N.N., J.S.S., M.A.E. and K.P.; Supervision, A.D.; Validation, N.N., J.S.S., M.A.E. and K.P.; Visualization, N.N., M.A.E. and A.D.; Writing—original draft, N.N., M.A.E. and A.D.; Writing—review and editing, N.N., J.O.V., M.J. and A.D. All authors have read and agreed to the published version of the manuscript.

Funding: This research was funded by the U.S. Department of Energy, grant numbers DE-FG36-06GO86070 and 09EE0002285, the New York State Energy Research and Development Authority (NYSERDA), grant numbers A50417 and J50367, and the New York State Office of Science, Technology and Academic Research.

Institutional Review Board Statement: Not applicable.

Informed Consent Statement: Not applicable.

Data Availability Statement: Data avaialable upon request.

Acknowledgments: These findings are an expansion of work presented at the 16th Conference on Sustainable Development of Energy, Water, and Environment Systems (SDEWES) held (on-site and virtually) in Dubrovnik, Croatia, 10–15 October 2021. Material support was provided by SOM, LLC.

Conflicts of Interest: The authors declare no conflict of interest. The funders had no role in the design of the study; in the collection, analyses, or interpretation of data; in the writing of the manuscript, or in the decision to publish the results.

Nomenclature

Variables	
c_p	specific heat (kJ/kg-K)
C	heat capacity (kWh/K)
E	electricity (kW)
G	solar power (kW)
i	instance of zone or cavity balance
I	solar irradiance (W/m^2)
K	proportional gain constant
n	time step (hour)
Q	heat collected or transferred (kW)
R	thermal resistance (W/m^2-K)
T	temperature (°C) or transmittance (n.d.)
Greek letters	
λ	tracker pitch angle (radians)
ϕ	tracker yaw angle (radians)
Subscripts and Abbreviations	
AEC	architecture, engineering, and construction sector
AIF	active integrated facade
ASHRAE	American Society of Heating, Refrigeration, and Air-Conditioning Engineers
BEM	building energy model
BITCoPT	building envelope-integrated, transparent concentrating photovoltaic and thermal collector
BL	baseline (energy model)
BL40	baseline energy model with 40% window-wall ratio
BL95	baseline energy model with 95% window-wall ratio
buffer	high-range buffer
cav	envelope cassette cavity
chilled	chilled distribution loop
cond	conduction and convection (non-radiative)
conv	energy conversion
CDD	cooling degree days
COP	coefficient of performance
db	dry-bulb (temperature)
Diff	diffuse (insolation component)
DN	direct normal (insolation component)
DOAS	dedicated outdoor air system
DOE	United States Department of Energy
Egen	electrical generation
env	environment
EPB	energy-positive building
EUI	energy use intensity
flush	cavity flushing
full	threshold for BITCoPT module gap function
gap	spacing between BITCoPT modules
gen	generated (by envelope-integrated collector)
HDD	heating degree days
HVAC	heating, ventilation, and air conditioning system
hz	horizontal
IGU	insulated glazing unit
ind	indoor
lim	limit
kWh-E	Electricity energy unit
kWh-Q	Thermal energy unit
loop	pertaining to chilled or rejection-stage hydronic loops
loss	energy lost to ambient
MTV	Mountain View, California, USA (climate)

NZEB	net-zero energy building
NYC	New York City, New York, USA (climate)
offset	temperature offset
outd	outdoor
PHX	Phoenix, Arizona, USA (climate)
Q-MEF	quality-matched energy flow network; also a model configuration
Q-MEF + Tilt	model configuration adding solar-optimized façade geometry
rej	rejection-range (heating) loop
SHW	service hot water
target	target temperature
TES	thermal energy storage component
vert	vertical
vis	visible (transmittance)
wall	insulated wall of TES component

References

1. Dyson, A. Interdisciplinary Co-Development of Intelligent Building Envelopes with On-Site Power Generation. In Proceedings of the 91st ACSA International Conference Proceedings, Helsinki, Finland, 27–30 July 2003. Available online: https://www.acsa-arch.org/chapter/interdisciplinary-co-development-of-intelligent-building-envelopes-with-on-site-power-generation/ (accessed on 18 November 2020).
2. Novelli, N.; Phillips, K.; Shultz, J.; Derby, M.M.; Stark, P.R.H.; Craft, J.; Salvas, R.; Derby, S.; Jensen, M.K.; Dyson, A. Experimental Investigation of a Building Envelope-Integrated, Transparent Concentrating Photovoltaic and Thermal Collector. *Renew. Energy* **2021**, *176*, 617–634. [CrossRef]
3. Novelli, N.; Gordon, R.; Varfolomeev, I. Separating direct from diffuse: Observations of visible transmittance through a tracking photovoltaic envelope. In Proceedings of the Facade Tectonics Institute 2018 World Congress Proceedings, Los Angeles, CA, USA, 12–13 March 2018; Volume 2, pp. 355–364. Available online: https://www.facadetectonics.org/publications/collection/publications (accessed on 27 March 2018).
4. Lechner, N. *Heating, Cooling, Lighting: Sustainable Design Methods for Architects*, 3rd ed.; Wiley: Hoboken, NJ, USA, 2008.
5. Wong, I.L. A review of daylighting design and implementation in buildings. *Renew. Sustain. Energy Rev.* **2017**, *74*, 959–968. [CrossRef]
6. Salcido, J.C.; Raheem, A.A.; Issa, R.R. From simulation to monitoring: Evaluating the potential of mixed-mode ventilation (MMV) systems for integrating natural ventilation in office buildings through a comprehensive literature review. *Energy Build.* **2016**, *127*, 1008–1018. [CrossRef]
7. Kuhn, T.E.; Erban, C.; Heinrich, M.; Eisenlohr, J.; Ensslen, F.; Neuhaus, D.H. Review of technological design options for building integrated photovoltaics (BIPV). *Energy Build.* **2021**, *231*, 110381. [CrossRef]
8. Lamnatou, C.; Chemisana, D.; Mateus, R.; Almeida, M.; da Silva, S.M. Review and perspectives on Life Cycle Analysis of solar technologies with emphasis on building-integrated solar thermal systems. *Renew. Energy* **2015**, *75*, 833–846. [CrossRef]
9. Sharaf, O.Z.; Orhan, M.F. Concentrated photovoltaic thermal (CPVT) solar collector systems: Part II—Implemented systems, performance assessment, and future directions. *Renew. Sustain. Energy Rev.* **2015**, *50*, 1566–1633. [CrossRef]
10. Li, G.; Xuan, Q.; Akram, M.W.; Akhlaghi, Y.G.; Liu, H.; Shittu, S. Building integrated solar concentrating systems: A review. *Appl. Energy* **2020**, *260*, 114288. [CrossRef]
11. Probst, M.M.; Roecker, C. Towards an improved architectural quality of building integrated solar thermal systems (BIST). *Sol. Energy* **2007**, *81*, 1104–1116. [CrossRef]
12. Elsayed, A.T.; Mohamed, A.A.; Mohammed, O.A. DC microgrids and distribution systems: An overview. *Electr. Power Syst. Res.* **2015**, *119*, 407–417. [CrossRef]
13. Kim, M.K.; Leibundgut, H.; Choi, J.-H. Energy and exergy analyses of advanced decentralized ventilation system compared with centralized cooling and air ventilation systems in the hot and humid climate. *Energy Build.* **2014**, *79*, 212–222. [CrossRef]
14. Pang, H.; Lo, E.; Pong, B. DC Electrical Distribution Systems in Buildings. In Proceedings of the 2nd International Conference on Power Electronics Systems and Applications, Hong Kong, China, 2–14 November 2006; pp. 115–119. [CrossRef]
15. Mumma, S.A. Designing dedicated outdoor air systems. *ASHRAE J.* **2001**, *43*, 28.
16. Roth, K.; Dieckmann, J.; Zogg, R.; Brodrick, J. Chilled Beam Cooling. *ASHRAE J.* **2007**, *49*, 84–86.
17. Kintner-Meyer, M.C.; Subbarao, K.; Kumar, N.P.; Bandyopadhyay, G.K.; Finley, C.; Koritarov, V.S.; Molburg, J.C.; Wang, J.; Zhao, F.; Brackney, L.; et al. The Role of Energy Storage in Commercial Building A Preliminary Report. In *Pacific Northwest National Laboratory*; Pacific Northwest National Laboratory: Benton County, WA, USA, 2010. [CrossRef]
18. Pintaldi, S.; Perfumo, C.; Sethuvenkatraman, S.; White, S.; Rosengarten, G. A review of thermal energy storage technologies and control approaches for solar cooling. *Renew. Sustain. Energy Rev.* **2015**, *41*, 975–995. [CrossRef]
19. MacCracken, M.M. Thermal Energy Storage Myths. *ASHRAE J.* **2003**, *45*, 36–43. [CrossRef]
20. Dincer, I. On thermal energy storage systems and applications in buildings. *Energy Build.* **2002**, *34*, 377–388. [CrossRef]

21. Nassif, N.; Tesiero, R.C.; Singh, H. Impact of Ice Thermal Storage on Cooling Energy Cost for Commercial HVAC Systems. *ASHRAE Trans.* **2013**, *119*, 1–7.
22. Lizana, J.; Chacartegui, R.; Padura, A.B.; Valverde, J.M. Advances in thermal energy storage materials and their applications towards zero energy buildings: A critical review. *Appl. Energy* **2017**, *203*, 219–239. [CrossRef]
23. Christopher, S.; Parham, K.; Mosaffa, A.; Farid, M.; Ma, Z.; Thakur, A.K.; Xu, H.; Saidur, R. A critical review on phase change material energy storage systems with cascaded configurations. *J. Clean. Prod.* **2021**, *283*, 124653. [CrossRef]
24. Zhang, Z.; Ci, Z.; Zhang, T. Heat-Storage Performance Optimization for Packed Bed Using Cascaded PCMs Capsules. *Int. J. Thermophys.* **2021**, *42*, 1–2. [CrossRef]
25. Lizana, J.; Chacartegui, R.; Barrios-Padura, A.; Ortiz, C. Advanced low-carbon energy measures based on thermal energy storage in buildings: A review. *Renew. Sustain. Energy Rev.* **2018**, *82*, 3705–3749. [CrossRef]
26. Herrmann, U.; Kearney, D.W. Survey of Thermal Energy Storage for Parabolic Trough Power Plants. *J. Sol. Energy Eng.* **2002**, *124*, 145–152. [CrossRef]
27. Schweigler, C.; Hiebler, S.; Keil, C.; Köbel, H.; Kren, C.; Mehling, H. Low-Temperature Heat Storage for Solar Heating and Cooling Applications. *ASHRAE Trans.* **2007**, *113*, 89–96.
28. Hartkopf, V.; Archer, D.H.; Loftness, V. Building As Power Plant–BAPP/Invention Works Project at Carnegie Mellon University, Pittsburgh PA, USA. In Proceedings of the Fourth International Conference for Enhanced Building Operations, Paris, France, 18–19 October 2004. Available online: http://hdl.handle.net/1969.1/5033 (accessed on 2 May 2012).
29. Ferrara, M.; Coleman, J.; Meggers, F. Exploring potentialities of energy-connected buildings: Performance assessment of an innovative low-exergy design concept for a building heating supply system. *Energy Procedia* **2017**, *122*, 1075–1080. [CrossRef]
30. Coventry, J.; Lovegrove, K. Development of an approach to compare the 'value' of electrical and thermal output from a domestic PV/thermal system. *Sol. Energy* **2003**, *75*, 63–72. [CrossRef]
31. Littlefair, P.J. The luminous efficacy of daylight: A review. *Light. Res. Technol.* **1985**, *17*, 162–182. [CrossRef]
32. Pattison, P.M.; Hansen, M.; Tsao, J.Y. LED lighting efficacy: Status and directions. *Comptes Rendus. Phys.* **2018**, *19*, 134–145. [CrossRef]
33. Dyson, A.; Stark, P.R.H.; Jensen, M.K. Integrated Concentrating (IC) Solar Facade System. Department of Energy Peer Review. 2007. Available online: https://www1.eere.energy.gov/solar/review_meeting/pdfs/sys_9_dyson_rensselaer.pdf (accessed on 1 April 2020).
34. Novelli, N.; Shultz, J.; Dyson, A. Development of a modeling strategy for adaptive multifunctional solar energy building envelope systems. In Proceedings of the Symposium on Simulation for Architecture & Urban Design, Washington, DC, USA, 12–15 April 2015; pp. 35–42.
35. Cabeza, L.F.; Chàfer, M. Technological options and strategies towards zero energy buildings contributing to climate change mitigation: A systematic review. *Energy Build.* **2020**, *219*, 110009. [CrossRef]
36. Tronchin, L.; Manfren, M.; Nastasi, B. Energy efficiency, demand side management and energy storage technologies—A critical analysis of possible paths of integration in the built environment. *Renew. Sustain. Energy Rev.* **2018**, *95*, 341–353. [CrossRef]
37. Gilbride, M.; Loveland, J.; Burpee, H.; Kriegh, J.; Meek, C. Occupant-Behavior-Driven Energy Savings at the Bullitt Center in Seattle, Washington. *ACEEE Summer Study Energy Effic. Build.* **2016**, *15*, 8-1–8-15.
38. Torío, H.; Angelotti, A.; Schmidt, D. Exergy analysis of renewable energy-based climatisation systems for buildings: A critical view. *Energy Build.* **2009**, *41*, 248–271. [CrossRef]
39. Nishikawa, R.; Shukuya, M. Numerical analysis on the production of cool exergy by making use of heat capacity of building envelopes. In Proceedings of the Sixth International IBPSA Conference, Kyoto, Japan, 13–15 September 1999. Available online: http://www.inive.org/members_area/medias/pdf/Inive/IBPSA/UFSC691.pdf (accessed on 27 January 2016).
40. Hepbasli, A. Low exergy (LowEx) heating and cooling systems for sustainable buildings and societies. *Renew. Sustain. Energy Rev.* **2012**, *16*, 73–104. [CrossRef]
41. Meggers, F.; Ritter, V.; Goffin, P.; Baetschmann, M.; Leibundgut, H. Low exergy building systems implementation. *Energy* **2012**, *41*, 48–55. [CrossRef]
42. Dunkelberg, E.; Schneller, A.; Bachmann, M.; Kriegel, M. LowExTra-Feasibility of a Multi-Conductor District Heating System. *Energy Procedia* **2018**, *149*, 427–434. [CrossRef]
43. Lehmann, B.; Dorer, V.; Koschenz, M. Application range of thermally activated building systems tabs. *Energy Build.* **2007**, *39*, 593–598. [CrossRef]
44. Lydon, G.; Hofer, J.; Svetozarevic, B.; Nagy, Z.; Schlueter, A. Coupling energy systems with lightweight structures for a net plus energy building. *Appl. Energy* **2017**, *189*, 310–326. [CrossRef]
45. Azami, A.; Sevinç, H. The energy performance of building integrated photovoltaics (BIPV) by determination of optimal building envelope. *Build. Environ.* **2021**, *199*, 107856. [CrossRef]
46. Moe, K. *Integrated Design in Contemporary Architecture*; Princeton Architectural Press: New York, NY, USA, 2008.
47. Moe, K. *Convergence: An Architectural Agenda for Energy*; Routledge: Oxfordshire, UK, 2013.
48. Dyson, A.; Ngai, T.; Vollen, J. Characterizing the Problem: Bioenergetic Information Modeling. In *BIM in Academia*; Yale School of Architecture: New Haven, CT, USA, 2011.
49. Sayadi, S.; Tsatsaronis, G.; Morosuk, T. Dynamic exergetic assessment of heating and cooling systems in a complex building. *Energy Convers. Manag.* **2019**, *183*, 561–576. [CrossRef]

50. Buonomano, A.; Calise, F.; Palombo, A.; Vicidomini, M. Transient analysis, exergy and thermo-economic modelling of façade integrated photovoltaic/thermal solar collectors. *Renew. Energy* **2019**, *137*, 109–126. [CrossRef]
51. Baeten, B.; Rogiers, F.; Helsen, L. Reduction of heat pump induced peak electricity use and required generation capacity through thermal energy storage and demand response. *Appl. Energy* **2017**, *195*, 184–195. [CrossRef]
52. Gagnon, P.J.; Govindarajan, A.; Bird, L.A.; Barbose, G.; Darghouth, N.; Mills, A. *Solar + Storage Synergies for Managing Commercial-Customer Demand Charges*; NREL: Golden, CO, USA, 2017. [CrossRef]
53. Deo, A.; Mishra, G.; Tiwari, G. A thermal periodic theory and experimental validation of building integrated semi-transparent photovoltaic thermal (BiSPVT) system. *Sol. Energy* **2017**, *155*, 1021–1032. [CrossRef]
54. Abdelalim, A.; O'Brien, W.; Shi, Z. Data visualization and analysis of energy flow on a multi-zone building scale. *Autom. Constr.* **2017**, *84*, 258–273. [CrossRef]
55. NREL and US DOE. Open Studio 2.7. 2018. Available online: https://www.openstudio.net/ (accessed on 30 November 2018).
56. Crawley, D.B.; Lawrie, L.K.; Winkelmann, F.C.; Buhl, W.; Huang, Y.; Pedersen, C.O.; Strand, R.K.; Liesen, R.J.; Fisher, D.E.; Witte, M.J.; et al. EnergyPlus: Creating a new-generation building energy simulation program. *Energy Build.* **2001**, *33*, 319–331. [CrossRef]
57. US Energy Information Administration. Commercial Buildings Energy Consumption Survey (CBECS) Data. 2015. Available online: http://www.eia.gov/consumption/commercial/data/2012/#b6 (accessed on 18 July 2015).
58. Etman, M.A.; Novelli, N.; Shultz, J.; Phillips, K.; Andow, B.; Dyson, A. Daylighting effect of separating direct and diffuse insolation with facade-integrated, transparent solar collector. In Proceedings of the 31st International PLEA Conference, Bologna, Italy, 9–11 September 2015.
59. Daßler, I.; Mittelbach, W. Solar Cooling with Adsorption Chillers. *Energy Procedia* **2012**, *30*, 921–929. [CrossRef]
60. Reinhart, C.F. Lightswitch-2002: A model for manual and automated control of electric lighting and blinds. *Sol. Energy* **2004**, *77*, 15–28. [CrossRef]
61. Hajiah, A.; Krarti, M. Optimal controls of building storage systems using both ice storage and thermal mass—Part II: Parametric analysis. *Energy Convers. Manag.* **2012**, *64*, 509–515. [CrossRef]
62. Chen, J.; Lu, L. Development of radiative cooling and its integration with buildings: A comprehensive review. *Sol. Energy* **2020**, *212*, 125–151. [CrossRef]

sustainability

MDPI

Article

An Evaluation of the Petroleum Investment Environment in African Oil-Producing Countries Based on Combination Weighting and Uncertainty Measure Theory

Hujun He [1,2,*], Wei Li [1], Rui Xing [1] and Yichen Zhao [1]

[1] School of Earth Science and Resources, Chang'an University, Xi'an 710054, China; 2021127075@chd.edu.cn (W.L.); 2020127068@chd.edu.cn (R.X.); 2021127080@chd.edu.cn (Y.Z.)
[2] Key Laboratory of Western Mineral Resources and Geological Engineering, Ministry of Education, Xi'an 710054, China
* Correspondence: hsj2010@chd.edu.cn

Abstract: Recognizing that the evaluation of the overseas petroleum investment environment is affected by many uncertain factors and that there are problems with current evaluation methods, this paper proposes a mathematical evaluation model of an overseas oil resources investment environment, based on a combination of the weighting and uncertainty measure theory. Combining international investment environment theory with the characteristics of the petroleum industry, this paper establishes an evaluation index system for the overseas petroleum investment environment and the linear uncertainty measure function of each index. Using the subjective weight obtained using an analytic hierarchy process together with the objective weight obtained using the entropy weight method, the optimal weight of each evaluation index was obtained using minimum relative information entropy. A multi-index evaluation matrix of the top 12 oil-producing countries in Africa was calculated. Finally, the credible degree recognition criterion was used to judge the order and level of the oil investment environment. This model provides an effective method for the evaluation of the overseas petroleum investment environment. The results show that Nigeria and Angola have the best investment climate, followed by Algeria, Egypt, and Libya. In general, Africa is an important strategic partner of China and is rich in oil resources. Although Africa's oil industry is fraught with complex challenges and headwinds, challenges also present opportunities.

Keywords: Africa; petroleum investment; entropy weight; information entropy; uncertainty measure

Citation: He, H.; Li, W.; Xing, R.; Zhao, Y. An Evaluation of the Petroleum Investment Environment in African Oil-Producing Countries Based on Combination Weighting and Uncertainty Measure Theory. *Sustainability* **2022**, *14*, 5882. https://doi.org/10.3390/su14105882

Academic Editors: Oz Sahin and Edoardo Bertone

Received: 13 April 2022
Accepted: 11 May 2022
Published: 12 May 2022

1. Introduction

In recent years, as a result of the rapid development of China's domestic production and relatively slow oil exploration and development, China's domestic dependence on crude oil imports has been increasing. At the same time, as the United States develops its shale oil and gas industry, making the United States the world's largest energy exporter for a time, China's consumption has been increasing. Although China is the world's sixth largest oil producer, in 2018 it surpassed the United States as the world's largest oil importer. China's imports of crude oil increased year by year during the 13th five-year plan period, and its dependence on foreign oil also increased year by year. The import volume of crude oil in 2016 was 380 million tons, with an external dependency of 65.4%; the import volume of crude oil in 2017 was 420 million tons, with an external dependency of 68.4%; the import volume of crude oil in 2018 was 462 million tons, with an external dependency of 70.8%; and the import volume of crude oil in 2019 was 506 million tons, with an external dependency of 72.6%. As a result of the impact of COVID-19, international oil prices fell sharply in 2020, so China's crude oil imports in 2020 still grew, with an import volume of crude oil in 2020 of 540 million tons and an external dependency of 73.5% (Figure 1) [1,2].

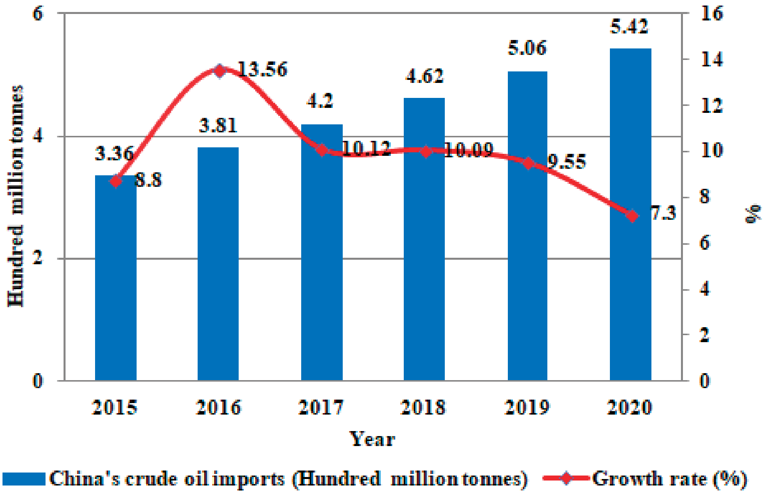

Figure 1. China's crude oil import statistics and growth 2015–2019 [1].

As a large oil-consuming country, China's oil consumption increases year by year, and its growth rate fluctuates. According to the latest data released by the China Federation of Petroleum and Chemical Industries, the apparent domestic consumption of crude oil reached 696 million tons in 2019, an increase of 7.4% year-on-year, representing an increase of 0.5 percentage points over 2018. As a result of the COVID-19 outbreak, the global economy deteriorated sharply, the industrial supply chain suffered a severe setback, and the growth of crude oil consumption slowed down. The apparent domestic consumption of crude oil is now 736 million tons, up 5.6% from 2019, the growth having slowed in a year [3–5].

Africa is an important strategic partner of China and is rich in oil resources. At the end of 2020, Africa had proven oil reserves of nearly 125.1 billion barrels, which represented 7.2% of the world's total proven oil reserves and is one of the eight largest oil-producing regions in the world. Africa's oil production and exports have grown rapidly in the past decade, playing an increasingly important role in the international energy landscape. As an important source of oil imports, the China–Africa oil trade has developed gradually since 1992. In the early stages of cooperation, China mainly imported oil from Angola, Libya and some other countries, with a total of 498,500 tons imported in the first year. The ever-expanding oil trade between China and Africa has laid a good foundation for China–Africa cooperation [6]. After the "Forum on China–Africa Cooperation", the two sides stepped up their cooperation in oil and other energy fields. In 2017, Africa was the second largest source of crude oil imports in China's oil trade, after the Middle East, accounting for 20% of China's total crude oil imports. On a country-by-country basis, 14 of the 44 countries of import origin are African and it is the region with the largest number of import origin countries. There is rapid growth in the China–Africa oil trading relationship. Therefore, given the increasing globalization of the world economy, the international political situation, and the volatility of the oil market, as well as China's increasing demand for oil and its increasing annual import volume and external dependence year by year, it is appropriate that China attaches great importance to Africa's oil resources. Systematic research on the investment environment of the African oil industry will lower the risks and increase the success of our enterprises when seeking to import oil and will also support China's energy security and develop China–Africa relations for mutual benefit [7–9].

With the gradual establishment of the global free trade and open economy system, experts and scholars from many institutions at home and abroad have conducted in-depth research in the field of overseas oil investment. Most of the initial domestic research focused on the risks of overseas oil investment. For example, Cai [10], in a discussion of the risk issues for Chinese oil enterprises, Zhang [11], in a risk analysis of overseas investment of Chinese oil enterprises, and Wang [12] in the overseas investment risk of Chinese petroleum enterprises and its countermeasures, respectively analyzed the political, policy, and economic (etc.) risks encountered in the process of overseas oil investment, and discussed how Chinese petroleum enterprises should take effective measures to avoid and reduce the risks associated with overseas investment. Ye [13] studied the mineral resources of the Democratic Republic of the Congo and concluded that the investment environment in that country needed to be improved. Feng et al. [14] studied Zambia's mining development and mining investment environment and concluded that Zambia's mining investment had good prospects. In recent years, with the rapid development of the theory and technology of mathematical comprehensive evaluation models, mathematical models are increasingly used to evaluate quantitatively the investment environment of the overseas petroleum industry. O'Regan and Moles [15] firstly determined the weight of each factor based on an analytic hierarchy process (AHP), and then, according to the principle of fuzzy relation synthesis, comprehensively graded the overseas investment environment based on many factors. Bo et al. [16] considered the dual attributes of economic attractiveness and investment risk of the investment environment of resource countries, established a decision making optimization model using a bivariate decision making matrix to realize the environmental goal of transnational investment of oil companies via economic attractiveness and risk indices. Li and Li [17] used fuzzy comprehensive evaluation, cluster analysis and principal component analysis to develop a comprehensive evaluation model for the transnational investment environment of Chinese petroleum enterprises. Mu and He [18] used the entropy weight method and matter–element model to evaluate the oil investment environment of five major oil-producing countries in Africa. Duan et al. [19] constructed a fuzzy comprehensive evaluation model of the overseas energy investment environment based on entropy weight. Lin [20] used principal component analysis to produce a comprehensive evaluation of integration management and cooperation among 15 African countries. Liu [21] used AHP to carry out a comprehensive evaluation of the mining investment environment in five central and southern African countries.

To sum up, at present there is no unified evaluation index system, and evaluation of the overseas oil investment environment is influenced by many factors, with each factor influencing other factors, resulting in complex uncertainty. Bringing the final evaluation result more in line with reality will make the forecasting result more accurate, therefore this paper proposes a combination weighting–uncertainty measure model to achieve an overall evaluation of the overseas oil investment environment. The uncertainty measure theory is an ideal mathematical tool because it is able to link various kinds of uncertainty information and comprehensively consider uncertainty factors, such as the fuzziness and complexity of factors impacting the overseas oil investment environment. In the process of applying the uncertainty measure model to a comprehensive evaluation, the determination of the weight plays a decisive role in the final result. However, at present, in the calculation of the weight of evaluation indices, methods such as the subjective expert consultation method and the analytic hierarchy process are used to determine the weight of the index; thus, subjective factors have a greater influence. If insufficient consideration is given to the index information of the evaluation object, it can be easy to deviate from objective reality leading to formation of a significant evaluation bias. On the other hand, if the objective entropy weight method is used to determine the weight of the index, the result of evaluation will be more accurate than using subjective evaluation, but it only considers the significance of data, and does not consider the reality of the evaluation index. In this paper, in order to make the result of evaluation as close as possible to reality, the weighting in the uncertainty measure model is optimized based on minimum relative information entropy to minimize the information loss and make the result of comprehensive evaluation more reasonable and reliable. In order to verify the validity of the model, the oil investment environment of African oil-producing countries was evaluated by the combination weighting–uncertainty measure model. This model provides a new approach to the evaluation of overseas petroleum resources investment environment.

2. Calculation of Combination Weight

For petroleum investment environment modeling, each index weighting is a key point in the evaluation process. The common weighting methods can be classified into two categories: the objective weighting method and the subjective weighting method. Objective weighting methods, such as the entropy weight method and the principal component analysis method, determine index weight based on actual data, using a specific algebraic equation [22]. Subjective weighting methods, for example, AHP, the Delphi method, and the expert grading method, involve a decision maker determining the attribute weight according to the importance degree of the index. The evaluation results are therefore often highly subjective.

In order to minimize the arbitrariness of subjective weighting and give consideration to the preference of decision makers for index weighting, our evaluation of the overseas petroleum investment environment combines the entropy weight method and AHP, improving the evaluation and making the results more accurate and reliable [23,24].

2.1. Determination of the Objective Weight–Entropy Weight Method

The index system generally constructed includes qualitative and quantitative indices, which need to be, respectively, weighted. To determine the weight of the qualitative index by entropy value, the membership degree of the index is taken as the basis. The entropy value and the entropy weight calculation formulae of the qualitative index are as follows:

$$E_i = \frac{\sum\limits_{j=1}^{n} \ln x_{ij}}{\ln n} \tag{1}$$

$$w_i = \frac{1 - E_i}{\sum\limits_{i=1}^{m} (1 - E_i)} \tag{2}$$

where E_i is the entropy value of evaluation index i, j is the criterion layer, n is the number of criterion layers in the system, x_{ij} is the mutual membership of the index, w_i is the weight of the i evaluation index, and m is the number of the evaluation index.

The formula for calculating the weight of the quantitative index using the entropy weight is different from that of the qualitative index. In the calculation of the weight of the quantitative index using the entropy weight, because of the difference of the units between the indices, all the original data should first be standardized. The entropy value and the entropy weight calculation formula of quantitative index are as follows:

$$v_i = 1 + \frac{1}{\lg n} \sum_{j=1}^{n} x_{ij} \lg x_{ij} (j = 1, 2, \cdots, n) \tag{3}$$

$$w_i = v_i / \sum_{i=1}^{m} v_i \, (i = 1, 2, \cdots, m) \tag{4}$$

where x_{ij} is the proportion of evaluation index i in criterion layer j and v_i is the peak value of evaluation index i.

2.2. Determination of the Subjective Weight–Analytic Hierarchy Process

Determining the importance scale between the indices is the basis for establishing the weight judgment matrix, and it is also the first step of AHP. At present, there are four types of importance scale values in common use in China and these are shown in Table 1. Selecting the best scale for the evaluation of the overseas oil investment environment can make the evaluation results more realistic. The order of performance for the above four scales from small to big is: 1–9 scale, index scale, (10/10–18/2) scale and (9/9–9/1) scale, so the best performance (9/9–9/1) scale value was chosen [24,25].

Table 1. Definition and description of importance scale.

Grade	Definition	1–9 Scale	Index Scale	9/9–9/1	10/10–18/2
1	The element *i* is more important than the element *j*	1	9^0	9/9	10/10
3	The element *i* is slightly more important than the element *j*	3	$9^{1/9}$	9/7	12/8
5	The element *i* is slightly obviously more important than the element *j*	5	$9^{3/9}$	9/5	14/6
7	The element *i* is strongly more important than the element *j*	7	$9^{6/9}$	9/3	16/4
9	The element *i* is extremely more important than the element *j*	9	$9^{9/9}$	9/1	18/2
Even number	An even number represents the corresponding scale between two grades				

Overseas investment decision makers use judgement to determine the relative importance of each index and determine the weight judgment matrix $\overline{R}$ according to the actual situation:

$$\overline{R} = \begin{bmatrix} r_{11} & r_{12} & \cdots & r_{1n} \\ r_{21} & r_{22} & \cdots & r_{2n} \\ \vdots & \vdots & \vdots & \vdots \\ r_{m1} & r_{m2} & \cdots & r_{mn} \end{bmatrix} \tag{5}$$

After scoring and obtaining the judgment matrix according to the importance scale table, the eigenvector p corresponding to the largest eigenvalue $\lambda_{\max}$ in the matrix is defined as the initial weight of the index, and the equation is

$$pw = \lambda_{\max} w \tag{6}$$

2.3. Determination of Combination Weight–Minimum Relative Information Entropy

The subjective weight w_{1i} and the objective weight w_{2i} can be combined to obtain the combination weight $w_i (i = 1, 2, \cdots, m)$, and w_i, w_{1i} and w_{2i} should be as close as possible. According to the principle of minimum relative information entropy,

$$\min F = \sum_{i=1}^{m} w_i (\ln w_i - \ln w_{1i}) + \sum_{i=1}^{m} w_i (\ln w_i - \ln w_{2i}) \tag{7}$$

where F is information entropy, $\sum\limits_{i=1}^{m} w_i = 1, w_i > 0, i = 1, 2, \cdots, m$.

The above optimization problem is solved using the Lagrange multiplier method, to obtain the combined weight equation:

$$w_i = \frac{(w_{1i} \cdot w_{2i})^{1/2}}{\sum\limits_{i=1}^{m} (w_{1i} \cdot w_{2i})^{1/2}} (i = 1, 2, \cdots m) \tag{8}$$

Equation (8) states that, in all the combined weights of the satisfiable Equation (7), the least information is required to obtain the geometric mean, and the other combination weights are taken to add the information that we do not actually obtain [25–27].

3. Uncertainty Measure Theory

The universe of n objects to be evaluated and m one-way evaluation index spaces are set as $X = \{x_1, x_2, \cdots, x_n\}$ and $I = \{I_1, I_2, \cdots, I_m\}$, respectively, and the evaluation space is $U = \{C_1, C_2, \cdots, C_p\}$, where C_k is the k evaluation grades, and the k degree is higher than the $k+1$ degree, namely $C_k > C_{k+1}$. The observed value x_{ij} of the object x_i under the index I_j determines x_i in C_k degree of the k evaluation level as $\mu_{ijk} = \mu\left(x_{ij} \in C_k\right)(i = 1,2,\cdots,n; j = 1,2,\cdots,m; k = 1,2\cdots,p)$, so μ_{ijk} is a measure of the degree. If μ_{ijk} meets the three measure criteria of "non-negative, unitary and additivity", then the matrix composed of μ_{ijk} is the evaluation matrix of a single-index measure:

$$\left(\mu_{ijk}\right)_{m\times p} = \begin{bmatrix} \mu_{i11} & \mu_{i12} & \cdots & \mu_{i1p} \\ \mu_{i21} & \mu_{i22} & \cdots & \mu_{i2p} \\ \vdots & \vdots & \vdots & \vdots \\ \mu_{im1} & \mu_{im2} & \cdots & \mu_{imp} \end{bmatrix} \tag{9}$$

When the value of each index and the evaluation level are determined, the weight $w_j(0 \le w_j \le 1, \sum\limits_{j=1}^{m} w_j = 1)$ of each index should be given. Based on the approach of combined weighting using the minimum relative information entropy, the optimal index weights obtained by balancing and optimizing the subjective and objective weight values are calculated, then the multi-index comprehensive measure $\mu_{ik} = \sum\limits_{j=1}^{m} w_j\mu_{ijk}(i = 1,2,\cdots,n; j = 1,2,\cdots,m; k = 1,2\cdots,p)$ is calculated, where $0 \le \mu_k \le 1$, $\sum\limits_{k=1}^{p} \mu_{ik} = 1$, so μ_{ik} is the uncertainty measure, $\left\{\mu_{i1}, \mu_{i2}, \cdots, \mu_{ip}\right\}$ is the evaluation vector of the multi-index comprehensive measure for x_i.

The final comprehensive evaluation level is determined using the credible degree recognition criterion. λ represents the credible degree ($\lambda \ge 0.5$, often $\lambda = 0.6$ or 0.7). When $k_0 = \min\left(k : \sum\limits_{l=1}^{k_p} \mu_{il} \ge \lambda, 1 \le l \le k\right)$, x_i is considered to belong to the C_{k_0} of the k_0 evaluation level.

In addition, to determine the x_i evaluation level, sometimes the order of importance for x_i is required. If $C_1 > C_2 > \cdots > C_p$, the value of C_{l_0} is set as n_{l_0}, so $n_{l_0} > n_{l+1}$, and $q_{x_i} = \sum\limits_{l=1}^{p} n_l\mu_{il}$, where q_{x_i} is the uncertainty importance of the evaluation factor x_i, $q = \left\{q_{x_1}, q_{x_2}, \cdots, q_{x_p}\right\}$ is called the uncertainty importance vector, which can be used to obtain the order of importance for x_i activity [28–34].

4. A Case

Africa, as the world's second largest continent by area and population after Asia, includes 56 countries and regions. According to the country investment guide data from the National Bureau of Statistics of some African countries, the World Bank, and the Ministry of Commerce of the People's Republic of China, Africa's total population is about 1.286 billion, of which Nigeria and Ethiopia each account for more than 100 million. Africa's nominal GDP reached USD 2.2 trillion in 2020, and although most of the world's economies experienced negative growth in 2020 as a result of COVID-19, Africa's economic performance was strong, with nearly half of the economies recording positive growth. Among them, the growth rate of Egypt's economy was 19.68%, the fastest in Africa, and the second fastest was Guinea, with a growth rate of 12.32%. As a result of political turmoil and a tough business climate, the fastest economic downturn in Africa was seen in Libya, where GDP reduced by 45.23% in 2020 [1,35,36].

Africa is very rich in energy and resources, and thus has a "world oil depot" reputation. Compared to other regions, Africa has very large oil reserves in more than 20 countries. According to the *bp Statistical Review of World Energy 2021*, the top five proven oil reserves in Africa by the end of 2020 were in Libya (6.3 billion tons, 48.4 billion barrels, total share 2.8%), Nigeria (5 billion tons, 36.9 billion barrels, total share 2.1%), Algeria (1.5 billion tons, 12.2 billion barrels, total share 0.7%), Angola (1.1 billion tons, 7.8 billion barrels, total share 0.4%), and South Sudan (500 million tons, 3.5 billion barrels, total share 0.2%) (Figure 2) [1,35,36].

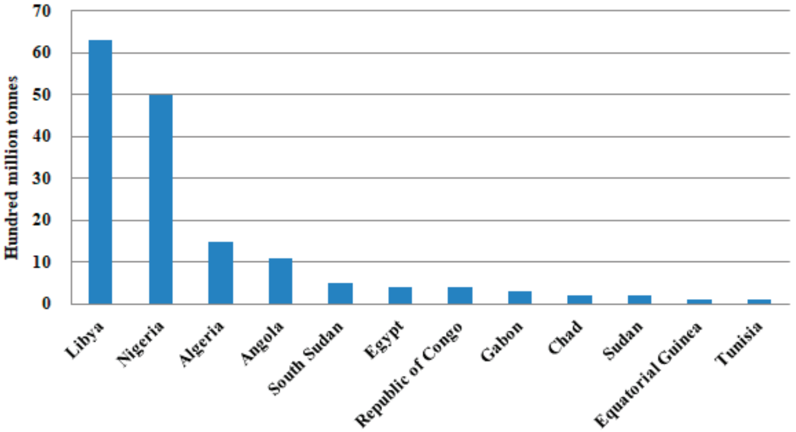

Figure 2. Top 12 countries with proven oil reserves in Africa [36].

As an important source of China's oil imports, Africa was the second largest source of crude oil imports in China's oil trade in 2017, second only to the Middle East, and accounted for 20% of China's total crude oil imports. On a country-by-country basis, 14 of the 44 countries of origin for imports are African countries and it is the region with the largest number of countries of origin for imports into China. China–Africa oil cooperation shows rapid growth. However, while political and regional security in Africa has been generally stable since the mid-1990s, in recent years there have been more frequent political risks, such as the "Arab Spring" in 2011, the north–south split in Sudan, Nigeria's "Boko Haram" terrorist activities, etc. These all pose a serious threat to the development of business related to oil resources. In addition, although some countries are currently stable, they have long been in a state of "Strongman Politics". Their social governance has not yet entered a stable period, and various types of social conflicts are prominent, so the risks of potential coups, civil wars, separatism, terrorism, etc., cannot be underestimated [1,2,7,8]. Therefore, in order to provide a useful reference for Chinese enterprises wishing to invest in the African oil field, it is necessary to carry out a comprehensive evaluation of the key African oil countries.

4.1. Construction of the Evaluation Index System

As an international investment environment, the petroleum industry not only involves specific countries and regions, but also wider factors relating to the petroleum industry. Thus, when analyzing the investment environment of the petroleum industry, we should not only consider the influence factors of the traditional international investment environment, but also consider the resource endowment factors of the resource country in question. Therefore, in order to comprehensively and objectively understand the investment environment of the overseas oil industry, the relevant literature was collected and analyzed. To capture the actual situation in Africa, we used accepted classification rules and data published by authoritative institutions, such as the World Bank, as the basis for the evaluation [17,18,20,35,37–39], selecting six factors related to resource endowment, political stability, economic development level, and economic stability.

The classification standard and valuation of each index are shown in Table 2. According to the classification standard and evaluation objectives, the risk was divided into four levels: I, II, III and IV, which reflect excellent, good, medium and poor, respectively. The index data for the oil investment environment in selected African countries are shown in Table 3.

Table 2. Evaluation indices and classification standard for investment environment evaluation in African oil-producing countries.

Evaluation Index		Evaluation Level			
		Excellent (C_1)	Good (C_2)	Medium (C_3)	Poor (C_4)
Resource endowment	Proved reserves/thousand million barrels (x_1)	40–60	20–40	5–20	0–5
	Production/million tons (x_2)	100–120	80–100	40–80	0–40
Political stability	Unemployment rate/% (x_3)	7–8	8–9	9–11	11–13
	Military expenditure/% of GDP (x_4)	0–1	1–2	2–4	4–8
Economic development level	GDP per capita/current US $ (x_5)	10,000–14,000	6000–10,000	4000–6000	1000–4000
Economic stability	GDP Growth/annual % (x_6)	>5	3–5	0–3	<0

Table 3. Evaluation index data for each African oil-producing country.

Evaluation Index		Algeria	Angola	Chad	Republic of Congo	Egypt	Equatorial Guinea	Gabon	Libya	Nigeria	South Sudan	Sudan	Tunisia
Resource endowment	Proved reserves/thousand million barrels	12.2	7.8	1.5	2.9	3.1	1.1	2.0	48.4	36.9	3.5	1.5	0.4
	Production/million tons	57.6	64.5	6.6	15.8	30.0	7.5	10.4	18.3	86.9	8.4	4.2	1.7
Political stability	Unemployment rate/%	11.4	31.6	2.3	10.3	7.3	9.2	20.5	18.63	33.3	12.7	17.7	17.8
	Military expenditure/% of GDP	6.7	1.6	3.1	3.4	1.2	1.3	1.8	3.7	0.6	3.6	1.1	2.9
Economic development level	GDP per capita/current US $	3310	1896	614	2092	3548	7157	6991	3700	2097	748	595	3320
Economic stability	GDP Growth/annual %	−5.5	−4.0	−0.9	−7.9	3.6	−4.9	−1.3	−31.3	−1.8	−3.6	−1.6	−8.6

Data source: 2020 Statistical data of World Bank collated, https://data.worldbank.org.cn/, accessed on 27 October 2021 [35].

4.2. Determination of Index Weights

In our study, firstly, the weight values of all the indices in the comprehensive evaluation index system were calculated using the subjective AHP. Then, the weight values of all indices were calculated using the objective entropy weight method (taking Algeria as an example). Finally, combining the index weights obtained using AHP and the entropy weight method, respectively, in accordance with the principle of minimum relative information entropy, all index weights in the comprehensive evaluation index system were obtained using the Lagrange multiplier optimization method. The final calculation is shown in Table 4.

Table 4. Index weights.

Evaluation Index	AHP	Entropy Weight Method	Minimum Relative Information Entropy
x_1	0.04	0.16	0.10
x_2	0.11	0.13	0.16
x_3	0.09	0.18	0.17
x_4	0.12	0.18	0.19
x_5	0.24	0.18	0.27
x_6	0.40	0.18	0.11

4.3. Single Index Function of Uncertainty Measure

Based on the widely used linear uncertainty construction method, the measure function of each rationality index was constructed according to the rationality index and classification standard of the investment environment evaluation data of the African oil-producing countries shown in Table 2 (Figure 3).

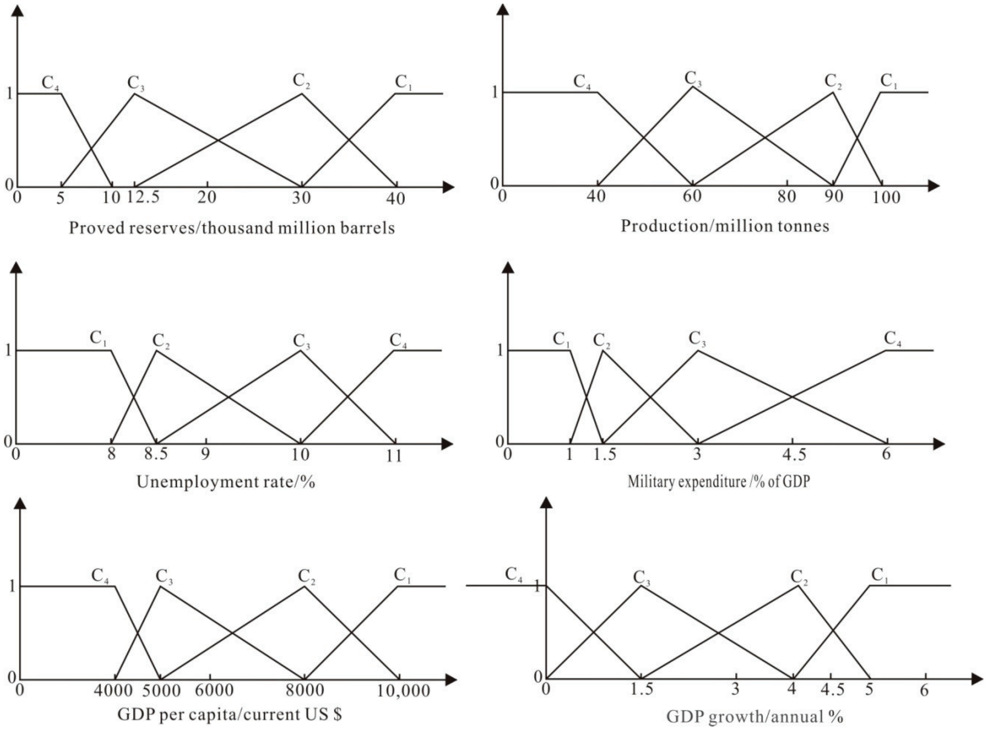

Figure 3. Single index measure function of each single index in evaluation index system.

Based on the single index measure function constructed in Figure 1 and the specific values of the survey of evaluation indices in Algeria in Table 2, the evaluation matrix of single index measure in Algeria can be obtained as follows:

$$\mu_{A_1} = \begin{bmatrix} 0 & 0 & 0.96 & 0.04 \\ 0 & 0 & 0.88 & 0.12 \\ 0 & 0 & 0 & 1 \\ 0 & 0 & 0 & 1 \\ 0 & 0 & 0 & 1 \\ 0 & 0 & 0 & 1 \end{bmatrix} \quad (10)$$

4.4. Calculation of Multi-Index Measure Evaluation Matrix

Based on the optimal combination weight of each evaluation index in the comprehensive evaluation index system calculated using the combination weight method of minimum relative information entropy, the weight of each evaluation index in Algeria $\{w_1, w_2, w_3, w_4, w_5, w_6\} = \{\ 0.10 \quad 0.16 \quad 0.17 \quad 0.19 \quad 0.27 \quad 0.11\ \}$, and, according to the single index measure matrix and the multi-index measure calculation formula, Algeria's multi-index measure vector is $\mu_1 = \varpi_1 \cdot \mu_{A_1} = [\ 0 \quad 0 \quad 0.24 \quad 0.76\ ]$.

4.5. Credible Degree Recognition

Credible degree λ is taken to be 0.6, k_0 = 1.00 > 0.6; that is, Algeria's level is C_3. Eleven other countries were evaluated in the same way. The results of the evaluation are shown in Table 5.

Table 5. Evaluation of the investment environment of African oil-producing countries based on the uncertainty measure model of combination weighting.

Country	Comprehensive Uncertainty Measure				Evaluation Result
	C_1	C_2	C_3	C_4	
Algeria	0	0	0.24	0.76	C_4
Angola	0	0.19	0.18	0.63	C_4
Chad	0.16	0	0.17	0.67	C_4
Republic of Congo	0	0	0.25	0.75	C_4
Egypt	0.25	0.14	0.02	0.59	C_4
Equatorial Guinea	0.06	0.34	0.13	0.47	C_4
Gabon	0	0.28	0.11	0.61	C_4
Libya	0.11	0	0.12	0.77	C_4
Nigeria	0.26	0.16	0.02	0.56	C_4
South Sudan	0	0	0.12	0.88	C_4
Sudan	0.12	0.03	0	0.85	C_4
Tunisia	0	0.01	0.16	0.83	C_4

4.6. Order-Arranging of Favorable

According to the order formula, because $C_1 > C_2 > C_3 > C_4$, take $n_l = 10 - 2q$, where $1 \leq q \leq 4$, then $q = \{q_1, q_2, q_3, \cdots, q_{12}\} = \{\ 2.48 \quad 3.12 \quad 3.30 \quad 2.50 \quad 4.10 \quad 3.98 \quad 3.34 \quad 2.90 \quad 4.24 \quad 2.24 \quad 2.84 \quad 2.36\ \}$. The ranking of the oil investment environment in 12 African countries from large to small is: Nigeria, Egypt, Equatorial Guinea, Gabon, Chad, Angola, Libya, Sudan, Republic of Congo, Algeria, Tunisia and South Sudan.

5. Analysis of Africa's Oil Investment Environment

Under the influence of the epidemic and energy transformation, Africa's production experienced the greatest decline in 2020, when overall production dropped by 18.7%. In 2020, oil production in Africa was 327.3 million tons, and the top 12 major oil-producing countries were Nigeria, Angola, Algeria, Egypt, Libya, Republic of Congo, Gabon, South Sudan, Equatorial Guinea, Chad, Sudan and Tunisia, their combined production accounting for 95% of Africa's total oil production. At the end of 2020, Africa's total proven oil reserves stood at 125.1 billion barrels, and the proven reserves of its top 12 major oil-producing countries accounted for 97% of Africa's total proven reserves [36]. Therefore, the evaluation of the investment environment of the oil industry in the top 12 oil-producing countries in Africa is representative and instructive for oil trade and oil security between China and Africa.

According to the evaluation results, when China invests in the African oil industry, it should give priority to Nigeria and Angola, followed by Algeria, Egypt and Libya, and so on. Investment in these countries should also focus on the country's extreme indices, such as the rising trend of civil violence and political confrontation in Africa in recent years. Ethnic and armed conflicts have become more common, such as in Libya, South Sudan, Central Africa, Republic of Congo, and Nigeria. Government governance as a whole is among the lowest in the world, and the public service provision is inadequate. In Africa, employment, education, health care, public transport, roads, and housing are all negative compared to other countries, and Sudan is now the most developed country in Africa. The two disadvantages of African countries are high political and economic risks, and high operational risks; whereas the two main advantages are the advantageous oil and gas cooperation terms, which are the best in the world. As some African countries do not have an existing oil and gas industry, there is scope to agree mutually advantageous terms. Africa and China enjoy good political relations and strong economic complementarity, which are our two key advantages.

Over the years, China has adhered to a principle of equal cooperation for oil development in Africa, taking mutual benefit and win-win as its goal, and working for the benefit of the local society, thus further cementing the traditional friendship between China and Africa. China's cooperation with African oil-producing countries is based on its deep financial strength and begins with active assistance for infrastructure construction, so as to win the support and understanding of local governments and people.

In general, Africa is rich in oil and gas resources, and African governments have been active in opening up their petroleum industries and formulating policies to support foreign investment in order to develop their own industries and promote the development of their economies. For example, Nigeria's long-delayed *Petroleum Industry Bill*, which was finally approved by the National Assembly and is expected to become law by the end of the year, will create a favorable investment environment for Nigeria's oil and gas industry. Angola and neighboring Zambia have signed a USD 5 billion memorandum of understanding to study the feasibility of building a pipe between the port city of Lobito in Angola and Lusaka, the capital of Zambia, which is expected to cost about USD 5 billion. At the same time, the international community has been of great help to Africa's political, military and economic sectors. For example, the Qatar Petroleum company, together with its partners, plans to invest about USD 7 billion in Angola over the next four years, for exploration, production, oil refining, and other purposes. In view of the economic burden on African countries which has been aggravated by COVID-19, on the basis of the implementation of the G20 debt relief initiative, China will cancel the interest-free loans to Africa by the end of 2020 under the Forum on China–Africa Cooperation. In short, Africa's oil investment environment is more positive than negative, with more opportunities than challenges.

6. Conclusions

As the second largest source of crude oil imports in China's oil trade, Africa plays a vital role in China's oil security. Therefore, in order to comprehensively and objectively understand and analyze the investment environment of the oil industry in African oil-producing countries, this paper systematically studied the investment environment of the petroleum industry in African oil-producing countries, and the main results were as follows:

(1) Based on the characteristics of overseas oil investment, an index system for the comprehensive evaluation of the overseas oil investment environment was constructed, and the uncertainty measure theory was applied in this process. The weighting of the multi-level index system was determined based on the combination weighting method of minimum relative information entropy. The results of the evaluation can effectively overcome the shortcomings of the single subjective weighting in terms of randomness and fuzziness, and the fact that the single objective weighting does not take into account the actual situation of the evaluation index. This makes the weight assignment more realistic and provides a new method for the evaluation of the overseas petroleum investment environment.

(2) The oil investment environment of the top 12 oil-producing countries in Africa was comprehensively evaluated based on the combination weighting–uncertainty measure evaluation model. The multi-index measure evaluation matrix of the top 12 oil-producing countries in Africa was calculated, and the oil investment environment of the top 12 oil-producing countries in Africa was classified according to the credible degree recognition and ordered. The result of the evaluation is basically consistent with the facts.

(3) Under the influence of the epidemic and energy transformation, the proven reserves of many oil companies have been greatly reduced. However, the search for new oil and gas production reserves has become an urgent task for the energy industry, and Africa, as one of the eight largest oil-producing regions in the world, has attracted much oil and gas capital because of its resource endowment and unique advantages. Along with the discovery of a series of oil and gas reserves, the investment in infrastructure in Africa has greatly increased, and the related technologies and services have also made excellent progress, paving the way for the development of the oil and gas industry.

In this paper, an evaluation model of overseas oil investment environment based on the combination weighting–uncertainty measure theory was established for the first time and applied in the example. However, because the evaluation of the overseas oil investment environment is influenced by many factors, and each factor influences the others, leading to complex uncertainty, the evaluation model needs to be constantly studied and improved to enhance the universal applicability and precision of the method and achieve an accurate evaluation of the overseas oil investment environment.

Author Contributions: H.H. conceived and designed the study and wrote the paper. W.L. helped to analyze and interpret the data. R.X. helped to analyze and manage the data. Y.Z. helped to draw the figures. All authors have read and agreed to the published version of the manuscript.

Funding: This research was supported by the Natural Science Foundation of Shaanxi Province (2016JM4001), the Special Fund for Basic Scientific Research of Central Colleges (310827151056, 310827153408, 310827173702 and 300102280401), the Science and Technology Project of Guizhou Province ([2021] 408), and the major project of the Bureau of Geology and Mineral Exploration and Development Guizhou Province ([2021] 1).

Institutional Review Board Statement: Not applicable.

Informed Consent Statement: Not applicable.

Data Availability Statement: All data generated or analyzed during this study are included in the paper.

Conflicts of Interest: The authors declare that there are no conflict of interest regarding the publication of this paper.

References

1. General Administration of Customs. P. R. China. Available online: http://www.customs.gov.cn/ (accessed on 25 October 2021).
2. Kong, Q.X.; Guo, R.; Wang, Y.; Sui, X.P.; Zhou, S.M. Home-country environment and firms' outward foreign direct investment decision: Evidence from Chinese firms. *Econ. Model.* **2020**, *85*, 390–399. [CrossRef]
3. China Federation of Petroleum and Chemical Industries. Available online: http://cpcia.org.cn/ (accessed on 25 October 2021).
4. Behdad, S.; Gholamhassan, N.; Mohammad, A.Z. A Review of the Existing Potentials in Biodiesel Production in Iran. *Sustainability* **2022**, *14*, 3284.
5. Behdad, S.; Gholamhassan, N. Impact of COVID-19 on biofuels global market and their utilization necessity during pandemic. *Energy Equip. Syst.* **2021**, *9*, 371–382.
6. Zhou, X.B.; Wu, J.X.; Zhao, Y. The strategic significance of China-Africa oil cooperation and key areas selection. *World Reg. Stud.* **2011**, *20*, 63–69.
7. Abdulrasheed, Z.; Guo, L.; Irfan, K.; Abhinav, J.; Vincent, T.; Rafael, A. Are abundant energy resources and Chinese business a solution to environmental prosperity in Africa? *Energy Policy* **2022**, *163*, 112829.
8. Zhao, Y.; Shi, X.P.; Song, F. Has Chinese outward foreign direct investment in energy enhanced China's energy security? *Energy Policy* **2020**, *146*, 111803. [CrossRef]
9. Odgaard, O.; Delman, J. China's energy security and its challenges towards 2035. *Energy Policy* **2014**, *71*, 107–117. [CrossRef]
10. Cai, J.G. *The Study of Foreign Investment Risk about Oil-Gas Enterprises China*; China University of Petroleum: Qingdao, China, 2009.
11. Zhang, Q. Discussion on the risk of oil enterprises in China. *Mod. Bus.* **2011**, *18*, 47–48.
12. Wang, F. The risks and countermeasures of China oil enterprises' overseas investment. *China Min. Mag.* **2012**, *21* (Suppl. S1), 189–192.
13. Ye, Q. Next stop, invest in Congo. *Bus. Obs.* **2018**, *12*, 86–89.
14. Feng, Z.S.; Han, K.H.; Zhang, G.; Tang, X. Analysis of new mines and minerals act and mining investment environment in Zambia. *Land Resour. Inf.* **2018**, *3*, 19–24.
15. O'Regan, B.; Moles, R. Modelling to learn a case study in international minerals investment. *Corp. Environ. Strategy* **2001**, *1*, 298–299. [CrossRef]
16. Bo, Q.L.; Zhang, Y.H.; Xue, L.Q.; Guo, X.Z. Dual-variable and objective programming of investment environment for international oil company. *Pet. Explor. Dev.* **2005**, *32*, 135–137.
17. Li, H.F.; Li, N. Building and analysis of a model for assessing the climate for overseas investment by Chinese oil companies. *Int. Pet. Econ.* **2007**, *15*, 41–46.
18. Mu, X.Z.; He, F. Evaluation of oil investment environment in five oil-producing countries in Africa based on entropy weight method and matter-element model. *Enterp. Econ.* **2015**, *5*, 119–122.
19. Duan, F.; Ji, Q.; Liu, B.Y.; Fan, Y. Energy investment risk assessment for nations along China's Belt & Road Initiative. *J. Clean. Prod.* **2017**, *170*, 535–547.
20. Lin, M. *A Study on the Comprehensive Evaluation of Sino-African Integrated Business Cooperation in Petroleum Industry*; China University of Geosciences: Beijing, China, 2019.
21. Liu, X.Y. *Study on the Prospect of Mining Investment in Five Central and Southern African Countries*; China University of Geosciences: Beijing, China, 2020.

22. Shao, L.; Chen, Y.; Zhang, S.S. Fuzzy synthetic evaluation of cross-border atmospheric environment risk source based on entropy and AHP. *China Popul. Resour. Environ.* **2010**, *20*, 135–138.
23. Gong, L.H. Establishment of the index system of clean production assessment of ferrous metal mines. *Met. Mines* **2003**, *33*, 57–59.
24. Zhou, H.L.; Yang, S.; Chen, J.H. Research and application of cleaner production evaluation index system in gold mine. *Gold Sci. Technol.* **2017**, *25*, 93–100.
25. Li SWei, H.; Ni, X.L.; Gu, Y.W.; Li, C.X. Evaluation of urban human settlements quality in Ningxia based on AHP and the entropy method. *Chin. J. Appl. Ecol.* **2014**, *25*, 2700–2708.
26. Jin, J.L.; Wu, K.Y.; Li, R.Z.; Hong, T.Q. Region water security evaluation method based on information entropy and improved fuzzy analytic hier-archy process. *J. Hydroelectr. Eng.* **2007**, *26*, 61–66, 110.
27. Wang, D.J.; Zhou, Q.M.; Chang, Z.L.; Sun, J. A new method of multi-factor synthesis evaluation. *Stat. Decis.* **2007**, *4*, 137–138.
28. Liu, K.D.; Wu, H.Q.; Wang, N.P. *Uncertainty Mathematics*; Huazhong University of Science and Technology Press: Wuhan, China, 1997.
29. Liu, K.D.; Wu, H.Q.; Pang, Y.J. *Mathematics Treatment and Application of Uncertainty Information*; Science Press: Beijing, China, 1999.
30. He, H.J.; Su, S.R.; Wang, X.J.; Li, P. Study and application on comprehensive evaluation model of landslide hazard based on uncertainty measure theory. *J. Cent. South Univ. Sci. Technol.* **2013**, *44*, 1564–1570.
31. He, H.J.; Liu, W.; Yang, X.K.; Luo, Y.Z.; Fan, Y. Mineral resource predication and evaluation based on uncertainty measure theory: A case of Hutouya mine field of Qinghai. *J. Northwest Univ. Nat. Sci. Ed.* **2014**, *44*, 615–620.
32. He, H.J.; Yan, Y.M.; Qu, C.X.; Fan, Y. Study and Application on Stability Classification of Tunnel Surrounding Rock Based on Uncertainty Measure Theory. *Math. Probl. Eng.* **2014**, *2014*, 626527. [CrossRef]
33. He, H.J.; Zhao, Y.N.; Yang, X.K.; Gao, Y.N.; Wu, X. Study and Application of Safety Risk Evaluation Model for CO2 Geological Storage Based on Uncertainty Measure Theory. *Math. Probl. Eng.* **2015**, *2015*, 964204. [CrossRef]
34. He, H.J.; Zhao, Y.N.; Zhang, Z.M.; Gao, Y.N.; Yang, L.W. Prediction of coalbed methane content based on uncertainty clustering method. *Energy Explor. Exploit.* **2016**, *34*, 273–281. [CrossRef]
35. The World Bank. Available online: https://data.worldbank.org.cn/ (accessed on 27 October 2021).
36. bp Statistical Review of World Energy July 2021. Available online: http://www.bp.com/statisticalreview (accessed on 26 October 2021).
37. Feng, G.; Mu, X.Z. Cultural challenges to Chinese oil companies in Africa and their strategies. *Energy Policy* **2010**, *38*, 7250–7256. [CrossRef]
38. Tao, F. An environmental assessment model construction of China's petroleum companies' investment in Africa-based on principal component analysis. *J. China Univ. Pet. Ed. Soc. Sci.* **2010**, *26*, 7–12.
39. Li, Z.X.; Liu, J.Y.; Luo, D.K.; Wang, J.J. Study of evaluation method for the overseas oil and gas investment based on risk compensation. *Pet. Sci.* **2020**, *17*, 858–871. [CrossRef]

MDPI
St. Alban-Anlage 66
4052 Basel
Switzerland
Tel. +41 61 683 77 34
Fax +41 61 302 89 18
www.mdpi.com

Sustainability Editorial Office
E-mail: sustainability@mdpi.com
www.mdpi.com/journal/sustainability

MDPI
St. Alban-Anlage 66
4052 Basel
Switzerland

Tel: +41 61 683 77 34

www.mdpi.com

ISBN 978-3-0365-6064-9